Tuning the Electronic Properties of Graphite for Enhanced and Sustained Electron Transfer Kinetics: Characterization, Properties and Applications

A Dissertation

Presented in Partial Fulfillment of the Requirements for the

Degree of Doctor of Philosophy

with a

Major in Chemistry

in the

College of Graduate Studies

University of Idaho

by

Okechukwu C. Nwamba

Major Professor: Jean'ne M. Shreeve, Ph.D.

Committee Members: D. Eric Aston, Ph.D.; Chien M. Wai, Ph.D.; Robert V. Fox, Ph.D.

Dean: Ginger E. Carney, Ph.D.

May 2019

Authorization to Submit Dissertation

This dissertation of Okechukwu C. Nwamba, submitted for the degree of Doctor of Philosophy with a Major in Chemistry and titled "Tuning the Electronic Properties of Graphite for Enhanced and Sustained Electron Transfer Kinetics: Characterization, Properties and Applications" has been reviewed in final form. Permission, as indicated by the signatures and dates below, is now granted to submit final copies to the College of Graduate Studies for approval.

Major Professor: _____ Date: _____
                                           Jean'ne M. Shreeve, Ph.D.

Committee Members: _____ Date: _____
                                           D. Eric Aston, Ph.D.

                                  _____ Date: _____
                                           Chien M. Wai, Ph.D.

                                  _____ Date: _____
                                           Robert V. Fox, Ph.D.

Dean: _____ Date: _____
                                           Ginger E. Carney, Ph.D.

Abstract

On thermal treatment, eight different graphite materials became resistant to air aging for at least nine weeks compared to the usual time of hours to a few days when assayed in 1mM ferri-ferrocyanide solution. In addition, resistance to aging was found for at least seven days, when immersed in 1mM ferri-ferrocyanide solution compared with the frequently reported few minutes to hours. Experimental results confirm that with heat treatment, HOPG-ZYH, graphite rods, pyrolytic graphites, graphite felts, and natural and artificial graphites undergo structural reorganization which leads to the restructuring of their electronic nature. It is this electronic restructuring that enhances and sustains their electrochemical properties. The extent of this reorganization is dependent on the initial disordered state, which in turn is important to the final structural and electronic conditions. The results strongly suggest that the primary factor enhancing the electronic response of heat-treated materials is from an *overall* higher density of states localized on delocalizing π bonds compared to their controls. This structural reorganization of the graphites also supports a degree of crystallinity along the lattice sites that enable carrier hopping irrespective of adventitious oxygen-containing and hydrocarbon moieties that is synonymous with aging induced sluggish electron transfer kinetics. The attributes of this electronic structure demonstrate a strongly correlated system which exhibit a non-perturbative behavior. A one-dimensional Hubbard model is applied to describe this behavior that explains the surface-to-electronic chemistry of treated graphites by addressing both their enhanced electrochemical performance and their depressed aging effects. Additionally, these thermally treated graphites were used as support systems for the growth of Prussian Blue nano particles. The PBNP doubled the capacitance of the high surface area graphite felt; a property that lends these PBNP@graphite felts for, amongst other things, ion-sieving, energy storage and conversion purposes. Since, increased electron transfer kinetics make materials more prone to corrosion, both the structure and corrosion resistance of the treated and pristine graphites were performed. The data collated suggest that the thermally treated graphites, with increased electron transfer kinetics, had similar corrosion resistance properties to the pristine and their work functions were no much different. Yet, the charge transfer parameter of the treated pyrolytic graphites was some three order of magnitude less to the pristine. The results suggest that a correlated electronic structure with enhanced quantum tunneling of electrons through the graphite surfaces, irrespective of surface functional groups or even edges, was responsible for the corrosion resistant nature of the treated graphites.

Acknowledgements

It is with deepest appreciation and emotions too, that I pen down the following: My very sincere and heart-felt thanks to my boss, mentor and adviser, Prof. Dr. Jean'ne M. Shreeve. I am writing these lines because Dr. Shreeve stood with me and by me as the amazon that she is. Without her, this dissertation probably would never have happened!

I sailed on the wings of an Eagle and was ushered into the world of Prof. Dr. D Eric Aston. As I did say several times in public, I couldn't have asked for a better co-boss and supervisor; I couldn't have scripted my life any better. Dr. Aston's keen mind, sharp observations and intellectual Prowers is indisputable to my success in this program. Thanks a million Dr. Aston, I am grateful. My sincere appreciations to Prof. Wai and Dr. Robert Fox for been there for me, in turbulent times that many would have preferred to shy away from. My warmest thanks to Dr. Fox for his kind words and encouragements.

My warmest appreciation to Dr. Ginger Carney, the dean of the College of Science and Dr. Jerry McMurtry, the dean of the College of Graduate Studies for their support – both morally and financially. It is on record that the office of the dean of science supported my dissertation via a research fund, while both deans would support a Research Assistantship in the semester of my defense. Besides and perhaps even more importantly, it took both deans standing firm to truth and principles, without which my degree would have been truncated to a non-thesis MS or worse, a no-degree situation. Thank you, I remain forever grateful.

My appreciation to Prof. David McIlroy and Dr. Elena Echeverria of the Physics Department, Oklahoma State University for their support with the collation of photoelectron spectroscopy data. Dr. Louis Scudiero of the Dept. of Chemistry and Material Science and Engineering Program at Washington State University is warmly thanked for helpful discussions on photoelectron spectroscopy. My warmest appreciation to Angstrom Sciences, CA for high resolution light microscopy-AFM images of some of my samples. My thanks also to Dr. Indrajit Charit and Dr. Raja Krishnan Raja for access to the use of their labs for the heating protocol and electrochemical tests respectively. Additionally, I am grateful to Dr. Krishnan for taking off time from very busy schedules to go through various electrochemical impedance spectroscopy data with me. I am grateful also to Dr. Batric Pesic for helpful discussions on corrosion measurements, techniques and data interpretations. My deepest appreciation to Dr. Tom Williams for working around various time schedules to accommodate my needs with electron microscopy imaging. My sincerest appreciation to James Moberly of the chemical engineering department and Dr. Kristopher Waynant of the chemistry department, university of Idaho for the use of their lab space and research equipment at the Integrated

Okechukwu Charles Nwamba

March 2019

Dedication

To Chinwendu my lovely wife, through thick and thin, you have been with me. To Dale and Cynthia Gentry, Linda and Verne Geidl, Bill and Wendy Kerr, Marilyn Lewis, Greg and Brenda Ahman, Larry and Maggie O'Keefe, Fr. Chase Hasenoehrl, my entire St. Augustine's Catholic Centre family, my families in Nigeria and Nnanyelugo, my Nobel brother.

… In a desert land He found *me*,
in a barren and howling waste.
He shielded *me* and cared for *me*;
He guarded *me* as the apple of His eye,
like an eagle that stirs up its nest
and hovers over its young,
that spreads its wings to catch them
and carries them aloft.
The Lord alone led *me*;…
(Deuteronomy 32: 10-12)

This work is dedicated to my Paraclete, the Holy Spirit.

Table of Contents

List of Tables

List of Figures

Statement of Contribution

Chapter 2: Thermal Modification of Graphite for Fast Electron Transport and Increased Capacitance.

OCN conceived the idea of the work. Photoelectron spectroscopy data were collated from Oklahoma State University. OCN did the remainder of the experiments and wrote the manuscript

Chapter 3: Electrochemical Stability and Capacitance of In-Situ Synthesized Prussian Blue on Thermally-Activated Graphite.

OCN conceived the idea of the work. Photoelectron spectroscopy data were collated from Oklahoma State University. OCN did the remainder of the experiments and wrote the manuscript.

Chapter 4: Increased Electron Transfer Kinetics and Thermally Treated Graphite Stability through Improved Tunneling Paths.

OCN conceived the idea of the work. Photoelectron spectroscopy data were collated from Oklahoma State University. Light-microscopy-AFM images were collated by Angstrom Sciences, CA. OCN did the remainder of the experiments and wrote the manuscript.

Chapter 1: Introduction

1.1   The Challenges

For over half a century, active researches into the carbon field have sought to understand the reason(s) and mechanism(s) of why and how carbon materials, especially graphite, become sluggish electron transporters on air exposure, sometimes within minutes to hours. Several techniques have been employed to try to restore the heterogeneous electron transfer (HET) kinetics of carbonaceous materials after air- or solution- induced oxidation (aging). Such techniques and/or procedures include mechanical polishing as commonly employed on glassy carbon electrodes, vacuum heat treatment, or heat treatment under an inert gas atmosphere; also, combined treatment such as laser-based thermal treatment protocols; further, electrochemical polarization such as pre-anodization, and plasma activation treatments such as radio-frequency plasma, among many others.[1–3] Yet despite all the available techniques thus far employed, the issue of aging remains a paramount consequence; limiting the use of carbon materials in several noteworthy applications. Every activation protocol employed thus far, has at most, sustained electron transport by just a few hours.[1–3] The problem remained insoluble and was neglected for a long period until the advent of graphene.

With the entry of graphene into the materials research race, the question arose again[4] since graphene for electrochemistry and optoelectronics was also susceptible to the same air oxidation induced sluggish electron transport (slow HET kinetics) or aging that is observed for its parent compound, graphite.[5–8] HET kinetics are fundamental in solid carbon materials (electrode)-electrolyte interactions, predicting the performance of a material in electrochemical applications, [9,10] and playing significant roles in molecular electronics, electrochemical energy storage and conversion, sensing, and electro-oxidative reactions.[5,11–19] The result is that even the purported "wonderful" applications of graphene have been called to question.[20]

1.2   The Surface Chemistry and Influence on Electrochemical Activities.

The surfaces of carbon materials, especially graphite, graphene, carbon nanotubes and fullerenes, do not remain pristine or inert even during a limited time span.[3,7,21,22] It is now generally accepted that solid electrode surfaces are gradually deactivated which may be due to the adsorption of adventitious impurities such as chemisorbed species, particularly oxygen[23–26] (either from air and or from adsorbed water molecules on the surfaces of the carbon materials)[27] and hydrocarbons.[7,8,21,28–30]

These surface adsorbents are ubiquitous, from ambient air [7,28,30] or electrolyte solutions, [26] and their presence always precede electrochemical experiments.[31] These surface-adsorbed species have been suggested to hamper electron transfer kinetics, resulting in sluggish electron transfer rates, due to oxidation-induced aging,[2] and accompanying impediments for various carbon material uses [4,15]. Given in Figure 1.1 is a plot of the cyclic voltammetry scans of natural graphite (aged and cleaved), highly ordered pyrolytic graphite (HOPG) (aged and cleaved), platinum (Pt) and gold (Au) and a bar chart showing the corresponding heterogeneous electron transfer (HET) rate constants. These figures highlight pictorially, the HET rate constants decay of graphites due to aging, in comparison to Pt and Au both of which are stable with respect to air- and solution-induced aging.
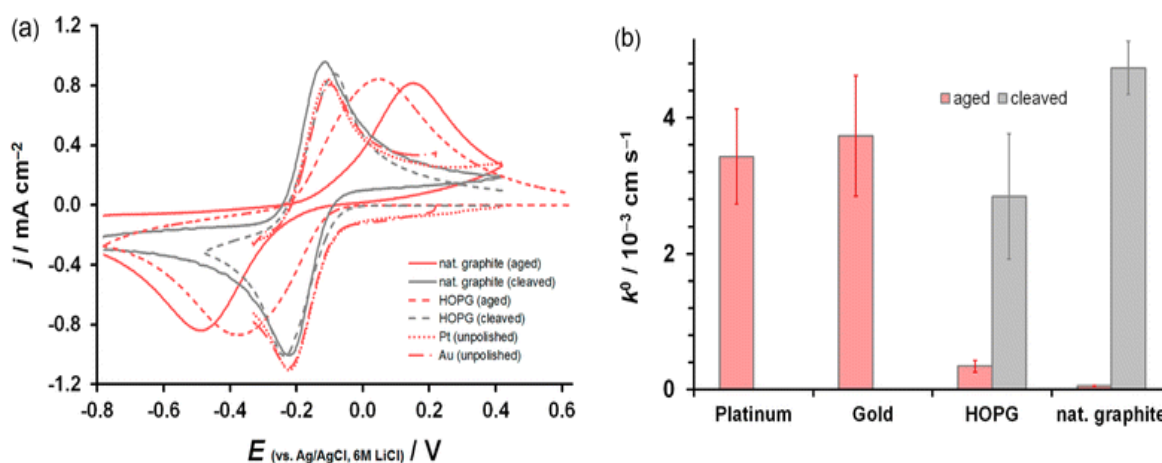
Figure 1.1: Correlation between (a) reversibility in CVs as a function of aging and (b) heterogeneous electron rate constants (k^o [cm^2 s^{-1}]) for graphite and metals. Reference 5

It is this aging of carbon materials that make Pt and Au very relevant in electrochemistry, electronics and the opto-electronic industries;[32–39] literally substituting for carbon materials in roles that should favor them (even though carbon is considered a semi-metal and a semiconductor, Au is preferentially used in computer and satellite mother boards). In addition, carbon materials have wider potential windows (electrochemical working ranges without hydrogen and oxygen interferences) than Au or Pt.[36,40–43] This potential window advantage is another reason why, in the absence of aging, carbon materials are naturally preferential to the noble metals, for semi-conductor-, electronics- and electrochemical-related applications.

Therefore, if the air- and solution-oxidation effects of carbon materials such as graphite and graphene can be curtailed, minimized or, at best, eliminated, it would open the doors to the effective use of

graphites and graphene markedly for sensing, electro-oxidative reactions in water purification, batteries and supercapacitors, catalysis, oxygen reduction for fuel cells, HPLC detectors, and in the semiconductor industry. These are just a few that can be suggested from the state of science and technology at this time.

1.3   Old vs New Views on Aging in Carbon Materials

It was, for over five decades, accepted that the basal planes of graphite were electrochemically inactive; so that electrochemical activity only resides on the edge planes of graphites.[3,44–47] This view was a main contributing factor on why it became common practice to create edges, pits, holes or even nanopores on graphite surfaces as a means of increasing HET kinetics and improving on electrochemical activity.[20,23,25,46,48,49] The improved electrochemical activity can be understood by a high DOS - via band gap opening- near the Fermi level of graphene in the vicinity of a point defect, so that there is a larger overlap between the electronic states of graphene and the redox couple. This overlap facilitates the HET from graphene to the redox couple. Thus, rational control of the defect density can tune the electrochemical activity of graphene, and carbon electrodes in general, in such a way as to result in better performance of graphene-based electrochemical devices.[49–51] However, defects - when in excess - can also scatter carriers, resulting in decreased conductivity.[52–54]

Thus, various techniques to create edges on the basal surfaces exist such as laser ablation technology, [23,48] thermal treatments meant to create pits or edges on graphite basal surfaces, abrasion techniques such as mechanical polishing, which are meant to not only create edges, but also remove existing surfaces to expose new or pristine surfaces.[1–3] Irrespective of the various techniques employed to increase edge density, even to the extent of some proposing to work with an array of edge electrodes,[12,55–57] the aging problem continued with no workable solution in sight.

At the turn of the second decade of the new millennium, using different HOPG grades with some having zero edge density and others with varying surface edge densities, it was discovered that the HET on the HOPG surface was not because of edges *per se*, and that its basal surfaces were themselves electrochemically active. [58–61] Again, these researchers noted that contrary to the old views that held that the HOPGs have inherently sluggish electron transport kinetics, they reported that these were so because cyclic voltammetry were performed on the HOPGs' electrodes long after the HOPG were exfoliated off their bulk – long enough for oxidation-induced sluggish electron transport or aging to have sufficiently deteriorated the HET kinetics. In fact, the electrochemical reactivity of these freshly exfoliated HOPG surfaces and freshly prepared graphene also responded to the

increased water contact angle (WCA) on exposure to ambient air. This increased WCA is due to surface contaminants such as hydrocarbons, which decrease the HET kinetics on the electrode-solution interfaces. [8,21]

1.3.1   What the New View Tells About the Misconceptions Held Previously

Most old view proponents believe that the *visible* edge or defect density would correlate to a high ratio of defect peak intensity (I_D), to the actual graphite (sp^2) peak intensity (I_G); that is, the I_D/I_G, on Raman spectrum, and a corresponding increase in fast HET kinetics. Little wonder the practice continued in a herd-like manner for some fifty years before the advent of the new view. The misconception held by the old view is because of the inadequate understanding of defect intensity (I_D) contributors and significance, what vibrations and carbons participate in the D band intensity of the Raman spectrum and even, what nature of sp^2 carbons contribute to the G band.

Indeed, low surface defects, such as those induced by laser bombardment, accelerate HET by inducing mono- and divacancy defects.[51,62] These defects, for example, point vacancy defects, induce midgap states with high DOS near the Dirac point. The induced midgap states by the point defects are spatially localized around the defects.[50,51] Thus, low defect carbon material electrodes, (for example, when graphene is employed as an electrode for cyclic voltammetry) provide higher DOS that enlarge the overlap potential between the electronic states of the graphene electrode and a corresponding redox probe, which facilitates HET from graphene to the redox-probe (reduction).[51]

When carbon material signatures are probed for defects using Raman spectroscopy, the Raman modes interrogated for, since these carbon materials such as graphite, graphene, and carbon nanotubes have finite-size domains, the selection rule is relaxed to allow the participation of phonons near Γ (Center of the Brillouin zone), on the Brillouin zone, with $\Delta q \approx 2\pi/d$, where d is the dimension of the crystalline domain. This is unlike the Raman modes in single crystals, which obey the fundamental selection rule $q \approx 0$, where q is the wave vector of the scattered phonon.[63] Therefore, defects show up on the Raman spectrum as shown in Figure 1.2, where at low defect density, the defects are separated and independent.[51]
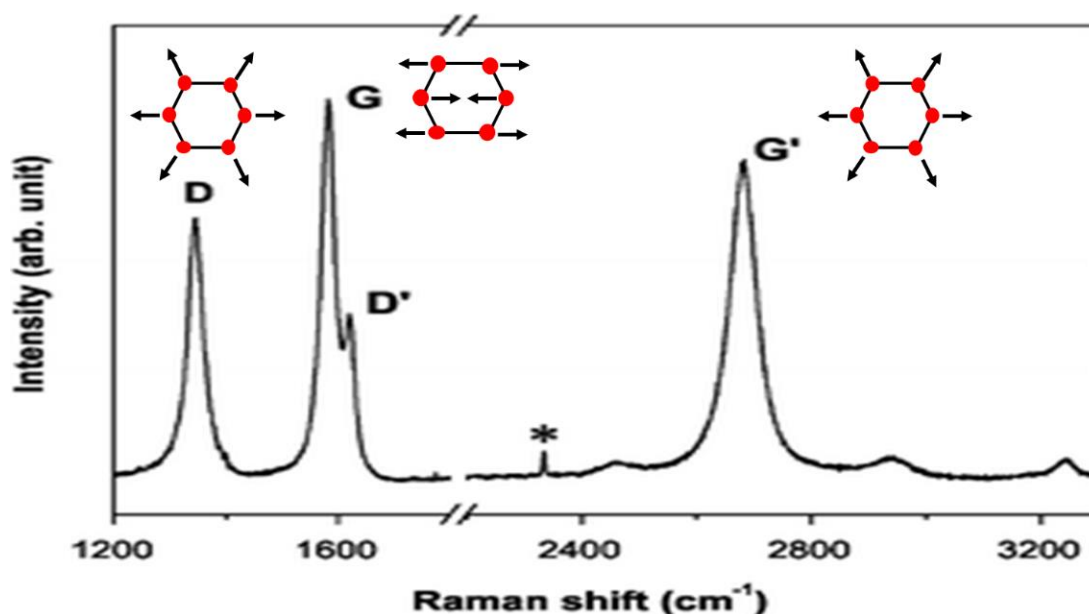
Figure 1.2: The Raman spectrum of a carbon material showing the vibrational modes responsible for various peaks and bands of the Raman carbon finger print. Modified from Reference 64

The D and D′ bands are disorder induced bands,[64,65] with the vibrational modes of the D bands arising from edge-zone phonons while those of the D′ bands arise from mid-zone phonons (Figure 1.2).[65] The D peak occurs at ca. 1355 cm^{-1} and is a breathing mode of A1g symmetry involving phonons near the K zone boundary in K space. This mode is forbidden in perfect graphite and is only Raman active in the presence of disorder. This mode is dispersive – varying with photon excitation energy. The intensity of the D peak is strictly connected to the presence of six-fold aromatic rings. The intensity of the D band (I_D) varies inversely with the interlamellar spacing, L_a.[63] When defect occurs such that misorientation occurs (as in high defect sites), and this misorientation is larger than the six-sided boundary structure offered by surrounding aromatic rings, the boundary structure is more complicated and is referred to as a region of disorder or structurally disordered area between two or more crystal grains (Figure 1.3a).[66] Eventually, these structurally disordered areas begin to coalesce, scattering charge careers responsible for conductivity, thus leading to a decrease in conductivity. Microscopically at this phase, the electrons are highly scattered, and the conductivity drops markedly because of the loss of the perfect sp^2 crystalline lattice, which supports the electron transport in the basal plane by forming the substratum for π delocalization along the various lattice sites of the hexagonal sp^2 structures.[51,63] Taken all together, even though the D peak is characteristic of

polycrystalline graphite, [67] it occurs in many less-ordered or structurally disordered carbons[65] and in fact, since the intensity of the D peak is inversely proportional to L_a, the ratio of the D to G peaks can signify the transition from polycrystalline to amorphous carbons,[68] in the so-called Tuinstra-Koenig transition. [67] The D band is an intervalley process between K and K′ points in the Brillouin zone, in which the excited electron is scattered by a phonon and a defect (one-phonon, double resonance Raman scattering).[69]

The G peak mode at ~ 1580 cm^{-1} is due to the E_{2g} symmetry (Figure 1.2), and is non-dispersive and so does not vary with photon excitation energy as a function of the probing laser intensity employed.[70] As seen from Figure 1.2, its eigenvectors are sensitive to and encompass the in-plane bond-stretching motion of sp^2 C atom pairs. This mode does not require the presence of six-fold rings and occurs on all sp^2 sites and not necessarily those in rings. Thus, it is active in aromatic as well as olefinic molecules with a broad band that lies between 1500 – 1630 cm^{-1}.

For less perfect graphites, that is disordered graphites, the phonon density of states is not associated with the mid-zone phonons, but solely with the edge zone phonon D peaks.[68] The appearance of the mid-zone phonon density of states is characteristic of the disorder induced D′ peak, which is also a characteristic feature of more perfect, more polycrystalline graphites. The D′ peak arises from a conformational excursion from the G band, due to disorder, which causes the G peak (1580 cm^{-1}) to broaden and upshift in frequency; thus, reflecting the high density of phonon states near 1620 cm^{-1} for midzone phonons.[65,71] Like the D′ peak precursor, the G peak mode is due to the E_{2g} symmetry (Figure 1.2),[63] and exhibits dispersive effects on the Raman spectrum.[70] The D′ peak, arising from vibrational density of states of mid-zone phonons, is indicative of in-plane crystallite size ordering, the onset of three-dimensional ordering, and the establishment of long-range three-dimensional ordering,[65,71] - all important conditions required for π-electron delocalization from one crystallite plane to another crystallite plane in a supposedly high order polycrystalline carbon material (Figure 1.3b). In fact, while the appearance of the D- and G-modes, is characteristic for nano-crystalline carbon colloids such as amorphous carbons, [72] the D′ peak is a major distinguishing trait for long-range three-dimensional ordering in polycrystalline carbon materials.[65] The D′ band arises from an intravalley process, - a phonon probing process and backscattering from a defect on the same Brillouin zone (one phonon, double resonance process).[69]

The G′ or 2D peak appears in the range 2500–2800 cm^{-1} (Figure 1.2) and corresponds to the overtone of the D band. This band is symmetry-allowed and appears in the second-order Raman spectra of crystalline graphite, even for those without any form of disorder.[64] Like the D band, it arises from the vibrational density of states of the edge zone phonons and is dispersive in nature – varying as a

function of the probing laser wavelength and intensity.[64,70,73] While the D peak arises from a one-phonon, second-order (double resonance) Raman scattering, the 2D peak arises from a two-phonon second-order (double resonance) Raman scattering event. The 2D two-phonon scattering events involve either the same phonon modes (overtone mode) as in the case of disordered carbons or different phonon modes (combination modes) as in the case of perfect crystals without disorder.
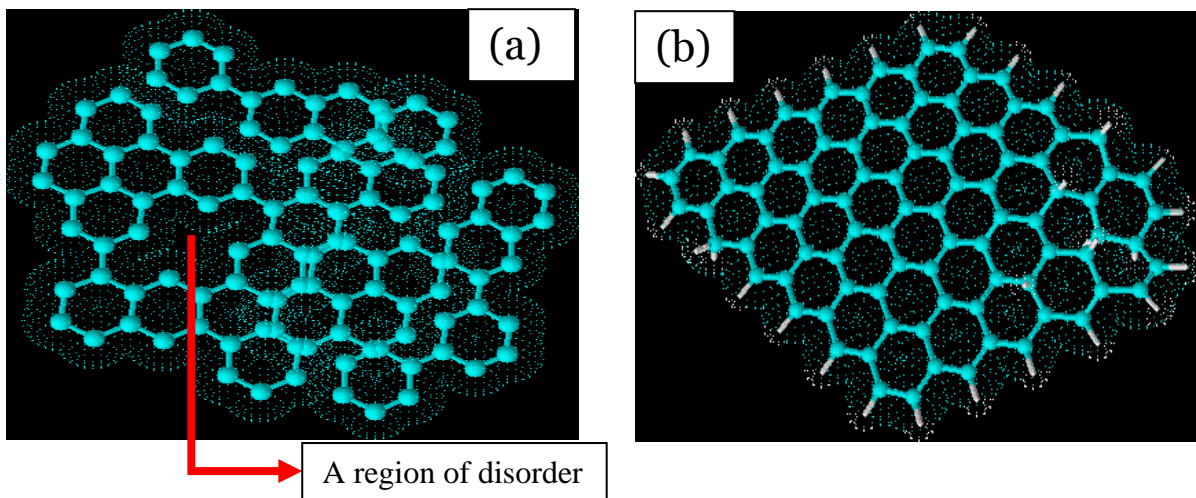
Figure 1.3: (a) A region of disorder or structurally disordered area between crystallite grains of surrounding aromatic rings. (b) Higher order polycrystalline carbon material with six-sided aromatic rings that are contiguous to each other. This condition permits π-electron delocalization from one crystallite plane to another.

For graphite, there are two equivalent-energy circles around the K and K′ points, which are two in nonequivalent hexagonal corners of the Brillouin Zone. Thus, a phonon scattering event is expected either near the K (or K′) points or a scattering event that takes an electron from the K to K′ (or from K′ to K) points (Figure 1.4). The former is referred to as an intravalley scattering, while the latter is referred to as intervalley scattering. [73] The 2D mode, is an overtone of the D peak, where the electron is backscattered by a second phonon instead of a defect.[74] Thus, the 2D band spectra arise from a two-phonon, inter-valley, second-order Raman scattering process, where this band (2D) is free from defect effects (Figure 1.5), and the corresponding experimental signal intensity is comparable to that of the G band signal intensity. [73]
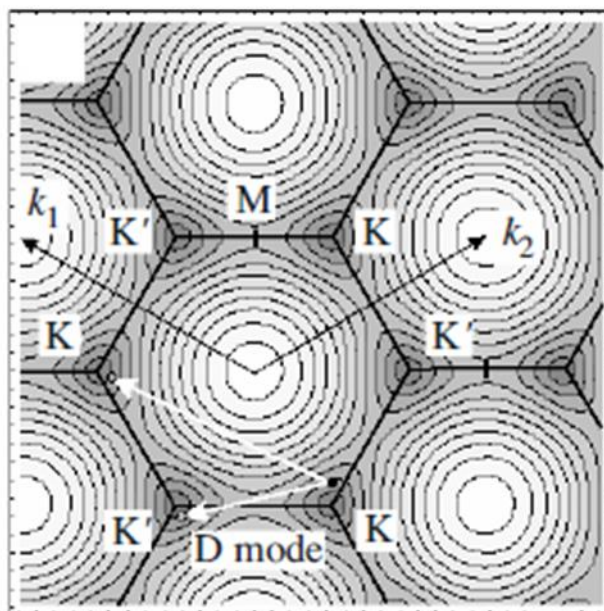
Figure 1.4: Brillouin zone and contour plot of the π∗ band of graphene. The arrows indicate the two-possible double-resonant transitions. The phonon wave vectors are close to the K or the Γ point of the Brillouin zone. Reference 74.
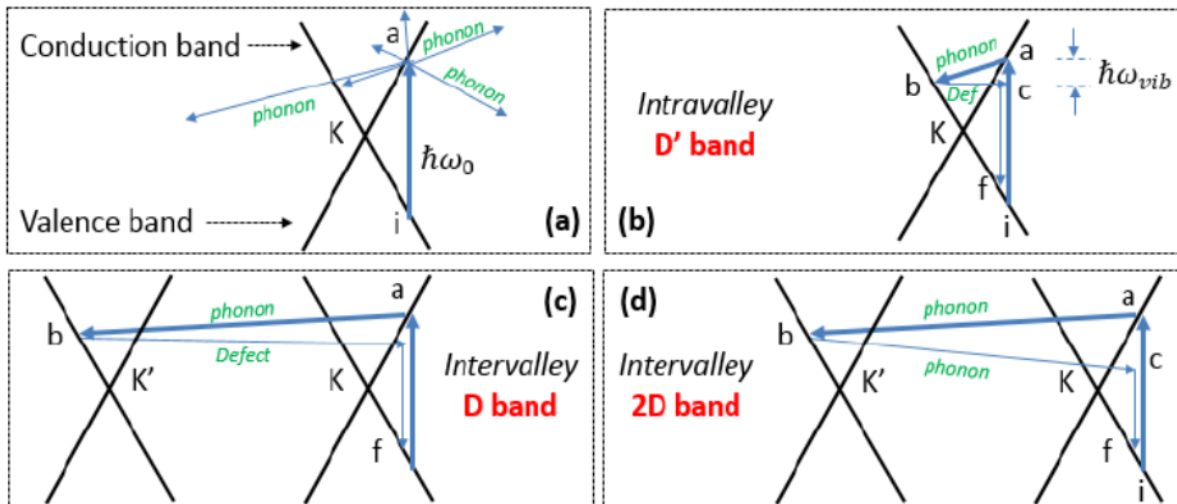
Figure 1.5: Double resonant scattering for the valence and conduction bands. (a) Electron-hole excitation followed by non-resonant phonon scattering. (b) Intravalley process giving rise to the D' band: Phonon (resonant) + defect scattering. (c,d) Intervalley processes giving rise to D and 2D processes with phonon (resonant) + defect and double phonon processes, respectively. Reference 69.

As the graphene layers in the graphites increases and are properly stacked up, there is a splitting of almost all the electronic and phonon bands, which are measurable. This splitting leads to a change in the 2D band from a one peak to a more-than-one peak structure.[75][76][77] The presence of only one 2D peak suggests a turbostratic graphite, where there is no stacking order between adjacent layers (c axis) and the interlayer separation (0.342 nm) is larger than that for crystalline graphite (0.335 nm). A turbostratic graphite can be considered as a 2D graphite. As the number of graphene layers increases, the shape of the 2D band tends to that of a 3D graphite (Figure 1.6). A reduction of the stacking faults, as in turbostratic graphite, is important for reducing the friction of graphitic materials.[64]
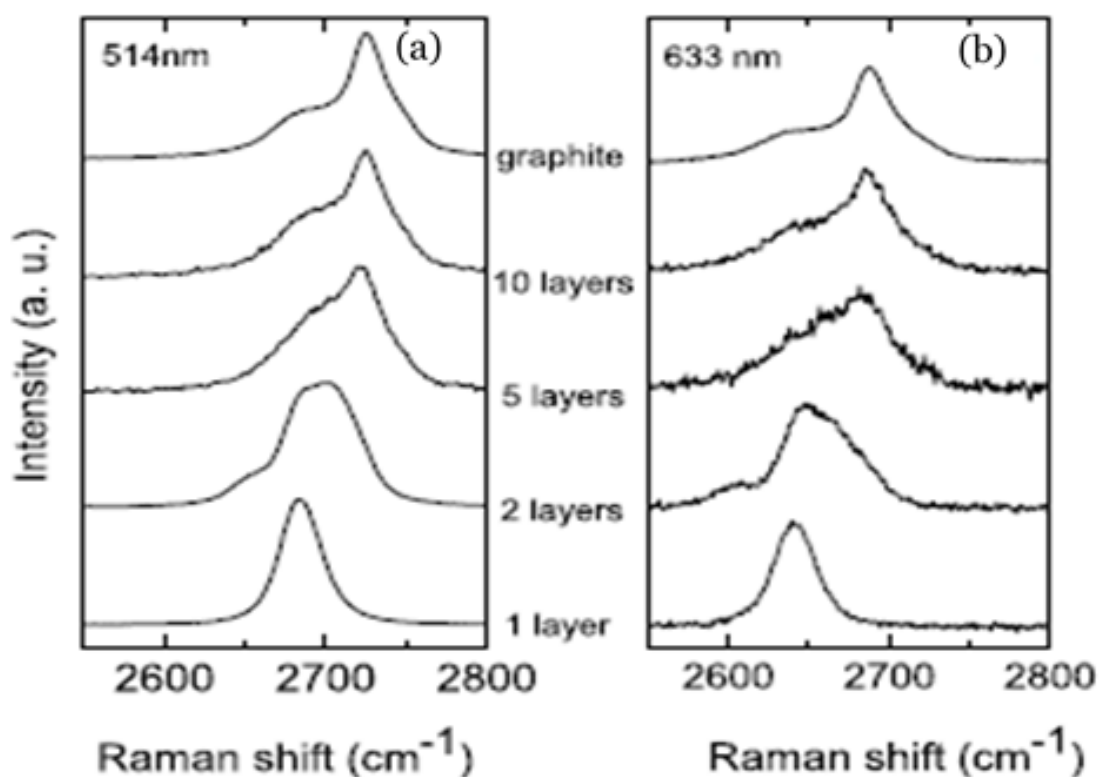
Figure 1.6: Evolution of the 2D band Raman spectra with the number of graphene layers increasing to form graphite for laser wavelength, λ of (a) 514nm and (b) 633nm. Reference 75.

The Raman modes at about 2450-, 2950- and 3250 cm^{-1} are also two-phonon processes referred to as the D+D″, D+D′, and 2D′, respectively. These bands arise from defect-related bands and their combinations and overtone modes.[78] The D″ is a disorder induced band occurring around 1100-1200 cm^{-1}.[69]

1.3.2 Old vs New: The Role of Oxygen Functional Groups for Electron Transport

There have been arguments and counter-arguments on the role of surface oxides in the HET kinetics of graphites and carbon materials in general. While some redox systems were classified as ones catalyzed by surface carbonyl groups, some other ones were not such as $Fe_{(aq)}^{2+/3+}$, $Eu_{(aq)}^{2+/3+}$, and $V_{(aq)}^{2+/3+}$, which were reported to be very sensitive to the density of surface C=0 groups. These C=0 groups provide a catalytic route to increase an inherently slow HET kintics.[25,79,80]

The above-mentioned redox couples are termed inner-sphere because contact is made between the electrode materials and the redox couple for electron transport to occur. In outer sphere redox couples, such as potassium hexachloroiridate(III), hexaammineruthenium(III) chloride, the HET kinetics are reportedly insensitive to the surface chemistry of the materials.[25] For ferri-ferrocyanide ($Fe(CN)_6^{3-/4-}$), the HET kinetics are even hampered by the presence of surface oxides. [26] In fact, electroreduction – to remove surface bound oxides- has been reported to specifically accelerate the HET on an outer sphere redox couple ($Fe(CN)_6^{3-/4-}$) (Figure 1.7) by specifically removing oxygen species.[81] The depressed HET involving $Fe(CN)_6^{3-/4-}$ and carbon materials with surface oxides is suggested to be due to electrostatic repulsion between negatively charged ferricyanide species and the negatively charged oxide moieties, resulting in a larger electron tunneling distance between the redox couple and the carbon material and thus, more sluggish HET kinetics. [82,83]

The HET is solely dependent on the DOS of the materials for inner sphere redox couples so that aquated complexes or other bridging complexes, as is requisite in the inner sphere couples, are not pre-requisites for fast HET.[80,84] However, the question remains: when the influence of redox couples is taken away, is oxygen important in fast HET kinetics? This question becomes even more paramount since fast HET on oxygen bound graphene species probed for HET kinetics with an outer sphere redox couple ($Fe(CN)_6^{3-/4-}$) has been documented in the literature.[85]

It has been documented that oxygen-containing groups disrupt π-conjugated sp^2 networks of graphene islands in graphene oxides, thus degrading electrical conductivity in these materials. [81,83,86] The elimination of these oxygen functionalities by either high temperature annealing or solution-based reduction have subsequently restored the sp^2 networked graphene islands, (Figure 1.8) increased the DOS, and partially restored or improved the HET kinetics.[14,49,81,83,86]
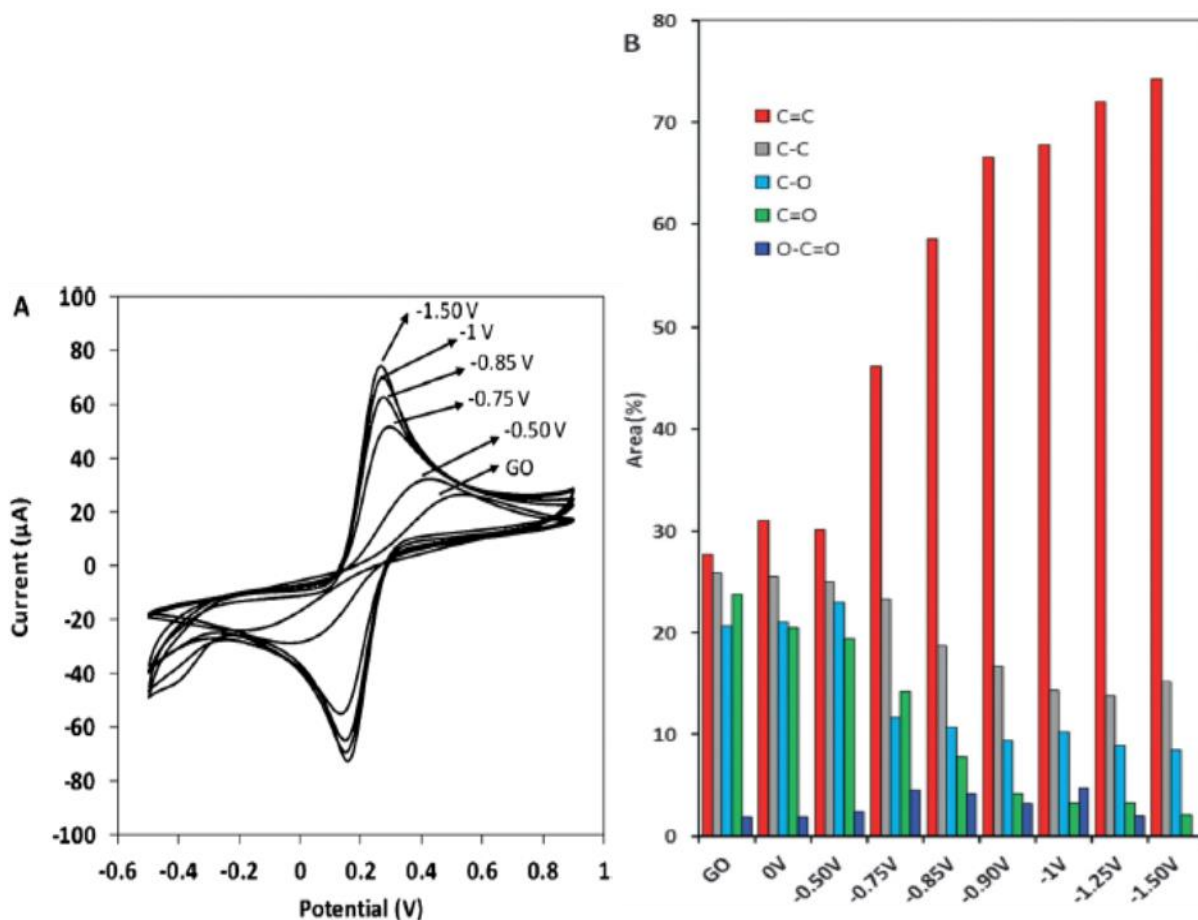
Figure 1.7: A) Representative cyclic voltammograms obtained with graphene oxide (GO) film-modified screen-printed carbon electrode (SPE) after the electrochemical reduction treatment at different potentials in the presence of an 5 mM ferro-/ferricyanide redox probe. B) Area percentages of the bars corresponding to: sp^2 carbon (red), sp^3 carbon (grey), C-O groups (blue), C=O groups (green) and O-C=O groups (violet) measured after the electrochemical reduction at different reduction potentials. Reference 81.

In terms of surface oxides enhancing HET with redox-couple ($Fe(CN)_6^{3-/4-}$) that is associated with sluggish HET on carbon materials, it has been reported that although oxides do not contribute to fast HET, they may not hinder electron transport if these oxide species are sequestered off graphene islands.[87] Thus, there could still be some fair amount of oxide on the surfaces of materials but with enough sp^2 π-conjugating network to permit shorter distance electron tunneling between core conjugating sp^2 networks and the $Fe(CN)_6^{3-/4-}$ as in the example above. In summary, oxygen functional groups do not enhance electron transport on graphite or graphene surfaces but in fact, hinder electron transport by disrupting sp^2 π-conjugating network.
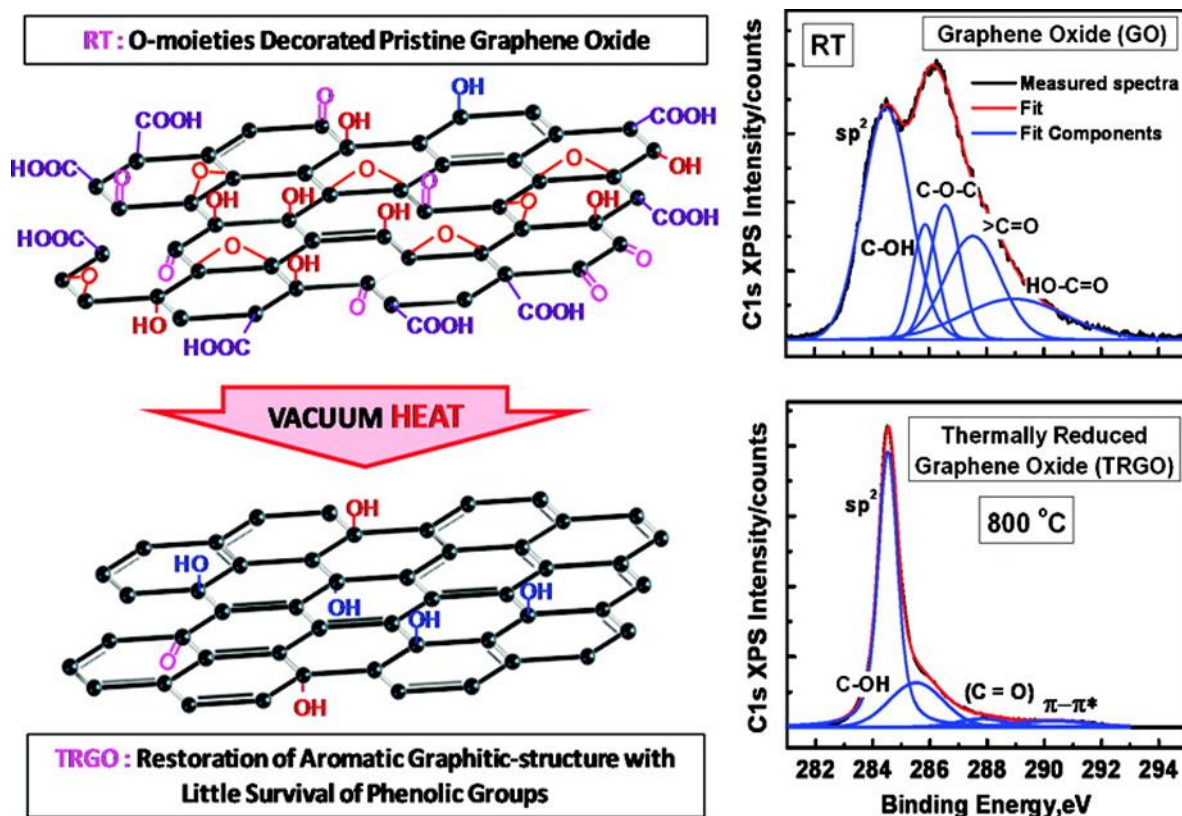
Figure 1.8: The partial restoration of conjugated sp^2 bonded carbon networks and its correlation with the removal of oxygen moieties from the chain. Reference 86.

Of importance also, is that the old view proponents did not factor the electronics of these carbon materials as being of much significance to their HET, since many believed that since electrochemistry is a surface science, then the HET would be solely controlled by surface chemistry without much bulk effect. However, it is currently an accepted view that even though the surface chemistry such as surface functional groups and edges have contributory effects on the surface properties of these materials such as WCA and HET, the electronic properties in the bulk layer ultimately control the overall surface properties of these materials.[6,51,62,88,89] In fact, when surface chemistry was pitted against the DOS, the DOS played a dominant effect upon surface chemistry.[62] Thus, it would be worthwhile to explore the electronic nature of carbon materials to understand their possible contribution to the DOS, which is an important contributor to HET kinetics.

1.4   The Electronic Nature of Carbon Materials

The electronic structures of graphite, graphene, carbon nanotubes and fullerenes are very similar [90–94] all being different allotropic forms of carbons. Graphene is a monolayer thick of graphite while carbon nanotubes and fullerenes are rolled up sheets and circularly folded sheets of graphene – the monolayer building block of graphite (Figure 1.9).

Monolayer graphene

Fullerene   Carbon nanotube   Graphite
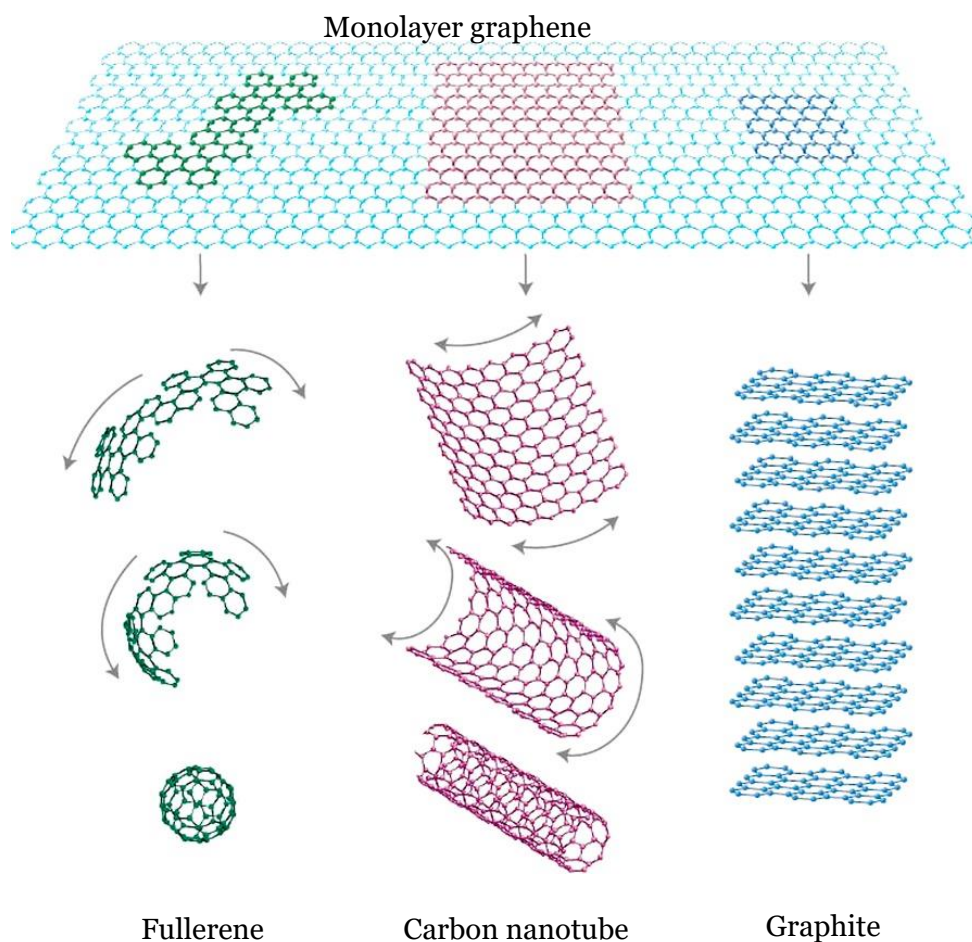
Figure 1.9: Monolayer graphene, a two-dimensional (2D) carbon material form the building block for fullerene (2D-material), when it is rolled up into "buckeyballs", or carbon nanotube (2D-material), when rolled into cylinders or stacked up into multilayers to form the three-dimensional graphite. Reference 95.

Basically, their hybridization status is sp^2, which leads to a trigonal planar structure with three in-plane *sp^2* σ bonds and one out-of-plane π bond.[69] This π bond, from a 2p$_z$ orbital overlaps or mixes by covalently bonding with a neighboring singly occupied 2p$_z$ orbital (a 2p$_z$–2p$_z$ overlap) to form the π bond housing the π electron - the so-called wandering, unhybridized π electron orbital -the fourth electron- as the charge carrier between neighboring site-to-site interactions by wandering across the two-dimensional crystal.[96] This wandering or delocalized π-electron – hopping from site to site on an *intact* sp^2 crystal lattice - determines the electronic and optical properties[92,94,97] and deductively the conductivity, electrochemical and electrical properties of the material under study. While the sp^2 contributes only to the intra-plane bonding, the 2p$_z$ orbitals contribute to π bonding both intra- and inter-plane; with an intraplane spacing of 142 nm and an interplane spacing of 335nm. The interplane interaction is comparatively weaker than the intraplane interaction. [98]
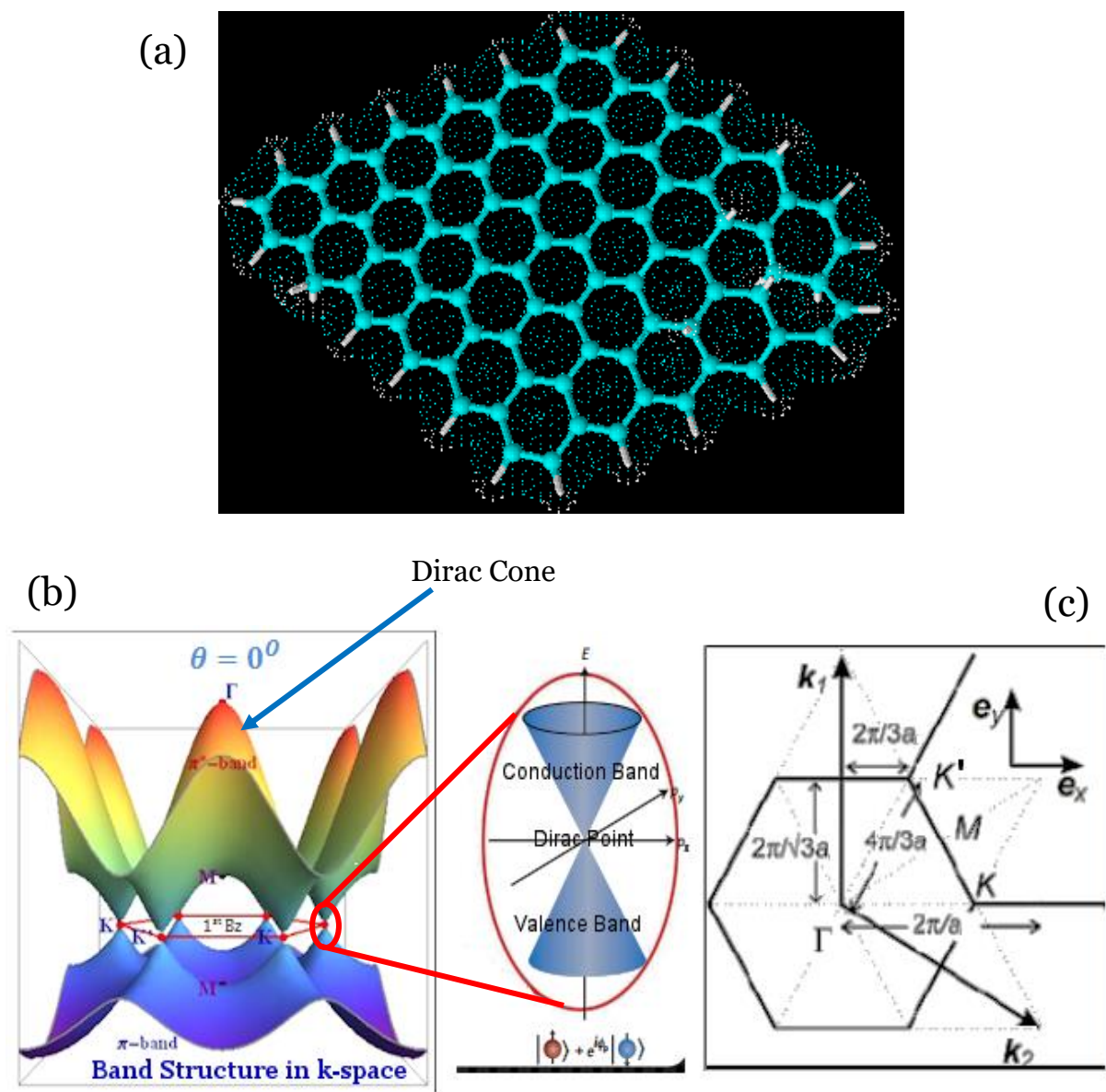
Figure 1.10: (a): A 2D structure of the polycrystalline lattice of a carbon material, e.g., graphene, showing the hexagonal, honeycomb-like lattice structure. The carbon atoms are covalently bonded to their neighboring carbon atoms, while 2p orbitals bond together to form the π-orbital. It is this orbital that houses the wandering π-electron, which hops from site-to-site along the polycrystalline lattice of the 2D material. (b) The band structure of graphene (a 2D carbon material) showing the 6 points of the Brillouin zone. A magnification of a Dirac point, showing the point where the conduction and valence bands just touch. (c) A 2D-representation of the hexagon along the Brillouin zone, showing the simple tetragonal (along K_1 and K' axis) and face-centered (FCC) (along K' and K_2 axis) Brillouin zones (Figures b and c were modified from https://universe-review.ca/R13-16-graphene.htm#top).

On the other hand, the σ bonds are responsible for the robustness of the lattice, in which each carbon atom in graphene's honeycomb lattice, for example, forms strong covalent bonds with its neighbors.[69,96] Figure 1.10 illustrates the dynamics of the hexagonal, honeycomb-like structure of a 2D sp^2 crystal lattice with the Brillouin zone and an elaboration of the Dirac points. While Figure 1.10a shows the polycrystalline lattice of a 2D component of carbon (e.g., graphene), exemplifying how a π-electron can hop along the crystalline lattice site, Figure 1.10b peeps into the electronic, band-structure of a hexagonal lattice to reveal the 6-sides of the Brillouin zone. This band-structure picture describes the energy dependence of the electronic motion of the π electron along the Kx and Ky axis. Graphene or monolayer graphite has valence and conduction bands that just touch at discrete points in the Brillouin zone. Since the Fermi level is very close (0.024 eV) to the baseline, $\in_i$ the energy (E) is approximated to be zero at the Fermi level. Now, the effective width of the bandgap at $\in_f$ is zero, the graphite monolayer or graphene is classified as a zero-overlap or zero bandgap semi-metal,[96,98][95] in that it is neither conducting nor insulating and with one type of electrons and one type of holes.[95] The DOS for graphene at $E = 0$ is symmetrical, reflecting the bipartite nature of the hexagonal, honey-comb lattice. [98] Therefore, for a single graphene sheet, the DOS is in (Equation 1):

$$\rho(E) = -\frac{1}{\pi} \text{Im} \left[\lim_{\in \to 0^+} \int_{1stBZ} d\kappa \frac{t}{t^2 - |\mu|^2 V_1^2} \right]$$

(1)

where BZ is the Brillouin zone; V_1 reflects nearest neighbor interactions in the hexagonal or honeycomb lattice; t, is a matrix operator of the eigenfunction μV; and μ reflects the geometry of the entire hexagon.

Monolayer graphite or graphene can then be described as a zero-band gap material where the energy–momentum dispersion relation becomes linear around those two points. Consequently, an electron has zero effective mass and behaves more like a photon than a conventional massive particle whose energy–momentum dispersion is parabolic. The symmetric topology of graphene, therefore, prompts its electrons to obey equations of motion derived from the relativistic (2+1)-dimensional Dirac Hamiltonian with an effective speed of light, $v_F \approx 10^6$ m/s. These quasiparticles, called massless Dirac fermions, could be described as electrons that lost their rest mass m_0 or as neutrinos that acquired the electron charge e.[95][96] The dispersion of the energy-momentum for these Dirac fermions can be described by the relativistic energy equation (Equation 2)

$$E = |\hbar k| v_F,$$

(2)

where v_F is the Fermi velocity and k its momentum.[96] The Fermi velocity v_F of electrons or holes (Dirac fermions) then replaces the speed of light in the Dirac equation so that the dispersion curve would imply that the electrons' mass vanishes throughout a large range of momentum values in the crystal lattice.[95,96]

A flat or 2D representation of the Brillouin zone is shown in Figure 1.10c. In a simple tetragonal lattice, an electron at the X point is scattered to a symmetry equivalent state either by a Γ- or an M-point phonon (along K_1 and K' axis). In the face-centered cubic (FCC) or diamond lattice, X or Γ-point phonon vibrations yield scattering from one X point to another X point (symmetry-imposed resonances) of the Brillouin zone (along K' and K_2 axis).[74]

The electronic bands are shaped in a cone structure, giving rise to the term, Dirac cone (Figure 1.10b). The curvature of the Dirac cone can be modified by the interaction of some molecules with the sp^2 carbon matrix to form mixed or hybrid sp^2/sp^3 state,[69,99] therefore disrupting the sp^2 π networks as earlier mentioned with the case of oxygen.[14,49,81,83,86]

For graphite which is multilayer graphene sheets, with graphene sheets above and below overlapping with a sheet stacked in between, the DOS at the Fermi level is nonzero. In fact, the DOS would be an infinite sum of the DOS of graphene sheets stacked one above the other with one sheet interacting with two sheets – one above and below (Equation 3).[98,100,101] The DOS for bilayer graphite is therefore the sum in the DOS of two single-layer graphene sheets as expressed below in Equation 3.[98]

$$\rho(E) = -\frac{1}{\pi} \text{Im} \left[\lim_{\epsilon \to 0^+} \int_{1stBZ} d\kappa \left\{ \frac{t + V_2}{(V_2 + t)^2 - |\mu|^2 V_1^2} + \frac{t - V_2}{(t - V_2)^2 - |\mu|^2 V_1^2} \right\} \right]$$

(3)

Where $+V_2$ and $-V_2$ reflect shifts (eV) in nearest neighbor interactions between two layers in the hexagonal or honeycomb lattice. For the case of simple hexagonal graphite with infinite number of graphene sheets (Equation 4),[98]

$$\rho(E) = -\frac{1}{\pi} \text{Im} \left[\lim_{\epsilon \to 0^+} \int_{1stBZ} d\kappa \times \frac{t + 2V_2 \cos(\kappa_z c) + 2V_4 \cos(2\kappa_z c)}{\left[t + 2V_2 \cos(\kappa_z c) + 2V_4 \cos(2\kappa_z c) \right]^2 - |\mu|^2 \left[V_1 + 2V_3 \cos(\kappa_z c) \right]} \right]$$

(4)

Where c is the interlayer spacing. Near neighbor interactions, V_3 is to make the DOS asymmetric about ϵ_F (the Fermi energy level), while the parameter V_4 effectively increases the strength of the interplane interaction, hence exaggerating the effect of V_2 (V_2 are interactions between atoms directly

above one another in the hexagonal or honeycomb lattice).[98] Due to the stacking of monolayer graphene sheets in the simple hexagonal graphite, there is a breakdown of symmetry, which is present in the monolayer graphite or graphene. Thus, the electronic density of states of graphite near the top of the filled band is asymmetric about the energy where this band touches the next, unfilled, band.[98,102]

1.5   New Concepts, New Paradigms, Possible Solutions

In recent times, there have been intense efforts to study the link or actual relationship between interfacial chemistry (reactivities on carbon electrode surfaces) and the electrode structure/electronics (bulk layer). [103–105] Most solutions to the aging problems of graphites, and graphenes, for example, have always depended on a top-down approach, i.e., modify the surface to enhance electron transport activity as noted above,[1–3] without consideration of the electronic nature of these materials. This is because it has been reported that surface chemistry has profound influence on the electronic configuration of these carbon materials. [106–108] However, since the results of the treatment or modification protocols have always been temporary with numerous and sometimes conflicting reason(s) for the variations in HET kinetics and even capacitance of carbon materials,[4,58–60,109] an alternative and probably, better approach was to try a bottom-up approach. That is, rather than move from surface chemistry to structure-function, the electronic properties of the carbon materials could be tuned to influence both the surface chemistry and structure-function properties. As a proof of concept, the wetting and porosity of graphene was tuned to become hydrophilic from hydrophobic (due to the adsorption of surface hydrocarbons) by doping.[110–112] These techniques increase the electron density around the aromatic rings, causing the displacement of the Fermi edge from the Dirac points (increasing the density of states around these points leads to band gap opening or non-zero band conductor properties)[112] and prove that the electronics can change the surface chemistry independent of surface functionalization.

In the present study, the electrochemistry, wettability and porosity of aged graphite materials were approached by tuning their electronic properties. These tuned materials were used as scaffolds for the deposition of highly crystalline, defect-free Prussian blue nanoparticles. Eventually, the stability of the tuned graphites to their pristine counterparts was probed via various techniques to elucidate how and why the tuned electronic structures of graphite could confer such stability in comparison to their pristine samples.

Table 1.1: Table of acronyms and meaning

Symbol	Meaning
Δq	Phonon energy difference required for a transition between states in the Brillouin zone
D	Disorder induced bands arising from edge-zone phonons at ~ 1355 cm^{-1} on the Raman spectrum of graphite
D′	disorder induced bands arising from mid-zone phonons at ~ 1620 cm^{-1} on the Raman spectrum of graphite
2D	Overtone of the D band or from different phonon modes (combination modes) and appears in the range 2500–2800 cm^{-1}
G′	Overtone of the D band or from different phonon modes (combination modes) and appears in the range 2500–2800 cm^{-1}
$\hbar$	Planck's constant
I_D	Defect peak intensity
I_G	Graphite (sp^2) peak intensity
I_D/I_G	Ratio of defect peak (I_D), to graphite (sp^2) peak (I_G) intensities
k	Momentum of a Dirac fermion (massless electron)
K points	The middle of an edge joining two hexagonal faces, in the Brillouin zone, in a face centered cubic (FFC). Lies adjacent to the K′ point
K′ points	The middle of an edge joining two hexagonal faces, in the Brillouin zone, in a face centered cubic (FFC). Lies adjacent to the K point
L_a	Interlamellar spacing between hexagonal units in graphite
Γ	Center of the Brillouin zone
m_0	Rest mass of a Dirac fermion
M-point	The center or midpoint of a rectangular face, between K and K′ points
v_F	Fermi velocity of a Dirac fermion (massless electron)

References

(1)   Štulík, K. Activation of Solid Electrodes. *Electroanalysis*. **1992**, *4*, 829-834.

(2)   Swain, G. M. Solid Electrode Materials: Pretreatment and Activation. In *Handbook of Electrochemictry*; Zoski, C. G., Ed.; Elsevier B.V.: Amsterdam, **2007**; pp 111–153.

(3)   McCreery, R. L. Advanced Carbon Electrode Materials for Molecular Electrochemistry. *Chem. Rev.* **2008**, *108*, 2646–2687.

(4)   McCreery, R. L.; McDermott, M. T. Comment on Electrochemical Kinetics at Ordered Graphite Electrodes. *Anal. Chem.* **2012**, *84*, 2602–2605.

(5)   Velický, M.; Bradley, D. F.; Cooper, A. J.; Hill, E. W.; Kinloch, I. A.; Mishchenko, A.; Novoselov, K. S.; Patten, H. V.; Toth, P. S.; Valota, A. T.; Worrall, S. D.; Dryfe, R. A. W. Electron Transfer Kinetics on Mono- and Multilayer Graphene. *ACS Nano* **2014**, *8*, 10089–10100.

(6)   Güell, A. G.; Cuharuc, A. S.; Kim, Y. R.; Zhang, G.; Tan, S. Y.; Ebejer, N.; Unwin, P. R. Redox-Dependent Spatially Resolved Electrochemistry at Graphene and Graphite Step Edges. *ACS Nano* **2015**, *9*, 3558–3571.

(7)   Li, Z.; Wang, Y.; Kozbial, A.; Shenoy, G.; Zhou, F.; McGinley, R.; Ireland, P.; Morganstein, B.; Kunkel, A.; Surwade, S. P.; Li, L.; Liu, H. Effect of Airborne Contaminants on the Wettability of Supported Graphene and Graphite. *Nat. Mater.* **2013**, *12*, 925–931.

(8)   Li, Z.; Kozbial, A.; Nioradze, N.; Parobek, D.; Shenoy, G. J.; Salim, M.; Amemiya, S.; Li, L.; Liu, H. Water Protects Graphitic Surface from Airborne Hydrocarbon Contamination. *ACS Nano* **2016**, *10*, 349–359.

(9)   Velický, M.; Bissett, M. A.; Toth, P. S.; Patten, H. V.; Worrall, S. D.; Rodgers, A. N. J.; Hill, E. W.; Kinloch, I. A.; Novoselov, K. S.; Georgiou, T.; et al. Electron Transfer Kinetics on Natural Crystals of MoS_2 and Graphite. *Phys. Chem. Chem. Phys.* **2015**, *17*, 17844-17853.

(10)   Laurila, T.; Sainio, S.; Caro, M. Hybrid Carbon Based Nanomaterials for Electrochemical Detection of Biomolecules. *Prog. Mater. Sci.* **2017**, *88*, 499-594.

(11)   Chandra, S.; Miller, A. D.; Bendavid, A.; Martin, P. J.; Wong, D. K. Y. Minimizing Fouling at Hydrogenated Conical-Tip Carbon Electrodes during Dopamine Detection in Vivo. *Anal. Chem.* **2014**, *86*, 2443–2450.

(12)   Hu, L.; Peng, X.; Huo, K.; Chen, R.; Fu, J.; Li, Y.; Lee, L. Y. S.; Wong, K.-Y.; Chu, P. K. Dominant Factors Governing the Electron Transfer Kinetics and Electrochemical Biosensing Properties of Carbon Nanofiber Arrays. *ACS Appl. Mater. Interfaces* **2016**, *8* (42), 28872–28879.

(13)   Sofer, Z.; Jankovský, O.; Šimek, P.; Sedmidubský, D.; Šturala, J.; Kosina, J.; Mikšová, R.; Macková, A.; Mikulics, M.; Pumera, M. Insight into the Mechanism of the Thermal Reduction of Graphite Oxide: Deuterium-Labeled Graphite Oxide Is the Key. *ACS Nano* **2015**, *9*, 5478–5485.

(14)   Mao, X.; Guo, F.; Yan, E. H.; Rutledge, G. C.; Alan Hatton, T. Remarkably High Heterogeneous Electron Transfer Activity of Carbon-Nanotube-Supported Reduced Graphene Oxide. *Chem. Mater.* **2016**, *28*, 7422–7432.

(15)   Parker, J. F.; Kamm, G. E.; McGovern, A. D.; Desario, P. A.; Rolison, D. R.; Lytle, J. C.; Long, J. W. Rewriting Electron-Transfer Kinetics at Pyrolytic Carbon Electrodes Decorated with Nanometric Ruthenium Oxide. *Langmuir* **2017**, *33*, 9416–9425.

(16)   Taylor, S. M.; Pătru, A.; Perego, D.; Fabbri, E.; Schmidt, T. J. Influence of Carbon Material Properties on Activity and Stability of the Negative Electrode in Vanadium Redox Flow Batteries: A Model Electrode Study. *ACS Appl. Energy Mater.* **2018**, *1*, 1166–1174.

(17)   Ferrari, A. C.; Bonaccorso, F.; Fal'ko, V.; Novoselov, K. S.; Roche, S.; Bøggild, P.; Borini, S.; Koppens, F. H. L.; Palermo, V.; Pugno, N.; et al. Science and Technology Roadmap for Graphene, Related Two-Dimensional Crystals, and Hybrid Systems. *Nanoscale* **2015**, *7*, 4598–4810.

(18)   Kong, Y.; Wang, Z.-L.; Wang, Y.; Yuan, J.; Chen, Z.-D. Degradation of Methyl Orange in Artificial Wastewater through Electrochemical Oxidation Using Exfoliated Graphite Electrode. *Xinxing Tan Cailiao/New Carbon Mater.* **2011**, *26*, 459-464.

(19)   Maljaei, A.; Arami, M.; Mahmoodi, N. M. Decolorization and Aromatic Ring Degradation of Colored Textile Wastewater Using Indirect Electrochemical Oxidation Method. *Desalination* **2009**, *249*, 1074–1078.

(20)   Brownson, D. A. C.; Munro, L. J.; Kampouris, D. K.; Banks, C. E. Electrochemistry of Graphene: Not Such a Beneficial Electrode Material? *RSC Adv.* **2011**, *1*, 978-988.

(21)   Kozbial, A.; Zhou, F.; Li, Z.; Liu, H.; Li, L. Are Graphitic Surfaces Hydrophobic? *Acc. Chem. Res.* **2016**, *49*, 2765–2773.

(22)   Kozbial, A.; Li, Z.; Sun, J.; Gong, X.; Zhou, F.; Wang, Y.; Xu, H.; Liu, H.; Li, L. ScienceDirect Understanding the Intrinsic Water Wettability of Graphite. *Carbon N. Y.* **2014**, *74*, 218–225.

(23)   Poon, M.; McCreery, R. L.; Engstrom, R. Laser Activation of Carbon Electrodes. Relationship between Laser-Induced Surface Effects and Electron Transfer Activation. *Anal. Chem.* **1988**, *60*, 1725–1730.

(24)   Ranganathan, S.; Kuo, T.; Mccreery, R. L. Facile Preparation of Active Glassy Carbon Electrodes with Activated Carbon and Organic Solvents. **1999**, *71*, 3574–3580.

(25)   Chen, P.; Fryling, M. A.; McCreery, R. L. Electron Transfer Kinetics at Modified Carbon Electrode Surfaces: The Role of Specific Surface Sites. *Anal. Chem.* **1995**, *67*, 3115–3122.

(26)   Ji, X.; Banks, C. E.; Crossley, A.; Compton, R. G. Oxygenated Edge Plane Sites Slow the Electron Transfer of the Ferro-/Ferricyanide Redox Couple at Graphite Electrodes. *ChemPhysChem* **2006**, *7*, 1337–1344.

(27)   Lai, C. Y.; Tang, T. C.; Amadei, C. A.; Marsden, A. J.; Verdaguer, A.; Wilson, N.; Chiesa, M. A Nanoscopic Approach to Studying Evolution in Graphene Wettability. *Carbon N. Y.* **2014**, *80*, 784–792.

(28)   Martinez-Martin, D.; Longuinhos, R.; Izquierdo, J. G.; Marele, A.; Alexandre, S. S.; Jaafar, M.; Gómez-Rodríguez, J. M.; Bañares, L.; Soler, J. M.; Gomez-Herrero, J. Atmospheric Contaminants on Graphitic Surfaces. *Carbon N. Y.* **2013**, *61*, 33–39.

(29)   Misra, R. P.; Blankschtein, D. Insights on the Role of Many-Body Polarization Effects in the Wetting of Graphitic Surfaces by Water. *J. Phys. Chem. C* **2017**, *121*, 28166–28179.

(30) Liu, H.; Li, L. Graphitic Materials: Intrinsic Hydrophilicity and Its Implications. *Extreme Mechanics Letts*. **2017**, *14*, 44–50.

(31) Morteza Najarian, A.; Chen, R.; Balla, R. J.; Amemiya, S.; McCreery, R. L. Ultraflat, Pristine, and Robust Carbon Electrode for Fast Electron-Transfer Kinetics. *Anal. Chem.* **2017**, *89*, 13532–13540.

(32) Davey, N. M.; Seymour, R. J. Platinum Metals in Electronics. *Platin. Met. Rev.* **1985**, *29*, 2–11.

(33) Rawashdeh-Omary, M. A.; Omary, M. A.; Fackler, J.; Galassi, R.; Pietroni, B. R.; Burini, A. Chemistry and Optoelectronic Properties of Stacked Supramolecular Entities of Trinuclear Gold(I) Complexes Sandwiching Small Organic Acids. *J. Am. Chem. Soc*. **2001**, *123*, 9689–9691.

(34) Zorić, I.; Zäch, M.; Kasemo, B.; Langhammer, C. Gold, Platinum, and Aluminum Nanodisk Plasmons: Material Independence, Subradiance, and Damping Mechanisms. *ACS Nano* **2011**, *5*, 2535–2546.

(35) Fontana, L.; Venditti, I.; Fratoddi, I.; Leahu, G.; Belardini, A.; Li Voti, R.; Sibilia, C.; Matassa, R.; Familiari, G. c. In *18th Italian National Conference on Photonic Technologies (Fotonica 2016)*; **2016**, **DOI:** 10.1049/cp.2016.0896.

(36) Coustan, L.; Shul, G.; Bélanger, D. Electrochemical Behavior of Platinum, Gold and Glassy Carbon Electrodes in Water-in-Salt Electrolyte. *Electrochem. Commun.* **2017**, *77*, 89-92.

(37) Bengio, D.; Mendes, E.; Pellet-Rostaing, S.; Moisy, P. Electrochemical Behavior of Platinum and Gold Electrodes in the Aprotic Ionic Liquid N,N-Trimethylbutylammonium Bis(Trifluoromethanesulfonyl)Imide. *J. Electroanal. Chem.* **2018**, *823*, 445–454.

(38) Cataldi, T. R. I.; Rubino, A.; Laviola, M. C.; Ciriello, R. Comparison of Silver, Gold and Modified Platinum Electrodes for the Electrochemical Detection of Iodide in Urine Samples Following Ion Chromatography. *J. Chromatogr. B Anal. Technol. Biomed. Life Sci.* **2005**, *827*,224-231.

(39) Shkir, M.; Yahia, I. S.; Ganesh, V.; Bitla, Y.; Ashraf, I. M.; Kaushik, A.; AlFaify, S. A Facile Synthesis of Au-Nanoparticles Decorated PbI_2 single Crystalline Nanosheets for Optoelectronic Device Applications. *Sci. Rep.* **2018**, *8*, 13806.

(40) Macpherson, J. V. A Practical Guide to Using Boron Doped Diamond in Electrochemical Research. *Phys. Chem. Chem. Phys.* **2015**, *17*, 2935-2949.

(41) Cobb, S. J.; Ayres, Z. J.; Macpherson, J. V. Boron Doped Diamond: A Designer Electrode Material for the Twenty-First Century. *Annu. Rev. Anal. Chem.* **2018**, *11*, 463-484.

(42) Kraft, A. Doped Diamond: A Compact Review on a New, Versatile Electrode Material. *Int. J. Electrochem. Sci*. **2007**, *2*, 355 - 385.

(43) Kelly, R. S. Analytical Electrochemistry: The Basic Concepts. *Anal. Electrochem.* **2007**, (https://community.asdlib.org/activelearningmaterials/analytical-electrochemistry-the-basic-concepts/ [Aceessed on 01/18/2019])

(44) Robinson, R. S.; Sternitzke, K.; McDermott, M. T.; McCreery, R. L. Morphology and Electrochemical Effects of Defects on Highly Oriented Pyrolytic Graphite. *J. Electrochem. Soc.* **1991**, *138*, 2412-2418.

(45) Bowling, R. J.; Packard, R. T.; McCreery, R. L. Activation of Highly Ordered Pyrolytic Graphite for Heterogeneous Electron Transfer: Relationship between Electrochemical Performance and Carbon Microstructure. *J. Am. Chem. Soc.* **1989**, *111*, 1217–1223.

(46) Poon, M.; Mccreery, R. L. In Situ Laser Activation of Glassy Carbon Electrodes. *Anal. Chem.* **1986**, *58*, 2745–2750.

(47) Rice, R. J.; McCreery, R. L. Quantitative Relationship between Electron Transfer Rate and Surface Microstructure of Laser-Modified Graphite Electrodes. *Anal.Chem.* **1989**, *61*, 1637–1641.

(48) Sternitzke, K. D.; McCreery, R. L. Laser Microfabrication and Activation of Graphite and Glassy Carbon Electrodes. *Anal. Chem.* **1990**, *62*, 1339–1344.

(49) Kaplan, A.; Yuan, Z.; Benck, J. D.; Govind Rajan, A.; Chu, X. S.; Wang, Q. H.; Strano, M. S. Current and Future Directions in Electron Transfer Chemistry of Graphene. *Chem. Soc. Rev.* **2017**, *46*, 4530-4571.

(50) Ugeda, M. M.; Brihuega, I.; Guinea, F.; Gómez-Rodríguez, J. M. Missing Atom as a Source of Carbon Magnetism. *Phys. Rev. Lett.* **2010**, *104*, 096804.

(51) Zhong, J. H.; Zhang, J.; Jin, X.; Liu, J. Y.; Li, Q.; Li, M. H.; Cai, W.; Wu, D. Y.; Zhan, D.; Ren, B. Quantitative Correlation between Defect Density and Heterogeneous Electron Transfer Rate of Single Layer Graphene. *J. Am. Chem. Soc.* **2014**, *136*, 16609–16617.

(52) Lherbier, A.; Dubois, S. M. M.; Declerck, X.; Roche, S.; Niquet, Y. M.; Charlier, J. C. Two-Dimensional Graphene with Structural Defects: Elastic Mean Free Path, Minimum Conductivity, and Anderson Transition. *Phys. Rev. Lett.* **2011**, *106*, 046803.

(53) Lherbier, A.; Dubois, S. M. M.; Declerck, X.; Niquet, Y. M.; Roche, S.; Charlier, J. C. Transport Properties of Graphene Containing Structural Defects. *Phys. Rev. B - Condens. Matter Mater. Phys.* **2012**, *86*, 075402.

(54) Hwang, J. Y.; Kuo, C. C.; Chen, L. C.; Chen, K. H. Correlating Defect Density with Carrier Mobility in Large-Scaled Graphene Films: Raman Spectral Signatures for the Estimation of Defect Density. *Nanotechnology* **2010**, *21*, 465705.

(55) Yuan, W.; Zhou, Y.; Li, Y.; Li, C.; Peng, H.; Zhang, J.; Liu, Z.; Dai, L.; Shi, G. The Edge- and Basal-Plane-Specific Electrochemistry of a Single-Layer Graphene Sheet. *Sci. Rep.* **2013**, *3*, 2248.

(56) Landis, E. C.; Klein, K. L.; Liao, A.; Pop, E.; Hensley, D. K.; Melechko, A. V.; Hamers, R. J. Covalent Functionalization and Electron-Transfer Properties of Vertically Aligned Carbon Nanofibers: The Importance of Edge-Plane Sites. *Chem. Mater.* **2010**, *22*, 2357–2366.

(57) Dimaki, M.; Vergani, M.; Heiskanen, A.; Kwasny, D.; Sasso, L.; Carminati, M.; Gerrard, J. A.; Emneus, J.; Svendsen, W. E. A Compact Microelectrode Array Chip with Multiple Measuring Sites for Electrochemical Applications. *Sensors (Switzerland)* **2014**, *14*, 9505-9521.

(58) Lai, S. C. S.; Patel, A. N.; McKelvey, K.; Unwin, P. R. Definitive Evidence for Fast Electron Transfer at Pristine Basal Plane Graphite from High-Resolution Electrochemical Imaging. *Angew. Chemie - Int. Ed.* **2012**, *51*, 5405–5408.

(59) Zhang, G.; Kirkman, P. M.; Patel, A. N.; Cuharuc, A. S.; McKelvey, K.; Unwin, P. R. Molecular Functionalization of Graphite Surfaces: Basal Plane versus Step Edge Electrochemical Activity. *J. Am. Chem. Soc.* **2014**, *136*, 11444–11451.

(60) Patel, A. N.; Collignon, M. G.; OConnell, M. A.; Hung, W. O. Y.; McKelvey, K.; MacPherson, J. V.; Unwin, P. R. A New View of Electrochemistry at Highly Oriented Pyrolytic Graphite. *J. Am. Chem. Soc.* **2012**, *134*, 20117–20130.

(61) Unwin, P. R.; Güell, A. G.; Zhang, G. Nanoscale Electrochemistry of Sp2 Carbon Materials: From Graphite and Graphene to Carbon Nanotubes. *Acc. Chem. Res.* **2016**, *49*, 2041–2048.

(62) Song, Y.; Hu, H.; Feng, M.; Zhan, H. Carbon Nanotubes with Tailored Density of Electronic States for Electrochemical Applications. *ACS Appl. Mater. Interfaces* **2015**, *7*, 25793–25803.

(63) Ferrari, A.; Robertson, J. Interpretation of Raman Spectra of Disordered and Amorphous Carbon. *Phys. Rev. B - Condens. Matter Mater. Phys.* **2000**, *61*, 14095-14107.

(64) Pimenta, M. A.; Dresselhaus, G.; Dresselhaus, M. S.; Cançado, L. G.; Jorio, A.; Saito, R. Studying Disorder in Graphite-Based Systems by Raman Spectroscopy. *Phys. Chem. Chem. Phys.* **2007**, *9*, 1276–1291.

(65) Chieu, T. C.; Dresselhaus, M. S.; Endo, M. Raman Studies of Benzene-Derived Graphite Fibers. *Phys. Rev. B* **1982**, *26*, 5867–5877.

(66) Morris, J. W. A Survey of Materials Science I . Structure. *Structure* **2008**, https://www.mse.berkeley.edu/groups/morris/MSE200/I-structure.pdf (Accessed 01/18/2019).

(67) Tuinstra, F.; Koenig, J. L. Raman Spectrum of Graphite. *J. Chem. Phys.* **1970**, *53*, 1126-1130.

(68) Heremans, J.; Rahim, I.; Dresselhaus, M. S. Thermal Conductivity and Raman Spectra of Carbon Fibers. *Phys. Rev. B* **1985**, *32*, 6742.

(69) Merlen, A.; Buijnsters, J.; Pardanaud, C. A Guide to and Review of the Use of Multiwavelength Raman Spectroscopy for Characterizing Defective Aromatic Carbon Solids: From Graphene to Amorphous Carbons. *Coatings* **2017**, *7*, 153.

(70) M. J. Matthews, M. A. Pimenta, G. Dresselhaus, M. S. Dresselhaus, and M. Endo. Origin of Dispersive Effects of the Raman D Band in Carbon Materials. *Phys. Rev. B - Condens. Matter Mater. Phys.* **1999**, *59*, R6585(R).

(71) Lespade, P.; Al-Jishi, R.; Dresselhaus, M. S. Model for Raman Scattering from Incompletely Graphitized Carbons. *Carbon N. Y.* **1982**, *20*, 427-431.

(72) Herrmann, U., Wendler, E., Dunken, H.H., Wesch, W., and Seifert, F. Formation of Amorphous and Nano-Crystalline Carbon in C+ Implanted Silica Glass. *Berichte der Bunsen-Gesellschaft für Phys. Chemie* **1996**, *100*, 1596–1601.

(73) Dresselhaus, M. S.; Dresselhaus, G.; Saito, R.; Jorio, A. Raman Spectroscopy of Carbon Nanotubes. *Phys. Rep.* **2005**, *409*, 47-99.

(74) Reich, S.; Thomsen, C. Raman Spectroscopy of Graphite. *Phil. Trans. R. Soc. Lond. A: Math Phys. Eng. Sci.* **2004**, *362*, 2271–2288.

(75) Ferrari, A. C.; Meyer, J. C.; Scardaci, V.; Casiraghi, C.; Lazzeri, M.; Mauri, F.; Piscanec, S.; Jiang, D.; Novoselov, K. S.; Roth, S.; Geim, A. K. Raman Spectrum of Graphene and Graphene Layers. *Phys. Rev. Lett.* **2006**, *97*, 187401.

(76) Ferrari, A. C. Raman Spectroscopy of Graphene and Graphite: Disorder, Electron-Phonon Coupling, Doping and Nonadiabatic Effects. *Solid State Commun.* **2007**, *143*, 47-57.

(77) Park, J. S.; Reina, A.; Saito, R.; Kong, J.; Dresselhaus, G.; Dresselhaus, M. S. G′ Band Raman Spectra of Single, Double and Triple Layer Graphene. *Carbon N. Y.* **2009**, *47*, 1303-1310.

(78) Ferrari, A. C.; Basko, D. M. Raman Spectroscopy as a Versatile Tool for Studying the Properties of Graphene. *Nature Nanotech.* **2013**, *8*, 235–246.

(79) Cline, K. K.; McDermott, M. T.; McCreery, R. L. Anomalously Slow Electron Transfer at Ordered Graphite Electrodes: Influence of Electronic Factors and Reactive Sites. *J. Phys. Chem.* **1994**, *98*, 5314–5319.

(80) McDermott, C.; Kneten, K.; McCreery, R. Electron Transfer Kinetics of Aquated $Fe^{+3/+2}$, $Eu^{+3/+2}$, and $V^{+3/+2}$ at Carbon Electrodes: Inner Sphere Catalysis by Surface Oxides. *J. Electrochem. Soc.* **1993**, *140*, 3–9.

(81) Ambrosi, A.; Pumera, M. Precise Tuning of Surface Composition and Electron-Transfer Properties of Graphene Oxide Films through Electroreduction. *Chem. - A Eur. J.* **2013**, *19*, 4748-4753.

(82) Ambrosi, A.; Chua, C. K.; Bonanni, A.; Pumera, M. Lithium Aluminum Hydride as Reducing Agent for Chemically Reduced Graphene Oxides. *Chem. Mater.* **2012**, *24*, 2292–2298.

(83) Boopathi, S.; Narayanan, T. N.; Senthil Kumar, S. Improved Heterogeneous Electron Transfer Kinetics of Fluorinated Graphene Derivatives. *Nanoscale* **2014**, *6*, 10140-10146.

(84) Weaver, M. J.; Anson, F. C. Distinguishing between Inner- and Outer-Sphere Electrode Reactions. Reactivity Patterns for Some Chromium(III)-Chromium(II) Electron-Transfer Reactions at Mercury Electrodes. *Inorg. Chem.* **1976**, *15*, 1871–1881.

(85) Alonso, R. M.; San-Martín, M. I.; Sotres, A.; Escapa, A. Graphene Oxide Electrodeposited Electrode Enhances Start-up and Selective Enrichment of Exoelectrogens in Bioelectrochemical Systems. *Sci. Rep.* **2017**, 13726.

(86) Ganguly, A.; Sharma, S.; Papakonstantinou, P.; Hamilton, J. Probing the Thermal Deoxygenation of Graphene Oxide Using High-Resolution in Situ X-Ray-Based Spectroscopies. *J. Phys. Chem. C* **2011**, *115*, 17009–17019.

(87) Yamaguchi, H.; Ogawa, S.; Watanabe, D.; Hozumi, H.; Gao, Y.; Eda, G.; Mattevi, C.; Fujita, T.; Yoshigoe, A.; Ishizuka, S.; Adamska, L.; Yamada, T.; Dattelbaum, A. M.; Gupta, G.; Doorn, S. K.; Velizhanin, K. A.; Teraoka. Y.; Chen, M.; Htoon, H.; Chhowalla, M.; Mohite, A. D.; Takakuwa, Y. Valence-Band Electronic Structure Evolution of Graphene Oxide upon Thermal Annealing for Optoelectronics. *Phys. Status Solidi Appl. Mater. Sci.* **2016**, *213* (9), 2380-2386.

(88) Mao, X.; Simeon, F.; Rutledge, G. C.; Hatton, T. A. Electrospun Carbon Nanofiber Webs with Controlled Density of States for Sensor Applications. *Adv. Mater.* **2013**, *25*, 1309-1314.

(89) Wiggins-Camacho, J. D.; Stevenson, K. J. Effect of Nitrogen Concentration on Capacitance, Density of States, Electronic Conductivity, and Morphology of N-Doped Carbon Nanotube Electrodes. *J. Phys. Chem. C* **2009**, *113*, 19082–19090.

(90) Dresselhaus, M. S.; Dresselhaus, G.; Saito, R. Physics of Carbon Nanotubes. *Carbon N. Y.* **1995**, *33*, 883–891.

(91)   Hamada, N.; Sawada, S. I.; Oshiyama, A. New One-Dimensional Conductors: Graphitic Microtubules. *Phys. Rev. Lett.* **1992**, *68*, 1579–1581.

(92)   Murzashev, A. I.; Shadrin, E. O. Energy Spectrum and Optical Absorption Spectra of Carbon Nanotubes with Chiralities of (10, 10), (11, 9), and (12, 8). *J. Exp. Theor. Phys.* **2014**, *118*, 935–944.

(93)   Saito, R.; Fujita, M.; Dresselhaus, G.; Dresselhaus, M. S. Electronic Structure of Graphene Tubules Based on C60. *Phys. Rev. B* **1992**, *46*, 1804–1811.

(94)   Kareev, I. E.; Bubnov, V. P.; Murzashev, A. I.; Lobanov, B. V. Endohedral Fullerene $Gd_2C_2@C_{82}$ as a Strongly Correlated Electron System. *Phys. Solid State* **2015**, *57*, 2323–2330.

(95)   Geim, A. K.; Novoselov, K. S. The Rise of Graphene. *Nat. Mater.* **2007**, *6*, 183–191.

(96)   Wilson, M. Electrons in Atomically Thin Carbon Sheets Behave like Massless Particles. *Physics Today*. **2006**, *59*, 21-23.

(97)   Bubnov, V. P.; Kareev, I. E.; Lobanov, B. V.; Murzashev, A. I.; Nekrasov, V. M. Energy and Optical Absorption Spectra of Endohedral Metallofullerenes with Gd or Ho as Strongly Correlated π-Electron Systems. *Phys. Solid State* **2016**, *58*, 1698–1704.

(98)   McKinnon, B.; Choy, T. A Tight Binding Model for the Density of States of Graphite-like Structures, Calculated Using Green's Functions. *Aust. J. Phys.* **1993**, *46*, 601-611.

(99)   Ivanovskaya, V. V.; Zobelli, A.; Teillet-Billy, D.; Rougeau, N.; Sidis, V.; Briddon, P. R. Hydrogen Adsorption on Graphene: A First Principles Study. *Eur. Phys. J. B* **2010**, *76*, 481–486.

(100)   Dahn, J. R.; Reimers, J. N.; Sleigh, A. K.; Tiedje, T. Density of States in Graphite from Electrochemical Measurements on $Li_x(C_{1-z}B_z)_6$. *Phys. Rev. B* **1992**, *45*, 3773-3773.

(101)   Niimi, Y.; Matsui, T.; Kambara, H.; Tagami, K.; Tsukada, M.; Fukuyama, H. Scanning Tunneling Microscopy and Spectroscopy of the Electronic Local Density of States of Graphite Surfaces near Monoatomic Step Edges. *Phys. Rev. B - Condens. Matter Mater. Phys.* **2006**, *73*, 085421.

(102)   Hove, J. E. Electronic Density of States of Graphite. *Phys. Rev.* **1955**, *97*, 1717–1718.

(103)   Schorr, N. B.; Jiang, A. G.; Rodríguez-López, J. Probing Graphene Interfacial Reactivity via Simultaneous and Colocalized Raman–Scanning Electrochemical Microscopy Imaging and Interrogation. *Anal. Chem.* **2018**, *90*, 7848–7854.

(104)   Peng, Z.; Yang, R.; Kim, M. A.; Li, L.; Liu, H. Influence of O_2, H_2O and Airborne Hydrocarbons on the Properties of Selected 2D Materials. *RSC Adv.* **2017**, *7*, 27048-27057.

(105)   Liu, J.; Lai, C. Y.; Zhang, Y. Y.; Chiesa, M.; Pantelides, S. T. Water Wettability of Graphene: Interplay between the Interfacial Water Structure and the Electronic Structure. *RSC Adv.* **2018**, *8*, 16918–16926.

(106)   Vosgueritchian, M.; Lemieux, M. C.; Dodge, D.; Bao, Z. Effect of Surface Chemistry on Electronic Properties of Carbon Nanotube Network Thin Film Transistors. *ACS Nano* **2010**, *4*, 6137–6145.

(107)   Chutia, A.; Cimpoesu, F.; Tsuboi, H.; Miyamoto, A. Influence of Surface Chemistry on the Electronic Properties of Graphene Nanoflakes. *Chem. Phys. Lett.* **2011**, *503*, 91–96.

(108) Ren, J.; Weber, F.; Weigert, F.; Wang, Y.; Choudhury, S.; Xiao, J.; Lauermann, I.; Resch-Genger, U.; Bande, A.; Petit, T. Influence of Surface Chemistry on Optical, Chemical and Electronic Properties of Blue Luminescent Carbon Dots. *Nanoscale* **2019**, DOI:10.1039/C8NR08595A.

(109) Moussa, G.; Matei Ghimbeu, C.; Taberna, P. L.; Simon, P.; Vix-Guterl, C. Relationship between the Carbon Nano-Onions (CNOs) Surface Chemistry/Defects and Their Capacitance in Aqueous and Organic Electrolytes. *Carbon N. Y.* **2016**, *105*, 628-637.

(110) Ashraf, A.; Wu, Y.; Wang, M. C.; Yong, K.; Sun, T.; Jing, Y.; Haasch, R. T.; Aluru, N. R.; Nam, S. Doping-Induced Tunable Wettability and Adhesion of Graphene. *Nano Lett.* **2016**, *16*, 4708–4712.

(111) Tian, T.; Lin, S.; Li, S.; Zhao, L.; Santos, E. J. G.; Shih, C. J. Doping-Driven Wettability of Two-Dimensional Materials: A Multiscale Theory. *Langmuir* **2017**, *33*, 12827–12837.

(112) Hong, G.; Han, Y.; Schutzius, T. M.; Wang, Y.; Pan, Y.; Hu, M.; Jie, J.; Sharma, C. S.; Müller, U.; Poulikakos, D. On the Mechanism of Hydrophilicity of Graphene. *Nano Lett.* **2016**, *16*, 4447–4453.

Chapter 2: Thermal Modification of Graphite for Fast Electron Transport and Increased Capacitance

Abstract

On thermal treatment, eight different graphite materials became resistant to air aging for at least nine weeks compared to the usual time of hours to a few days when assayed in 1 mM ferri-ferrocyanide solution. In addition, resistance to aging lasted at least seven days when immersed in 1 mM ferri-ferrocyanide solution compared to the frequently reported few minutes to hours. Experimental results confirm that with heat treatment, HOPG-ZYH, graphite rods, pyrolytic graphites, graphite felts, and natural and artificial graphites undergo structural reorganization that leads to restructuring of their electronic nature. This electronic restructuring enhances and sustains their electrochemical properties. The extent of reorganization is dependent on the initial disordered state, which in turn is important to the final structural and electronic conditions. These results strongly suggest that the primary factor enhancing the electronic response of heat-treated materials is from an overall higher density of states (DOS) localized on delocalizing π bonds compared to their controls. This structural reorganization of the graphites also supports a degree of crystallinity along the lattice sites that enables carrier hopping irrespective of adventitious oxygen-containing and hydrocarbon moieties that are associated with aging-induced sluggish electron transfer kinetics. The attributes of this electronic structure demonstrate a strongly correlated system that exhibits a non-perturbative behavior. A one-dimensional Hubbard model describes this behavior to explain the surface-to-electronic chemistry of treated graphites by addressing both their enhanced electrochemical performance and their delayed or reduced aging effects.

Keywords: graphites, aging, fast HET, disorder, density of states, electronic structure

Introduction

Heterogeneous electron transfer (HET) kinetics are fundamental in solid carbon materials (electrode)-electrolyte interactions and play significant roles in molecular electronics, electrochemical energy storage and conversion, sensing, and electro-oxidative reactions.[1–10] The electronic density of states (DOS) dominates the HET kinetics of these carbon materials due to the probability that an electron with the appropriate energy may transfer to a redox probe.[11–14] Thus, the HET rate increases when the electrode having sufficient electronic states with energies near the formal potential level of the redox probe involved has overlap between its (electrode) energy levels and those of the redox states in solution.[5,12–16] Electronic states of carbon electrodes could be determined by surface states or structures[11,14,17] such as defects[14,18,19] and functional groups.[14,20] It is thought that the kinetic preferences of these functional groups for electron transport, even though often unknown,[20] remain a key component for the resultant electrochemical responses of carbon materials to redox probes.[20] Thus, techniques and/or procedures aimed at increasing the DOS by either introducing, modulating, and/or manipulating surface functional groups and defects ultimately result in reciprocated responses to electrochemical activities of carbon electrodes. These include mechanical polishing−as commonly employed on glassy carbon electrodes, vacuum heat treatment or heating under inert gas, combined treatment of the electrode with organic solvents and activated carbon, laser ablation or laser-based thermal treatment protocols, electrochemical polarization such as pre-anodization, various chemical exposures, and plasma activation treatments with radio-frequency (RF), hydrogen, and microwave.[21,22]

Treatment procedures aim to improve one or more properties of the graphite and/or carbon materials, such as capacitance[23–26] and/or the HET kinetics property of solid electrodes[27,28] via various mechanisms, though sometimes similar. Regarding electron transport, different treatment procedures yield structurally distinct surfaces with varying electron transfer rate constants.[27] For example, laser ablation and vacuum thermal treatments can promote electron transfer by desorption of impurities and formation[28–30] or exposure of active regions[28,29] without the contribution of oxygen-containing functional groups.[28] Additionally, laser treatment and anodization promote fast electron transfer by creating edge plane defects,[27] while treatment with organic reagents promotes electron transfer by desorbing impurities from electrode surfaces.[31] However, chemisorbed species can hamper electron transfer kinetics, particularly oxygen containing groups[28,31–33] and hydrocarbons[34–37] on carbon electrode surfaces such as graphite and graphene. Thus, it is generally accepted that the surfaces of solid carbonaceous electrodes are gradually deactivated during exposure and adsorption of adventitious impurities from air or electrolyte solutions preceding electrochemical experiments[38] and

resulting in sluggish heterogeneous electron transfer (HET) kinetics due to aging[22] and accompanying impediments for various uses of carbon materials.[6] [11]

The present work focuses on resistance to aging of graphite materials thermally treated in air for at least 9 weeks and in ferri-ferrocyanide redox couple [(Fe(CN)$_6$]$^{3-/4-}$ (1 M KCl)) for 7 days. Results include a total of eight carbon materials including HOPG-ZYH, two different pyrolytic graphites, artificial and natural graphites, graphite rod, and two graphite felts (GFA3 and GFA5). Investigations on material behaviors through FTIR, Raman, XPS, UPS and water contact angle measurements were designed for periodic monitoring and evaluation of resistance to aging relative to control samples undergoing no heat treatment. Graphite heat treatments typically result in higher-ordered physicochemical states, which can be described via the folding funnel model.[39–41] Empirical data in support of the model implies that there exists a path to a minimum Gibbs free energy of extent of crystallinity—or more probably a multiconfigurational ensemble of localized minima of metastable and stable states in real materials—irrespective of the starting graphite (with respect to the graphites employed herein) such that the converted microscopic graphite state is mainly aromatic. This new graphite state would possess a degree of crystallinity along the lattice sites that enables carrier hopping irrespective of adventitious oxygen-containing and hydrocarbon moieties, which are synonymous with aging-induced sluggish electron transfer kinetics. This would suggest an unperturbed or lesser-perturbed electronic structure signifying a diminution of Coulombic (repulsive) contributive forces. A one-dimensional Hubbard model[42] facilitates an explanation of the surface-to-electronic (or vice-versa) chemistry of the treated graphite materials where the heat treated materials have enhanced and sustained electronic/electrochemical properties in contrast to the controls and irrespective of any adventitious functional surface groups.

Results and Discussion

Cyclic voltammograms (CVs) of control and treated graphite materials in 1 mM $[Fe(CN)_6]^{3-/4-}$ redox couple solution are shown in Figure 2.1 for the HOPG-ZYH samples as an example comparator while the other graphitic materials are in the Supporting Information (Figure S2.1). The ΔE_p of the control graphites widened on subsequent scans signifying increasingly sluggish electron transfer. This is unlike the treated materials that had steady and consistent CVs on scanning several times in the redox solution since in general, electron transfer response of carbon electrodes deteriorates on subsequent scans in redox couples.[17,43,44] The ΔE_p of the control HOPG-ZYH was 65±5 mV when peeled fresh. These electrodes aged to 760±5 mV in 24 hours and did not age more afterwards even at the end of 38 days when testing halted on its control (Table 2.1). The other control graphites behaved similarly to the HOPG, having much higher ΔE_p at the end of the air-aging experiment. The treated HOPG had a higher than usual ΔE_p at the end of 64 days unlike the other treated graphites.

The CVs of the treated graphites, when compared to their controls and graphite/carbon materials from the literature,[2,12,35,44,45] suggest that surface structural and/or electronic changes are responsible for our observations. Additionally, the increase in HET across eight different graphite materials from various graphitic strata indicates that whatever mechanism is responsible for the trend is common for graphitic materials. In addition to fast HET, the increased capacitance of graphite felts (GFA3 and GFA5 (Figure S2.1 (h1-i2)) and the symmetric behavior of the treated graphite rod capacitance, even at high scan rates (Figure S2.1 (g2)), suggest that thermal treatment modulates not just the pathway for fast HET kinetics alone, but probably other electrochemical properties of the graphites (in this case, the graphite felt capacitance). Whatever the mechanism(s) of change involved would have likely modulated the fundamental structure(s) of these materials. These would include, for example, their degree of crystallinity, Raman signatures such as the intensity ratios of their D-to-G bands and other electronic properties such as their LUMO and HOMO bands. Enhanced HET in aged control graphite felts over the fresh controls without a corresponding increase in capacitance is noteworthy and its importance is further discussed with the XPS results.
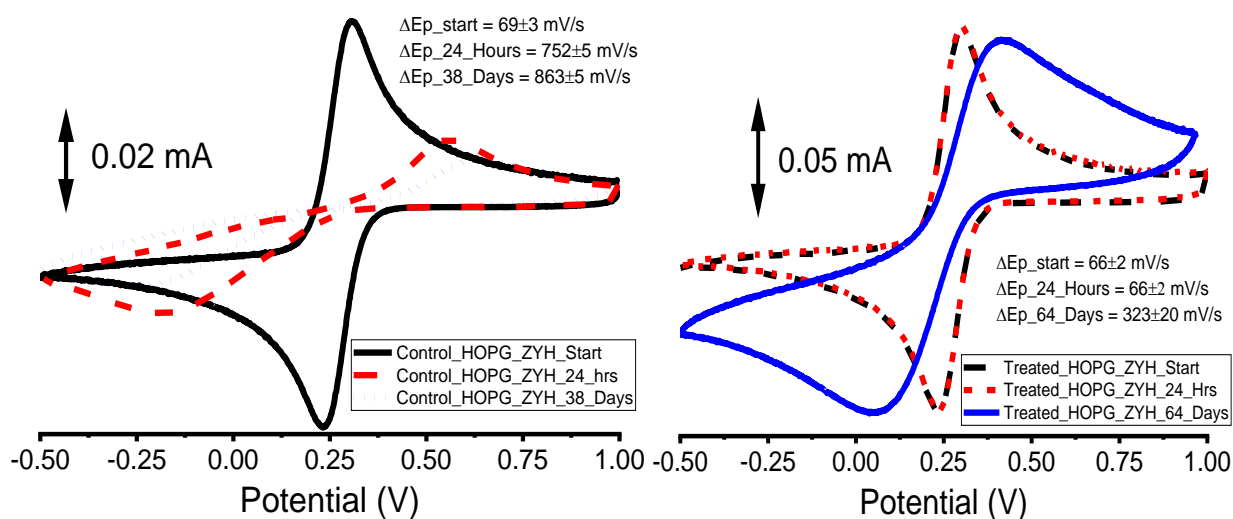
Figure 2.1: Cyclic voltammogram (CV) trends for the control (a) and treated (b) HOPG-ZYH at the start (black), 24 hours (red dashed line), and end of the experiment (v= 0.05 V/s in 1 mM ferri-ferrocyanide; n = 3): (a) dotted blue CV at 38 days, (b) solid blue CV at 64 days.

The heterogeneous electron transfer rate constants (k^o [cm/s]) for the pristine control (denoted with "C") and thermally-treated graphites (denoted with "T") in Table 2.1 derive from the relationship between peak potential separation (ΔEp [mV]) and the kinetic parameter ψ (see [46] for ψ values) according to the Nicholson equation:[46]

$$k^o = \psi \left[D_O \pi v \left(\frac{nF}{RT} \right) \right]^{1/2} \left(\frac{D_O}{D_R} \right)^{-\left(\alpha/2 \right)}$$

(1)

The rate constant results apply for $\alpha = 0.5$ and diffusion coefficients values for $Fe(CN)_6^{3-/4-}$ (1 M KCl) of DO (7.32×10^{-6} cm^2-s^{-1}) and DR (6.67×10^{-6} cm^2-s^{-1}).[47]

Table 2.1: ΔEp (mV) and Accompanying Rate Constants[a] of the Treated and Control Graphites Aged in Air.

Electrode	Type	$\Delta Ep_{(Start)}$ (mV)	$K^0_{(Start)}$ $(cm^2.s^{-1})$	End Day	$\Delta EP_{(End)}$ (mV)	$K^0_{(End)}$ $(cm^2.s^{-1})$
HOPG-ZYH	C	69±3	$1.79\times10^{-2}\pm6.5\times10^{-3}$	38	863±5	$6.32\times10^{-7}\pm5.7\times10^{-8}$
	T	66±2	$2.61\times10^{-2}\pm1.8\times10^{-2}$	64	323±20	$3.40\times10^{-4}\pm2.9\times10^{-5}$
PG_(K&J)	C	312±48	$3.53\times10^{-4}\pm8.0\times10^{-5}$	63	532±56	$1.76\times10^{-4}\pm2.3\times10^{-5}$
	T	65±1	$3.26\times10^{-2}\pm2.0\times10^{-2}$	64	76±2	$1.09\times10^{-2}\pm1.1\times10^{-3}$
PG_(UN)	C	183±30	$1.10\times10^{-3}\pm4.0\times10^{-4}$	63	430±69	$2.30\times10^{-4}\pm5.0\times10^{-5}$
	T	65±2	$3.26\times10^{-2}\pm9.8\times10^{-3}$	64	84±2	$6.52\times10^{-3}\pm4.0\times10^{-4}$
Art Graphite	C	425±14	$2.33\times10^{-4}\pm9.5\times10^{-6}$	63	573±23	$1.19\times10^{-4}\pm5.1\times10^{-5}$
	T	66±4	0.026±(*)	64	93±2	$4.77\times10^{-3}\pm2.9\times10^{-4}$
			±(*) = 0.026-0.016 to 0.026+0.036			
Nat Graphite	C	74±7	$1.20\times10^{-2}\pm5.0\times10^{-3}$	63	105±4	$3.26\times10^{-3}\pm3.8\times10^{-4}$
	T	65±2	$3.26\times10^{-2}\pm9.8\times10^{-3}$	64	90±4	$5.30\times10^{-3}\pm7.6\times10^{-4}$
Mech stressed Natural graphite	C	145±25	$1.60\times10^{-3}\pm5.0\times10^{-4}$	63	245±6	$5.10\times10^{-4}\pm2.0\times10^{-5}$
	T	67±2	$2.28\times10^{-2}\pm7.3\times10^{-3}$	64	89±8	$5.50\times10^{-3}\pm2.0\times10^{-3}$
Graphite rod	C	69±2	$1.80\times10^{-2}\pm4.0\times10^{-3}$	63	94±8	$4.60\times10^{-3}\pm1.2\times10^{-3}$
	T	40±2	1.02±0.09	64	40±2	1.02±0.08
GFA3	C	211±22	$6.50\times10^{-4}\pm2.5\times10^{-4}$	82	66±2	$2.61\times10^{-2}\pm9.8\times10^{-3}$
	T	171±14	$1.20\times10^{-3}\pm2.0\times10^{-4}$	82	118±4	$2.50\times10^{-3}\pm2.0\times10^{-4}$
GFA5	C	165±19	$1.30\times10^{-3}\pm3.0\times10^{-4}$	85	93±9	$4.76\times10^{-3}\pm1.4\times10^{-3}$
	T	150±7	$1.50\times10^{-3}\pm1.0\times10^{-4}$	85	128±3	$2.10\times10^{-3}\pm1.0\times10^{-4}$

[a]k0 [cm/s] in 1 mM Fe[(CN)6]3–/4– and at ν = 0.05 V/s. n = 3.

Unlike previous reports where HOPG-ZYH heated at 650 °C formed multilayer pits,[48,49] the treated HOPG-ZYH surface shows no pits and limited flaking with step defects seen also in control samples (Figure 2.2). Higher magnifications hint at limited surface exfoliation to expose few layers. Control samples show only surface roughness and defects attributable to the typical process of removing from bulk samples. A lack of pitting on treated samples suggests that the facile electron transport even when aged cannot be mainly attributed to edge exposure.

Other extended and planar graphites when treated show no changes in surface morphology when compared to their controls (Figure S2.2), although fiber felts GFA3 and GFA5 do (Figure S2.2). Even though the formation[28–30] or exposure of active regions[28,29] such as step or edge defects on graphite basal planes facilitate HET,[17,45,50–55] the SEM micrographs reveal only slight etching on the graphite felts. This strongly implies that surface defects are not generally responsible for facile HET in the treated graphites, since all sets displayed heat-treatment-induced HET kinetics enhancement.
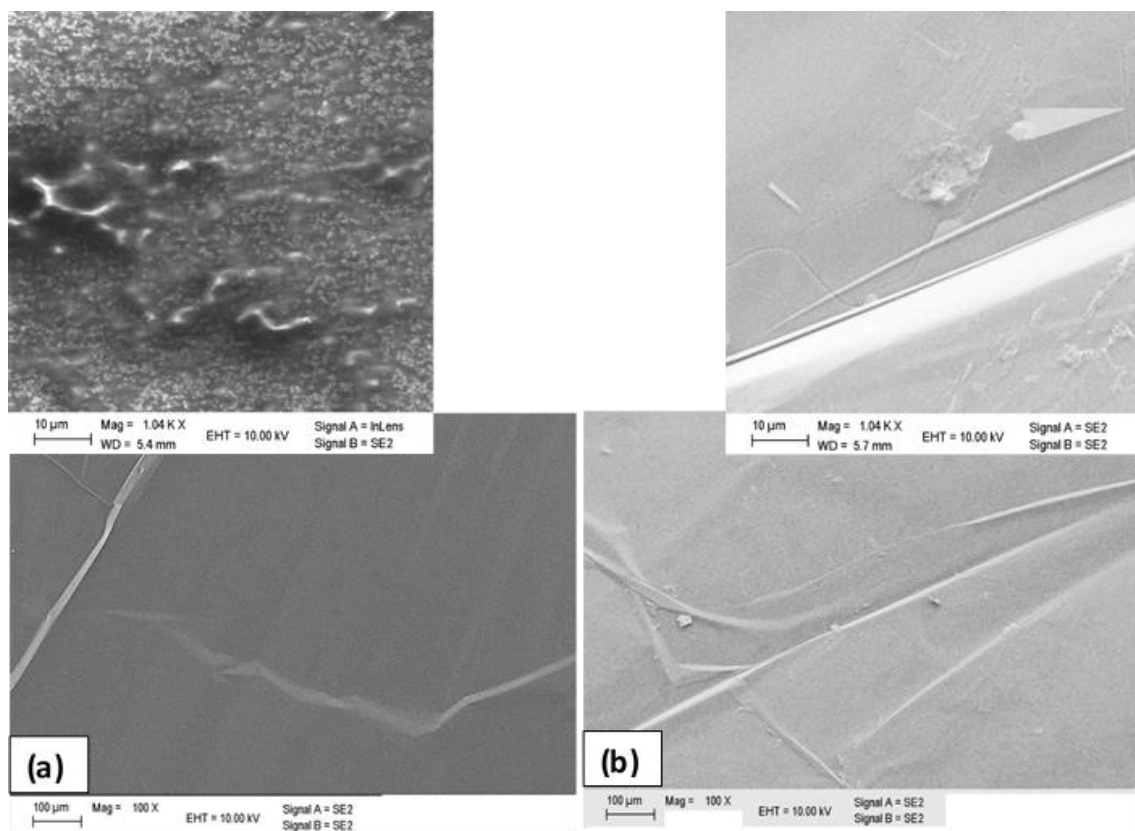
Figure 2.2: SEM micrographs of (a) the control and (b) treated HOPG-ZYH (scale bars: 100 μm); higher magnifications (1.04k×), respectively (top scale bars: 10 μm).

Graphite felts have disordered or mutually-disoriented crystallites, with exposed edges, on their carbon fibers that are prone to oxidative attack from thermal treatment.[56] However, such edge density exposure leading to accelerated HET are known to be deactivated quickly,[12,21] even within minutes or hours when exposed in air.[57,58] This is unlike the treated graphites employed in this study that still show very good HET kinetics even at the end of, at least, 64 days in air. The PG aged in 1 mM ferri-ferrocyanide increased in ΔE_p by about 40 mV in 7 days (Figure S2.2) unlike reported increases in ΔEP of several hundreds of mV over a few hours.[59]

Water contact angles (WCA) of both control and treated graphite groups over the course of aging show that thermal treatment increases wettability (Figure 2.3), even from fully hydrophobic (Figure 2.3b) to completely wet out (0° not shown) in the cases of porous graphites (see video uploads i through iii for the dynamic contact angles of treated graphite felts, natural graphite, and graphite rod respectively). WCA correlate with surface chemistry and roughness as well as heterogeneity or patterns thereof.[60,61] WCA values near 60° for treated samples are consistent with the definition of hydrophilicity for graphite and its graphene derivatives. Those of the controls (WCA ≥ 80°) are also consistent with hydrophobicity of graphites and graphenes.[62,63] Artificial graphite show hydrophobic WCAs ≥ 90° unlike the HOPG-ZYH and PGs of roughly 80°. Lower WCA in controls are attributed to native edge densities on their basal planes, which reportedly lowers WCA in otherwise hydrophobic graphitic materials.[64] Also of note is the wetting of control graphite felts (GFA3 and 5) from the 35th day and onwards (see video upload iv) even though individual fibers still exhibit clear hydrophobicity, for example, in residual water beading at apparent angles approaching 180° indicating extreme surface chemical heterogeneities (Figure S2.3 and Supporting video iv and v). The WCA results suggest that it is likely that surface functional group differences between the control and treated materials could be responsible for the differences in wetting behavior.[65–67]
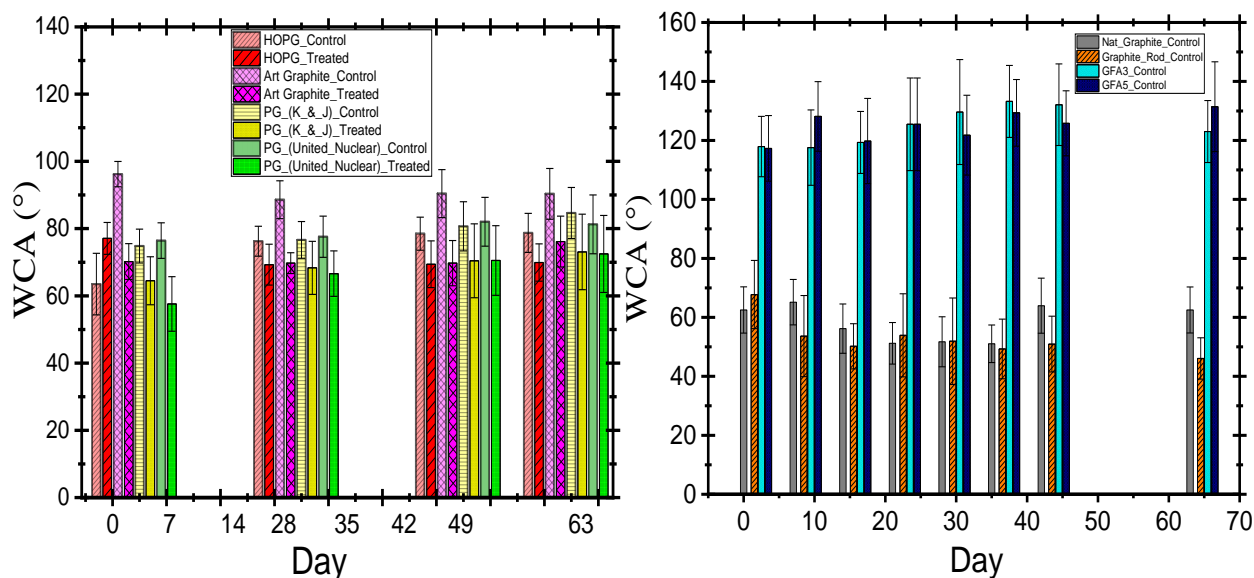
Figure 2.3: Water contact angles (WCA) with (a) HOPG at the numbered day of test (0, 21, 42, 63) clustered from left-to-right with artificial graphite, PG(K&J), and PG(UN) treated sample data overlaying the control data of mostly higher values. For clarity, only four data cluster sets are shown here. The entire cluster set for the entire nine weeks are shown in Figure S2.3a; (b) natural graphite clustered left-to-right with graphite rod and felts (GFA3 and GFA5) control samples with all thermally-treated samples as totally wetting and not shown (see video uploads i to iii).

ATR-FTIR spectra of aged samples for both control and treated HOPG show peaks near 2100 cm^{-1} associated with silanol polymers, ~3740 cm^{-1} associated with reactive Si-OH and 3350 cm^{-1} arising from normal polymeric OH stretches[68] compared to fresh samples (Figure 2.4). The Si-related modes derive from contaminants of exposure to air-borne soil particles.[69] Prominent peaks at ~2850 cm^{-1} and 2920-2930 cm^{-1} also arise in aged (control and treated) samples, being modes from symmetric and asymmetric methylene vibrations, respectively, widely expected to cause high WCA of graphene and graphites during air aging.[34–36,62,70–73] Since both peaks appeared in spectra of control and heat-treated samples, then the observed increase in wetting of the treated samples, over their controls, would not seem to be moderated merely through surface bound adventitious hydrocarbon (HC) and oxygen functional groups as previously reported.[34,36,70–72,74] Thus, the change in wetting properties of the treated samples may be explained through their electronic structure, including more than surface-

bound functional group arrangements alone.[63,75,76] The hypothesis is that WCA most strongly reflects consistency with surface functional constituencies when they also correlate with electronic structural effects.

Micrographs reveal that some fibers in aged felts, which are fiber bundles, begin to separate into individual fibrils (**Figure S2.4**), increasing surface area and effective porosity of the felt. This degradation allows water to be forced through some areas of the felt (Supporting video iv) but not others (Supporting video v). Therefore, the wetting behavior of the aged graphite felts is not solely because of surface oxide accumulation during aging.[77] Thus, some combination of hydrophobic and hydrophilic fibers facilitated water penetration through the felt channels to increase the overall porosity of the fibers, as seen from the CVs of the aged control fibers,[78] even though the hydrophilicity of these aged graphite felts was not sufficient enough to cause a build-up of non-Faradaic charges (capacitance increase).
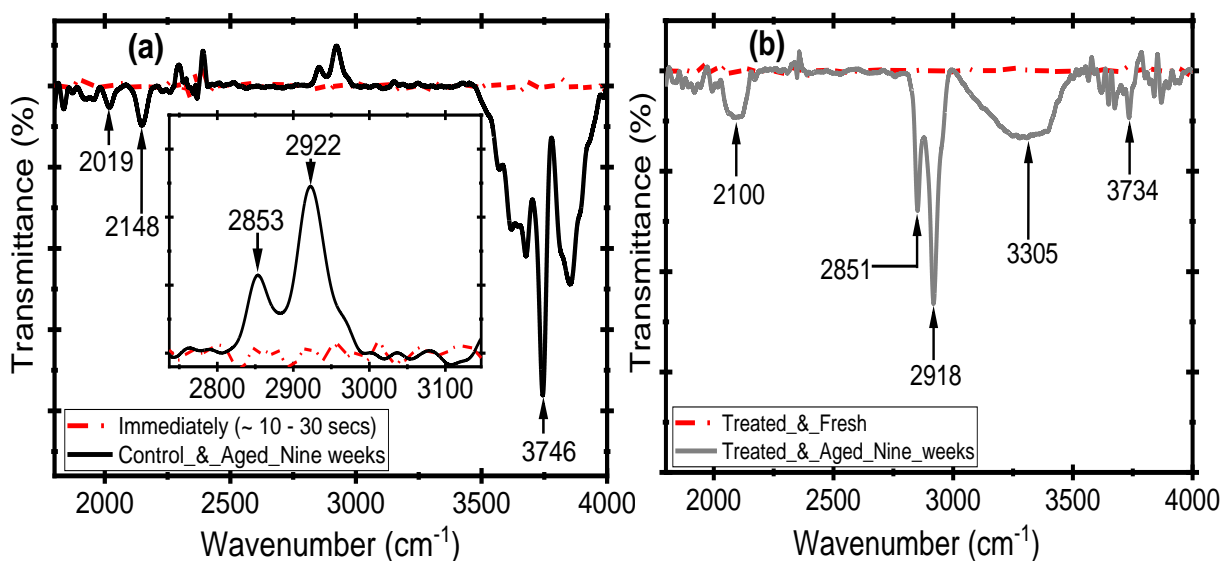
Figure 2.4: ATR-FTIR spectra of (a) control and (b) treated HOPG-ZYH at the start of experiment (red dash-dot) and at the end of nine weeks of aging in the lab atmosphere (solid). Inset: magnified region.

Raman spectroscopy reveals both chemistry and morphology that may impact the electronic properties of graphites,[19] complementing both SEM imaging and ATR-FTIR spectroscopy.[64,79] When applied to investigate carbon materials, microRaman explores local properties including crystallinity[80] and defect density or disorder impacting the DOS[64,79,80], which is important for HET.[19] The Raman spectra for HOPG show the so-called D band ca. 1350 cm^{-1}, characteristic of disorder and/or defects, in heat-treated samples but not the control (**Figure 2.5**) Additionally, peaks at ~1625 cm^{-1} appeared only for the spectra of the treated samples, which are identified with the D′ band. For other graphites employed in this research, both control and treated samples exhibit a D band and all treated samples show the 1625 cm^{-1} D′ band as well as the graphite rod control (**Figure S2.5**). The D and D′ bands reflect the high DOS for zone-edge and midzone phonons, respectively.[80,81] All sample spectra have the 2D band at ~2720 cm^{-1}. The 2D band in graphite is due to graphite phonon backscattering and is dependent on the probing laser intensity and wavelength.[79]
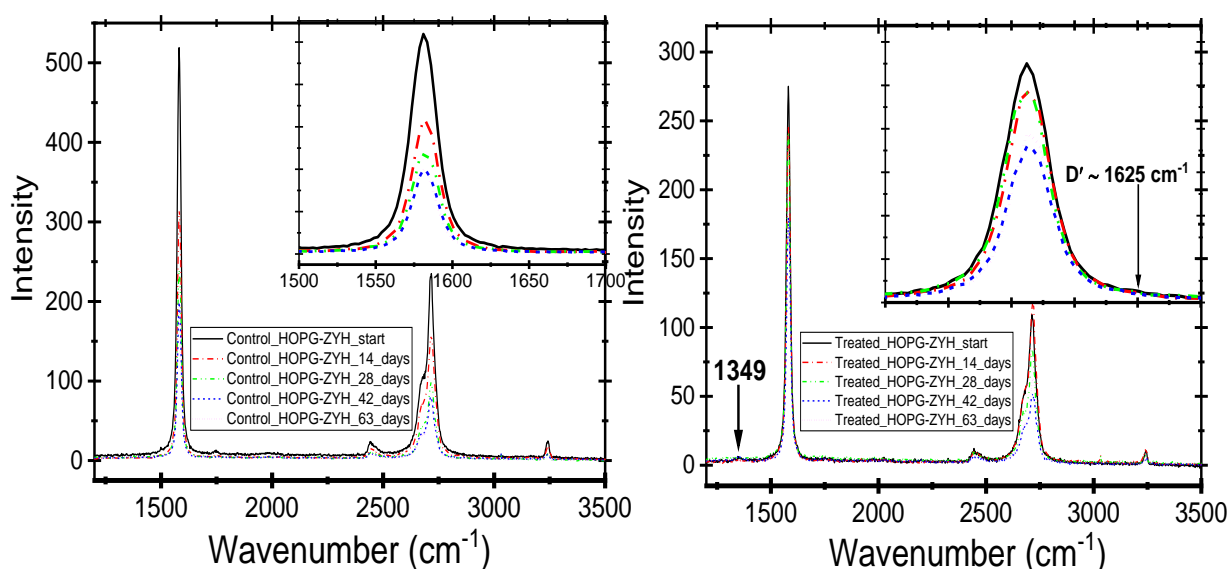
Figure 2.5: Raman spectra of (a) control and (b) treated HOPG-ZYH. Insets: Graphite (G) bands magnified. The treated HOPG now has a small bump near 1350 cm^{-1} synonymous with the disorder-induced D band and another disorder-induced band near 1625 cm^{-1}, the D′ band.

Peak intensity (I) ratios of Raman bands provide an internally-consistent and semi-quantitative measure of disorder and other feature differences among similar materials and specifically herein track changes and stability over time. I_D/I_G is a measure of the disorder in the system. The common factor of I_D/I_G for the treated materials was consistently higher relative to their control samples. In natural graphite, graphite rod, and GFA5 (at day 63, end of experiment), control I_D/I_G values were higher than treated samples. To understand better what is happening, I_D/I_G was resolved into two different components:

$$I_D/I_G = I_D/I_{2D} \times I_{2D}/I_G \tag{2}$$

Whereby, the I_D/I_{2D} is defined as the intrinsic defect density ratio, independent of the graphite (G) band. The I_{2D}/I_G value is suggestively dependent on changes in the graphite (G) component – without the I_D contribution – under constant incident laser power, which was approached through optical sample focus. Any inconsistencies in laser power impact only the 2D peak, leaving the D-to-G constant (I_{2D} is a strong indicator of the crystallinity in carbon materials and has been suggested as appropriate for relatively high-quality carbon determination).[82] All treated graphites show greater I_D/I_G, lower I_{2D}/I_G and greater I_D/I_{2D} vs. their control, indicating that increasing disorder is primarily responsible for material property enhancements, where G-band quality is preserved or even improved (Figure 2.6).

Conversely, the graphite mode is weaker in the control samples relative to their disorder species/structure content as probed by vibrational spectroscopy. This Raman analysis indicates thermally-modulated restructuring in the treated samples. Natural graphite shows lower overall quality due to diminished G-band effects. The high I_{2D}/I_G of the graphite felts and the low I_D/I_{2D} imply that the higher I_D/I_G in the GFA5 control is not a function of more defects per se but of the graphite quality degradation over time (Figure S2.4). When all three trends are considered for the graphite rod, it is deduced that the now very porous nature and enhanced electrochemical properties, such as fast HET kinetics and symmetric capacitive behavior at fast scan rates, of the treated over the control graphite rods is due to the pronounced D′ band in the treated to the control and less on the I_D/I_G as was previously thought. Thus, the treatment protocol fine-tuned the electronics of the graphite rod without drastic alteration of the defect density.

The in-plane crystallite spacing along the a-xis, L_a (in nm) values of the control and treated graphites were calculated from the Raman intensity ratio, I_D/I_G as previously proposed.[83]

$$L_a(nm) = (2.4 \times 10^{10})\lambda^4 (I_D/I_G)^{-1} \tag{3}$$

Whereby λ is the wavelength (in nm) of the probing laser intensity employed in the Raman analysis (in this case, 532.5 nm). The results of the calculations for the control and treated samples at various days of the aging cycles are as shown in Table S2.1. The results show that besides the graphite rod and natural graphite, the L_a decreased for the treated groups in comparison with the control groups. The decrease in L_a between planes corresponds to an increase in crystallite sizes and transition to a lamellar structure from a diffusive one.[84,85] This corresponds to a well-ordered honey-comb like structure with good electrical conductivity.[86] The deviation of the graphite rod from the trend is in tandem to the explanations given above for the I_D/I_G.

The D′ band and the higher D/G ratios in treated samples vs. controls suggest an annealing that depends on the initial graphitic disorders to form, on the average, with enhanced HET kinetics. Disorder in the controls is the foundation for structural and electronic re-configurations on heat treatment. Besides, it has been reported that a certain degree of defect density is necessary for enhancing and even optimizing electrochemical and other electronics-based performance.[19] Intrinsic structural change altering the DOS, rather than surface chemistry and roughness, is the more important factor for improved HET rates.[87]
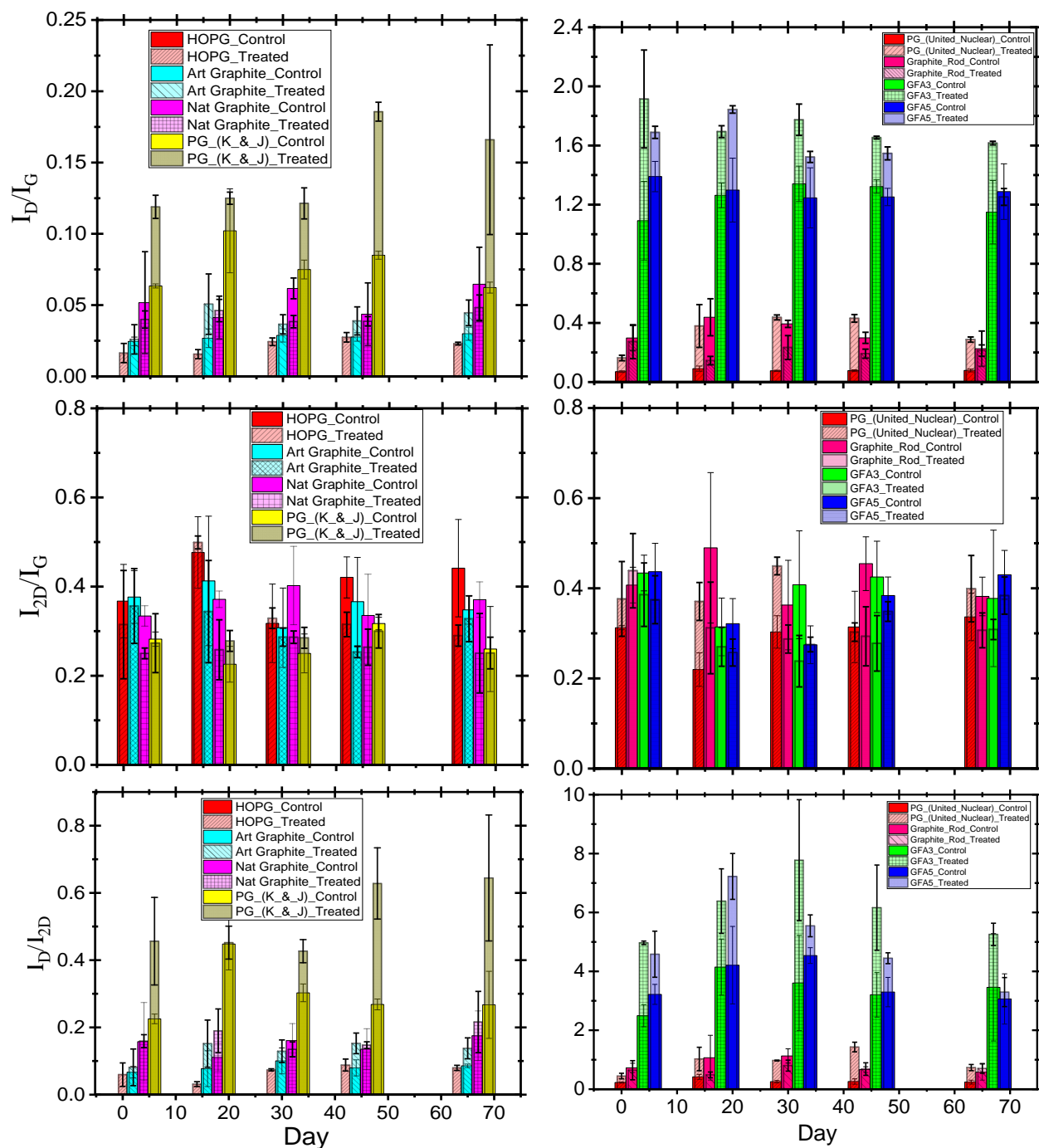
Figure 2.6: Raman band peak intensity ratios vs. days of aging in air (n = 4 per sample type): (a-b) D-to-G band (ID/IG) indicating degree of disorder; (c-d) 2D-to-G band (I_{2D}/I_G) and (e-f) D-to-2D (I_D/I_{2D}) deconvolve the intrinsic graphite quality and intrinsic disorder, respectively. All sample types stacking treated sample values over control sample types in clusters that begin on their respective days of evaluation aligned left-to-right as HOPG, artificial, natural, and PG (K&J) graphites (left-hand graph sets) and PG(UN), graphite rod, and felts GFA3 and GFA5 (right-hand graph sets).

Four selected sample types – HOPG-ZYH, PG(K&J), GFA3 and artificial graphite – of the more dissimilar graphites analyzed with XPS reveal surface and near-sub-surface impacts of aging between control and treated samples freshly prepared (CF and TF) and fully aged (CA and TA). From XPS data for HOPG-ZYH, control and treated fresh samples (CF and TF) have significant amounts of sp^2-bonded carbons at 284.4 eV (Figure 2.7) while other graphites show that thermal treatment increased the sp^2 carbons over the sp^3 at ~285.6 eV (Figure S2.6). The results suggest that the oxides and Si (for the aged samples) groups did not modulate the fast-HET kinetics in the treated samples. Summarily, thermal treatment increased the sp^2 content of the treated over their controls in some cases to $\geq$ 90% at start of the experiment. By the time of XPS analysis (~100 days from start of experiment), these sp^2 ratios were about 85%. From high resolution XPS, the oxygen-containing species content of the TF GFA3 is 3.8 times greater than the CF sample. The treated and aged (TA) GFA3 had about 1.6 times the oxygen content of the treated and fresh (TF) sample just as the capacitance of the TA sample decreased to about half of those of the TF samples. This is also corroborated by the control and aged (CA) sample with roughly 90% of the oxygen content of the TF and yet, it had no measurable capacitance (Figure S2.1). These results suggest that the surface bound oxides, during aging, did not contribute to the capacitance of both the control and treated felts. These results suggest that the capacitance loss in the TA graphite felts, which could not have been compensated by the surface bound oxides during aging, is an indication that probably, sub-surface bound oxygen is responsible for capacitance building. This would be true since the CA had appreciable oxygen content and capacitance. These findings imply that harsh treatment protocols, such as excess heating or acid treatments,[77,88,89] used by most investigators may have masked the subtle but important impact of sub-surface oxygen on both wetting and capacitance.

The XPS data from artificial graphite samples (TF and CF types) have similar sp^2 carbon compositions as their aged counterparts though their electrochemistry varied drastically (**Table 2.1**). Thus, the nature of the sp^2 carbon fractions for treated and control samples cannot be the same at the electroactive surface. For example, graphite felts at 90% sp^2 content had no appreciable wetting and facile HET kinetics.[90] This correlates with the high CH_2 content of these graphite felts did not influence their electronic nature to enhance their wettability and facile HET kinetics. A further example showed no correlation of electronic properties with sp^2 content in certain graphene oxides.[91] High sp^2 content alone does not guarantee facile HET kinetics or optimal electronic properties.

UPS provides valence-band spectra for HOMO-level chemical materials analysis toward understanding the relationship of the sp^2 content with optimal electronic properties such as facile HET and increased capacitance. From previous UPS works, the He_1 (21.2 eV) and He_2 (40.2 eV) lines

for graphites[92,93] help to interpret HOPG valence band spectra (**Figure 2.8**) and the valence bands of artificial graphites, GFA3 and PG(K&J) (the spectral lines of the He$_1$ and He$_2$ of the graphites studied in this research yielded similar interpretations).

(a)

Peak	Position (eV)	Area	FWHM (eV)	% L	% G
CH$_2$	284.351	7076.341	1.600	11	89
CH$_3$	285.922	450.432	1.667	0	100

(b)

Peak	Position (eV)	Area	FWHM (eV)	% L	% G
CH$_2$	284.340	6084.594	1.595	12	88
CH$_3$	285.869	461.689	1.763	0	100

(c)

Peak	Position (eV)	Area	FWHM (eV)	% L	% G
CH$_2$	284.399	4612.07	1.6	22	78
CH$_3$	285.437	1193.125	2.454	0	100

(d)

Peak	Position (eV)	Area	FWHM (eV)	% L	% G
CH$_2$	284.348	5370.095	1.598	9	91
CH$_3$	285.599	892.686	2.273	7	93
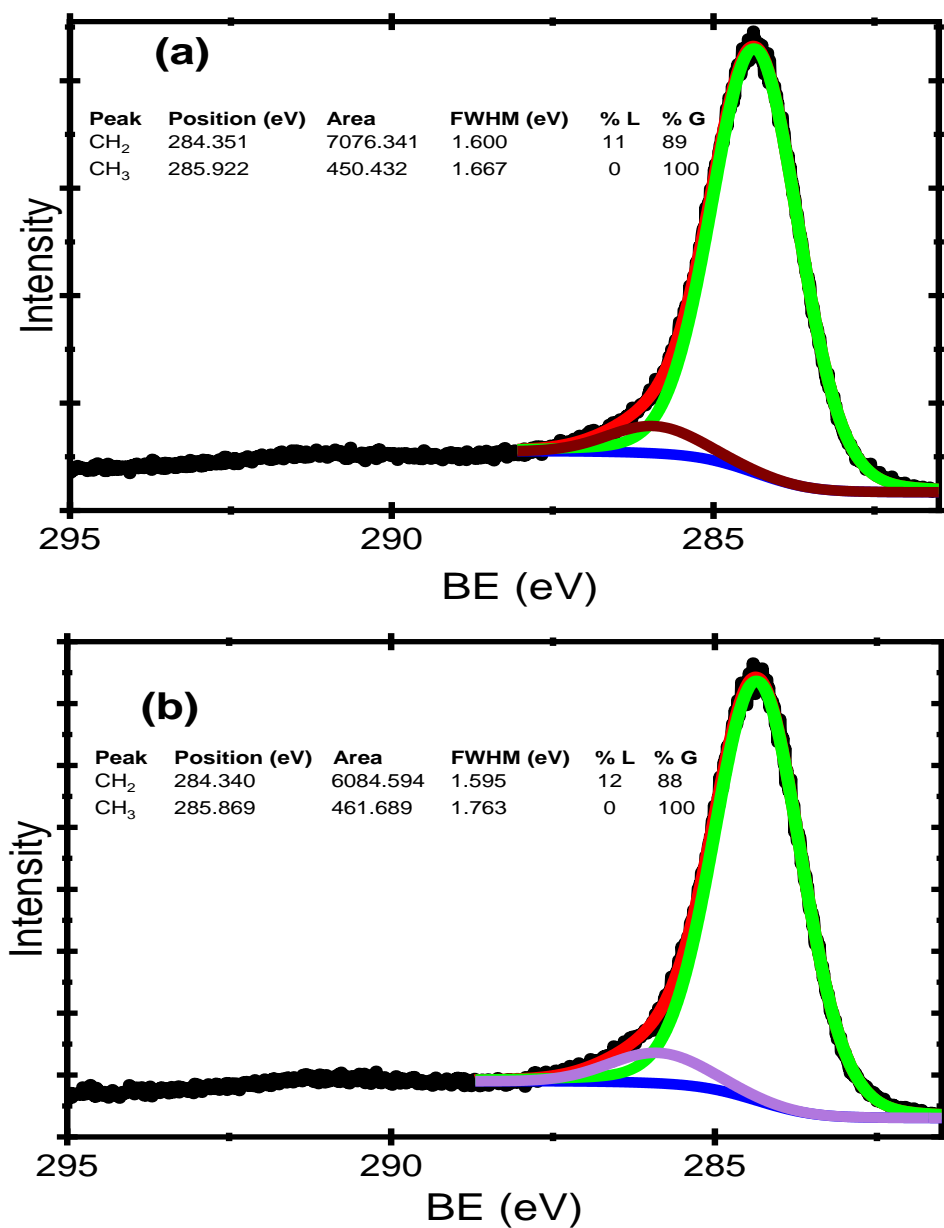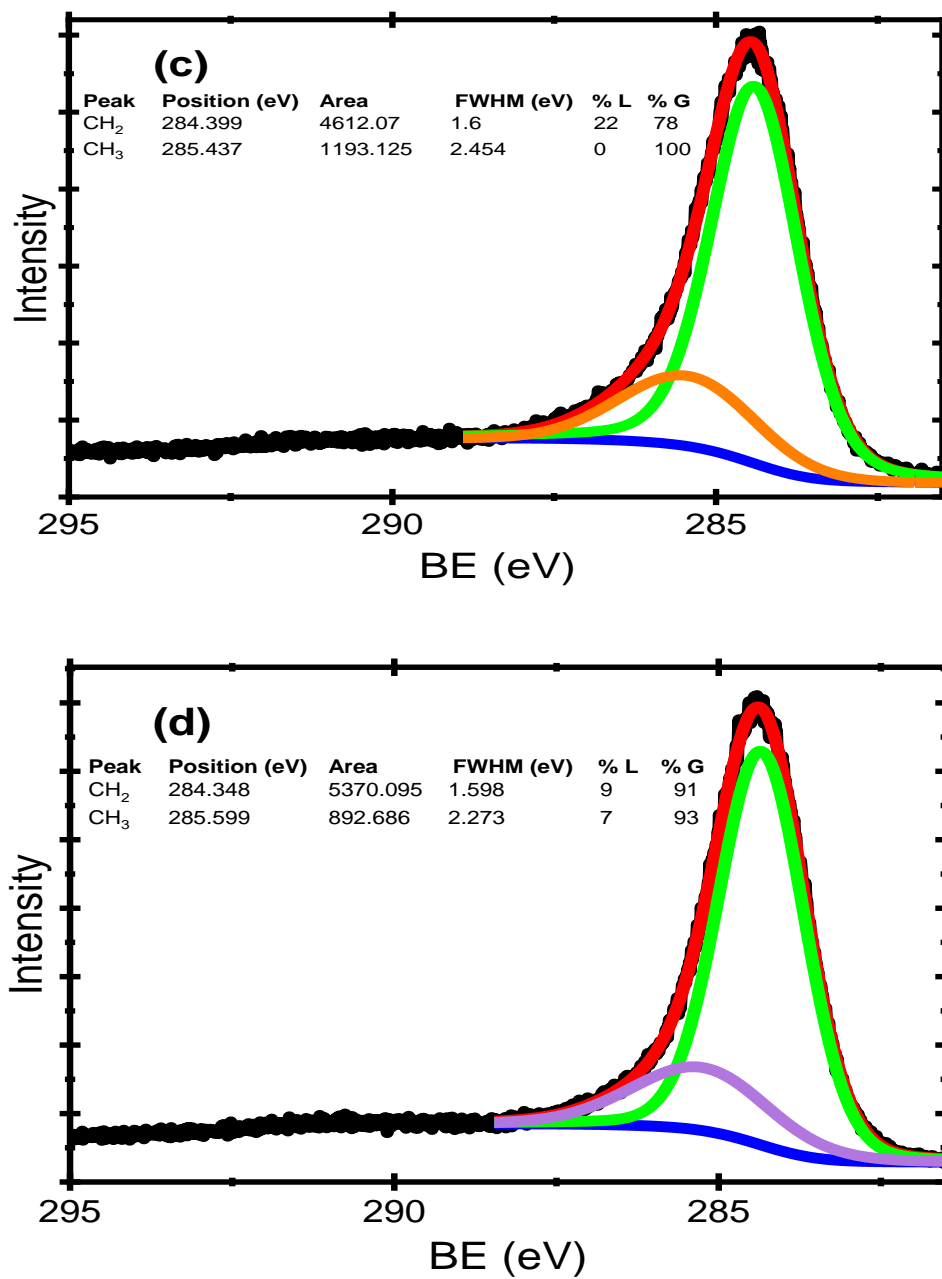
Figure 2.7: The XPS plots of HOPG-ZYH samples for (a) Treated & Fresh HOPG-ZYH (C 1s), (b) Control & Fresh HOPG-ZYH (C 1s), (c) Control & Aged HOPG-ZYH (C 1s), and (d) Treated & Aged HOPG-ZYH (C 1s).

The UPS plots of HOPG-ZYH control (C) and treated (T) samples comparing fresh (F) and aged (A) states (Figure 2.8) indicate the propensity of their π over σ interactions (or vice versa) is interrogated using the intensity ratios, $\left(I_{\pi_i}/I_{\sigma_i}\right)$ at certain π and σ regions.[94]

Peak $P_1{}^*$ is due to the high DOS in the Brillouin zone,[92] which may be explained in the context of the band-structure calculation with the width of the valley reflecting the separation of σ2 and σ3 bands at the symmetry point P. The parameter Δ(σ2-σ3), measured at half of the well depth, reflects the nearness of σ2 and σ3 bonds such that a smaller value is a closer attraction and greater repulsion, where σ bonds are treated as point charges (Figure 2.8a).

Larger Δ(σ2-σ3) values indicate decreased magnitude of Coulombic interaction. The Δh reflects energy well depths positively correlated with greater σ bond interaction strength,[95] stability[96] and even molecular size.[97] The present work reveals (a) higher DOS near $P_1{}^*$ (as the intensity at $P_1{}^*$) in treated vs. control analogues (Table 2.2) and demonstrates a higher density of phonon states of the treated to the controls, (b) an increase of the Δ(σ2-σ3) for treated over control. This means a decreased magnitude of Coulombic interaction for the treated over the controls. (c) An increase in Δh for control over treated, imply the greater σ bond interaction strength and stability and (d) an overall increase in I_{π_i}/I_{σ_i} of treated vs. control, which means the overall increase in the propensity for π bond formation over those of the σ bonds.
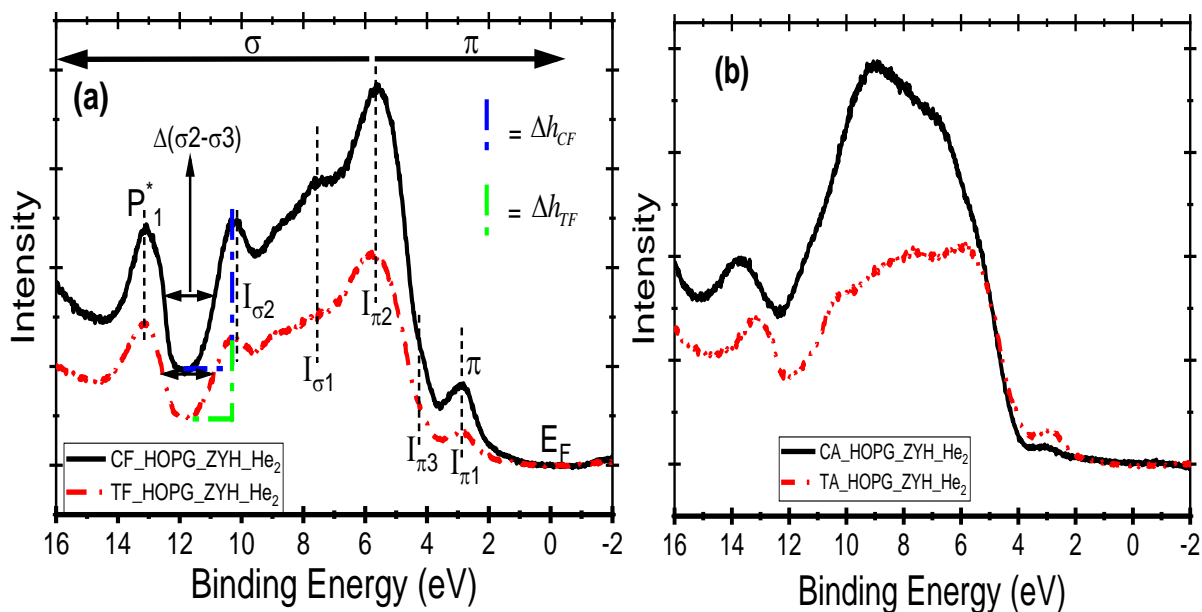
Figure 2.8: (a) Valence band spectra of fresh control (CF) and heat-treated (TF) HOPG. The blue and green vertical lines on the right are used to depict the heights, Δh_{CF} and Δh_{TF} respectively of the energy wells in the diagram; (b) Valence band spectra of aged counter examples. Spectral lines emanating from the He$_2$.

Additionally, the treated samples have either higher HOMO or DOS at the valence band maximum relative to the controls [a prominent exception is the CF HOPG of higher DOS at E_F than in the treated samples but diminished for the CA sample (Figure 2.8)] or were roughly the same. However, irrespective of the nature of their HOMOs, the control samples had deeper and more greatly interacting σ-bond energy wells compared to the treated. On the other hand, the treated sample spectra had pronounced π bonds relative to the controls. This suggests that the prominence of the DOS at the HOMO may not be the primary factor for enhanced electronic response of heat-treated materials but an overall higher DOS, compared to their controls, and localized on the π bonds. These π bonds, being delocalized, have greater probabilities for conduction.[98] A drastic increase in DOS, as viewed by UPS, of the π bonds and E_F at 600-650 °C of graphene oxide species was also reported,[91] even though the XPS results did not differentiate between low and high DOS sp^2.
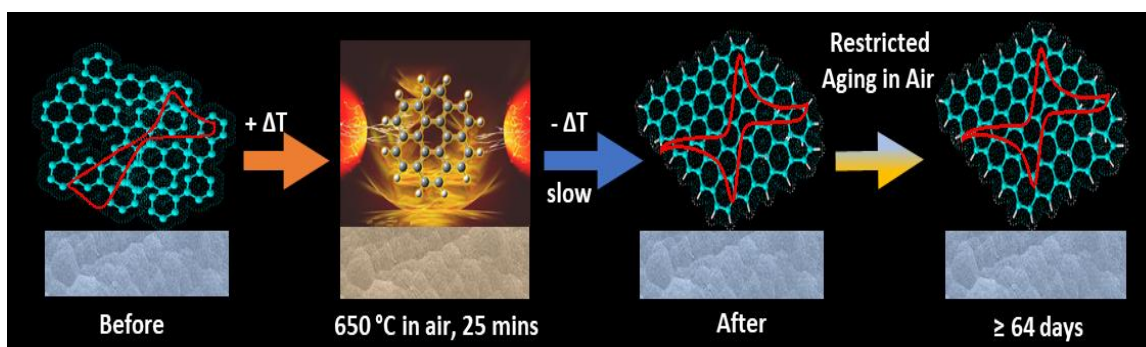
Scheme 2.1: Thermal treatment protocol of the pristine graphite (before) for enhanced and sustained HET (after). Thermal treatment results in structural and electronic reconfigurations without surface morphological changes (before vs after). The consequence of this restructuring is that sluggish HET kinetics (before) becomes fast (after) and is sustained afterwards ($\geq$ 64 days).

When coherently analyzed, the sp^2 nature in the treated materials are conjugating with high DOS localized on the π bonds. Hence, heat treatment resulted in a structural re-organization at the molecular level of the graphite resulting also in tuning the electronic nature to enhance electrochemical behavior as depicted in Scheme 2.1. The degree of change possible is dependent on the initial disordered state as important to the final structural and electronic condition. Less disorder in HOPG-ZYH relative to other studied graphites would account for its accelerated aging in comparison. There exists a balance between the formation of disordered regions, clearly seen in the D´ band, that contribute to the high density of energy states and the degree of crystallinity along the lattice sites that enable carrier hopping.

Table 2.2: Ratios of the intensities of the π to σ transitions in the He1 and He2 lines of the control and treated HOPG-ZYH

He$_1$ (21.2 eV)

	$I_{\pi2}/I_{\sigma1}$	$I_{\pi2}/I_{\sigma2}$	$IP*_1/I_{\sigma2}$	$I_{\pi1}/I_{\sigma1}$
CF_HOPG-ZYH	1.3535	1.5638	0.9788	0.2845
TF_HOPG-ZYH	1.4087	1.6629	1.1094	0.2166
CA_HOPG-ZYH	0.8667	1.0981	0.6526	0.0463
TA_HOPG-ZYH	1.0197	1.2705	0.8582	0.1657

He$_2$ (40.8 eV)

	$I_{\pi2}/I_{\sigma1}$	$I_{\pi2}/I_{\sigma2}$	$IP*_1/I_{\sigma2}$	$I_{\pi1}/I_{\sigma1}$
CF_HOPG-ZYH	1.5823	1.6010	1.6845	0.2467
TF_HOPG-ZYH	1.4190	1.6758	1.5323	0.1419
CA_HOPG-ZYH	0.8051	1.3042	0.9141	0.0323
TA_HOPG-ZYH	0.9170	1.1353	1.0711	0.0921

These findings suggest the same and or very similar underlying mechanism(s) to the formation of the end structure after thermal treatment. Heat treatment results in a well-ordered state, which when described via the folding funnel model,[39–41] implies that there exists a path to a minimum ΔG of crystallinity irrespective of the starting graphite material (with respect to the graphite employed in our work) such that the new microscopic graphite state is mainly aromatic with a degree of crystallinity along the lattice sites that enable carrier hopping irrespective of adventitious oxygen-containing and hydrocarbon moieties, synonymous with aging induced sluggish electron transfer kinetics. This then suggests that the electronic structure is unperturbed signifying a diminution of Coulombic (repulsive) contributive forces. This carrier hopping, from site-to-site, would be aromatic (sp^2 hybridized) and delocalized π electrons. This suggests that the new microscopic graphitic states are mainly aromatic with a degree of crystallinity favoring enhanced and sustained electron transport. The implication is an electronic structure unperturbed by oxygen or HC surface functional group contaminants for a diminished Coulombic contribution. The attributes of this electronic structure demonstrate a strongly correlated system, exhibiting non-perturbative behavior.[99] The one-dimensional Hubbard model[42] describes this non-perturbative behavior, explaining the surface-to-electronic chemistry of treated graphite materials in addressing both their enhanced electrochemical performance and depressed aging effects. The consequences of the thermally induced microstructures and strongly correlated electronic structures could be used to explain the wetting characteristics of the thermally-treated graphites over those of the controls.

Thus, to describe the wetting behavior of the treated materials (now assumed to be non-perturbative) and their resistance to aging, it is postulated that the electric fields of polar molecules such as water[37] are sensitive to the electron cloud of the correlated π system. Tribological charging is well-known to produce large electrostatic effects[100–102] when a graphite block is peeled to reveal fresh surface[102] that can be wet out to zero WCA even where the fully discharged material is known to be hydrophobic. Adventitious HC can dissipate excess π-electrons to form sp^3-bonded carbon[103,104] or utilize tribo-charges to form sp^2-bonded methylene groups to the graphite surface, also damping the electronics and increasing the WCA. Thermally treated graphite, possessing a well correlated, non-perturbed electronic nature, is shielded from the influence of the HC or oxygen groups via a mechanism well illustrated by the Hubbard model, so that the π electron clouds are unperturbed (see Supporting Information).

Conclusion

A new thermal treatment protocol for graphites resulted in steady and consistent ΔE_P values from aqueous cyclic voltammetry over 64 days with no appreciable aging from air oxidation on storage. The initially enhanced and sustained heterogeneous rate constants of graphite samples when probed with the $Fe(CN)_6^{3-/4-}$ redox couple remains essentially unchanged over the test periods. All graphite types exhibit the same resistance to aging and very similar behaviors relative to their controls through results from FTIR, Raman, XPS, UPS and water contact angle measurements. The facile and sustained HET kinetics in 1 mM ferri-ferrocyanide solution is attributable to structural and electronic changes and not from surface functional group changes or edge-density contributions.

These findings suggest that the same or very similar underlying mechanism(s) via thermal treatment promote a more stable structure as a well-ordered or higher-order state (e.g., mainly aromatic, crystalline microstates) than the original graphites, being described by the folding funnel model.[39–41] This new graphite state, or ensemble, possesses a degree of crystallinity along the lattice sites that enables carrier hopping irrespective of adventitious oxygen-containing and hydrocarbon moieties synonymous with aging-induced sluggish electron transfer kinetics. This then suggests that the electronic structure is less perturbed and signifies a reduction of Coulombic (repulsive) contributions. The one-dimensional Hubbard model[42] explains the surface-to-electronic chemistry of heat-treated graphite materials having enhanced and sustained electronic/electrochemical properties compared to their controls regardless of any adventitious functional surface groups indicated or even those changes that would remain potentially undetected as below the limits of investigation.

Water contact angles reveal sensitivity to the electronic nature of the treated graphites as distinct from the expected surface chemistry effects. Additionally, capacitance of graphite felts arises from sub-surface and not surface-bound oxygen-containing species as previously suggested. The overall increase in DOS with enhanced and delocalized π over σ traits cause electronic property enhancements in the treated graphites. Chemical structural disorder in graphite provides preferential initiation sites for the thermally-induced structural and electronic re-organization in the treated samples. Based on the fast and sustained HET kinetics of the thermally-treated graphite electrode materials, this new treatment protocol can be used in applications hinging on fast electron transfer and/or increased capacitance, such as sensing, electro-oxidative reactions in water purification, batteries and supercapacitors, catalysis, oxygen reduction for fuel cell, HPLC detectors, and in the semiconductor industry.

Methods and Materials

Chemicals and Materials

All chemicals were used as received from the suppliers. HOPG ZYH block (NT-MDT Spectrum Instruments, Inc). Natural graphite (T62) (50 $\times$ 20 $\times$ 0.13 mm^3) and artificial graphite sheets (T68) (50 mm $\times$ 20 mm $\times$ 25 µm) were gifts (t-Global Technology Co. Ltd, Taiwan). Pyrolytic graphite blocks, PG1 (32 $\pm$ 2 mm $\times$ 16 $\pm$ 2 mm $\times$ 0.75 $\pm$ 0.5 mm thick) (K & J Magnetics [Plumsteadville, PA, USA]) and pyrolytic graphite blocks (United Nuclear [Laingsburg, MI, USA]). Graphite rods (40767-KD: Graphite rod, 6.15 mm (0.242 in) dia. $\times$ 152 mm (6 in) long, 99.9995% (metals basis) (Alfa Aesar [Haverhill, MA, USA]). Graphite blocks (99.99%, 40 $\times$ 40 $\times$ 3 mm^3 thick) (Fujiansheng, China). Ag/AgCl/3 M NaCl (aq) reference electrodes (0.209 V vs. SHE) and reference electrode cells [Bioanalytical Systems Inc (BASi), (West Lafayette, IN, USA)]. Battery Felt SIGRACELL® GFA3 (297 $\times$ 210 $\times$ 3 mm^3 thick) and Soft Felt SIGRATHERM® GFA5 (297 $\times$ 210 $\times$ 5 mm^3 thick) were gifts (SGL Carbon Company GmbH, Postfach, Meitingen, Germany).

Potassium hexacyanoferrate (III) (Fe(CN)$_6^{3/4-}$; ACS reagent, $\geq$99.0%) and potassium chloride crystal (SigmaUltra; >99.0%, Sigma Chemical Co., [St. Louis, MO, USA]). Advanced abrasives (SandBlaster, 3M [St. Paul, MN, USA]); Teflon tape (Dupont, Elk Grove Village, IL, USA).

The high temperature furnace was a Lindberg/Blue M type model [Thermo Scientific (Asheville NC, USA)]. All chemicals were used as received and all aqueous stock solutions were prepared with MilliQ ® (18 MΩ) water.

Sample Preparation

Graphite rods were cut into small pieces and their ends polished with a 100-grit sandblaster followed by a finishing polishing with a 320-grit sandblaster. The final lengths of the finished products were 1 to 2 cm. The artificial graphite was peeled off from its nylon protective wrap and used as is. The natural graphite and graphite felts (GFA3 and GFA5) were used as received. The PG blocks were exfoliated using Scotch® tape to expose fresh and pristine surfaces prior to thermal treatment and or the start of control experiments using these pristine surfaces. The HOPG-ZYH was peeled off its block using Scotch tape.

Thermal Treatment

Samples loaded onto a ceramic block were inserted into a quartz tube furnace pre-heated to 650°C, exposed to air at both ends, and heated for 25 min. Then the furnace was turned off, cooled to ~500 °C in ~15 minutes and further cool to ~200 °C with its hatches left open until the samples were removed. Scheme 2.1 also depicts the thermal synthesis protocol.

SEM Imaging

Scanning electron microscope (SEM) images for the pristine (control) and freshly treated samples were obtained with a JEOL 2010J 200 kV Analytical TEM/STEM, with a vacuum pressure of less than 10^{-6} torr. Images were obtained at various magnifications.

Aging in Air

The control graphite samples for air aging (artificial and natural graphites, GFA3 and GFA5) were used as is from the suppliers. However, they were only unwrapped and exposed to air immediately at the point of starting the aging experiments. The surfaces of the pyrolytic graphite were renewed by peeling off several graphene layers via the Scotch® tape method.[105] HOPG-ZYH was peeled off fresh via the Scotch® tape method and thus used fresh for the aging experiments. At the beginning of the aging experiment, the surface of the graphite rod was cleaned by polishing slightly using a 320 grit (very fine) sandblaster.

No additional processing for surface regeneration of the heated graphite samples prior to the start of experiment was required. The surfaces used for thermal treatment were then left exposed to air for the period of the aging experiment.

Aging in 1 mM [Fe(CN)$_6$]$^{3-/4-}$ (1 M KCl)

Freshly exfoliated PG blocks (controls) as well as thermally treated samples were formed into electrodes and left in solutions of 1 mM [Fe(CN)$_6$]$^{3-/4-}$ (1 M KCl) for the duration of the experiments. Cyclic voltammograms of the electrodes were recorded at start and end of the experiment.

Contact Angle Measurements

Contact angle measurements were carried out using a Model 250-U1 Ramé-Hart goniometer (Succasunna, NJ, USA) with illumination provided by a Ramé-Hart 150w Fiber Optic illuminator (Model FOI-150-UL). Images were captured using a Ramé-Hart live stream camera with a CCD. Single volumes of 2 μL were automatically dispensed via a model p/n 100-22 Ramé-Hart auto dispensing system. Both the goniometer and auto dispenser were automatically controlled via DROPimage Advanced software (version 2.10.01) with the capability of taking pictures and processing images for contact angle measurements. For expediency, static contact angles were measured, as the generally-accepted approximate for the more proper advancing contact angle, by spotting 2-μL volumes on at least five different spots on both sides of each graphite material studied. The DROPimage software provided digital processing for precise contact angle determination. The average of the angles for all spots photographed served as the contact angle for any given sample measurement. The humidity of the environment during these measurements ranged from 20-55% and temperatures from 20°C to 23°C.

For treated graphite rods, graphite felts, and natural graphite with strong wetting, dynamic contact angles were recorded via the DROPimage Advanced software trigger command.

Attenuated Total Reflection (ATR)-FTIR

Attenuated total reflection (ATR)-Fourier transform infrared (FTIR) spectroscopy was performed using a Thermo Scientific Nicolet™ iS™ 10 FT-IR spectrometer with the Smart iTR accessory. The crystal plate was diamond with a ZnSe lens. The samples were clamped onto the crystal plate and lens using the pressure tower. Spectral scans of 64 were averaged to generate a spectrum for any point on the desired graphite material. Spectral scans were recorded on a minimum of three different spots on both sides of the graphite surfaces.

Raman Spectroscopy

Raman scattering spectra were collected with a WITec™ alpha300 R Raman instrument (GmbH, Germany): A 100-mW, frequency doubled, Nd:YAG (λ = 532.5 nm) laser focused through a 20× Nikon objective (NA = 0.4, WD = 3.9 mm) creates a spot size of ~10 μm. The laser power was attenuated manually to reduce fluorescence background and thermal effects during the first two weeks of measurements to achieve sufficient signal-to-noise ratio to distinguish graphite bands of all sample types with qualitative similarity, giving a final incident sample irradiation power of the order of 10

mW across all samples in all weeks, considering sample-day variations that are not precisely controllable. After week 2, the laser power was never adjusted. Single spectrum "spot" scans were acquired using the alpha300 R via a UHT-300 spectrometer (grating = 600 grooves/mm, entrance aperture = 50 μm), with the Andor™ DU970N-BV, 1600×200-pixel, CCD array detector. Each Raman spectrum was an average of 10 spectral accumulations at 0.50 seconds integration time. Optical images were saved from each sample area interrogated. Raman measurements, for samples that had some degree of visible defects, were done on the defect-free surfaces as judged from the optical images now acquired.

X-Ray Photoelectron Spectroscopy (XPS) and Ultraviolet Photoelectron Spectroscopy (UPS)
XPS, or Electron Spectroscopy for Chemical Analysis (ESCA), measurements occurred in an ultrahigh vacuum (UHV) with a base pressure $< 10^{-10}$ Torr using a dual anode X-ray source, XR 04-548 (Physical Electronics), and an Omicron EA 125 hemispherical energy analyzer with a resolution of 0.02 eV. The X-ray source was the Al-Kα source operated at 400 W and an X-ray incident angle of 54.7° and normal emission. A freshly exfoliated HOPG-ZYH sample served as the reference spectrum for the C 1s binding energy.

XPS Peak 4.1 software provided the peak-fitting while peak quantifications came from both XPS Peak 4.1 and Origin version 2018b. The background type, using XPSPEAK41, was Shirley.

UPS spectra were acquired with the same analyzer as the XPS, using both He I (21.2 eV) and He II (40.8 eV) excitation lines.

Cyclic Voltammetry
Cyclic voltammetry of the various carbon materials as working electrodes was performed with a VersaStat 3 potentiostat/galvanostat (Princeton Applied Research). The working electrodes were the graphite materials investigated while graphite block (99.99%, $40 \times 40 \times 3$ mm^3 thick) served as the counter electrode and Ag/AgCl (3M NaCl) was the reference electrode. The electrolyte was a 1 mM $[Fe(CN)_6]^{3-/4-}$ (1 M KCl) solution.

Data Processing

All data were processed using both Microsoft Excel 2016® version and Origin version 2018b® software. All graphs were plotted using the Origin version 2018b graph plotting component.

ASSOCIATED CONTENT

Supporting Information

The Supporting Information is available free of charge on the ACS Publications website at DOI:

More information on the CVs, and SEM micrographs of other graphites employed in this work. Additionally, the micrographs of aged and control graphite felts showing areas of differential wetting and their SEM micrographs highlighting areas of bundle splitting; thus, permitting porosity. The Raman spectra of the other graphite materials. Inserts in these Raman spectra are the magnifications of their G bands to reveal the D′ bands occurrence in the treated. The Hubbard model employed to explain the surface-to-electronic structure of the thermally treated graphite. Video upload i: Video showing the total wetting (0°) of the treated graphite felt. Video upload ii: Video showing the porosity of treated natural graphite. Video upload iii: Video showing the porosity of treated graphite rod. Video upload iv: video shows that degradation allows water to be forced through some areas of the felt but not others (video upload v).

References

(1)   Chandra, S.; Miller, A. D.; Bendavid, A.; Martin, P. J.; Wong, D. K. Y. Minimizing Fouling at Hydrogenated Conical-Tip Carbon Electrodes during Dopamine Detection in Vivo. *Anal. Chem.* **2014**, *86*, 2443–2450.

(2)   Velický, M.; Bradley, D. F.; Cooper, A. J.; Hill, E. W.; Kinloch, I. A.; Mishchenko, A.; Novoselov, K. S.; Patten, H. V.; Toth, P. S.; Valota, A. T.; Worrall, S.D.; Dryfe, R. A. W. Electron Transfer Kinetics on Mono- and Multilayer Graphene. *ACS Nano* **2014**, *8*, 10089–10100.

(3)   Hu, L.; Peng, X.; Huo, K.; Chen, R.; Fu, J.; Li, Y.; Lee, L. Y. S.; Wong, K.-Y.; Chu, P. K. Dominant Factors Governing the Electron Transfer Kinetics and Electrochemical Biosensing Properties of Carbon Nanofiber Arrays. *ACS Appl. Mater. Interfaces* **2016***, 8,* 28872–28879.

(4)   Sofer, Z.; Jankovský, O.; Šimek, P.; Sedmidubský, D.; Šturala, J.; Kosina, J.; Mikšová, R.; Macková, A.; Mikulics, M.; Pumera, M. Insight into the Mechanism of the Thermal Reduction of Graphite Oxide: Deuterium-Labeled Graphite Oxide Is the Key. *ACS Nano* **2015**, *9*, 5478–5485.

(5)   Mao, X.; Guo, F.; Yan, E. H.; Rutledge, G. C.; Alan Hatton, T. Remarkably High Heterogeneous Electron Transfer Activity of Carbon-Nanotube-Supported Reduced Graphene Oxide. *Chem. Mater.* **2016***, 28,* 7422–7432.

(6)   Parker, J. F.; Kamm, G. E.; McGovern, A. D.; Desario, P. A.; Rolison, D. R.; Lytle, J. C.; Long, J. W. Rewriting Electron-Transfer Kinetics at Pyrolytic Carbon Electrodes Decorated with Nanometric Ruthenium Oxide. *Langmuir* **2017**, *33*, 9416–9425.

(7)   Taylor, S. M.; Pătru, A.; Perego, D.; Fabbri, E.; Schmidt, T. J. Influence of Carbon Material Properties on Activity and Stability of the Negative Electrode in Vanadium Redox Flow Batteries: A Model Electrode Study. *ACS Appl. Energy Mater.* **2018***, 1,* 1166–1174.

(8)   Ferrari, A. C.; Bonaccorso, F.; Fal'ko, V.; Novoselov, K. S.; Roche, S.; Bøggild, P.; Borini, S.; Koppens, F. H. L.; Palermo, V.; Pugno, N.; et al. Science and Technology Roadmap for Graphene, Related Two-Dimensional Crystals, and Hybrid Systems. *Nanoscale* **2015**, *7*, 4598–4810. (This reference now occurs in SI refrences as reference #5, with the full list of authors)

(9)   Kong, Y.; Wang, Z.-L.; Wang, Y.; Yuan, J.; Chen, Z.-D. Degradation of Methyl Orange in Artificial Wastewater through Electrochemical Oxidation Using Exfoliated Graphite Electrode. *Xinxing Tan Cailiao/New Carbon Mater.* **2011***, 26,* 459–464.

(10)   Maljaei, A.; Arami, M.; Mahmoodi, N. M. Decolorization and Aromatic Ring Degradation of Colored Textile Wastewater Using Indirect Electrochemical Oxidation Method. *Desalination* **2009**, *249*, 1074–1078.

(11)   McCreery, R. L.; McDermott, M. T. Comment on Electrochemical Kinetics at Ordered Graphite Electrodes. *Anal. Chem.* **2012**, *84*, 2602–2605.

(12)   McCreery, R. L. Advanced Carbon Electrode Materials for Molecular Electrochemistry. *Chem. Rev.* **2008**, *108*, 2646–2687.

(13)   Brownson, D. A. C.; Kampouris, D. K.; Banks, C. E. Graphene Electrochemistry: Fundamental Concepts through to Prominent Applications. *Chem. Soc. Rev.* **2012**, *41*, 6944.

(14)   Song, Y.; Hu, H.; Feng, M.; Zhan, H. Carbon Nanotubes with Tailored Density of Electronic States for Electrochemical Applications. *ACS Appl. Mater. Interfaces* **2015**, *7*, 25793–25803.

(15)   Chen, S.; Liu, Y.; Chen, J. Heterogeneous Electron Transfer at Nanoscopic Electrodes: Importance of Electronic Structures and Electric Double Layers. *Chem. Soc. Rev.* **2014**, *43*, 5372–5386.

(16)   Barbieri, P. F.; Marques, F. C. The Effect of Stress in the Density of States of Amorphous Carbon Films Determined by X-Ray Excited Auger Electron Spectroscopy. *Adv. Mater. Sci. Eng.* **2017***,* Article ID 5826527, https://doi.org/10.1155/2017/5826527.

(17)   Unwin, P. R.; Güell, A. G.; Zhang, G. Nanoscale Electrochemistry of Sp2 Carbon Materials: From Graphite and Graphene to Carbon Nanotubes. *Acc. Chem. Res.* **2016**, *49*, 2041–2048.

(18)   McDermott, M. T.; Kneten, K.; McCreery, R. L. Anthraquinonedisulfonate Adsorption, Electron-Transfer Kinetics, and Capacitance on Ordered Graphite Electrodes: The Important Role of Surface Defects. *J. Phys. Chem.* **1992**, *96*, 3124–3130.

(19)   Zhong, J. H.; Zhang, J.; Jin, X.; Liu, J. Y.; Li, Q.; Li, M. H.; Cai, W.; Wu, D. Y.; Zhan, D.; Ren, B. Quantitative Correlation between Defect Density and Heterogeneous Electron Transfer Rate of Single Layer Graphene. *J. Am. Chem. Soc.* **2014**, *136*, 16609–16617.

(20)   Sun, T.; Levin, B. D. A.; Guzman, J. J. L.; Enders, A.; Muller, D. A.; Angenent, L. T.; Lehmann, J. Rapid Electron Transfer by the Carbon Matrix in Natural Pyrogenic Carbon. *Nat. Commun.* **2017***, 8,* 14873 doi: 10.1038/ncomms14873.

(21)   Štulík, K. Activation of Solid Electrodes. *Electroanalysis*. **1992**, *4*, 829–834.

(22)   Swain, G. M. Solid Electrode Materials: Pretreatment and Activation. In *Handbook of Electrochemictry*; Zoski, C. G., Ed.; Elsevier B.V.: Amsterdam, 2007; pp 111–153.

(23)   Shrestha, S.; Morse, N.; Mustain, W. E. Effect of Surface Chemistry on the Double Layer Capacitance of Polypyrrole-Derived Ordered Mesoporous Carbon. *RSC Adv.* **2014**, *4*, 47039–47046.

(24)   Ramani, M.; Haran, B. S.; White, R. E.; Popov, B. N.; Arsov, L. Studies on Activated Carbon Capacitor Materials Loaded with Different Amounts of Ruthenium Oxide. *J. Power Sources* **2001**, *93*, 209–214.

(25)   Ruiz, V.; Blanco, C.; Raymundo-Piñero, E.; Khomenko, V.; Béguin, F.; Santamaría, R. Effects of Thermal Treatment of Activated Carbon on the Electrochemical Behaviour in Supercapacitors. *Electrochim. Acta* **2007**, *52*, 4969–4973.

(26)   Sánchez-González, J.; Stoeckli, F.; Centeno, T. A. The Role of the Electric Conductivity of Carbons in the Electrochemical Capacitor Performance. *J. Electroanal. Chem.* **2011**, *657*, 176–180.

(27)   Bowling, R. J.; Packard, R. T.; McCreery, R. L. Activation of Highly Ordered Pyrolytic Graphite for Heterogeneous Electron Transfer: Relationship between Electrochemical Performance and Carbon Microstructure. *J. Am. Chem. Soc.* **1989**, *111*, 1217–1223.

(28)   Poon, M.; McCreery, R. L.; Engstrom, R. Laser Activation of Carbon Electrodes. Relationship between Laser-Induced Surface Effects and Electron Transfer Activation. *Anal. Chem.* **1988**, *60*, 1725–1730.

(29)   Batrakov, A. V.; Markov, A. B.; Ozur, G. E.; Proskurovsky, D. I.; Rotshtein, V. P. The Effect of Pulsed Electron-Beam Treatment of Electrodes on Vacuum Breakdown. *IEEE Trans. Dielectr. Electr. Insul.* **1995**, *2*, 237–242.

(30)   Malmgren, S.; Ciosek, K.; Lindblad, R.; Plogmaker, S.; Kühn, J.; Rensmo, H.; Edström, K.; Hahlin, M. Consequences of Air Exposure on the Lithiated Graphite SEI. *Electrochim. Acta* **2013**, *105*, 83–91.

(31)   Ranganathan, S.; Kuo, T.; Mccreery, R. L. Facile Preparation of Active Glassy Carbon Electrodes with Activated Carbon and Organic Solvents. *Anal. Chem.* **1999**, *71*, 3574–3580.

(32)   Chen, P.; Fryling, M. A.; McCreery, R. L. Electron Transfer Kinetics at Modified Carbon Electrode Surfaces: The Role of Specific Surface Sites. *Anal. Chem.* **1995**, *67*, 3115–3122.

(33)   Ji, X.; Banks, C. E.; Crossley, A.; Compton, R. G. Oxygenated Edge Plane Sites Slow the Electron Transfer of the Ferro-/Ferricyanide Redox Couple at Graphite Electrodes. *ChemPhysChem* **2006**, *7*, 1337–1344.

(34)   Martinez-Martin, D.; Longuinhos, R.; Izquierdo, J. G.; Marele, A.; Alexandre, S. S.; Jaafar, M.; Gómez-Rodríguez, J. M.; Bañares, L.; Soler, J. M.; Gomez-Herrero, J. Atmospheric Contaminants on Graphitic Surfaces. *Carbon N. Y.* **2013**, *61*, 33–39.

(35)   Kozbial, A.; Zhou, F.; Li, Z.; Liu, H.; Li, L. Are Graphitic Surfaces Hydrophobic? *Acc. Chem. Res.* **2016**, *49*, 2765–2773.

(36)   Li, Z.; Kozbial, A.; Nioradze, N.; Parobek, D.; Shenoy, G. J.; Salim, M.; Amemiya, S.; Li, L.; Liu, H. Water Protects Graphitic Surface from Airborne Hydrocarbon Contamination. *ACS Nano* **2016**, *10*, 349–359.

(37)   Misra, R. P.; Blankschtein, D. Insights on the Role of Many-Body Polarization Effects in the Wetting of Graphitic Surfaces by Water. *J. Phys. Chem. C* **2017**, *121*, 28166–28179.

(38)   Morteza Najarian, A.; Chen, R.; Balla, R. J.; Amemiya, S.; McCreery, R. L. Ultraflat, Pristine, and Robust Carbon Electrode for Fast Electron-Transfer Kinetics. *Anal. Chem.* **2017**, *89*, 13532–13540.

(39)   Leopold, P. E.; Montal, M.; Onuchic, J. N. Protein Folding Funnels: A Kinetic Approach to the Sequence-Structure Relationship. *Proc. Natl. Acad. Sci.* **1992***, 89,* 8721–8725.

(40)   Bryngelson, J. D.; Onuchic, J. N.; Socci, N. D.; Wolynes, P. G. Funnels, Pathways, and the Energy Landscape of Protein Folding: A Synthesis. *Proteins Struct. Funct. Bioinforma.* **1995***, 21,* 167–195.

(41)   Onuchic, J. N.; Socci, N. D.; Luthey-Schulten, Z.; Wolynes, P. G. Protein Folding Funnels: The Nature of the Transition State Ensemble. *Fold. Des.* **1996***. 1,* 441–450.

(42)   Hubbard, J. Electron Correlations in Narrow Energy Bands. *Proc. R. Soc. A Math. Phys. Eng. Sci.* **1963**, *276*, 238–257.

(43)   Hu, L.; Peng, X.; Huo, K.; Chen, R.; Fu, J.; Li, Y.; Lee, L. Y. S.; Wong, K.-Y.; Chu, P. K. Dominant Factors Governing the Electron Transfer Kinetics and Electrochemical Biosensing Properties of Carbon Nanofiber Arrays. *ACS Appl. Mater. Interfaces* **2016***, 8,* 28872–28879.

(44)   Zhang, G.; Tan, S.; Patel, A. N.; Unwin, P. R. Electrochemistry of $Fe^{3+/2+}$ at Highly Oriented Pyrolytic Graphite (HOPG) Electrodes: Kinetics, Identification of Major Electroactive Sites and Time Effects on the Response. *Phys. Chem. Chem. Phys.* **2016***, 18,* 32387–32395.

(45)   Güell, A. G.; Cuharuc, A. S.; Kim, Y. R.; Zhang, G.; Tan, S. Y.; Ebejer, N.; Unwin, P. R. Redox-Dependent Spatially Resolved Electrochemistry at Graphene and Graphite Step Edges. *ACS Nano* ***2015***, 9,* 3558–3571.

(46)   Nicholson, R. S. Theory and Application of Cyclic Voltammetry f m Measurement of Electrode Reaction Kinetics. *Anal. Chem.* **1965***, 37*, 1351–1355.

(47)   Konopka, S. J.; McDuffie, B. Diffusion Coefficients of Ferri- and Ferrocyanide Ions in Aqueous Media, Using Twin-Electrode Thin-Layer Electrochemistry. *Anal. Chem.* **1970***, 42*, 1741–1746.

(48)   Poler, J. C. Surface Oxidation Kinetics: A Scanning Tunneling Microscopy Experiment. *J. Chem. Educ.* **2000***, 77*, 1198–1200.

(49)   Stevens, F.; Kolodny, L. a.; Beebe, T. P. Kinetics of Graphite Oxidation: Monolayer and Multilayer Etch Pits in HOPG Studied by STM. *J. Phys. Chem. B* **1998***, 102*, 10799–10804.

(50)   Gonc̃alves, L. M.; Batchelor-Mcauley, C.; Barros, A. A.; Compton, R. G. Electrochemical Oxidation of Adenine: A Mixed Adsorption and Diffusion Response on an Edge-Plane Pyrolytic Graphite Electrode. *J. Phys. Chem. C* **2010***, 114,* 14213-14219.

(51)   Zhang, G.; Kirkman, P. M.; Patel, A. N.; Cuharuc, A. S.; McKelvey, K.; Unwin, P. R. Molecular Functionalization of Graphite Surfaces: Basal Plane versus Step Edge Electrochemical Activity. *J. Am. Chem. Soc.* **2014***, 136,* 11444-11451.

(52)   Davies, T. J.; Hyde, M. E.; Compton, R. G. Nanotrench Arrays Reveal Insight into Graphite Electrochemistry. *Angew. Chemie - Int. Ed.* **2005***, 44,* 5121-5126.

(53)   Tang, C.; Zhang, Q. Nanocarbon for Oxygen Reduction Electrocatalysis: Dopants, Edges, and Defects. *Adv. Mater.* **2017***, 29,* 1604103.

(54)   Yuan, W.; Zhou, Y.; Li, Y.; Li, C.; Peng, H.; Zhang, J.; Liu, Z.; Dai, L.; Shi, G. The Edge- and Basal-Plane-Specific Electrochemistry of a Single-Layer Graphene Sheet. *Sci. Rep.* **2013***, 3,* Article number: 2248.

(55)   Patel, A. N.; Tan, S. Y.; Miller, T. S.; MacPherson, J. V.; Unwin, P. R. Comparison and Reappraisal of Carbon Electrodes for the Voltammetric Detection of Dopamine. *Anal. Chem.* **2013**, *85,* 11755–11764.

(56)   Desimoni, E.; Casella, G. I.; Morone, A.; Salvi, A. M. XPS Determination of Oxygen-containing Functional Groups on Carbon-fibre Surfaces and the Cleaning of These Surfaces. *Surf. Interface Anal.* **1990**, *15,* 627–634.

(57)   Sternitzke, K. D.; McCreery, R. L. Laser Microfabrication and Activation of Graphite and Glassy Carbon Electrodes. *Anal. Chem.* **1990**, 62, 1339–1344.

(58)   Poon, M.; Mccreery, R. L. In Situ Laser Activation of Glassy Carbon Electrodes. *Anal. Chem.* **1986***, 58,* 2745-2750.

(59)   Patel, A. N.; Collignon, M. G.; OConnell, M. A.; Hung, W. O. Y.; McKelvey, K.; MacPherson, J. V.; Unwin, P. R. A New View of Electrochemistry at Highly Oriented Pyrolytic Graphite. *J. Am. Chem. Soc.* **2012**, *134*, 20117–20130.

(60)   Yuan, Y.; Lee, T. R. Contact Angle and Wetting Properties. In *Surface Science Techniques*; Bracco G., Holst B. (eds). Springer Series in Surface Sciences, vol 51. Springer, Berlin, Heidelberg, 2013.

(61)   Park, J.; Han, H. S.; Kim, Y. C.; Ahn, J. P.; Ok, M. R.; Lee, K. E.; Lee, J. W.; Cha, P. R.; Seok, H. K.; Jeon, H. Direct and Accurate Measurement of Size Dependent Wetting Behaviors for Sessile Water Droplets. *Sci. Rep.* **2015***, 5,*18150.

(62)   Kozbial, A.; Li, Z.; Sun, J.; Gong, X.; Zhou, F.; Wang, Y.; Xu, H.; Liu, H.; Li, L. ScienceDirect Understanding the Intrinsic Water Wettability of Graphite. *Carbon N. Y.* **2014**, *74*, 218–225.

(63)   Hong, G.; Han, Y.; Schutzius, T. M.; Wang, Y.; Pan, Y.; Hu, M.; Jie, J.; Sharma, C. S.; Müller, U.; Poulikakos, D. On the Mechanism of Hydrophilicity of Graphene. *Nano Lett.* **2016***, 16,* 4447-4453.

(64)   Kozbial, A.; Trouba, C.; Liu, H.; Li, L. Characterization of the Intrinsic Water Wettability of Graphite Using Contact Angle Measurements: Effect of Defects on Static and Dynamic Contact Angles. *Langmuir* **2017**, *33*, 959–967.

(65)   Vashist, S. K.; Zheng, D.; Al-Rubeaan, K.; Luong, J. H. T.; Sheu, F. S. Advances in Carbon Nanotube Based Electrochemical Sensors for Bioanalytical Applications. *Biotechnol. Adv.* **2011***, 29,* 169–188.

(66)   Papakonstantinou, P.; Kern, R.; Robinson, L.; Murphy, H.; Irvine, J.; McAdams, E.; McLaughlin, J.; McNally, T. Fundamental Electrochemical Properties of Carbon Nanotube Electrodes. *Fullerenes Nanotub. Carbon Nanostructures* **2005***, 13,* 91-108.

(67)   Li, X.; Forouzandeh, F.; Kakanat, A. J.; Feng, F.; Banham, D. W. H.; Ye, S.; Kwok, D. Y.; Birss, V. Surface Characteristics of Microporous and Mesoporous Carbons Functionalized with Pentafluorophenyl Groups. *ACS Appl. Mater. Interfaces* **2018**, *10*, 2130–2142.

(68)   Coates, J. Interpretation of Infrared Spectra, A Practical Approach. In *Encyclopedia of Analytical Chemistry: Applications, Theory and Instrumentations*; Myers, R. A (Ed).; John Wiley & Sons Ltd: Chichester, 2000; pp. 10815–10837..

(69)   Smidt, E.; Lechner, P.; Schwanninger, M.; Haberhauer, G.; Gerzabek, M. H. Characterization of Waste Organic Matter by FT-IR Spectroscopy: Application in Waste Science. *Appl. Spectrosc.* **2002**, *56*, 1170–1175.

(70)   Mücksch, C.; Rösch, C.; Müller-Renno, C.; Ziegler, C.; Urbassek, H. M. Consequences of Hydrocarbon Contamination for Wettability and Protein Adsorption on Graphite Surfaces. *J. Phys. Chem. C* **2015***, 119,* 12496–12501.

(71)   Taherian, F.; Marcon, V.; Van Der Vegt, N. F. A.; Leroy, F. What Is the Contact Angle of Water on Graphene? *Langmuir* **2013***, 29,* 1457–1465.

(72)   Li, Z.; Wang, Y.; Kozbial, A.; Shenoy, G.; Zhou, F.; McGinley, R.; Ireland, P.; Morganstein, B.; Kunkel, A.; Surwade, S. P.; Li, L.; Liu, H. Effect of Airborne Contaminants on the Wettability of Supported Graphene and Graphite. *Nat. Mater.* **2013**, *12*, 925–931.

(73)   Wei, Y.; Jia, C. Q. Intrinsic Wettability of Graphitic Carbon. *Carbon N. Y.* **2015**, *87* (C), 10–17.

(74)   Liu, H.; Li, L. Graphitic Materials: Intrinsic Hydrophilicity and Its Implications. *Extreme Mechanics Letts.* **2017***, 14,* 44–50.

(75)   Ashraf, A.; Wu, Y.; Wang, M. C.; Yong, K.; Sun, T.; Jing, Y.; Haasch, R. T.; Aluru, N. R.; Nam, S. Doping-Induced Tunable Wettability and Adhesion of Graphene. *Nano Lett.* **2016***, 16,* 4708–4712.

(76)   Tian, T.; Lin, S.; Li, S.; Zhao, L.; Santos, E. J. G.; Shih, C. J. Doping-Driven Wettability of Two-Dimensional Materials: A Multiscale Theory. *Langmuir* **2017***, 33,* 12827–12837.

(77)   Sun, B.; Skyllas-Kazacos, M. Modification of Graphite Electrode Materials for Vanadium Redox Flow Battery Application—I. Thermal Treatment. *Electrochim. Acta* **1992***, 37,* 1253–1260.

(78)   Smith, R. E. G.; Davies, T. J.; Baynes, N. D. B.; Nichols, R. J. The Electrochemical Characterisation of Graphite Felts. *J. Electroanal. Chem.* **2015***, 747,* 29–38.

(79)   Pimenta, M. A.; Dresselhaus, G.; Dresselhaus, M. S.; Cançado, L. G.; Jorio, A.; Saito, R. Studying Disorder in Graphite-Based Systems by Raman Spectroscopy. *Phys. Chem. Chem. Phys.* **2007***, 9,* 1276–1291.

(80)   Chieu, T. C.; Dresselhaus, M. S.; Endo, M. Raman Studies of Benzene-Derived Graphite Fibers. *Phys. Rev. B* **1982**, *26*, 5867–5877.

(81)   Stobinski, L.; Lesiak, B.; Kövér, L.; Tóth, J.; Biniak, S.; Trykowski, G.; Judek, J. Multiwall Carbon Nanotubes Purification and Oxidation by Nitric Acid Studied by the FTIR and Electron Spectroscopy Methods. *J. Alloys Compd.* **2010**, *501*, 77–84.

(82)   Wu, J.-B.; Lin, M.-L.; Cong, X.; Liu, H.-N.; Tan, P.-H. Raman Spectroscopy of Graphene-Based Materials and Its Applications in Related Devices. *Chem. Soc. Rev.* **2018**, *47*, 1822-1873.

(83)   Cancado, L.; Takai, K.; Enoki, T. General Equation for the Determination of the Crystallite Size L a of Nanographite by Raman Spectroscopy. *Appl. Phys. Lett.* **2006**, *88*, 163106.

(84)   Vázquez-Santos, M. B.; Geissler, E.; László, K.; Rouzaud, J. N.; Martínez-Alonso, A.; Tascón, J. M. D. Comparative XRD, Raman, and TEM Study on Graphitization of PBO-Derived Carbon Fibers. *J. Phys. Chem. C* **2012**, *116*, 257–268.

(85)   Xie, X.; Zhou, Y.; Bi, H.; Yin, K.; Wan, S.; Sun, L. Large-Range Control of the Microstructures and Properties of Three-Dimensional Porous Graphene. *Sci. Rep.* **2013**, *3*, Article number: 2117.

(86)   Kuang, J.; Liu, L.; Gao, Y.; Zhou, D.; Chen, Z.; Han, B.; Zhang, Z. A Hierarchically Structured Graphene Foam and Its Potential as a Large-Scale Strain-Gauge Sensor. *Nanoscale* **2013**, *5*, 12171-12177.

(87)   Mao, X.; Simeon, F.; Rutledge, G. C.; Hatton, T. A. Electrospun Carbon Nanofiber Webs with Controlled Density of States for Sensor Applications. *Adv. Mater.* **2013***, 25,* 1309–1314.

(88)   Sun, B.; Skyllas-Kazacos, M. Chemical Modification of Graphite Electrode Materials for Vanadium Redox Flow Battery Application-Part II. Acid Treatments. *Electrochim. Acta* **1992**, *37*, 2459–2465.

(89)   Ding, C.; Zhang, H.; Li, X.; Liu, T.; Xing, F. Vanadium Flow Battery for Energy Storage: Prospects and Challenges. *J. Phys. Chem. Lett.* **2013**, *4*, 1281–1294.

(90)   Mazúr, P.; Mrlík, J.; Beneš, J.; Pocedič, J.; Vrána, J.; Dundálek, J.; Kosek, J. Performance Evaluation of Thermally Treated Graphite Felt Electrodes for Vanadium Redox Flow Battery and Their Four-Point Single Cell Characterization. *J. Power Sources* **2018**, *380*, 105–114.

(91)   Yamaguchi, H.; Ogawa, S.; Watanabe, D.; Hozumi, H.; Gao, Y.; Eda, G.; Mattevi, C.; Fujita, T.; Yoshigoe, A.; Ishizuka, S.; Adamska , L.; Yamada, T.; Dattelbaum, A. M.; Gupta, G.; Doorn, S. K.; Velizhanin, K. A.; Teraoka. Y.; Chen, M.; Htoon, H.; Chhowalla, M.; Mohite, A. D.; Takakuwa, Y.Valence-Band Electronic Structure Evolution of Graphene Oxide upon Thermal Annealing for Optoelectronics. *Phys. Status Solidi Appl. Mater. Sci.* **2016**, *213*, 2380–2386.

(92)   McFeely, F. R.; Kowalczyk, S. P.; Ley, L.; Cavell, R. G.; Pollak, R. A.; Shirley, D. A. X-Ray Photoemission Studies of Diamond, Graphite, and Glassy Carbon Valence Bands. *Phys. Rev. B* **1974**, *9*, 5268–5278.

(93)   Jeong, H. K.; Hong, L.; Zhang, X.; Vega, E.; Dowben, P. A. Evidence of Band Bending and Surface Fermi Level Pinning in Graphite Oxide. *Carbon N. Y.* **2013**, *57*, 227–231.

(94)   Ganguly, A.; Sharma, S.; Papakonstantinou, P.; Hamilton, J. Probing the Thermal Deoxygenation of Graphene Oxide Using High-Resolution in Situ X-Ray-Based Spectroscopies. *J. Phys. Chem. C* **2011**, *115*, 17009–17019.

(95)   Verkhovtsev, A. V.; Schramm, S.; Solov'Yov, A. V. Molecular Dynamics Study of the Stability of a Carbon Nanotube atop a Catalytic Nanoparticle. *Eur. Phys. J. D* **2014**, *68*: 246. https://doi.org/10.1140/epjd/e2014-50371-4.

(96)   Solov'yov, I. A.; Mathew, M.; Solov'Yov, A. V.; Greiner, W. Liquid Surface Model for Carbon Nanotube Energetics. *Phys. Rev. E - Stat. Nonlinear, Soft Matter Phys.* **2008**, *78*, 051601.

(97)   Norris, D.; Bawendi, M. Measurement and Assignment of the Size-Dependent Optical Spectrum in CdSe Quantum Dots. *Phys. Rev. B - Condens. Matter Mater. Phys.* **1996**, *53*, 16338–16346.

(98)   Joachim, C.; Gimzewski, J. K.; Aviram, A. Electronics Using Hybrid-Molecular and Mono-Molecular Devices. *Nature* **2000**, *408*, 541-548.

(99)   Korepin, V. E.; Frahm, H.; Göhmann, F.; Klümper, A. The One-Dimensional Hubbard Model; **2005**, ArXiv: cond-mat/0207529, DOI: 10.1017/CBO9780511534843.

(100)   Guerret-Piecourt, C.; Bec, S.; Treheux, D. Electrical Charges and Tribology of Insulating Materials. *Comptes Rendus l'Academie des Sci. - Ser. IV Physics, Astrophys.* **2001**, *2*, 761–774.

(101)   Borodinov, N.; Ievlev, A. V; Carrillo, J.; Calamari, A. Probing Static Discharge of Polymer Surfaces with Nanoscale Resolution. arXiv:1806.05169v1 [physics.app-ph].

(102)   Hod, O. Graphite and Hexagonal Boron-Nitride Have the Same Interlayer Distance. Why? *J. Chem. Theory Comput.* **2012**, *8*, 1360–1369.

(103)   Poenitzsch, V. Z.; Winters, D. C.; Xie, H.; Dieckmann, G. R.; Dalton, A. B.; Musselman, I. H. Effect of Electron-Donating and Electron-Withdrawing Groups on Peptide/Single-Walled Carbon Nanotube Interactions. *J. Am. Chem. Soc.* **2007**, *129*, 14724–14732.

(104)   Kamaras, K.; Itkis, M. E.; Hu, H.; Zhao, B.; Haddon, R. C. Covalent Bond Formation to a Carbon Nanotube Metal. *Science* **2003**, *301*, 1501.

(105)   Geim, A. K.; Novoselov, K. S. The Rise of Graphene. *Nat. Mater.* **2007**, *6*, 183–191.

Chapter 3: Electrochemical Stability and Capacitance of *In-Situ* Synthesized Prussian Blue on Thermally-Activated Graphite

Electrochemical Stability and Capacitance of *In-Situ* Synthesized Prussian Blue on Thermally-Activated Graphite. *Submitted to Springer-Nature Applied Sciences*.

Table of Contents Graphics
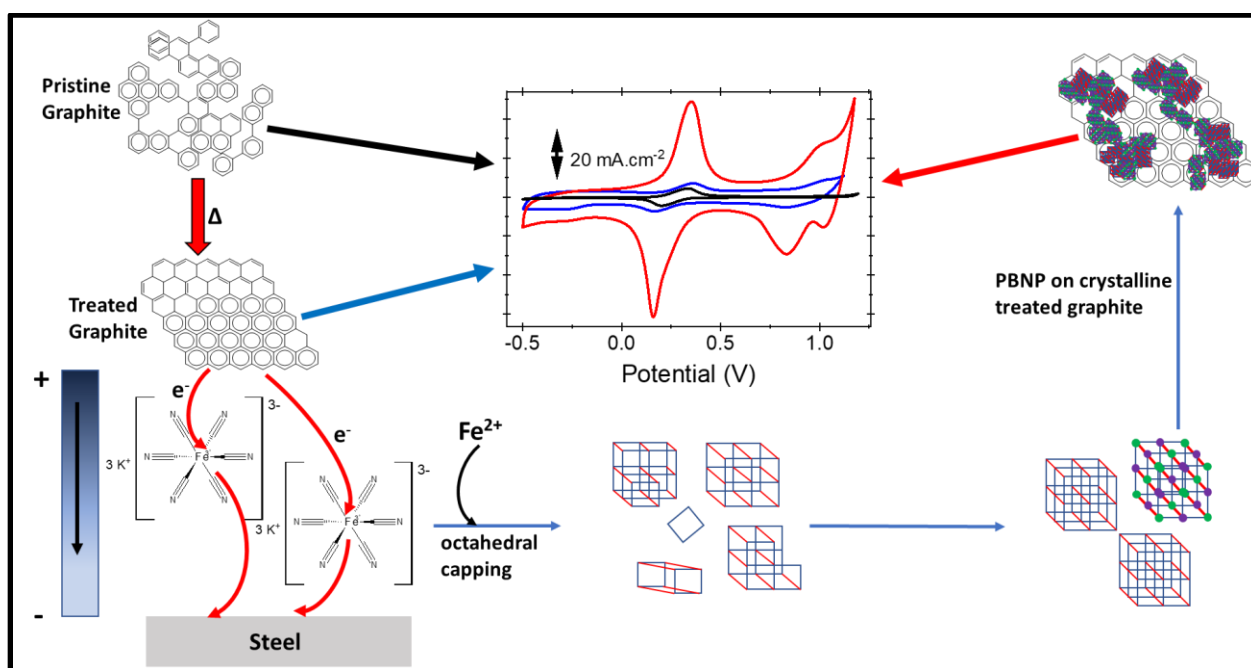
Table of Contents (TOC) Graphics: Thermal activation of graphite felt increases capacitance while Prussian blue formation, either by metal-aided catalysis or the solution-dip method, further increases capacitance for the composite matrix.

Abstract

The search has been on for years to find at least, a stable, high surface area scaffold for Prussian blue (PB) and its analogs. If successful, PB's vast potential applications could be practicable. This is besides other innate issues with PB such as poor cycle stability, low electronic conductivity to mention a few. For the first time, a stable Prussian blue@thermally activated graphite felt scaffold, with cycling stability of 2100 cycles, from -0.5V to 1.3 V, and in 1 M KCl, for at least 36 hours is reported. At the end of 2100 CV loops, sample capacitance more than tripled (381 mF cm-2 compared to 120 mF cm-2 at start of experiment). These properties suggest a practical ion-sieve for Cs removal from Cs contaminated water. Two new synthesis protocols were employed to achieve this: (a) a first time, single solution PB synthesis without externally applied potential, current or even elevated temperature and (b) a two-step solution-dipping process not involving acidic conditions. PB from both protocols exhibited similar electrochemical characteristics even though the electron relay paths along their charge transfer complexes are different. When probed for its HOMO characteristics, the PB@thermally-treated graphite showed no significant electronic difference from the thermally-treated felt scaffold, suggesting non-compromise of the treated graphite by the PB. Besides Cs removal, the electrochemical and electronic properties of these PB@treated graphites suggest multiple electrochemical, non-electrochemical and electronic applications with intact structural and functional integrity.

Key words: Prussian blue, graphite, coordination polymers (CPs), thermal treatment, capacitance, charge relay path.

Introduction

Metal coordination polymers (CPs), generated by the self-assembly of inorganic ligands and metal ions, are attractive materials for molecular capture, deliver/release, and sensing in aqueous media [1]. The design of these compounds is based on the formation of inorganic ligand coordination networks—polycyanometalate (PCM) anions—and "capping" metal cations. It also depends on hydrogen bonding between the PCMs and organic proton donors to transition from purely inorganic to metal−organic frameworks (MOFs). These transitions broaden the scope of MOF properties, allowing for their fine-tuning: a necessary requirement for the rational design of functional materials [2].

One such CPs, similar to MOFs, is Prussian blue (PB), a cyanide-bridged coordination compound between two Fe species in different oxidation states. PB is traditionally synthesized by mixing the metal ion, Fe^{3+} (Fe^{2+}) and a corresponding metal octahedral complex, hexacyanoferrate (hexacyanoferric) in an acidic solution [3]. It has the general formula $A_xFe^{III}[Fe^{II}(CN)_6]_y \cdot \square_{1-y} \cdot nH_2O$ (n = 14-16), where A is an alkali metal ion, K^+ or Na^+, (for the "soluble" PB which is often a dispersed yet lyophobic colloid) and $\square$ represents $[Fe(CN)_6]^{4-}$ vacancies occupied by coordinating water ($0 < x < 1$; $0.75 < y < 1$) [4,5]. The "capping" cation (Fe^{3+}) in PB can be substituted for some other cation or polycation to tune the chemistry for application of the resultant PB analogue (PBA).

Due to their porosity and host-guest chemical features, PB, PBAs and their composites act as ion-sieve zeolites and membranes [6] to capture (and subsequently release) ions such as Cs^+, Rb^+ and Tl^+ from radioactive waste-contaminated lands or environments [7–9] and even from the human body (i.e., detoxification) [1,9–12]. PB is electrochromic [13], exhibiting three stable oxidation states at different potentials [4,13–15]. It also exhibits electrochemical and magnetic properties [15], making PB and PBAs viable applicants in photoelectrochemical, photocatalytic, photomagnetic and magneto-optic devices [16]. Its electrochromic property is exploited in sensing [17,18], photothermal therapy and optical imaging [19–21], photoacoustic imaging [12,22], electrocatalysis [9,16,23], and theranostics—drug delivery/release agents in sites with poor drug accessibility, for example in cancer therapy [12,24,25]. PB, PBAs or their composites are further used as energy storage and conversion devices [9,23] in batteries [4,26–29], supercapacitors [30,31], and fuel cells [28,32].

Irrespective of the current and prospective applications of PB and PBAs for advanced functions, some serious shortcomings limit or even eliminate their utilization potentials. These failings include the large interstitial voids in PB, the localized valence electrons of the metals, which prohibit full electron delocalization, and the defects in the PB(A)s frameworks, thus resulting in low electronic conductivity [4,33,34]. The consequences are sluggish electron transport kinetics from

widening the cathodic and anodic peak potential differences, ΔE_p [34], and poor cycling stability [1,35,36]. Thus, proposed applications that depend, for example, on the above-mentioned properties would be severely impeded, such as in catalysis, electrochromic applications and, by inference, delivery/uptake systems, sensing, energy storage and conversion devices.

In contrast, refined, processed, or functional carbon materials often do not have the requisite large surface area and structural stability [37,38] for efficacious PB surface coverage. In the case of graphite felts, their total surface areas are not exploited fully due to the harsh conditions necessary for felt activation such as boiling in concentrated hot acids [39] or elevated temperatures [40,41]. These treatments damage the felt fibers [42,43]. Thus, the use of PB/felt even as ion-sieving agents is underutilized. Besides, most existing porous carbon materials are generally brittle, even in the absence of any activation protocols [44] and are even less so after thermal or acid activation. Therefore, the rarer porous yet stable carbon structures have attracted wide attention from bioengineering to electrochemical devices [37]. Next-generation electronics, energy storage/conversion devices and biological scaffolds will benefit from both the structural and functional integrity of carbon materials, especially as scaffolds in composites involving large surface area nanomaterials such as PB and PBAs.

The in-situ PB formation on thermally-treated and fully-activated, high surface area and flat graphite materials is reported herein showing substantial improvements in their structural and functional integrity over comparable extent material systems. PB deposition onto the thermally-activated graphites was achieved via two new synthetic routes: For the first time, a one-solution PB formation medium with a solid steel initiator without applied potential; secondly, a solution dipping approach in high K^+ (1 M). Both protocols circumvent the intermediary acid solution phases traditionally held to be necessary for PB synthesis and stability [3]. The electrochemical and electronic properties of these PB@treated graphite materials suggest multiple electrochemical, non-electrochemical and electronic applications without compromise to the structural and functional integrity of these composites.

Methods and Materials

Sample Preparation

Battery Felt SIGRACELL® GFA3 ($297 \times 210 \times 3$ mm thick) (gifts from SGL Carbon Company GmbH, Meitingen, Germany) were used as received. Pyrolytic graphite blocks, PG1 (32 ± 2 mm $\times$ 16 ± 2 mm $\times 0.75 \pm 0.5$ mm thick) (K & J Magnetics, Plumsteadville, PA, USA) were exfoliated using Scotch® tape to expose fresh pristine surfaces prior to thermal treatment and or the start of control experiments using these pristine surfaces. For pristine surfaces of GFA3, wettability was achieved by wetting in acetone and then rinsing with plenty of DI.

Thermal Treatment

The thermal treatment protocol is as reported elsewhere [45]. Briefly, samples were loaded onto a ceramic block and inserted into a quartz tube furnace (Lindberg/Blue M type model, Thermo Scientific, Asheville NC, USA) pre-heated to 650 °C with both ends open to air. The contents were heated for 25 min, the tube furnace was then turned off, and the contents allowed to cool naturally.

Solution dip -method for In-situ Prussian Blue Nanoparticle (PBNP) Formation on Graphites

The PBNP were formed *in-situ* onto the GFA3 and PG blocks by first, soaking the graphites in 1mM ($Fe(CN)_6^{3/4-}$ (1M KCl)) (Potassium hexacyanoferrate (III) ($Fe(CN)_6^{3/4-}$); ACS reagent, ≥99.0%) and potassium chloride crystal (SigmaUltra, >99.0%, Sigma Chemical Co., St. Louis, MO, USA), prepared with DI water for two hours. Specifically, the pristine GFA3 was wetted, prior to soaking in 1mM ($Fe(CN)_6^{3/4-}$ (1M KCl)), by soaking in acetone for 5 minutes and rinsing with plenty of DI. The graphites were then transferred immediately into a 2mM solution of $FeCl_2$ (Iron (II) Chloride, anhydrous, 99.5% [metal basis] Alfa Aesar, Haverhill, MA, USA) to form the PBNP on the graphites. The graphites-PBNP were then brought out after two hours of setting in the 2mM $FeCl_2$ solution and allowed to air dry. The air-dried graphites were then rinsed with water, acetone and plenty of water and left to air dry again. This cycle was repeated for the number of times required to obtain a given surface coverage of PBNP and or achieve specific electrochemistry signals. These reactions occurred at room temperature.

One-Solution, Metal-catalyzed in-situ Prussian Blue Nanoparticle (PBNP) Formation on Graphites

As in above, graphite samples were soaked for two hours in 1mM ($Fe(CN)_6^{3/4-}$ (1M KCl)) prepared with DI water. The pristine GFA3 was wetted as described above. The soaked graphites were removed from solution and stainless steel (General UltraTech, General tools & instruments, New York, USA) run over the graphite surfaces; the stainless steel and graphites just making contact via the electrolyte (a circuit if formed at this stage), until a blue solution-graphite-stainless steel interface appeared (the yellow color of the 1mM ($Fe(CN)_6^{3/4-}$ (1M KCl)) is changed to blue). These wet surfaces were air dried, rinsed with DI and allowed to air dry again. This process was done twice on the electrodes used for this work. These reactions occurred at room temperature.

UV-Visible Spectrophotometry of PBNP from the One- and Two-Solution Methods

The PB was formed on the graphites from the one-solution, metal (steel) catalyzed reaction as explained above. When the yellow coloration of $Fe(CN)_6^{3-/4-}$ turned to blue, the blue color was rinsed off the fibers into a 2 mL cuvette. More PBNP were formed and rinsed off into the cuvette until a desired volume (2 mL) was attained. This same approach was used to obtain PB solution from the two-solution method. In this case, the PB formed on the GFA3 fibers were not allowed to dry but were rinsed off into a cuvette. Their UV-Vis spectral scans, from 190 nm to 1100 nm, were acquired using a ThermoScientific Evolution 60S UV-Vis Spectrophotometer.

SEM Imaging

Scanning electron microscope (SEM) images for the PBNP deposited on GFA3 and PG(K&J) and their corresponding controls were obtained, using beam voltages of 15 KV, via a JEOL 2010J 200 kV Analytical TEM/STEM, with a vacuum of less than 10^{-6} Torr. Images were obtained at various magnifications.

Energy-Dispersive X-Ray Spectroscopy (EDX)

An EDX detector fitted unto the JEOL 2010J 200 kV Analytical TEM/STEM was used for elemental composition determination for the PBNP-graphites and their corresponding controls (graphites without PBNP). The probing beam, also used for the SEM imaging, was 15 kV.

Attenuated Total Reflection (ATR) – FTIR

The infrared (IR) vibrations of the cyanido groups arising from the PBNP on the graphites were obtained using the attenuated total reflection (ATR)-Fourier transform infrared (FTIR) spectroscopy technique. This analytical technique was performed using a Thermo Scientific Nicolet™ iS™ 10 FT-IR spectrometer, with the Smart iTR accessory, and the instrument interfaced to a Pentium operated desktop computer. The crystal plate for sample holding was diamond with a ZnSe lens. The samples were clamped down onto the crystal plate and lens using the pressure tower. Spectral acquisitions were averaged over 64 spectral scans to obtain a single spectrum. Spectral scans were recorded on both sides of the graphite surfaces and on a minimum of three different spots.

Raman Spectroscopy

Raman spectroscopy as previously described [45] utilized a WITec™ alpha300 R(aman) instrument (GmbH, Germany) with a 100-mW, frequency-doubled, Nd:YAG (λ = 532.5 nm) laser focused through a 20× Nikon objective (NA = 0.4, WD = 3.9 mm) for an excitation spot of ~10 μm diameter. Laser power attenuated manually to reduce fluorescence and localized thermal effects during sampling produced a final incident irradiation power of the order of 10 mW. Single spectrum "spot" scans acquired through the UHT-300 spectrometer (600 grooves/mm grating, 50-μm fiber core/collection aperture) used an Andor™ DU970N-BV, 1600×200-pixel CCD array detector. Each recorded Raman spectral plot came from an average of 10 spectral accumulations at 0.50-s integration time. Optical images of the sample location were saved from each area interrogated.

X-Ray Photoelectron Spectroscopy (XPS) and Ultraviolet Photoelectron Spectroscopy (UPS)

To interrogate the valence states of constituent elemental compositions of the PBNP@graphite, XPS, or Electron Spectroscopy for Chemical Analysis (ESCA), measurements were carried out in an ultrahigh vacuum (UHV) environment, with a base pressure < 10^{-10} Torr. The X-ray lamp was a dual anode XR 04-548 (Physical Electronics) while the kinetic energy of the photoelectrons was measured with an Omicron EA 125 hemispherical energy analyzer having a resolution of 0.02 eV. The X-ray

source used was the Al-Kα source operated at 400 W. The X-ray incident angle was 54.7° and normal emission. A freshly exfoliated HOPG-ZYH sample served as the reference spectrum for the C 1s binding energy. Peak-fitting was carried out using the XPS Peak 4.1 software. The background type, using XPSPEAK41, was Shirley. The UPS spectra, used to investigate the nature of the valence electrons at the HOMO, were acquired with the same analyzer as the XPS, using both He I (21.2 eV) and He II (40.8 eV) excitation lines.

Cyclic Voltammetry

Cyclic voltammetry with the various carbon materials as working electrodes operated with a VersaStat 3 potentiostat/galvanostat (Princeton Applied Research), while the counter electrode was a graphite block 99.99% pure, 40 mm × 40 mm × 3 mm thick (Fujiansheng, China). The reference electrode was Ag/AgCl in 3 M NaCl(aq) as reference electrode (0.209 V vs. SHE) from Bioanalytical Systems Inc. (West Lafayette, IN, USA). The electrolyte was a 1-mM ($Fe(CN)_6^{3/4-}$ (1M KCl)) redox-couple solution.

Data Processing

The Origin version 2018b® (version 9.55) software package was used for plotting all graphs.

Results and Discussion

We report the synthesis and characterization of a first-time in-situ PB from only one solution precursor (1mM $Fe(CN)_6^{3-/4-}$ in 1M KCl) mediated by solid steel, and an in-situ PB formation from 1mM $Fe(CN)_6^{3-/4-}$ (in 1M KCl) and Fe^{2+}. These PB nanoparticles (PBNP) were deposited onto thermally-activated yet stabilized graphites. The PBNP doubled the thermally-activated graphite felt capacitance without compromising their structural and functional integrity. Essentially, the steel-catalyzed and solution-dip cycles correlate electrochemically with each other in terms of their corresponding synthesis cycles and resultant electrochemistry.

The PBNP@thermally-treated graphite SEM micrographs are shown in Fig. 3.1. The PB cube-like crystals are shown (Figs. 3.1a, b and d). Fig. 3.1c shows the spatial distribution of the crystals on the fibers at lower magnification. On the other hand, no distinguishable morphological differences exist between the pristine GFA3 and the pristine GFA3-PBNP-2×dipped (Figs. S3.1 a and b), while at 2×dipped, the treated GFA3-PBNP had enough PBNP surface coverage (Fig. S3.1f). Again, no distinguishable morphological differences exist between the pristine and treated GFA3, (Fig. S3.1a and e) to allude to morphological differences as the reason for the preferential PBNP deposition on the treated rather than the pristine GFA3. These results suggest that the thermal treatment altered the crystallinity and electronic properties of the graphites without any visible morphological changes, as earlier reported [45]. This implies that the treated GFA3 fibers are more receptive to the PBNP formation and growth (because of its enhanced crystallinity) compared to the pristine GFA3 fibers. The same apply to the pyrolytic graphite (PG) and graphite rods. The broader implication of these finding is that the substrate nature for PB deposition plays a role in determining the eventual chemistry of the PBNP [46,47]. By the third dipping cycles for both treated GFA3 (Fig. S3.1; c and d) and pristine (Fig. S3.1; g and h), the cuboidal nature of the PB at the 2×dipped cycles for the treated GFA3 had given way to a more spherical PBNP as earlier reported [48]. This is most likely due to clustering, which forced the shapes to morph from cubes into more irregular shapes.

The graphite@PBNP electron dispersive X-ray spectroscopy (EDS) results (Fig. 3.1 inserts and S3.2) show elemental Fe, a key PB constituent, and sharp K^+ signals. The pristine GFA3-PBNP-2×dipped Fe signal intensity is weak (Fig. S3.2a) compared to those of treated GFA3-PBNP-2×dipped. These results further support the argument that treated graphite fibers are more receptive to support PB crystallization.
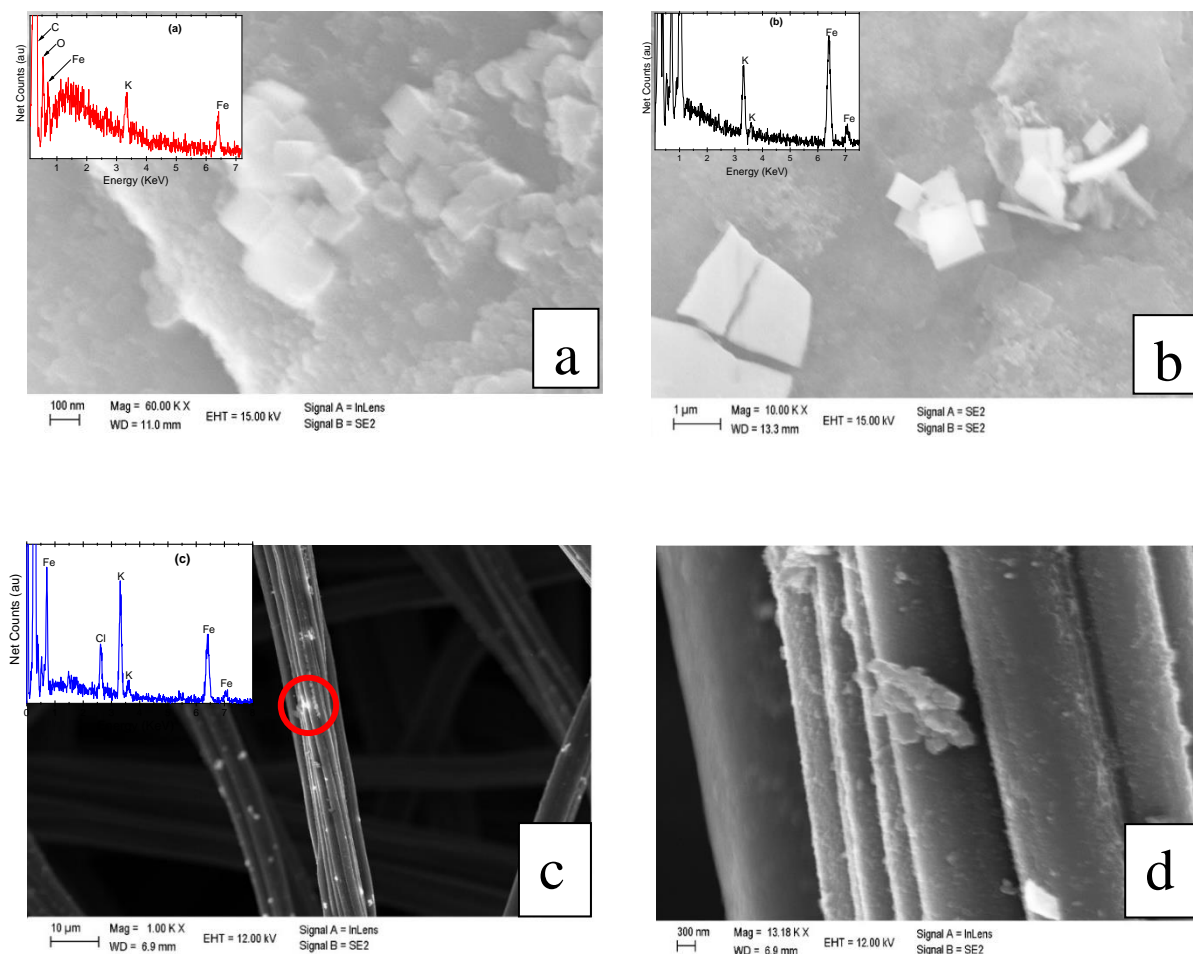
Figure 3.1: Surface morphology images acquired via SEM of a: Treated GFA3-PBNP-2× dipped; b: Treated PG(K&J)-PBNP-6× dipped; and c: GFA3-PBNP-2× metal-catalyzed showing the crystals glistening on various points on the graphite. (d) A higher magnification of the red highlighted region on Figure 3.1c. The images show the cube structure of Prussian Blue (PB). Inserts of Figure 3.1: The EDS plots of (a) Treated-GFA3-PBNP-2× dipped; (b) Treated-PG(K&J)-PBNP-6× dipped and (c) Treated GFA3-PBNP-2×metal catalyzed.

The PB, UV-Visible spectra, from the solution dip- and metal-catalyzed methods show peaks between 250-300 nm and at ca. 700 nm (Fig. 3.2). These traits are diagnostic for PB. However, the PB from the metal catalysis had an obvious peak at 400-410 nm (*Fig. 3.2) not present in the PB spectrum from the solution dip method. This implies an electron-relay path difference between PB forms for charge transfer from one metal, M, to the other metal, M′, in the complex. Therefore, the PB formed by metal catalysis probably has an electron travel path in its charge-transfer complex not present in that from the solution dip method.
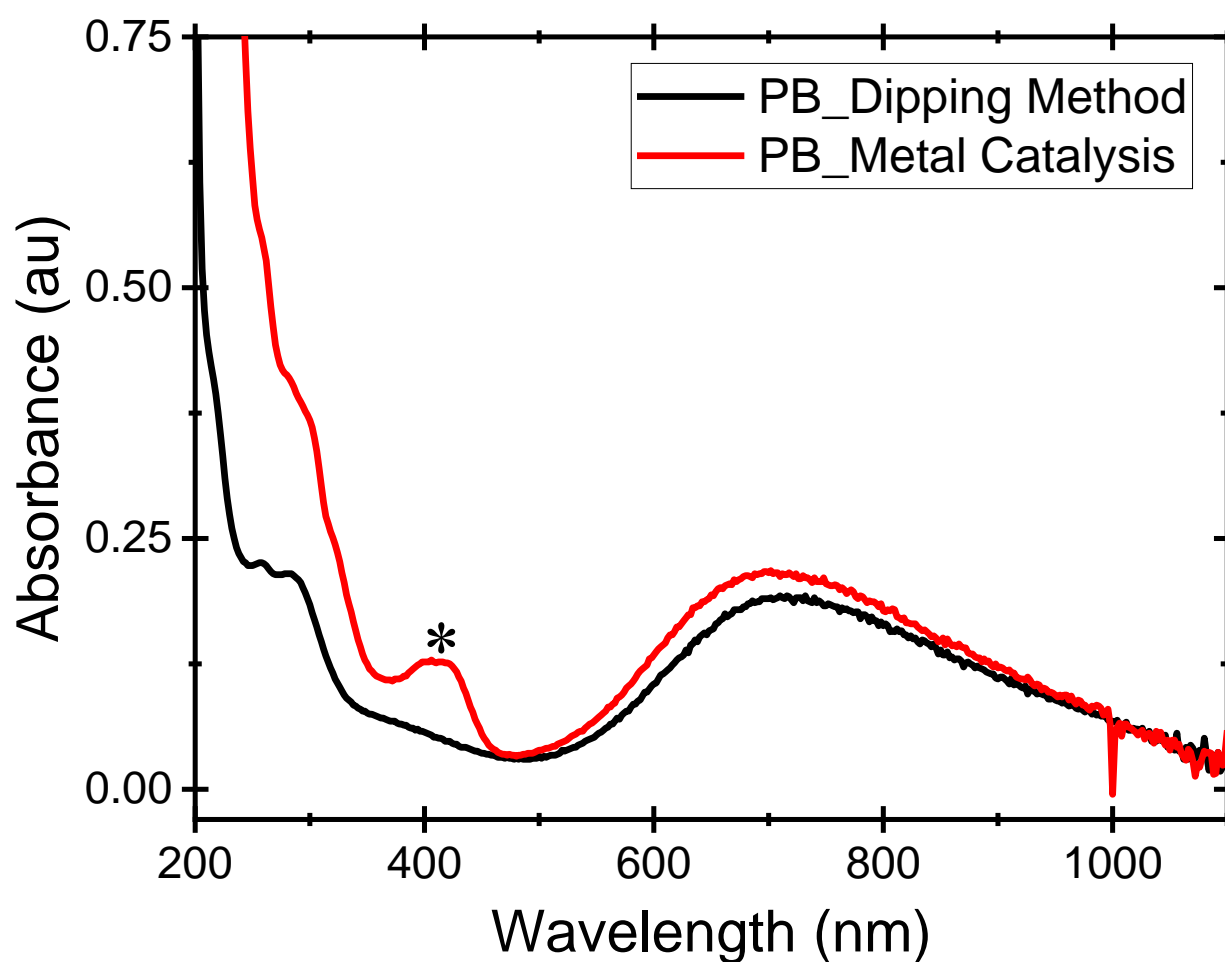
Figure 3.2: The UV-visible spectroscopy of PB formed from the dipping- and metal-mediated metal catalyzes methods on treated GFA3. *The mode near 400 nm appears only for metal-catalyzed samples.

Representative ATR-FTIR results for the PBNP@GFA3 (Figs. 3.3 and S3.3) show the ~2084 cm^{-1} peak commonly characterizing PB and its analogues. They correspond to the CN-stretching [ν(CN)] in a dinuclear compound, M-CN-M′ [47,49]. The magnification of this ν(CN) region is shown in Fig. 3.3b and suggests a PBA analogue, Fe^{II}[Fe^{II}(CN)$_6$] [50]. The PBNP@graphite felt spectra from the solution dip methods show less interstitial OH vibrations at ca 1646 cm^{-1}. This peak is assigned to H$_2$O deformation or bending modes (δH$_2$O) [47,51] and suggests a relatively low number concentration of coordinated water in the PB formed from this method. The PB FTIR spectrum from the one-solution method (Fig. 3.3c) shows δ(HOH) modes at 1595 cm^{-1} and 1673 cm^{-1} indicating lattice bound or trapped water. The peak at 2088 cm^{-1} for ν(CN) in a M-CN-M′ bond structure. The magnification of the regions around the ν(CN) is shown in Fig. 3.3d. The peaks at ca. 2088 cm^{-1}, 2137 cm^{-1}, and 2187 cm^{-1} suggest that the CN are bonded to Fe(II)/M(II), Fe(II)/M(III), and Fe(III)/M(II), respectively [16]. These findings imply that by the reversible loss of an electron at each stage, these three oxidation states are accessed by the metal catalysis-formed PB.
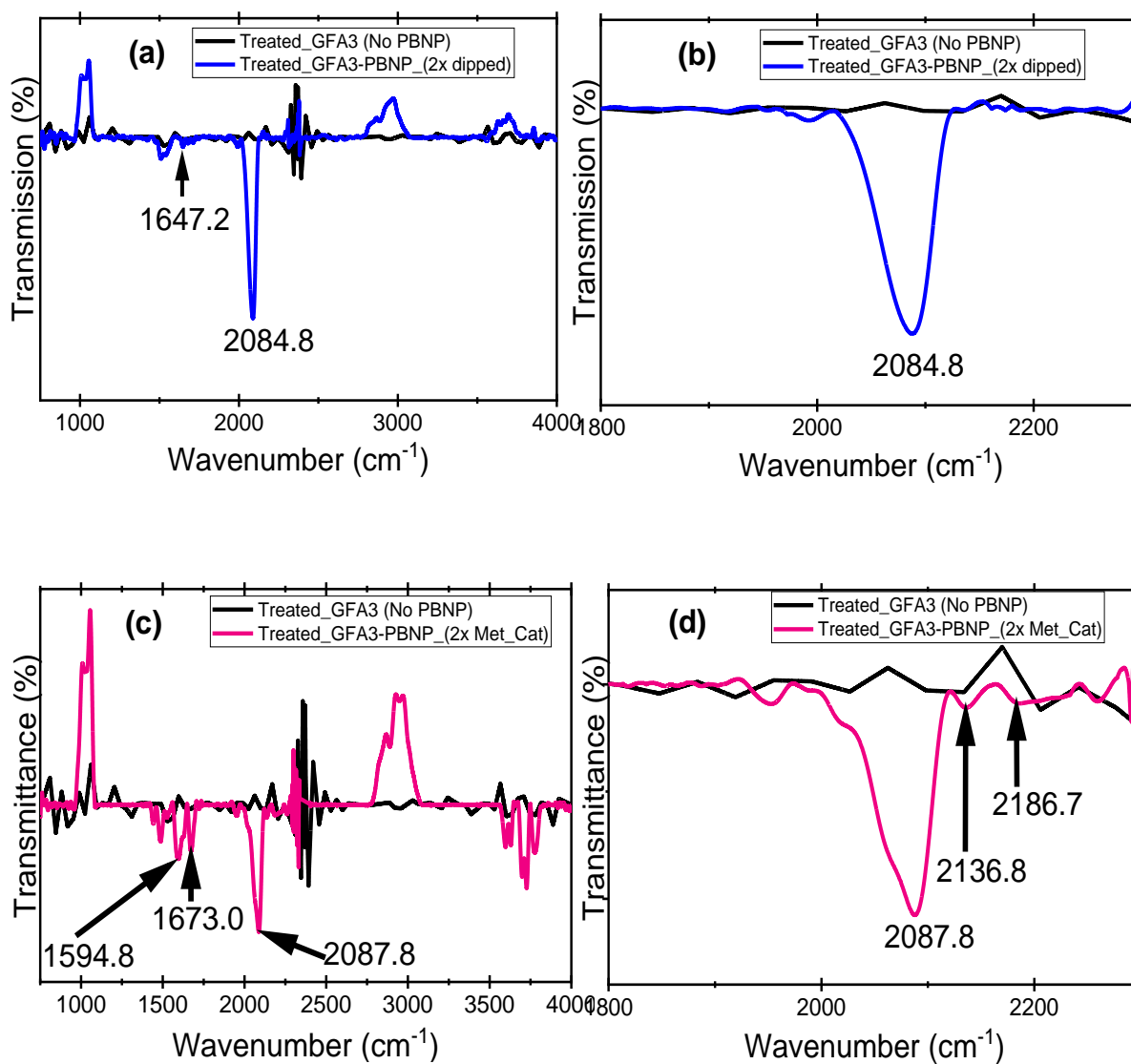
Figure 3.3: ATR-FTIR spectrum of (a) treated GFA3-PBNP_(2×_dipping method), (b) magnification of the ν (CN) region of (a), (c)) treated GFA3-PBNP_(2×_metal-catalyzed method), (d) magnification of the ν (CN) region of (c).

The treated GFA3-PBNP and PG-PBNP micro Raman spectra (Figs 3.4 and S3.4, respectively) show peaks at ~2153 cm^{-1} from some sample locations, which are assigned to vibrational frequencies of the bridging CN ligands in PB [46]. These are indications of surface anchored or physisorbed CN containing groups [46,52]. They are prominent on every scan of the PG (flat electrode) while being weak or not observable on the GFA3, appearing clearly on only one fiber probed with the focused Raman laser. This strengthens the collective points above that the substrate nature (crystallinity and morphology) contributes to defining the resultant chemistry of the PB and the PB@substrate composite.

Other metal-ligand Raman modes at less than 650 cm^{-1} are due to the presence of inorganic groups, metalorganic groups or lattice vibrations [53]. Generally, the peaks at less than 250 cm^{-1} are attributed to lattice mode vibrations, originating from crystals [54,55], while the Raman bands between 250 and 600 are from M-CN-M′ vibrations. These vibrations could be resolved into ν(MC), δ(MCN), δ(CMC), δ(CMN) and combination modes, which all appear in the region below 550 cm^{-1} [54]. These vibrational modes indicate the presence of PB (Figs. 3.4 and S3.4). For example, the treated GFA3-PBNP samples spectra have ~384 and ~401 cm^{-1} peaks, corresponding to the in-plane E_{2g}^1 and the out-of-plane A_{1g} modes, respectively. Also, the 519 cm^{-1} (E_{1g}) modes are evident. These results suggest octahedral-coordinated ligand-to-metal centers, stacked-up in a layered fashion [56–59].
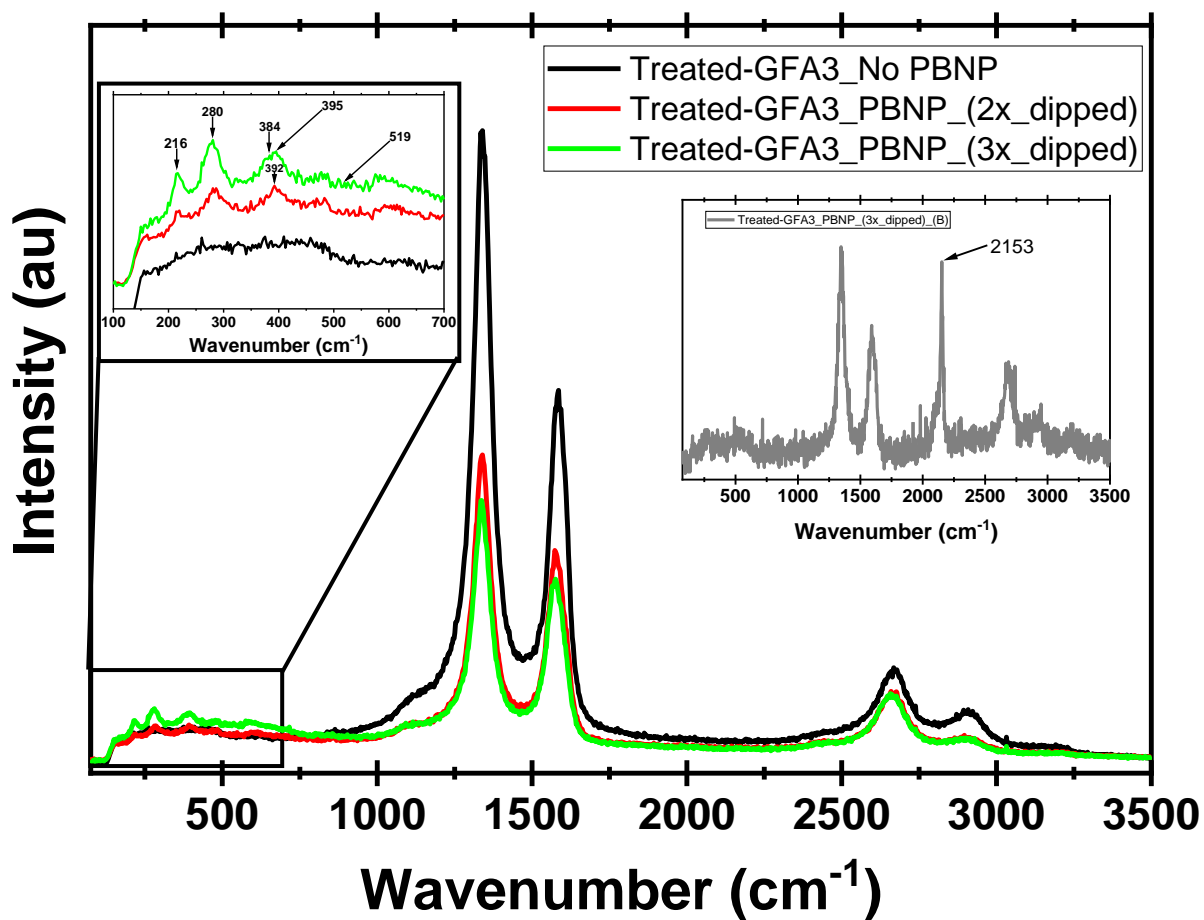
Figure 3.4: Raman spectra of treated-GFA3 in the absence and presence of PBNP (2×- and 3×-dipped). Raman inserts: Left, the region at 700 cm^{-1} and lower shifts magnify stretching and deformation modes of the M-CN, offset on the arbitrary intensity scale for clear comparison. Right, a single carbon fiber showed a PB mode at 2153 cm^{-1}.

Electrochemical spectroscopy for chemical analysis (ESCA), or XPS, was used to determine both the chemical composition and spin states of the PB elemental constituents. The wide angle XPS ("survey") results of treated GFA3-PBNP-2× dipped (Fig. 3.5a) and other treated graphite-PBNP (Fig. S3.5a and b) show elemental Fe and N not present in their controls. At high resolution XPS scan (Fig. 3.5b-5d), their Fe nitrides binding energy is at ~397 eV, indicating that the PB nitrogen is present as a metal-bound nitride [60]. The metal in this case been Fe. However, in addition to the 397.4 eV peaks of the nitrides of the treated GFA3-PBNP, there is another peak at ~ 398.1 eV. In the M-CN-M′ charge transfer complex, overlap of the molecular orbitals of the cyanide complex clusters with the atomic orbitals of K do occur [61]. Such interaction has been reported of CN clusters with cations in its vicinity to result in a XPS metal-nitride peak near 398 eV [62]. Thus, for the T-GFA3-PBNP-2×dipped, the ratio of the areas of the peaks at 397.4 eV to that of 398.2 eV is ~3, while the ratio for the T-GFA3-PBNP-2× metal catalysis is approximately 1. These ratio values suggest that the 398.2 eV conformation is a minor contributor to the overall state of the N-metal interaction for PB in the solution dip method but is a major conformational state for PB from metal catalysis. An implication of this finding is that the CN clusters associated with K^+ in the PB from solution dip method is a minor and less likely pathway for charge delocalization along the charge-relay complex of its metal-cyanide. On the other hand, these CN clusters-K^+ association would be a probable pathway for charge delocalization along the M-CN-M′ of the PB from metal catalyzes. Additionally, Fe in the PB matrix contains both divalent and trivalent states, in integer proportions, as shown in the representative Fe 2P states in the treated GFA3-PBNP-2×dipped (Fig. 3.5e and S3.5c). Thus, the actual structure is an Fe^{II}-CN-Fe^{III} dinuclear compound with a Fe^{2+}/Fe^{3+} ~ 1 or 2.
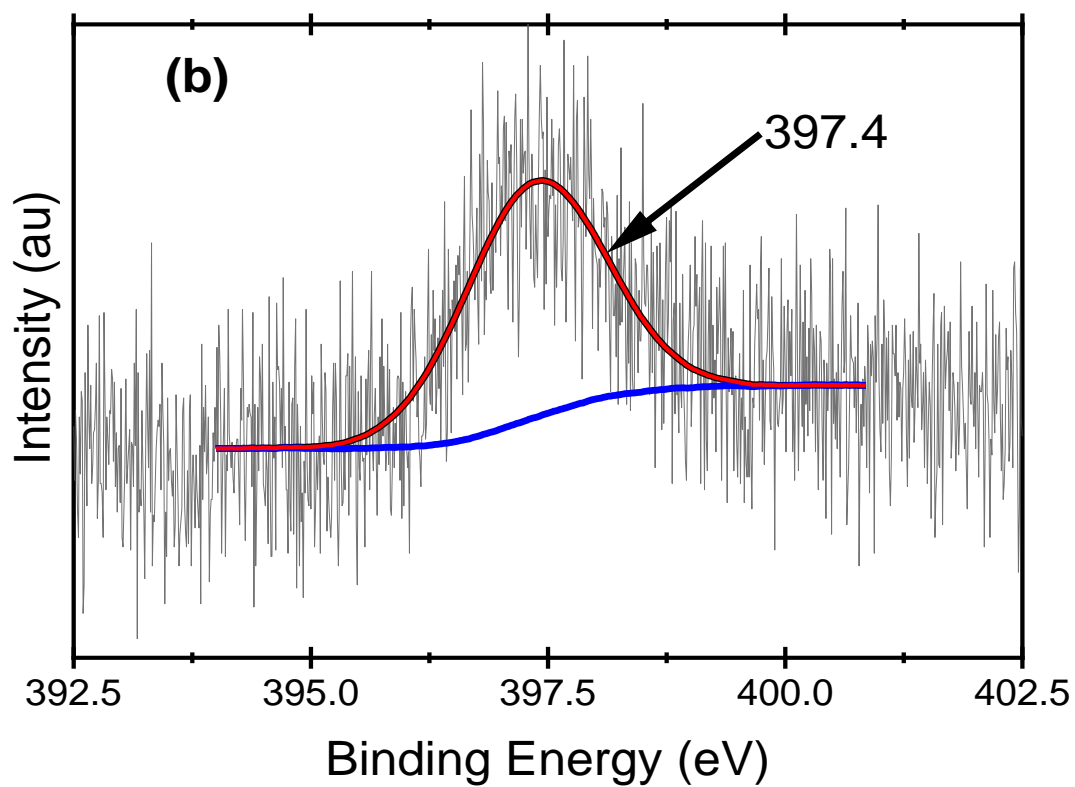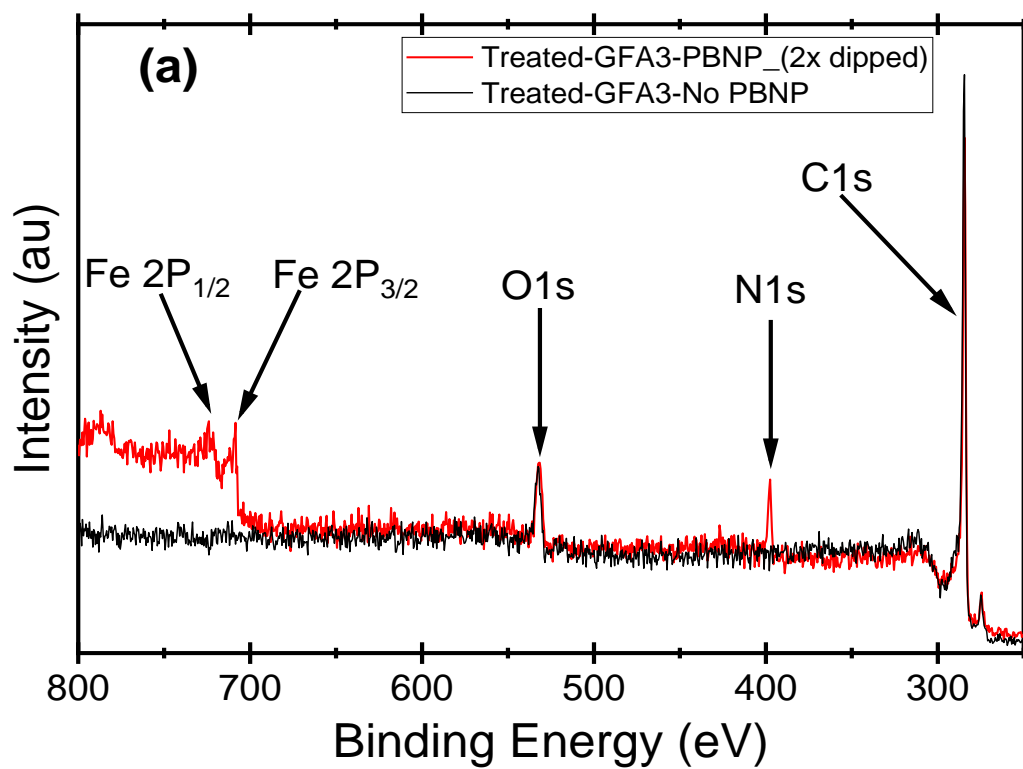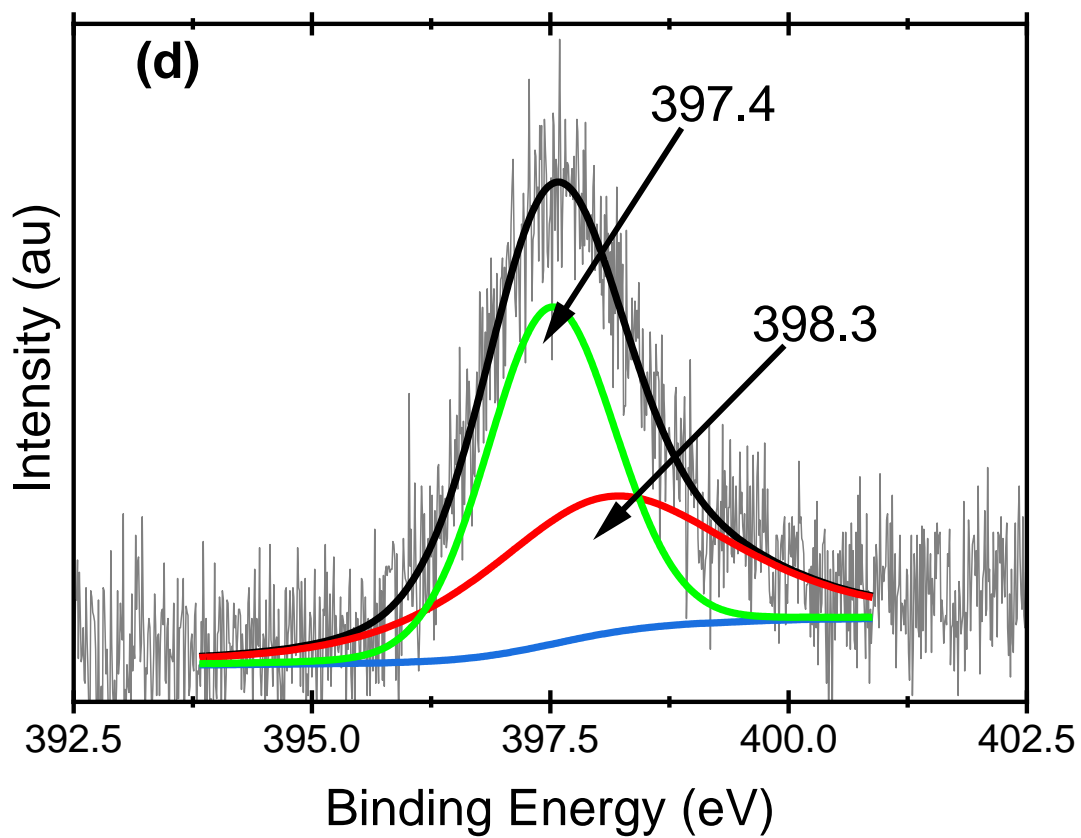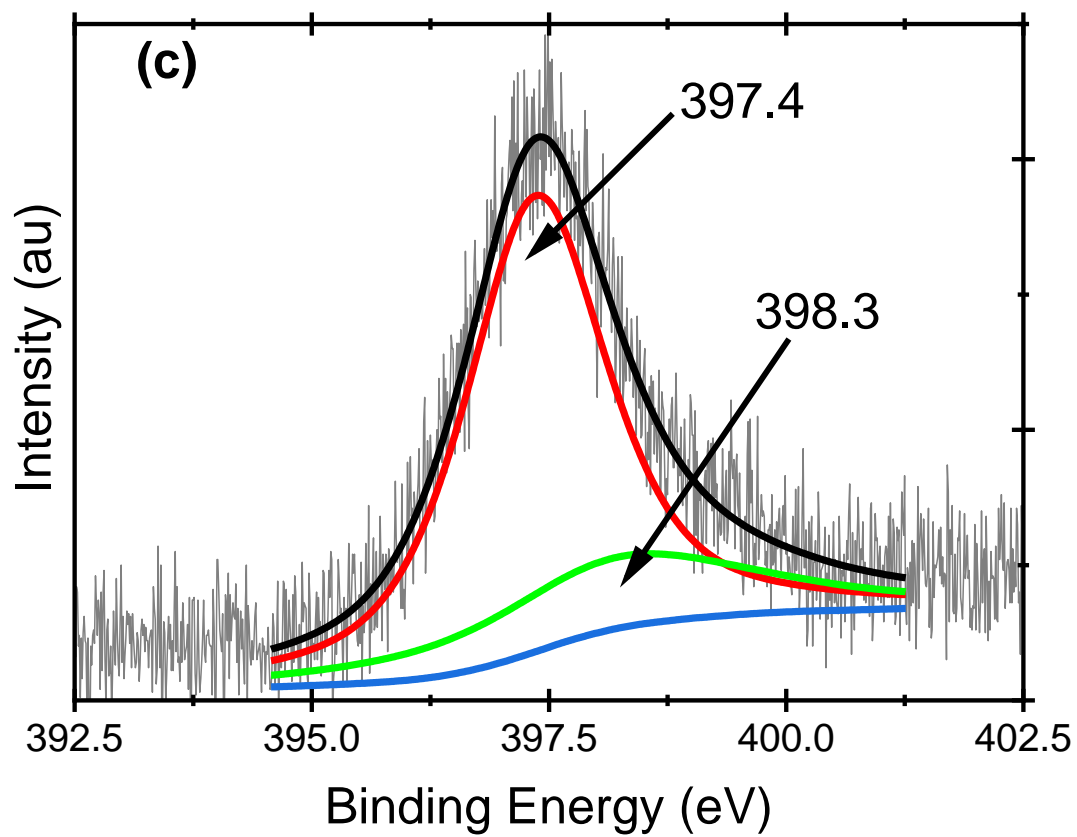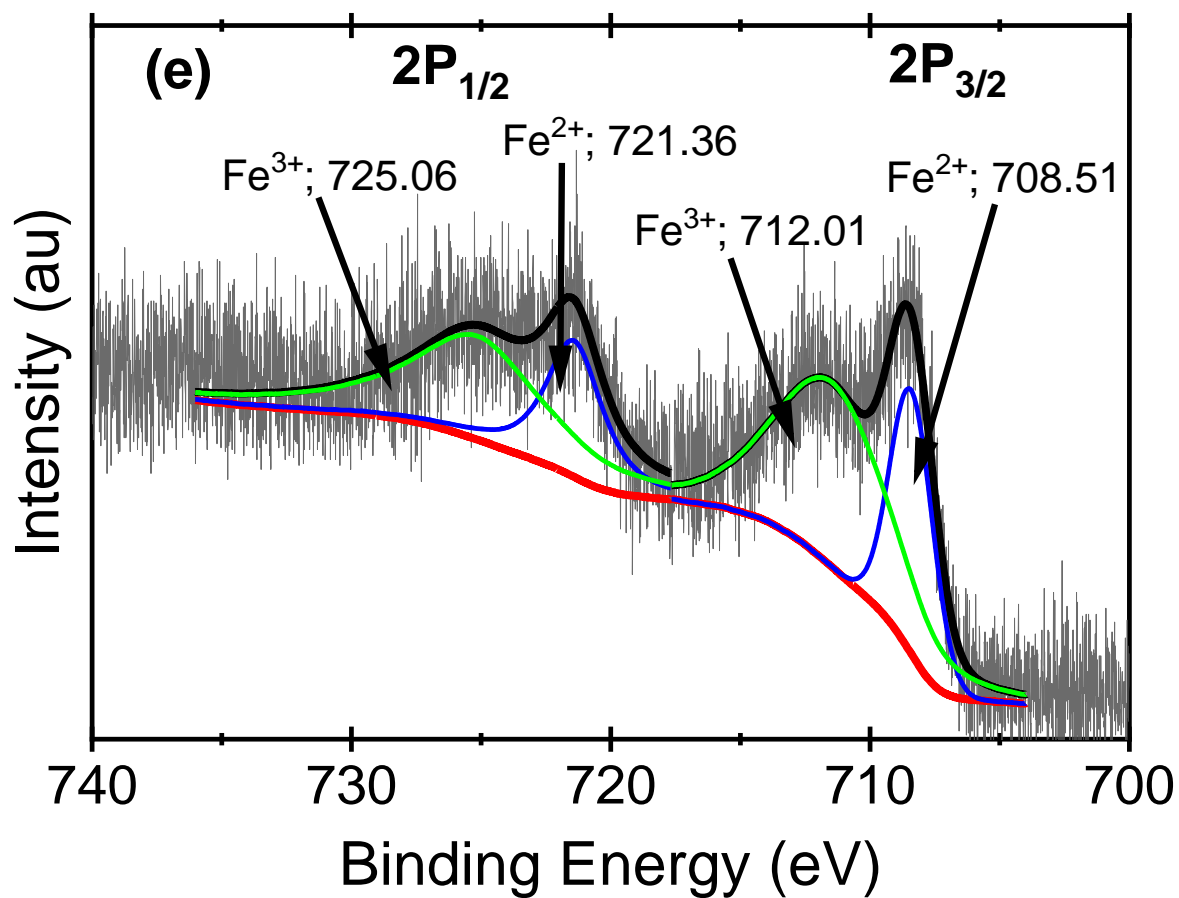
Figure 3.5: (a) Wide angle ("survey") XPS spectra of treated GFA3-PBNP-2× dipped and treated GFA3-No PBNP; High resolution XPS spectra of (b) N1s in treated PG(K&J)-PBNP-3× dipped; (c) N1s in treated GFA3-PBNP-2× dipped; (d) N1s in treated GFA3-PBNP-2× Met Cat; and (e) Fe2P in treated GFA3-PBNP-2× dipped.

To understand the impact of the PBNP on the electronic properties of the thermally-treated graphite, graphite-PBNP Ultraviolet Photoelectron Spectroscopy (UPS) data were compared with those of the treated graphite (no PBNP) (Fig. 3.6). The aim was to investigate if, and how, the PB interaction with the treated graphite surfaces distort (or leave unchanged) the valence electron (HOMO level) properties of the treated graphites. To interrogate these electronic properties, an analysis of the π-band peak intensities over those of the σ bands (Fig. 3.6) were calculated as already explained elsewhere [45]. The results show that treated graphites and graphite-PBNP had about the same signal intensities and peak values up to the E_F region. However, the graphite-PBNP $I_{\pi 2}/I_{\sigma 1}$ was higher than that without PBNP. This suggests an enhancement by specific heat-treatment of π over σ character (Fig. 3.6a). Additionally, the difference between the two σ bonds, $\Delta(\sigma 2 - \sigma 3)$, is greater for the treated graphite-PBNP than without PBNP, indicative of a stronger σ-bond interaction facilitated by the PB, while the π-bond nature of the PB@graphite is enhanced. This enhancement of π over σ bonds is a common trait of conjugation and conductivity [63]. On the other hand, the He_1 probed spectrum (Fig. 3.6b) suggests the reverse is true for thermally-treated graphite having a slightly enhanced π over σ trait ($I_{\pi 2}/I_{\sigma 1}$) and a shorter $\Delta(\sigma 2 - \sigma 3)$ distance. However, the treated graphite with PB has a smaller energy well depth, Δh, than without PB, reflecting a stronger σ-bond interaction in terms of bond strength [64], stability [65], and molecular size [66]. In summary, the electronic properties of the PBNP@treated graphite-2×dipped are similar to those of the treated graphite without PBNP. The UPS of the treated PG and PG-PBNP (Fig. S3.6) show a similar trend.

The UPS data suggest that the 2×dipping cycles employed for PB formation did not perturb or disrupt the electronic nature of the treated graphite nor, by extension, of the PB from the metal-catalyzed phase since the UPS from both synthesis cycles are very similar. This suggests, as was earlier postulated, a Hubbard-type model characteristic [67] conferred by the thermal treatment protocol on the graphites. Briefly, the Hubbard model implies that the electronic structure of the treated structure is correlated (cannot be explained by a single electron wavefunction) and non-perturbative (not disrupted) even by non-native surface properties [68]. In this case, it is the PB on the graphite surfaces. One of the implications of these findings is that the electrochemistry of the heat-treated graphites could be improved upon without repercussions on the integrity of its electronics and other electronics-dependent properties.
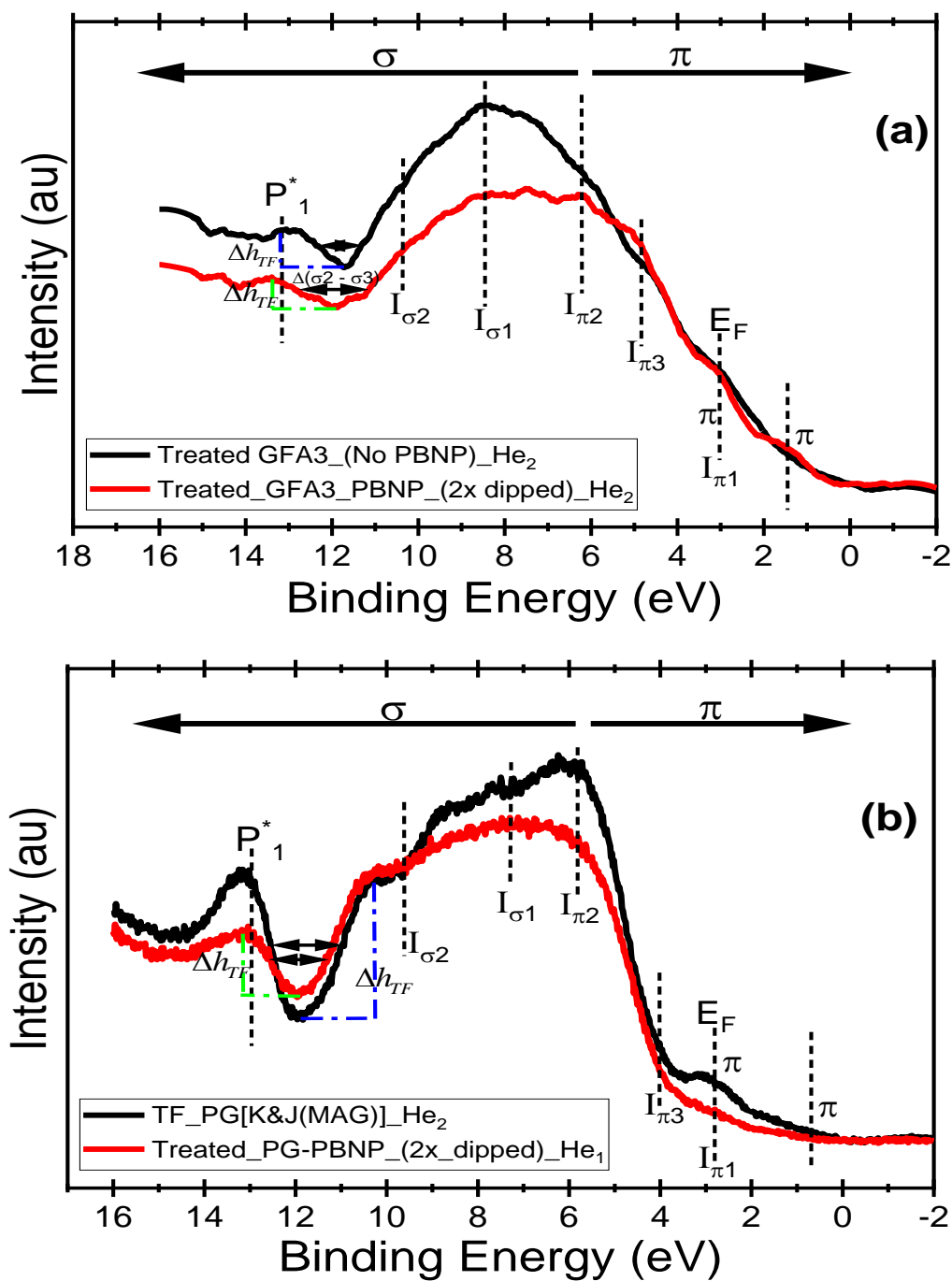
Figure 3.6: (a) the valence band spectra at the HOMO obtained from the He₂ and (b) He₁ lines of the treated GFA3-PBNP-2×dipped and its control, treated GFA3 (no PBNB) with highlights of the various intensity bands.

The CVs in 1mM $Fe(CN)_6^{3-/4-}$ of treated (Fig. 3.7) and pristine GFA3 (Fig. S3.7) with and without PBNP show that thermal treatment improved both the kinetics and capacitance even without PBNP. This improvement is due to the increased crystallinity and proper electronic tuning of the treated graphite as discussed [45]. In the presence of PBNP ($2\times$ and $3\times$dipped), the treated GFA3 capacitance doubled while those of the pristine GFA3-PBNP nearly doubled by the third dipping cycle (Table 3.1). However, the pristine GFA3-PBNP-$3\times$dipped capacitance is eight times less to the treated GFA3-PBNP-$3\times$dipped, even though their morphologies are very similar (Fig. S3.1; c and d). The explanation for these discrepancies in the PB carrying-capacities on the treated and pristine graphites lies with the treated GFA3 crystalline nature, which is also responsible for its capacitance increase by making available more usable and more receptive surfaces for PB formation. This contrasts with the less crystalline and less receptive pristine GFA3 surfaces. In other words, the PB only optimizes the surfaces presented to it.

Again, as in above, the substrate nature contributes in defining the resultant PB and or PB@graphite chemistry [46,47]. Additionally, the consistency of the PB chemistry on both the treated and pristine GFA3 indicates the homogeneity of these PB forms on the carbon types employed. The TT graphite-PBNP ($3\times$dipped) capacitance was slightly less than after only two dips. This slight decrease may come from PB stacking so that agglomeration of the octahedral structures (SEM images in Figs. S3.1; g and h) could have introduced more defects, thus decreasing the volume carrying capacity of the PB. Irregular to spherical PB agglomerates have more disordered vacancies and smaller specific surface area compared to cubic PB [69]. This could explain the widening cathodic and anodic peak potentials of the treated GFA3-PBNP-$3\times$dipped, reflected also as increased ΔEp (slower kinetics).
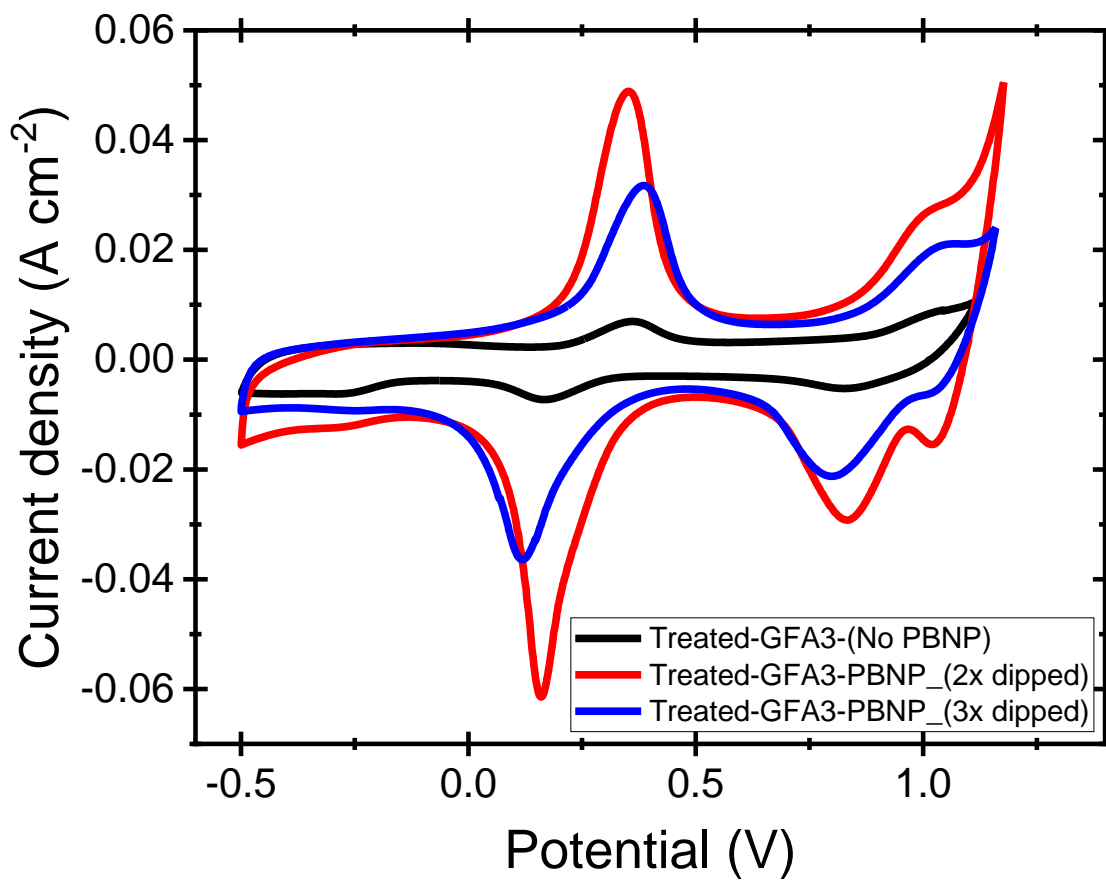
Figure 3.7: The CV in 1 mM Fe(CN) 1M KCl of treated-GFA3 (No PBNP), treated-GFA3-PBNP-2×dipped and treated-GFA3-PBNP-3×dipped. ν = 0.05 V.s⁻¹.

Table 3.1: Capacitance (mF.cm^{-2}) and peak potential differences (ΔEp (mV)) of pristine and treated GFA3 in the presence and absence of PBNP, deposited via different dipping cycles (n =3 for each electrode type).

Electrode Type	ΔEp (mV) @ ν = 0.05 V s^{-1}	Capacitance (mF cm^{-2})
Pristine GFA3	179±27	8.5±1.0
Pristine GFA3-PBNP_(2x dipped)	158±2	10.7±0.5
Pristine GFA3-PBNP_(3x dipped)	299±2	15.6±1.2
Treated GFA3	209±17	70.6±4.0
Treated GFA3-PBNP_(2x dipped)	215±39	137.4±7.0
Treated GFA3-PBNP_(3x dipped)	262±18	125±7.9

The PBNP@treated graphite CVs at various scan rates is shown in Fig. 3.8a. A plot of their anodic peak current densities to its corresponding scan rates indicates diffusion-controlled kinetics at these peaks (Fig. 3.8b). The poor cycle stability of PB [1,35], and instability in neutral and alkaline solutions [46,47], impose constraints on the CV cycle numbers that could be performed on PB and its composites. For example, a comparable work involving graphite fibre-Pt-PB with CV cycles of 150 has been reported [70]. To investigate the PB@treated felts cycle stability, 2100 CV cycles ran from 1.3 V to -0.5 V in 1M KCl. Initial and final CV curves (2100 cycles) show that the PB@treated felts are highly consistent against these cycling conditions (Fig. 3.9).

The CV stabilities across the entire potential window range, -0.5 to +1.3V, indicate Prussian white to PB (and vice versa) and PB to Berlin green (reversibly) transition stabilities [70]. These stabilities show the PB-zeolite nature stabilities to the constant motions of deintercalating /intercalating ions during the CV cycles. Thus, our results show highly porous and stable PB structures, unlike carbon materials in general [44]. Besides, such low-defect PB with high capacity, strong rate capability and long cycle life have been associated with PB synthesis in concentrated K$^+$ [36], such as was used in this work.
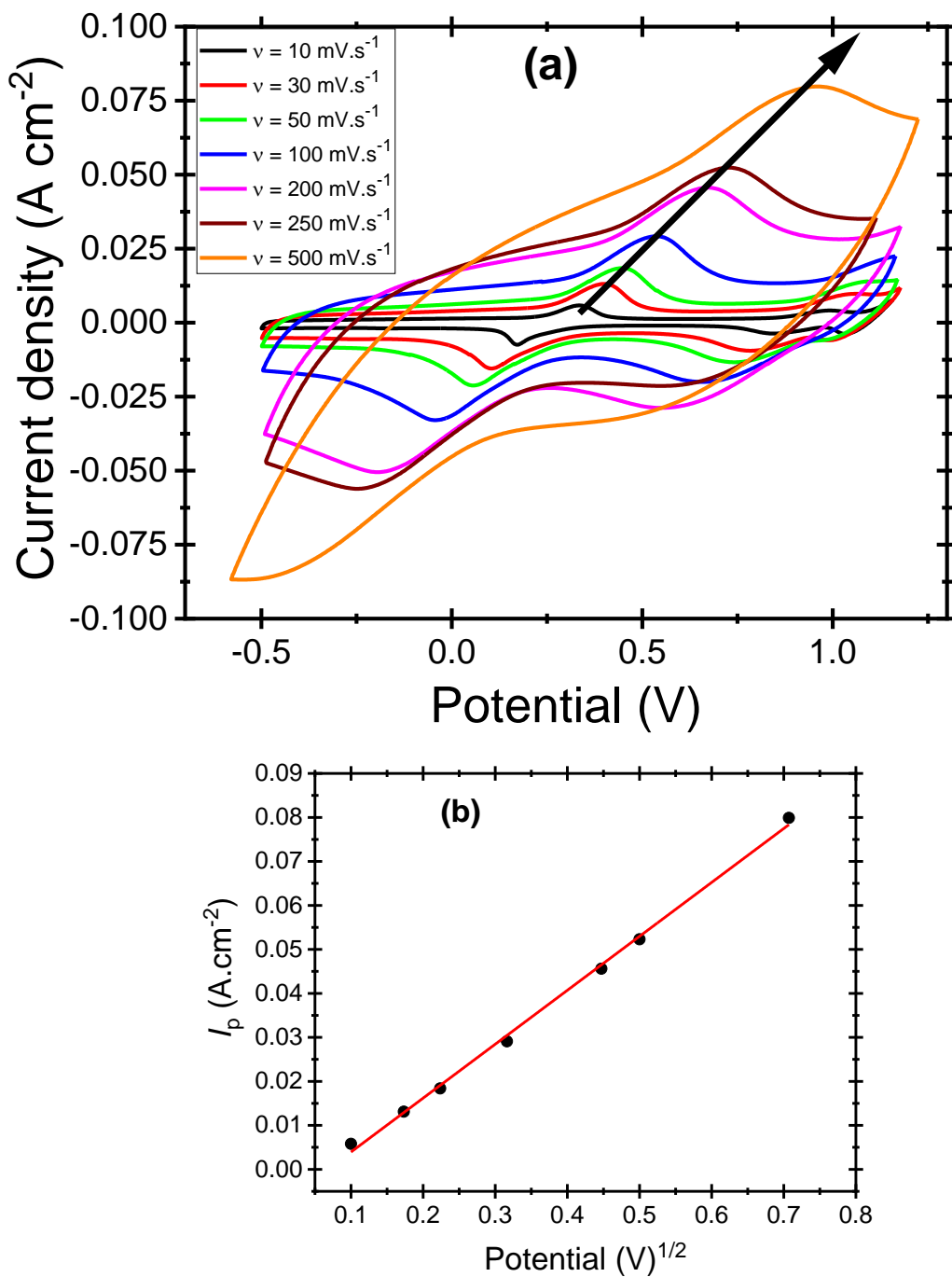
Figure 3.8: (a) The CV in 1M KCl of the treated-GFA3-PBNP-2×dipped and at various scan rates from 10 mV to 500 mV. (b) the peak current density of the various scan rates, showing the diffusion-controlled kinetics of the treated-GFA3-PBNP-2×dipped.
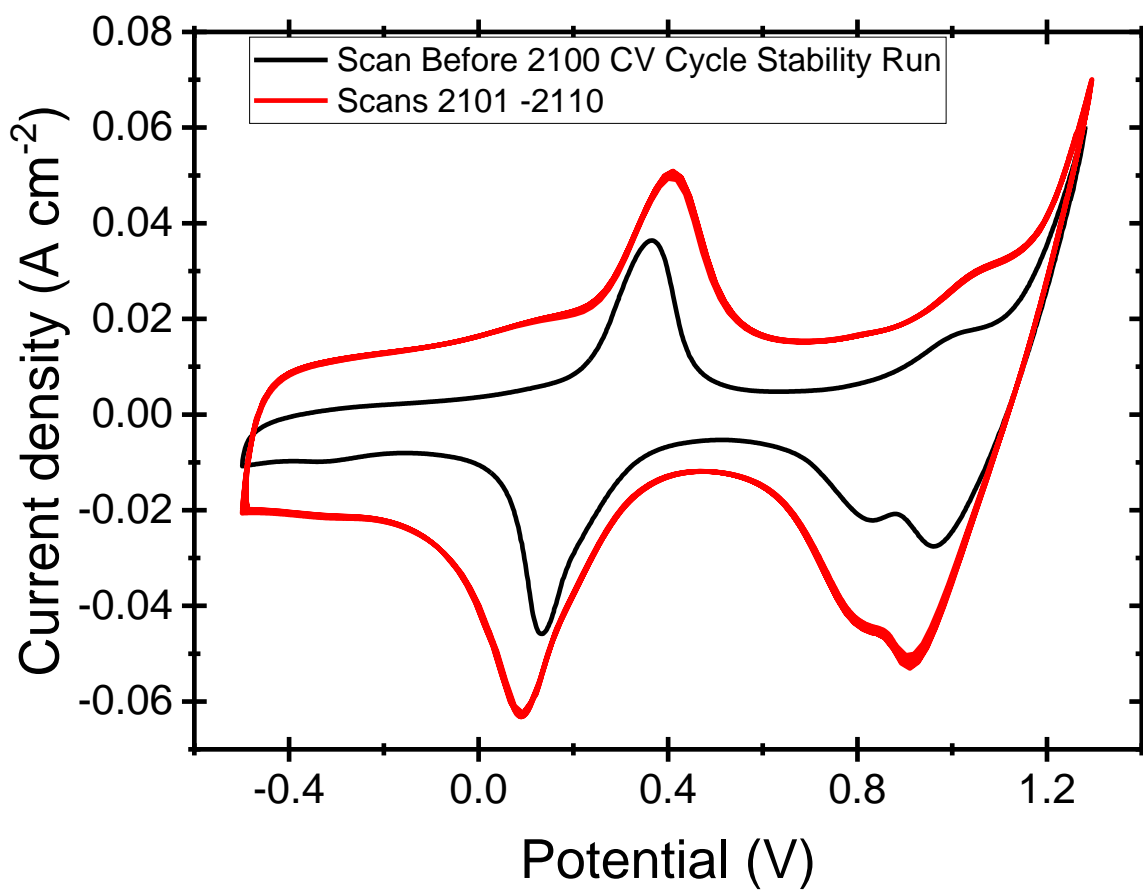
Figure 3.9: Cycle stability test of the treated GFA3-PBNP (2x dipped) in 1mM Fe(CN)$_6^{3-/4-}$ (1 M KCl), from -0.5 V to 1.3 V. The cyclic voltammograms before and after 2100 consecutive cycles as stability indicator.

The electrochemistry of PB from the metal catalysis correlates strongly with those of the solution dip-cycles (Fig. 3.10), even though their UV-visible and IR spectra suggests that the charge transfer between the metals, M and M′ in the complex, M-CN-M′ are via different electron relay paths. The PB XPS (Fig. 3.5) shows a Fe^{II}-CN-Fe^{III} dinuclear compound with $Fe^{2+}/Fe^{3+} \sim 1$ or 2. PB with an M/Fe = 1 or integers indicate absence of dangling bonds or defect-free lattices, where M is a transition metal with +2 oxidation state and Fe is in the +3 oxidation state [16]. Thus, their CV data imply defect-free PB lattices.
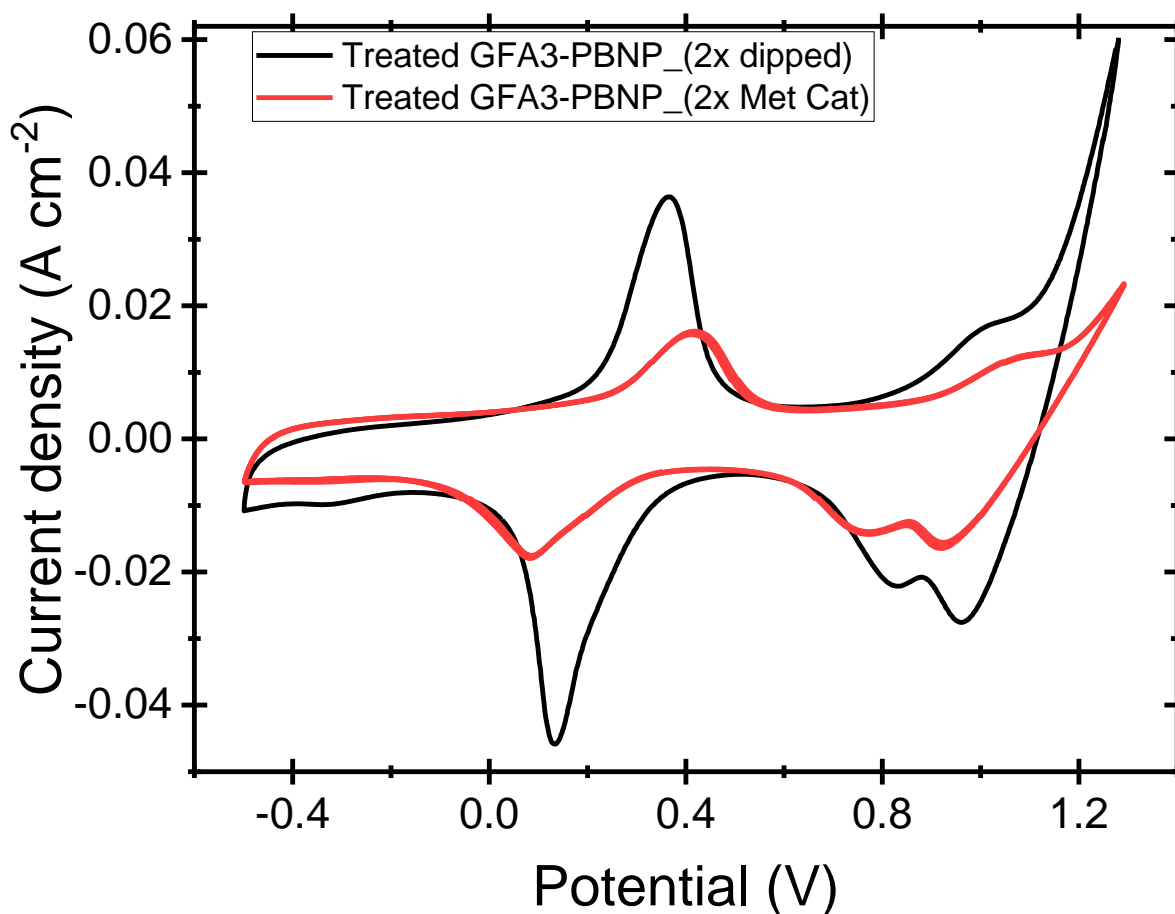
Figure 3.10: The cyclic voltammetry of PBNP from metal catalysis (2x catalyzed) and from the solution dip method (2x dipped) on treated GFA3. The CV was in 1mM $Fe(CN)_6^{3-/4-}$ (1 M KCl) and $\nu = 0.05$ V/s.

Also, from the UV-vis, FTIR, and high resolution XPS N1s fitted spectra, the metal-catalyzed PB form has one intermediary path of electron travel from the metals M to M′ in the M-CN-M′ complex and more interstitially coordinated water to that from the dipping method. Scheme 3.1 shows the paths to accessible oxidation states and K^+ coordination during a charge-relay process.

$$[M / Fe = 1]$$

(a)

$$Fe(II), M(II) \xleftrightarrow{K^+, e^-} Fe(III), M(II)$$

$$K_2Fe\left[Fe(CN)_6\right] \qquad KFe\left[Fe(CN)_6\right]$$

$$(\square\ 2085\ cm^{-1}) \qquad (\square\ 2172\ cm^{-1})$$

(b)

$$Fe(II), M(II) \xleftrightarrow{K^+, e^-} Fe(II), M(III) \xleftrightarrow{K^+, e^-} Fe(III), M(II)$$

$$K_2Fe\left[Fe(CN)_6\right] \qquad KFe\left[Fe(CN)_6\right] \qquad Fe\left[Fe(CN)_6\right]$$

$$(\square\ 2088\ cm^{-1}) \qquad (\square\ 2137\ cm^{-1}) \qquad (\square\ 2187\ cm^{-1})$$
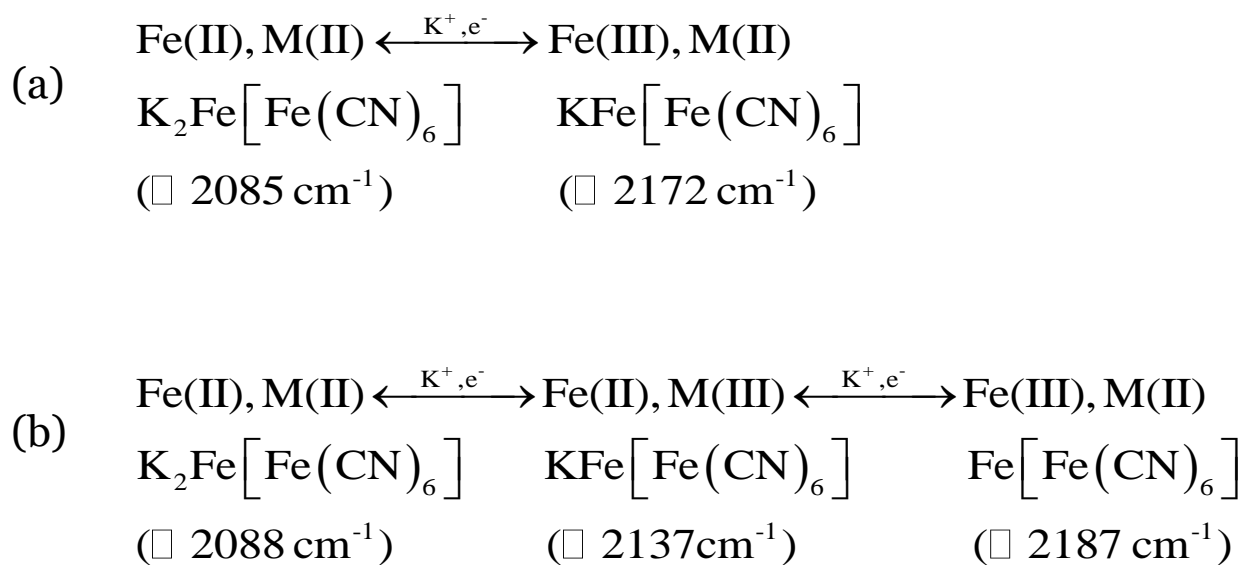
Scheme 3.1: Electron relay pathway for the charge-transfer complexes formed by the (a) solution dip and (b) metal-catalyzed methods for PB formation. Scheme modified from ref 16.

The PG electrode CVs and highlights on their peak potential regions are shown in Fig. 3.11 (and Fig. S3.8 for the treated graphite rod@PBNP). For example, the pristine electrode had ΔEp of 194 ± 23 mV and 59 ± 2 mV for the treated PG. The treated PG- PBNP-2×dipped rose to 75 ± 1 mV, then dropped after subsequent dips (Table 3.2).
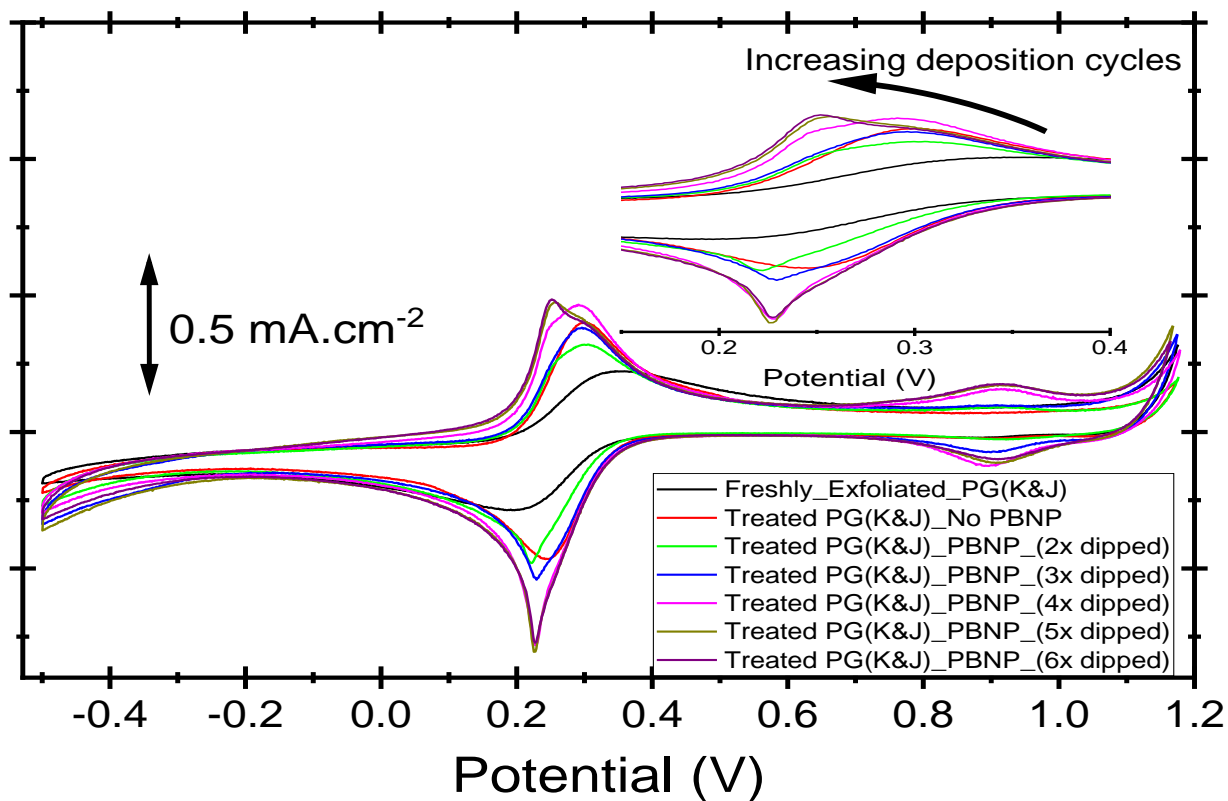
Figure 3.11: The CV in 1M KCl of freshly exfoliated, treated PG(K&J) and treated PG(K&J)-PBNP at various dipping cycles of the synthesis reagents. Insert is the magnification of the area around the cathodic and anodic peak potentials.

Table 3.2: Cyclic voltammetry of Pristine PG, Treated PG and Treated PG-PBNP at various deposition cycles of PBNP on the Treated PG (n = 3).

Electrode	ΔEp (mV) @ ν = 0.05 V/s
Freshly exfoliated PG	194±23
Treated PG (no PBNP)	59±2
Treated PG - PBNP_(2x dipped)	75±1
Treated PG - PBNP_(3x dipped)	66±1
Treated PG - PBNP_(4x dipped)	61±2
Treated PG - PBNP_(5x dipped)	28±3
Treated PG - PBNP_(6x dipped)	22±2

The ΔEp increase (slow kinetics) before a decrease highlights the poor conductivity of PB [34], mainly because of large interstitial voids [4], coordination of the metals to water [71], and/or even defect or disordered valences [69]. However, since further PB formation and deposition cycles decreased the ΔEp, it implies that the formed PB have very little or no defect valences [36] so that further stacking of the PB zeolite structures resulted in coordinated and interacting structures with sufficient conductivities to decrease the ΔEp. This inference is supported by the work that suggests that zeolite-like PB with soluble K^+ (for example, as seen from our EDS results; Fig. 3.1 inserts and S2) usually results in less defective PB with large crystallite sizes [69] (as seen, for example, from our SEM; Figs. 3.1 and the XPS Fe^{2+}/Fe^{3+} which suggests less defective PB) and less water within its lattices [29]. This could account for the apparent lack of ν(OH) in the PBNP@graphite IR spectra (Figs. 3.3 and S3.3). The K^+ located inside the lattice cavities [71] serves as a PB coordinating unit, increasing the PB conductivity on the graphites. For comparison, the two-solution dip method is more than 5 times more efficient than a similar synthetic path to deposit PB on porous alumina [72]. The PBNP@treated PGs and PBNP@treated graphite rods have comparable electrochemistry to PB on Pt [70] or Au [73,74], making the PBNP@treated graphites cheap and commercially feasible alternatives to these other expensive ones. These findings are important to sensing, ion selectivity for capture/release systems, energy storage and conversion systems.

Metal-Catalyzed PBNP on Graphite

The PB CVs from the metal catalyzed and solution dip methods have similar electrochemistry at the same synthesis cycles (see, for example, Fig. 3.10). This suggests that about the same cation and anion concentrations were involved at every stage of both PB synthetic pathways. A common route for free or liberated iron in solution would be Fe^{3+} from ferri-cyanide solution decomposition [75]. However, this pathway cannot account for the PB formation since no PB formed by either soaking the graphites in $Fe(CN)_6^{3-/4-}$ or by running CVs of these electrodes in $Fe(CN)_6^{3-/4-}$. It is postulated that a closed electrochemical circuit is formed between the graphite, 1mM $Fe(CN)_6^{3-/4-}$ (1 M KCl) and the stainless steel (all three components being congruous at the instance of PB formation). The stainless steel is lower on the galvanic or electropotential series to the graphite and would serve as the anode in this galvanic circuit. In this circuit, the graphite (cathode) loses electrons en route to the anode. However, the electrolyte captures these electrons, disrupting the octahedral structure of the $Fe(CN)_6^{3-/4-}$ to liberate Fe^{3+}. The liberated Fe^{3+} is immediately reduced to Fe^{2+} by more in-streaming electrons from the graphite. The Fe^{2+} then reacts with the $Fe(CN)_6^{3-/4-}$, closing the vertices or "capping" the octahedral structure of the $Fe(CN)_6^{3-/4-}$ to form PB (Scheme 3.2).
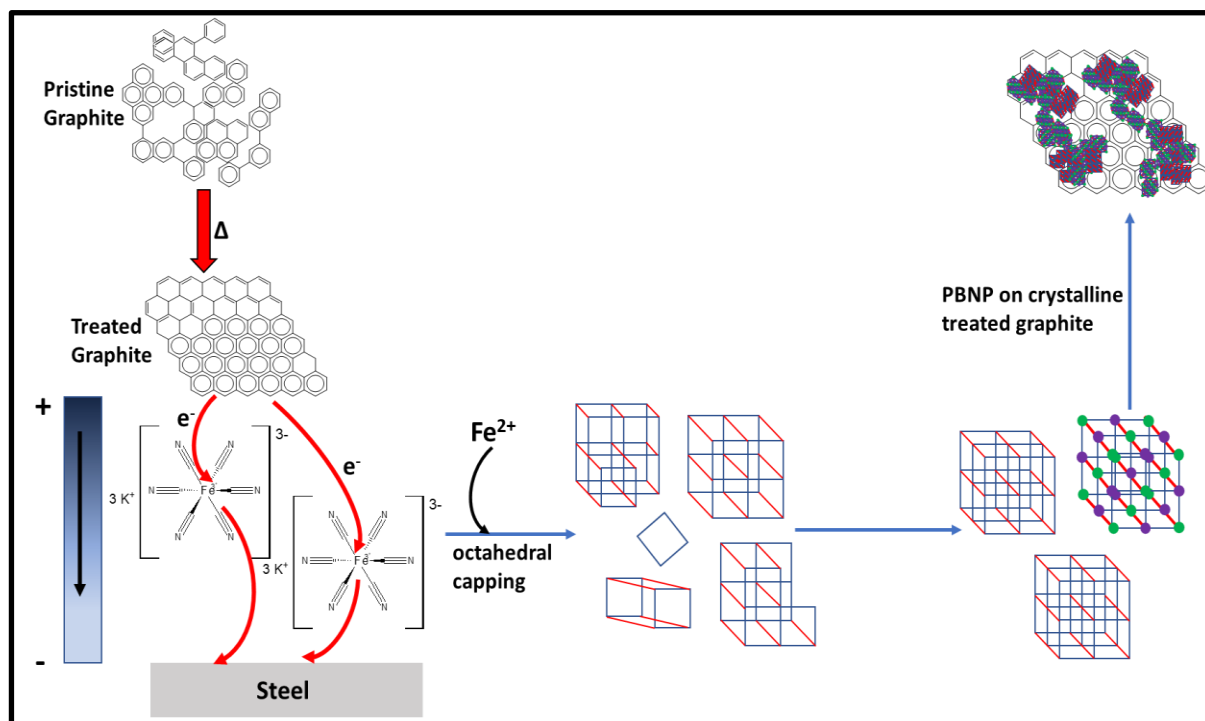
Scheme 3.2: Depiction of the mechanism of PB formation from a galvanic series-based circuit formed by the $Fe(CN)_6^{3-/4-}$, graphite and steel.

Conclusion

Since most porous carbon materials are generally brittle [44], and even more so after thermal or acid activation [39–41], the PBNP@treated graphite composites is not commonly reported. The present work shows highly porous and stable PBNP composited on thermally-treated and activated graphite materials. These PBNP on fully-activated, high surface area graphite materials without compromise to their structural and functional integrity, meet the demands for the next generation electronics, energy storage/conversion devices and biological scaffolds. These newly stable structure-function properties of PBNP on graphites are unlike carbon materials in general [44]. An important implication of the present work is that the synthesis method influences the intermediacy of electron travel in the M-CN-M′ charge transfer complex. Also, the substrate nature for PB deposition plays a critical role in the eventual chemistry of the PB and PB@substrate. The PBNP@treated graphite felts have a very competitive potential window, the highest capacitance in 1mM $Fe(CN)_6^{3-/4-}$ (1M KCl), remained stable for over 2100 cycles in 1M KCl solution, and its synthesis method some five times more efficient than a similarly reported method [72]. Moreover, these new synthesis methods are green, avoiding harsh or corrosive solvents and require no charge or voltage applications to achieve their synthesis. Also, these methods circumvent the traditionally required low pH phases for PB synthesis. Their electrochemistry suggests competitive material behavior for applications in aqueous-based energy storage and conversion devices.

The current findings highlight carbon materials, with structural and functional integrity, and low-cost, for energy storage/conversion devices such as, in this case, aqueous-based supercapacitors, batteries and fuel cells. Also, the PBNP@treated carbon felt capacitance increases, relative to the bare thermally-treated felt itself, make these composites practical for ion selectivity in capture/release systems. The treated PG and graphite rod electrochemistry are now feasible substitutes not just for Au and Pt in electrochemical and electronic devices but also for potential Au-PBNP and Pt-PBNP replacements. Future work would explore PBNP@thermally-treated graphite applications for sensors and other applications commonly associated with Au- and Pt-PBNP composite electrodes.

Notes

The authors declare no conflict of interest.

Electronic Supporting Material

Supplementary material (More SEM micrographs of PBNP@pristine and thermally treated graphite; EDS of PBNP@pristine GFA3 and on thermally treated pyrolytic graphite; FTIR of PBNP@pristine GFA3; Raman spectra of PBNP@thermally treated pyrolytic graphite; XPS spectra of PBNP@thermally treated pyrolytic graphite and PBNP@thermally treated GFA3 from the metal-catalyzed PBNP scheme; UPS data of PBNP@thermally treated pyrolytic graphite; CV of PBNP@pristine GFA3 and PBNP@thermally treated graphite rod) is available in the online version of this article at http: //dx.doi.org/10.1007/*********************).

References

[1]   Koshiyama, T.; Tanaka, M.; Honjo, M.; Fukunaga, Y.; Okamura, T.; Ohba, M. Direct Synthesis of Prussian Blue Nanoparticles in Liposomes Incorporating Natural Ion Channels for Cs + Adsorption and Particle Size Control. Langmuir 2018, 34, 1666–1672.

[2]   Cvrtila, I.; Stilinovic, V. New Tricks by Old Anions: Hydrogen Bonded Hexacyanoferrous Anionic Networks. Cryst. Growth Des. 2017, 17, 6793–6800.

[3]   Karyakin, A. Chemical and Biological Sensors Based on Electroactive Inorganic Polycrystals. In Electrochemical Sensors, Biosensors and their Biomedical Applications; Zhang, X., Ju, H.,Wang, J. (Eds), Elsevier Inc. 2008, pp. 411-439.

[4]   Morant-Giner, M.; Sanchis-Gual, R.; Romero, J.; Alberola, A.; García-Cruz, L.; Agouram, S.; Galbiati, M.; Padial, N. M.; Waerenborgh, J. C.; Martí-Gastaldo, C.; et al. Prussian Blue@MoS2Layer Composites as Highly Efficient Cathodes for Sodium- and Potassium-Ion Batteries. Adv. Funct. Mater. 2018, 28, 1706125.

[5]   Buser, H. J.; Ludi, A.; Schwarzenbach, D.; Petter, W. The Crystal Structure of Prussian Blue: Fe4[Fe(CN)6]3·xH2O. Inorg. Chem. 1977, 16, 2704–2710.

[6]   Pyrasch, M.; Toutianoush, A.; Jin, W.; Schnepf, J.; Tieke, B. Self-Assembled Films of Prussian Blue and Analogues: Optical and Electrochemical Properties and Application as Ion-Sieving Membranes. Chem. Mater. 2003, 15, 245–254.

[7]   Chen, R.; Tanaka, H.; Kawamoto, T.; Asai, M.; Fukushima, C.; Kurihara, M.; Ishizaki, M.; Watanabe, M.; Arisaka, M.; Nankawa, T. Thermodynamics and Mechanism Studies on Electrochemical Removal of Cesium Ions from Aqueous Solution Using a Nanoparticle Film of Copper Hexacyanoferrate. ACS Appl. Mater. Interfaces 2013, 5, 12984–12990.

[8]   Thammawong, C.; Opaprakasit, P.; Tangboriboonrat, P.; Sreearunothai, P. Prussian Blue-Coated Magnetic Nanoparticles for Removal of Cesium from Contaminated Environment. J. Nanoparticle Res. 2013, 15,1689.

[9]   Catala, L.; Mallah, T. Nanoparticles of Prussian Blue Analogs and Related Coordination Polymers: From Information Storage to Biomedical Applications. Coordination Chemistry Reviews. 2017, 346, 32-61.

[10]   Vipin, A. K.; Fugetsu, B.; Sakata, I.; Isogai, A.; Endo, M.; Li, M.; Dresselhaus, M. S. Cellulose Nanofiber Backboned Prussian Blue Nanoparticles as Powerful Adsorbents for the Selective Elimination of Radioactive Cesium. Sci. Rep. 2016, 6, 37009.

[11]   Jang, S.-C.; Hong, S.-B.; Yang, H.-M.; Lee, K.-W.; Moon, J.-K.; Seo, B.-K.; Huh, Y.; Roh, C. Removal of Radioactive Cesium Using Prussian Blue Magnetic Nanoparticles. Nanomaterials 2014, 4, 894–901.

[12]   Qin, Z.; Li, Y.; Gu, N. Progress in Applications of Prussian Blue Nanoparticles in Biomedicine. Adv. Healthc. Mater. 2018, 7, 1800347.

[13]   DeLongchamp., D. M.; Hammond, P. T. High-Contrast Electrochromism and Controllable Dissolution of Assembled Prussian Blue/Polymer Nanocomposites. Adv. Funct. Mater. 2004, 14, 224-232.

[14]   Schmidt, D. J.; Cebeci, F. Ç.; Kalcioglu, Z. I.; Wyman, S. G.; Ortiz, C.; Van Vliet, K. J.; Hammond, P. T. Electrochemically Controlled Swelling and Mechanical Properties of a Polymer Nanocomposite. ACS Nano 2009, 3, 2207–2216.

[15]   Wood, K. C.; Zacharia, N. S.; Schmidt, D. J.; Wrightman, S. N.; Andaya, B. J.; Hammond, P. T. Electroactive Controlled Release Thin Films. Proc. Natl. Acad. Sci. 2008, 105, 2280-2285.

[16]   De Tacconi, N. R.; Rajeshwar, K.; Lezna, R. O. Metal Hexacyanoferrates: Electrosynthesis, in Situ Characterization, and Applications. Chemistry of Materials. 2003, 15, 3046–3062.

[17]   Wang, H.; Huang, Y. Prussian-Blue-Modified Iron Oxide Magnetic Nanoparticles as Effective Peroxidase-like Catalysts to Degrade Methylene Blue with H2O2. J. Hazard. Mater. 2011, 191, 163-169.

[18]   Haghighi, B.; Hamidi, H.; Gorton, L. Electrochemical Behavior and Application of Prussian Blue Nanoparticle Modified Graphite Electrode. Sensors Actuators, B Chem. 2010, 147, 270-276.

[19]   Peng, X.; Wang, R.; Wang, T.; Yang, W.; Wang, H.; Gu, W.; Ye, L. Carbon Dots/Prussian Blue Satellite/Core Nanocomposites for Optical Imaging and Photothermal Therapy. ACS Appl. Mater. Interfaces 2018, 10, 1084–1092.

[20]   Zhou, J.; Li, M.; Hou, Y.; Luo, Z.; Chen, Q.; Cao, H.; Huo, R.; Xue, C.; Sutrisno, L.; Hao, L.; et al. Engineering of a Nanosized Biocatalyst for Combined Tumor Starvation and Low-Temperature Photothermal Therapy. ACS Nano 2018, 12, 2858–2872.

[21]   Fu, G.; Liu, W.; Li, Y.; Jin, Y.; Jiang, L.; Liang, X.; Feng, S.; Dai, Z. Magnetic Prussian Blue Nanoparticles for Targeted Photothermal Therapy under Magnetic Resonance Imaging Guidance. Bioconjug. Chem. 2014, 25, 1655–1663.

[22]   Kim, T.; Lemaster, J. E.; Chen, F.; Li, J.; Jokerst, J. V. Photoacoustic Imaging of Human Mesenchymal Stem Cells Labeled with Prussian Blue–Poly(L-Lysine) Nanocomplexes. ACS Nano 2017, 11, 9022–9032.

[23]   Zakaria, M. B.; Chikyow, T. Recent Advances in Prussian Blue and Prussian Blue Analogues: Synthesis and Thermal Treatments. Coordination Chemistry Reviews. 2017, 352, 328-345.

[24]   Patra, C. R. Prussian Blue Nanoparticles and Their Analogues for Application to Cancer Theranostics. Nanomedicine (Lond.). 2016, 11, 569-572.

[25]   Zhou, B.; Jiang, B. P.; Sun, W.; Wei, F. M.; He, Y.; Liang, H.; Shen, X. C. Water-Dispersible Prussian Blue Hyaluronic Acid Nanocubes with Near-Infrared Photoinduced Singlet Oxygen Production and Photothermal Activities for Cancer Theranostics. ACS Appl. Mater. Interfaces 2018, 10, 18036–18049.

[26]   Peng, Y.; Li, B.; Wang, Y.; He, X.; Huang, J.; Zhao, J. Prussian Blue: A Potential Material to Improve the Electrochemical Performance of Lithium-Sulfur Batteries. ACS Appl. Mater. Interfaces 2017, 9, 4397–4403.

[27]   Ji, Z.; Han, B.; Liang, H.; Zhou, C.; Gao, Q.; Xia, K.; Wu, J. On the Mechanism of the Improved Operation Voltage of Rhombohedral Nickel Hexacyanoferrate as Cathodes for Sodium-Ion Batteries. ACS Appl. Mater. Interfaces 2016, 8, 33619–33625.

[28]   Zhang, C.; Xu, Y.; Zhou, M.; Liang, L.; Dong, H.; Wu, M.; Yang, Y.; Lei, Y. Potassium Prussian Blue Nanoparticles: A Low-Cost Cathode Material for Potassium-Ion Batteries. Adv. Funct. Mater. 2017, 27, 1604307.

[29]   Qian, J.; Wu, C.; Cao, Y.; Ma, Z.; Huang, Y.; Ai, X.; Yang, H. Prussian Blue Cathode Materials for Sodium-Ion Batteries and Other Ion Batteries. Advanced Energy Materials. 2018, 8, 1702619.

[30]   Zhao, F.; Wang, Y.; Xu, X.; Liu, Y.; Song, R.; Lu, G.; Li, Y. Cobalt Hexacyanoferrate Nanoparticles as a High-Rate and Ultra-Stable Supercapacitor Electrode Material. ACS Appl. Mater. Interfaces 2014, 6, 11007–11012.

[31]   Zhang, M.; Hou, C.; Halder, A.; Ulstrup, J.; Chi, Q. Interlocked Graphene–Prussian Blue Hybrid Composites Enable Multifunctional Electrochemical Applications. Biosens. Bioelectron. 2017, 89, 570-577.

[32]   Wang, X.; Zou, L.; Fu, H.; Xiong, Y.; Tao, Z.; Zheng, J.; Li, X. Noble Metal-Free Oxygen Reduction Reaction Catalysts Derived from Prussian Blue Nanocrystals Dispersed in Polyaniline. ACS Appl. Mater. Interfaces 2016, 8, 8436–8444.

[33]   Murase, R.; Leong, C. F.; D'Alessandro, D. M. Mixed Valency as a Strategy for Achieving Charge Delocalization in Semiconducting and Conducting Framework Materials. Inorganic Chemistry. 2017, 56,14373–14382.

[34]   Bocharova, V.; Gorodyska, G.; Kiriy, A.; Stamm, M.; Simon, P.; Mönch, I.; Elefant, D.; Lou, X.; Stoffelbach, F.; Detrembleur, C.; et al. Synthesis and Deposition of Water-Dispersed Prussian Blue Nanocrystals on Polymers and CNTs. In: Grundke K., Stamm M., Adler HJ. (eds) Characterization of Polymer Surfaces and Thin Films. Prog. Colloid Polym. Sci. 2006, 132, 161-167.

[35]   Xu, Y.; Zheng, S.; Tang, H.; Guo, X.; Xue, H.; Pang, H. Prussian Blue and Its Derivatives as Electrode Materials for Electrochemical Energy Storage. Energy Storage Materials. 2017, 9, 11-30.

[36]   Wu, X.; Luo, Y.; Sun, M.; Qian, J.; Cao, Y.; Ai, X.; Yang, H. Low-Defect Prussian Blue Nanocubes as High Capacity and Long Life Cathodes for Aqueous Na-Ion Batteries. Nano Energy 2015, 13, 117-123.

[37]   Ni, N.; Barg, S.; Garcia-Tunon, E.; MacUl Perez, F.; Miranda, M.; Lu, C.; Mattevi, C.; Saiz, E. Understanding Mechanical Response of Elastomeric Graphene Networks. Sci. Rep. 2015, 5, 13712.

[38]   Qiu, L.; Liu, J. Z.; Chang, S. L. Y.; Wu, Y.; Li, D. Biomimetic Superelastic Graphene-Based Cellular Monoliths. Nat. Commun. 2012, 3, 1241.

[39]   Sun, B.; Skyllas-Kazakos, M. Chemical Modification and Electrochemical Behaviour of Graphite Fibre in Acidic Vanadium Solution. Electrochim. Acta 1991, 36, 513-517.

[40]   Pupkevich, V.; Glibin, V.; Karamanev, D. The Effect of Activation on the Electrochemical Behaviour of Graphite Felt towards the Fe3+/Fe2+ Redox Electrode Reaction. Electrochem. commun. 2007, 9, 1924-1930.

[41]   Sun, B.; Skyllas-Kazacos, M. Modification of Graphite Electrode Materials for Vanadium Redox Flow Battery Application—I. Thermal Treatment. Electrochim. Acta 1992, 37, 1253-1260.

[42]	Trogadas, P.; Taiwo, O. O.; Tjaden, B.; Neville, T. P.; Yun, S.; Parrondo, J.; Ramani, V.; Coppens, M. O.; Brett, D. J. L.; Shearing, P. R. X-Ray Micro-Tomography as a Diagnostic Tool for the Electrode Degradation in Vanadium Redox Flow Batteries. Electrochem. commun. 2014, 48, 155-159.

[43]	Lim, T. H.; Yeo, S. Y. Investigation of the Degradation of Pitch-Based Carbon Fibers Properties upon Insufficient or Excess Thermal Treatment. Sci. Rep. 2017, 7, 4733.

[44]	Gogotsi, Y. High-Temperature Rubber Made from Carbon Nanotubes. Science. 2010, 330, 1332-1333.

[45]	Nwamba, O.C., Echeverria, E., McIlroy, D., Austin, A., Shreeve, J.M.S. and Aston, D. E. Thermal Modification of Graphite for Fast Electron Transport and Increased Capacitance. ACS Appl. Nano Mater. 2018, DOI: 10.1021/acsanm.8b01887.

[46]	Bustos, E.; Manríquez, J.; Orozco, G.; Godínez, L. A. Preparation, Characterization, and Electrocatalytic Activity of Surface Anchored, Prussian Blue Containing Starburst PAMAM Dendrimers on Gold Electrodes. Langmuir 2005, 21, 3013–3021.

[47]	Qiu, J. D.; Peng, H. Z.; Liang, R. P.; Li, J.; Xia, X. H. Synthesis, Characterization, and Immobilization of Prussian Blue-Modified Au Nanoparticles: Application to Electrocatalytic Reduction of H2O2. Langmuir 2007, 23, 2133–2137.

[48]	Dacarro, G.; Taglietti, A.; Pallavicini, P. Prussian Blue Nanoparticles as a Versatile Photothermal Tool. Molecules 2018, 23, 1–20.

[49]	Nie, P.; Shen, L.; Pang, G.; Zhu, Y.; Xu, G.; Qing, Y.; Dou, H.; Zhang, X. Flexible Metal-Organic Frameworks as Superior Cathodes for Rechargeable Sodium-Ion Batteries. J. Mater. Chem. A 2015, 3, 16590-16597.

[50]	Sato, O.; Einaga, Y.; Fujishima, A.; Hashimoto, K. Photoinduced Long-Range Magnetic Ordering of a Cobalt−Iron Cyanide. Inorg. Chem. 1999, 38, 4405–4412.

[51]	Liu, D.; Lv, Y.; Zhang, M.; Liu, Y.; Zhu, Y.; Zong, R.; Zhu, Y. Defect-Related Photoluminescence and Photocatalytic Properties of Porous ZnO Nanosheets. J. Mater. Chem. A 2014, 2, 15377-15388.

[52]	Xia, L.; McCreery, R. L. Structure and Function of Ferricyanide in the Formation of Chromate Conversion Coatings on Aluminum Aircraft Alloy. J. Electrochem. Soc. 1999, 146, 3696-3701.

[53]   Smith, E.; Dent, G. Modern Raman Spectroscopy - A Practical Approach; John Wiley & Sons, Ltd. 2005.

[54]   Verón, M. G.; Castañeda Trujillo, L. D.; Piro, O. E.; Güida, J. A. Infrared and Raman Spectra of [Re(CN)5NO]3- Complex Isolated in KCl Matrix. J. Mol. Struct. 2014, 1076, 160-164.

[55]   Suffren, Y.; Rollet, F.-G.; Reber, C. Raman Spectroscopy of Transition Metal Complexes: Molecular Vibrational Frequencies, Phase Transitions, Isomers, and Electronic Structures. Comments Inorg. Chem. 2011, 32, 246-276.

[56]   Lee, C.; Yan, H.; Brus, L. E.; Heinz, T. F.; Hone, J.; Ryu, S. Anomalous Lattice Vibrations of Single- and Few-Layer MoS2. ACS Nano 2010, 4, 2695–2700.

[57]   Yan, R.; Simpson, J. R.; Bertolazzi, S.; Brivio, J.; Watson, M.; Wu, X.; Kis, A.; Luo, T.; Hight Walker, A. R.; Xing, H. G. Thermal Conductivity of Monolayer Molybdenum Disulfide Obtained from Temperature-Dependent Raman Spectroscopy. ACS Nano 2014, 8, 986–993.

[58]   Yang, D.; Sandoval, S. J.; Divigalpitiya, W. M. R.; Irwin, J. C.; Frindt, R. F. Structure of Single-Molecular-Layer MoS2. Phys. Rev. B 1991, 43, 12053.

[59]   Verble, J. L.; Wieting, T. J. Lattice Mode Degeneracy in MoS2 and Other Layer Compounds. Phys. Rev. Lett. 1970, 25, 362.

[60]   Mattson, E. C.; Michalak, D. J.; Veyan, J. F.; Chabal, Y. J. Cobalt and Iron Segregation and Nitride Formation from Nitrogen Plasma Treatment of CoFeB Surfaces. J. Chem. Phys. 2017, 146, 052805.

[61]   Naslusov, V. A.; Kondratenko, A. V.; Neyman, K. M.; Mazalov, L. N. An SCF XαSW Study of the Electronic Structure and X-Ray and Photoelectron Spectra of Fe(II) and Fe(III) Hexacyano Complexes in a Cluster Approach. Theor. Chim. Acta 1986, 70, 429–441.

[62]   Cataldi, T. R. I.; Salvi, A. M.; Centonze, D.; Sabbatini, L. Voltammetric and XPS Investigations of Polynuclear Ruthenium-Containing Cyanometallate Film Electrodes. J. Electroanal. Chem. 1996, 406, 91-99.

[63]   Joachim, C.; Gimzewski, J. K.; Aviram, A. Electronics Using Hybrid-Molecular and Mono-Molecular Devices. Nature. 2000, 408, 541–548.

[64]   Verkhovtsev, A. V.; Schramm, S.; Solov'Yov, A. V. Molecular Dynamics Study of the Stability of a Carbon Nanotube atop a Catalytic Nanoparticle. Eur. Phys. J. D 2014, 68, 246.

[65]   Solov'yov, I. A.; Mathew, M.; Solov'Yov, A. V.; Greiner, W. Liquid Surface Model for Carbon Nanotube Energetics. Phys. Rev. E - Stat. Nonlinear, Soft Matter Phys. 2008, 78, 051601.

[66]   Norris, D.; Bawendi, M. Measurement and Assignment of the Size-Dependent Optical Spectrum in CdSe Quantum Dots. Phys. Rev. B - Condens. Matter Mater. Phys. 1996, 53, 16338.

[67]   Hubbard, J. Electron Correlations in Narrow Energy Bands. Proc. R. Soc. A Math. Phys. Eng. Sci. 1963, 276, 238–257.

[68]   Essler, F. H. L.; Frahm, H.; Göhmann, F.; Klümper, A.; Korepin, V. E. The One-Dimensional Hubbard Model; Cambridge University Press; 2005.

[69]   Samain, L.; Grandjean, F.; Long, G. J.; Martinetto, P.; Bordet, P.; Strivay, D. Relationship between the Synthesis of Prussian Blue Pigments, Their Color, Physical Properties, and Their Behavior in Paint Layers. J. Phys. Chem. C 2013, 117, 9693–9712.

[70]   Han, L.; Tricard, S.; Fang, J.; Zhao, J.; Shen, W. Prussian Blue @ Platinum Nanoparticles/Graphite Felt Nanocomposite Electrodes: Application as Hydrogen Peroxide Sensor. Biosens. Bioelectron. 2013, 43, 120-124.

[71]   Yang, Y.; Liu, E.; Yan, X.; Ma, C.; Wen, W.; Liao, X.-Z.; Ma, Z.-F. Influence of Structural Imperfection on Electrochemical Behavior of Prussian Blue Cathode Materials for Sodium Ion Batteries. J. Electrochem. Soc. 2016, 163, A2117-A2123.

[72]   Johansson, A.; Widenkvist, E.; Lu, J.; Boman, M.; Jansson, U. Fabrication of High-Aspect-Ratio Prussian Blue Nanotubes Using a Porous Alumina Template. Nano Lett. 2005, 5, 1603–1606.

[73]   Pingarrón, J. M.; Yáñez-Sedeño, P.; González-Cortés, A. Gold Nanoparticle-Based Electrochemical Biosensors. Electrochim. Acta 2008, 53, 5848-5866.

[74]   Bishop, G. W.; Ahiadu, B. K.; Smith, J. L.; Patterson, J. D. Use of Redox Probes for Characterization of Layer-by-Layer Gold Nanoparticle-Modified Screen-Printed Carbon Electrodes. J. Electrochem. Soc. 2017, 164, B23-B28.

[75]   Kolthoff, I. M.; Pearson, E. A. Stability of Potassium Ferrocyanide Solutions. Ind. Eng. Chem. - Anal. Ed. 1931, 3, 381–382.

Chapter 4: Increased Electron Transfer Kinetics and Thermally Treated Graphite Stability through Improved Tunneling Paths
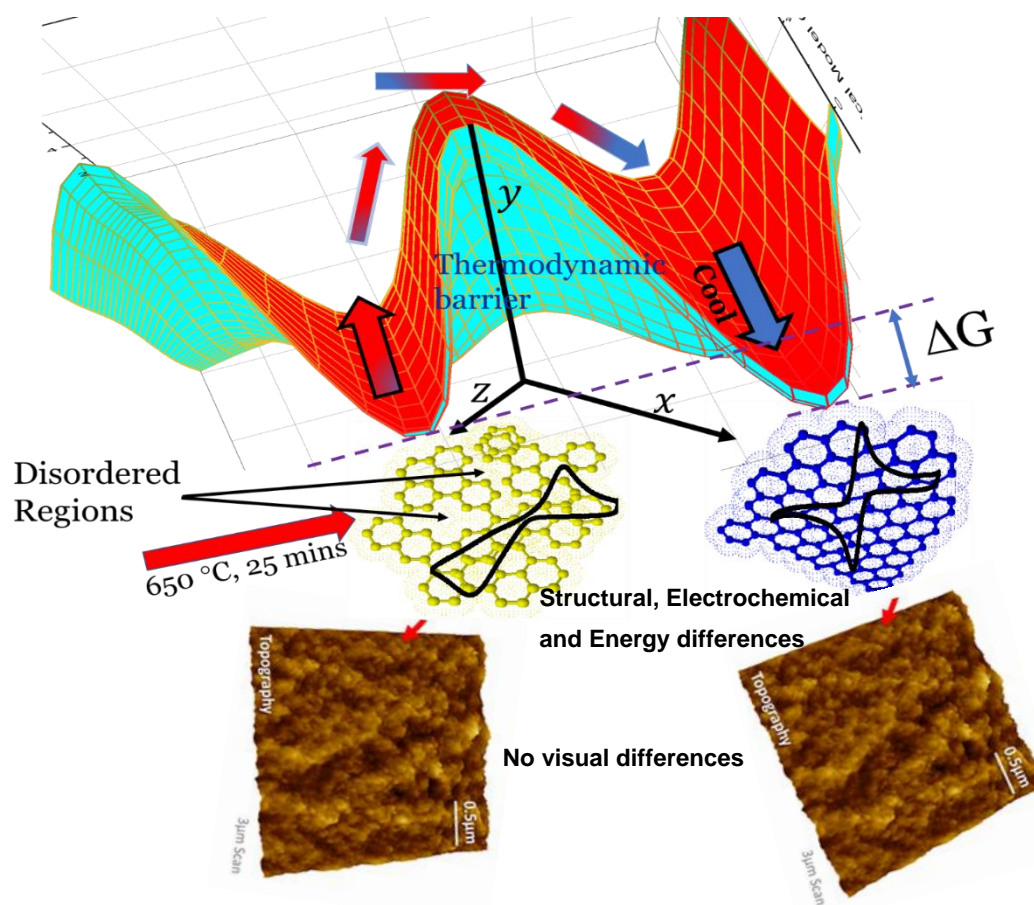
TOC/Abstract Graphic: Thermal treatment transforms the pristine graphite to a structure with well-ordered lattices. AFM Images show no visual differences between the pristine and thermally treated graphite even though their electronic structures and resultant electrochemistry are different. Despite minimal energy differences between both structures, a large thermodynamic barrier hinders the backward movement of the treated to the pristine-like state.

Abstract

A Thermal treatment protocol reportedly increased and sustained the heterogeneous electron transfer (HET) kinetics of graphites by at least nine weeks. To investigate the consequences of such HET increases on graphite stabilities, Raman 2D peak evolution show ordered graphene stacking in flexible samples of the treated and pristine samples. However, thermal treatment was necessary to activate properties, previously thought unique to ordered 2D materials only. Potential window values of the treated increased over the pristine. However, edges on basal planes of flexible sheets lowered the potential window values and increased ion intercalation stages of the treated over the pristine. The EIS results suggest two de-coupled kinetic steps for electron transfer in the treated PG: a slow surface-dependent step and a fast step, which is independent of the electrode-surface/electrolyte interactions. Yet, both graphite sets have similar corrosion kinetics and mechanisms in 0.10 M Na_2SO_4. TGA analysis show that five of the six graphites investigated were more structural stable for the treated to their pristine. The UPS data show no differences in work functions, suggesting similarities in potential energy barriers for both sets. The electronic band structure suggests increased crystallinity of the treated to the pristine via increased $\square$ to $\square$ transitions. Structure-induced electronic changes are suggested to trigger improved tunneling paths through the interfaces (fast step) from the bulk layer; thus, improving (and sustaining) HET kinetics by orders of magnitude. Conclusively, the thermal treatment protocol reported herein increased HET kinetics without compromises to their electrochemical, structural and corrosion stabilities. In fact, in most instances, these properties improved over the pristine graphites.

Keywords: Thermal treatment, graphites, aging, fast (HET) kinetics, quantum tunneling, structures, charge transfer resistance.

Introduction

For over a half century, active researches in the carbon field have sought to know why and how carbon materials, especially graphite, become sluggish electron transporters on air exposure, sometimes within minutes to hours. Several techniques have been employed to restore the heterogeneous electron transfer (HET) kinetics of carbonaceous materials after air- or solution-induced oxidation (viz., aging). Such procedures include mechanical polishing as commonly employed on glassy carbon electrodes, vacuum heat treatment, or heat treatment under an inert gas atmosphere. Included, also, are combined treatments such as laser-based thermal treatment protocols, electrochemical polarization such as pre-anodization, and plasma activation protocols such as radio-frequency plasma, among many others.[1–3] In spite of attempts employed to date, the issue of aging remains a major limit on the use of carbon materials in many applications. Every activation protocol employed thus far has sustained HET kinetics by just a few hours at most.[1–3] The problem remained insoluble and largely neglected until the advent of graphene.

With graphene in the materials research race, the question arose again,[4] since graphene for electrochemistry and optoelectronics was also susceptible to air oxidation induced sluggish HET kinetics or aging. [5–8] HET kinetics are fundamental in solid carbon electrode-electrolyte interactions, determining the performance of materials in electrochemical applications,[9,10] and playing significant roles in molecular electronics, electrochemical energy storage/conversion, sensing, and electro-oxidative reactions.[5,11–19] The result is that even the purported "wonderful" applications of graphene have been questioned.[20]

In light of aging of carbon materials, their surfaces do not remain pristine even during a limited time span, especially for graphite, graphene, carbon nanotubes and fullerenes.[3,7,21,22] These carbon surfaces are gradually deactivated by adsorbing ubiquitous oxygen,[23–26] and hydrocarbon[7,8,21,27–29] species from ambient air and/or water.[30] These adsorbed species are claimed to hinder electron transfer across carbon surfaces to redox probes,[2] thus aging and hindering their functional uses.[4,15] It is this aging of carbon materials that makes Pt and Au very relevant in electrochemistry, electronics and the opto-electronic industries[31–38] by substituting for carbon materials in roles that should favor them. Carbon materials are more cost-effective compared to Au, Pt and other noble metals such as Ir.[39,40] In addition, carbon materials have wider potential windows than Au or Pt.[35,41–43] This potential window advantage is another reason that carbon materials are naturally preferential to the noble metals, for semi-conductor, electronics and electrochemical-related applications.

Graphite was reported to age in an inert nitrogen atmosphere, being no different electrochemically from graphite aged in air.[6] This finding rules out the concept of surface contaminants as culprits for aging and shifts attention away from the surface properties and to the electronics for some observed surface phenomena, such as water-contact angles,[44–46] which reportedly increase with aging in graphite and graphene.[7,8,21,47]

Recently, a thermal treatment protocol was reported to have tuned the electronics of eight different graphites from at least four different graphite families. [48] This electronic tuning increased by over two to three orders of magnitude in some cases and maintained the HET kinetics of these graphites for at least nine weeks. The protocol also boosted the capacitance of the graphite felts employed in the research. These results raise the question of the functional and structural stabilities of these treated materials. For example, faster electron transfer is associated with increased corrosion rates. [49–51] In order to investigate the consequences of these fast-HET kinetics on the electrochemical, structural and corrosion stabilities of the thermally-treated graphite, a consortium of techniques was employed to elucidate their stability profiles, and the reasons and mechanisms behind the observed patterns.

Results and Discussion

The graphite cyclic voltammograms (CVs) in 1mM $Fe(CN)_6^{3-/4-}$ and 1M H_2SO_4 for HET rates (k_0) and potential window determinations, respectively, are shown in Figures 4.1 and S4.1. The k_0 values determined using the Nicholson method,[52] and the potential window values (anodic and cathodic limits at 200 μA cm^{-2} onset for oxygen and hydrogen evolution respectively), are tabulated in Table 4.1. The potential window values of the treated pyrolytic graphite (PG) and artificial graphite decreased by about 0.2 V with a two-fold increase in k_0, compared to the pristine samples. These potential window decreases were mainly from the cathodic and anodic limits for the PG and artificial graphites, respectively (Table 4.1). The graphite (Equalseal) had nearly the same k_0 with a slight potential window increase of ca 0.60V for the treated over the pristine. The treated graphite rod showed k_0 increase of roughly an order of magnitude and potential window increase of ca 0.30 V over its pristine. The treated GFA3 k_0 decreased but its capacitance increased five-folds over its pristine (Figure S4.1b). It was thought that some magnitude increases in k_0 would result in a drastic decrease in stability of the treated materials.[50,51,53] However, this was not the case. To understand this somewhat unusual property of the thermally treated graphites, various spectroscopic and electrochemical techniques were employed to probe both the surface and sub-surface features of the treated and pristine graphites.
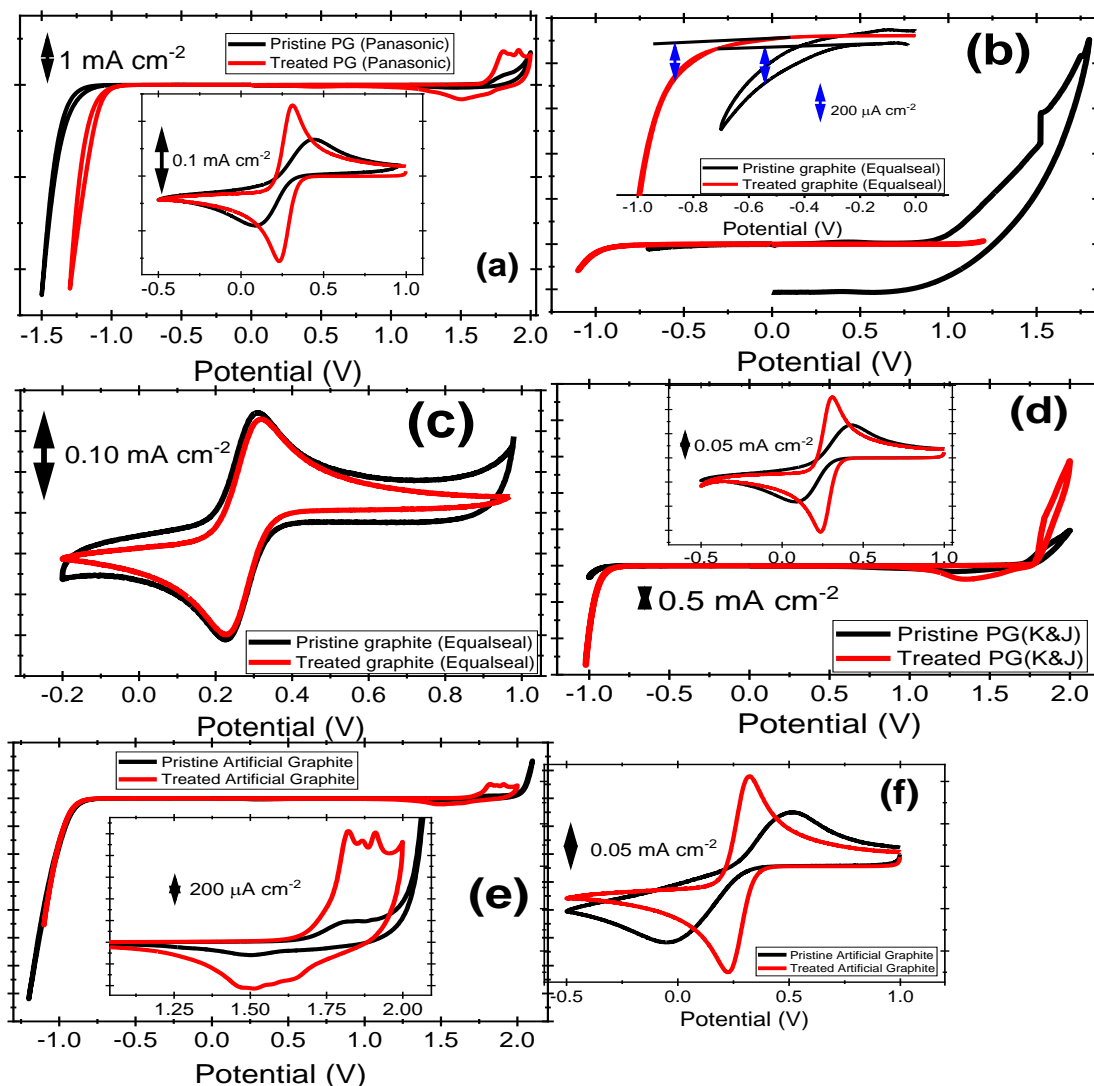
Figure 4.1: The potential windows in 1 M H_2SO_4 of pristine and treated (a) PG (Panasonic), (b) Graphite (Equalseal). Insert of (a) is their cyclic voltammograms (CVs) for HET determination in 1mM $Fe(CN)_6^{3-/4-}$ (1M KCl). Insert of (b) is the magnification of the cathodic region of the graphite (Equalseal) to highlight the decreased cathodic limit of the pristine to the treated material and to explain the extrapolation method employed for the determination of the on-set current at 200 $\mu A/cm^2$ for the hydrogen evolution reaction. (c) CV for HET determination for pristine and treated graphite. (d) The potential windows in 1 M H_2SO_4 of pristine and treated PG (K&J). Insert of (d) are their CVs. (e) The potential windows of pristine and treated artificial graphite. Insert is the magnification of the anodic arm to highlight the increased intercalation stages of the treated material at 200 $\mu A/cm^2$ on-set current for oxygen evolution. (f) The CV of pristine and treated artificial graphite. CVs for both potential window and HET determination were run at $\nu = 0.05$ V/s.

Table 4.1: ΔEp (mV) and accompanying rate constants[a], Cathodic and Anodic limits of the Potential Windows @ 200 µA/cm2 onset limit for Hydrogen and Oxygen evolution respectively. The Corrosion Current (i_o), Potentials (E_o) and Electron Work Function (Φ) of the Treated and Pristine Graphites.

Electrode	Type	ΔEp (mV)	k^0 (cm² s⁻¹)	@ 200 µA/cm² Cathode (V)	Anode (V)	Pot Win (V)	i_0 (A cm⁻²)	E_{corr} (mV)	EWF, Φ (eV)
PG (K&J)	C	300 ± 28	3.74±0.52E-04	-1.05 ± 0.16	1.84 ± 0.11	2.89 ± 0.05	1.65± 0.25E-09	32.45 ± 16.3	3.99±0.15
	T	68 ± 1	1.96E±0.24-02	-0.90 ± 0.01	1.80 ± 0.01	2.70 ± 0.003	4.51± 0.20E-09	3.20 ± 24.3	4.05±0.05
PG (Panasonic)	C	345 ± 46	3.07E±0.58-04	-1.19 ± 0.04	1.81 ± 0.02	3.00 ± 0.02	1.09± 0.12E-09	-136.40 ± 7.8	4.20±0.10
	T	66 ± 2	2.61E-02± (*)	-1.03 ± 0.01	1.75 ± 0.02	2.78 ± 0.01	6.78± 4.22E-10	-113.45 ± 55.7	4.08±0.004
Graphite (Equalseal)	C	80 ± 5	8.69±2.5E-03	-0.55 ± 0.07	0.80 ± 0.05	1.35 ± 0.02	2.47± 0.50E-08	-88.40 ± 2.3	2.28±1.16
	T	82 ± 6	7.60±2.6E-03	-0.83 ± 0.02	1.13 ± 0.04	1.96 ± 0.02	4.04± 2.23E-09	-78.20 ± 5.5	2.49±1.29
GFA3	C	213 ± 25	6.47±1.4E-04	-0.59 ± 0.09	1.15 ± 0.06	1.74 ± 0.03	5.38± 6.71E-07	-17.3 ± 30.1	3.78±0.28
	T	303 ± 29	3.68±0.52E-04	-0.77 ± 0.13	0.99 ± 0.06	1.76 ± 0.06	4.12± 2.96E-06	-186 ± 89	3.61±0.69
Graphite Rod	C	61 ± 1	0.13±0.04	-0.52 ± 0.05	0.82 ± 0.18	1.34 ± 0.12	5.31± 3.00E-08	-71.03 ± 25.2	3.29±0.58
	T	40 ± 1	1.021±0.04	-0.56 ± 0.08	0.83 ± 0.03	1.39 ± 0.05	4.17± 2.10E-08	-100.5 ± 0.7	3.63±0.13
Artificial Graphite	C	564 ± 22	1.64±0.08E-04	-0.83 ± 0.01	1.97 ± 0.04	2.80 ± 0.03	**	**	3.91±0.08
	T	69 ± 2	1.79±0.41E-02	-0.84 ± 0.02	1.76 ± 0.01	2.60 ± 0.004	**	**	3.98±0.01

(*) = 0.0261-0.0065 to 0.0261+0.0130

[a] k^0 [cm/s] in 1 mM Fe[(CN)$_6$]$^{3-/4-}$ and at v = 0.05 V/s. n = 3. C = Control; T = Treated

Raman spectroscopy probed three different layer levels of the graphite samples to discern how graphene layer stacking – via the 2D peak evolution – could lead to an understanding of the influence of monolayer graphene stacking on the electrochemistry of these materials. These electrochemical properties include differences in potential windows for reactions such as intercalation intensities and stages; and hydrogen and oxygen evolution capabilities of the pristine and treated samples. The Raman 2D peak changes from a one-peak to a four-peak band for single to bilayer graphene transition.[56–58] As the graphene layer increases to more than five sheets, the 2D spectrum becomes similar to that of bulk graphite, [57,58] which suggests anisotropy in the graphite 2D band.[57,59,60] A typical Raman 2D-graphite spectrum has two peaks,[58,61–64] consistent with that of multilayer graphene (greater than 5 layers), [57,58] and indicative of 3D ordering.[63,64]

The pristine PG (Panasonic) spectra show anisotropy for the three different levels probed: the surface spectrum is consistent with the double-structure of graphite,[58,61–64] while, the sub-surface and deep-layer spectra differ from each other and from that of the surface spectrum (Figure 2a).
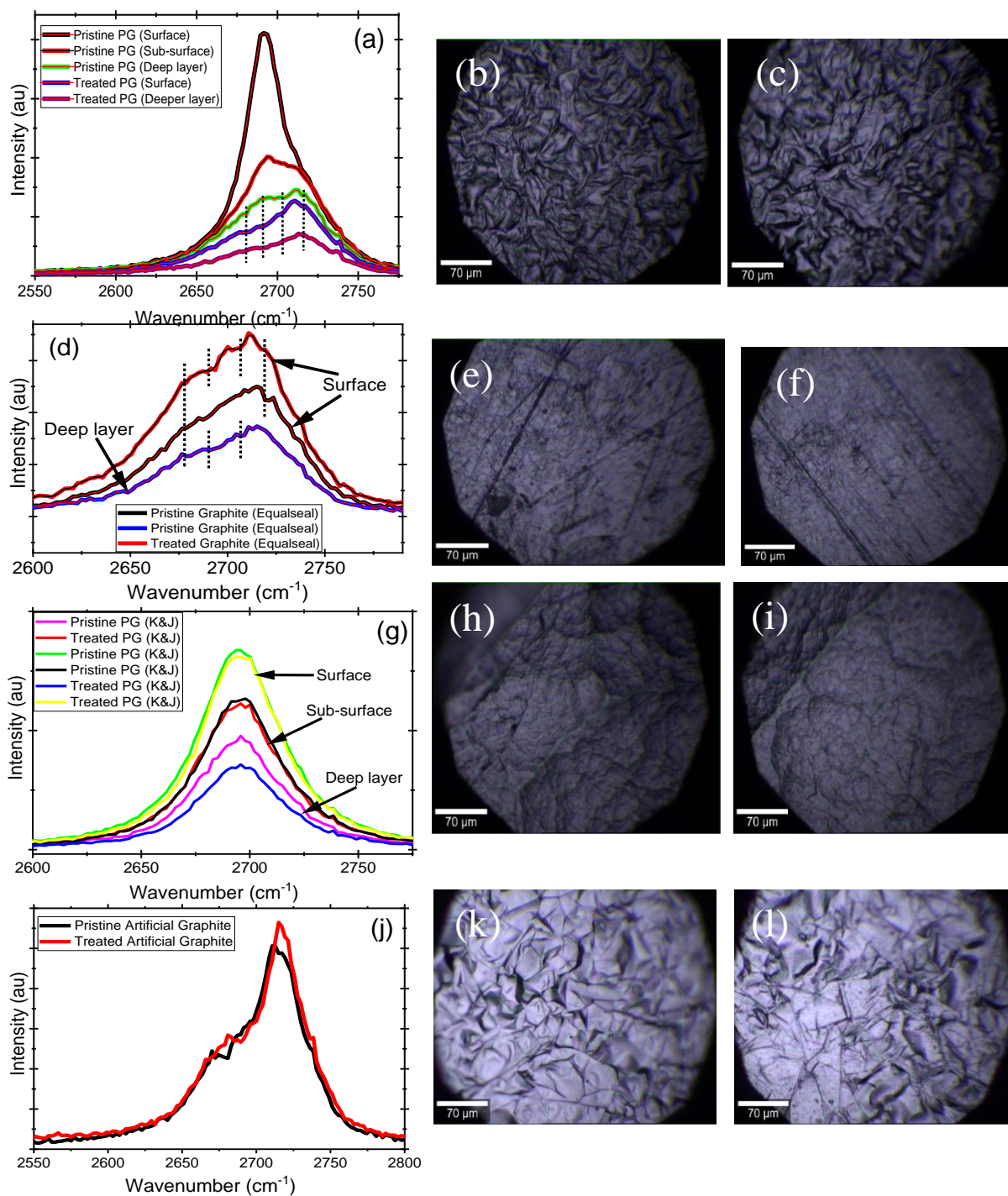
Figure 4.2: Raman spectra of the 2D band of pristine and treated (a) PG (Panasonic), (d) graphite (Equalseal), (g) PG (K&J) and (j) artificial graphite. Optical images respectively of pristine and treated (c, d) PG (Panasonic), (e, f) Graphite (Equalseal), (h, i) PG (K&J), and (k, l) artificial graphite.

This anisotropic property may arise from the laser power-dependent coupling to a distribution of layer sizes.[62] Thus, each layer responds in an anisotropic manner to the others in the same bulk material. The treated PG showed isotropism at the different depths probed (the sub-surface spectrum was not shown to reduce cluster) (Figure 4.2a). All three spectra have four peaks, similar to five to ten layer graphene, with $\lambda = 514$ nm.[57] For this work, $\lambda = 532.5$ nm was used. These results suggest that thermal treatment abolished the anisotropy reported for graphite so that the graphene layers were more orderly stacked, from the nano- to the macroscopic scale. Ordered graphene stacking,[65–69] and edge-density[70,71] may be responsible for the enhanced catalytic hydrogen evolution reaction (HER) of the treated over the pristine PG samples (Table 4.1). This is because bulk layer materials (e.g., MoS_2) with improper layer stacking display little HER activity,[72,73] but the 2D-layered MoS_2 has enhanced HER activity.[72,74,75] Well-ordered graphene sheet layering and enhanced HER activity of the treated PG are traits previously ascribed to 2D materials only.[76–78]

Here, isotropic Raman behavior of the 2D band is reported for graphite, which is unconventional for graphite, a 3D material. Additionally, the treated PG samples exhibited four-stage intercalation of H^+ into various graphene layers within their matrices in contrast to the one-stage intercalation of the pristine PG (Figure 2a). Higher ion intercalation stages and current densities are promising traits for metal-ion batteries.[77–81] In fact, well-ordered monolayer stacking in multilayered 2D-materials have some three-fold higher charge storage and rate capabilities to conventional graphites. [82] Therefore, it is suggested that well-ordered graphene stacking is responsible for this enhanced ion intercalation stages of the treated PG.[83] Based on the optical images (Figures 2b and 2c, respectively), no surface morphology differences exist to suggest that the observed electrochemistry of the treated PG is surface mediated. Thus, thermal treatment of the PG (Panasonic) brought about (a) electronic tuning (increased density of states (vibrational and electronic) and increased π to σ characteristics) of the material for fast and sustained HET kinetics as earlier reported;[48] (b) isotropic graphene sheet layering at all levels of the material; (c) increased HER; and (d) increase in the number of intercalation stages over those of the pristine materials.

The treated graphite (Equalseal) surface spectrum has four peaks, which are not present in the pristine surface spectrum and not even observed in the deep layer spectrum (Figure 2d). This finding indicates that the pristine graphite exhibits anisotropy while the treated graphite exhibits isotropism in the bulk material. Additionally, no visible morphological difference(s) exist (Figures 2e and 2f) to account for the increased potential window values of the treated over the pristine (Figure 1b and Table 1). The

anode (Figure 2b) and the CV in 1mM Fe (CN)$_6$$^{3-/4-}$ suggest that thermal treatment increased the overpotential for HER and OER of treated graphite (Equalseal) due to loss of active sites for these reactions:

Cathodic $\qquad$ $2H_2O + 2e^- \rightarrow H_2 + 2OH^-$ $\qquad\qquad\qquad\qquad$ (1)

Anodic $\qquad$ $4OH^- \rightarrow 2H_2O + O_2 + 4e^-$ $\qquad\qquad\qquad\qquad\qquad$ (2)

These two reactions are site specific for adsorption of water ($2H_2O$) and OH^- species. Surface defects are potential sites for adsorption of these species. Here, such sites are edges of graphites (edge defects), carbon vacancies (point defects), and stacking defects. The treated graphite in this report has low edge defects (I_D/I_G from Raman data; results not shown), carbon vacancies (see section on photoelectron spectroscopy), and stacking defects (see Raman spectra; Figure 2d). thus, the treated graphite has inherently low defect concentration and therefore show high overpotentials for HER and OER.[84]

There are no graphene sheet stacking differences for all layer levels of the pristine and treated PG (K&J) (Figure 4.2g). This is likely because of sample rigidity, unlike the other samples already discussed. There was no higher stage ion intercalation for the treated PG even though it had increased current density relative to the pristine. There was also a slight decrease in the cathodic potential (Table 4.1) because of the HER but not comparable to those of the PGs. Their optical images (Figures 4.2h and 4.2i) show no visible morphological differences between either material set. These Raman 2D results suggest that proper electronic tuning of the materials is responsible for activating the catalytic ability of the step edges for HER but that the HER catalytic potential could not be maximized in the absence of uniform graphene sheet ordering.

Artificial graphite showed isotropy in the layer stacking for both treated and pristine samples (Figure 4.2j). Yet, the treated graphite exhibits a four-stage ion intercalation compared to the pristine (Figure 4.1e). The pristine artificial graphite data suggest that ordered graphenic layering without electronic restructuring would not increase the ion intercalation stages. Also, the reverse is true as in the PG (K&J), where electronic tuning without proper layering did not make much difference in the number of ion intercalation stages. Also, the optical images show no difference between the treated and pristine graphite surfaces (Figures 4.2k and 4.2l). These suggest that the nature of the edges [probably edge density differences between the artificial graphite and the PG (Panasonic)] are responsible for the higher HER activity of the PG to the artificial graphite. Thus, electronic reconfiguration and

native edge densities are suggested as being responsible for the higher stage ion intercalation of the treated artificial graphite compared to the pristine.

A Raman three-level probe of graphite rod material shows that thermal treatment did not significantly alter the layering scheme of the treated graphite rod relative to the pristine (Figure S4.2a) just as their optical images show no surface differences between them (Figure S4.2b and S4.2c). Since graphite rod has more edges compared to even basal planes, this suggests that edge density in the absence of proper graphene layering will not trigger efficient HER catalysis. The Raman data (Figure S4.2d) and optical images (Figures S4.2 e and f) of the pristine and treated GFA3 are the same although the treated displayed increased potential window from both its cathodic and anodic arms compared to the pristine. Also, the electronic tuning of the treated materials was responsible for the slight increase in their potential windows.

The potential window values (Table 4.1) and Raman spectra (Figure 4.2) suggest that thermal treatment brought about (a) electronic restructuring, (b) proper graphene layering or stacking, and (c) increased electrochemical activity of the edges for enhanced HER. In fact, all three conditions need to be present to affect efficient HER catalysis (and decreased cathodic limit).

The bulk electrolysis results at 1.6 V and in 0.10 M Na_2SO_4 (Figure 3 and Figure S3) show no stability compromise of the treated graphites when used as anodes, despite the magnitude increases in k_0 for some of the samples. For example, the current density of the treated PG was about same with its pristine (Figure 3a), despite their two orders of magnitude difference in k_0. The pristine graphite (Equalseal) had about a 1 mA/cm^2 higher current density relative to its treated counterpart (Figure 3b) even though their k_0 were about the same (Table 1). The difference in the pristine PG current density was about 20 µA/cm^2 lower than that of the treated (Figure 3c). Also, the pristine and treated graphite rods and GFA3 current densities (Figures S3a and S3b, respectively) were not very different from each other. Thus, the treatment did not make these materials any more susceptible to possible degradation reactions – such as water hydrolysis to protons, H^+ (intercalation of surface adsorbed H^+ within the graphene layers and crumbling of the layers) and oxygen, O_2 (which can degrade the carbon matrix via CO_2 evolution as shown in equations 3 and 4) – than their pristine versions.

$$2C + O_2 \rightarrow 2CO \tag{1}$$

$$2CO + O_2 \rightarrow 2CO_2 \tag{2}$$

There were no optically observable difference(s) in the surfaces of the pristine and the treated samples (Figure 2), and we have shown previously that both surface-types have essentially the same functional

groups on air-exposure.[48] Therefore, it was thought that neither differences in edge-exposure nor surface functional groups were responsible for the stability of the treated materials to corrosion from oxygen evolution. It is suggested that the little or no difference in the current densities of the treated to the pristine graphite is because of the proper electronic tuning and polycrystalline nature of the treated materials. The tuned electronic structure of the treated graphites ensure the enhancement of their π over σ traits compared to the pristine materials,[48] since free σ-electrons exacerbate corrosion.[85,86] These findings imply that this type of thermal treatment of graphites can yield materials for use as batteries, anodes and support systems in fuel cell technology.
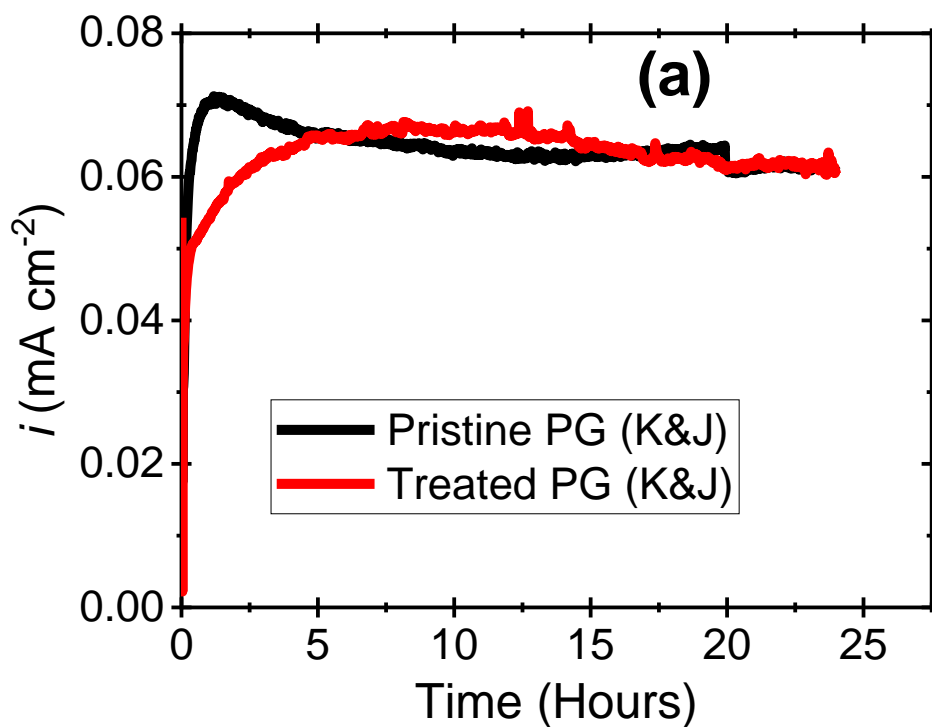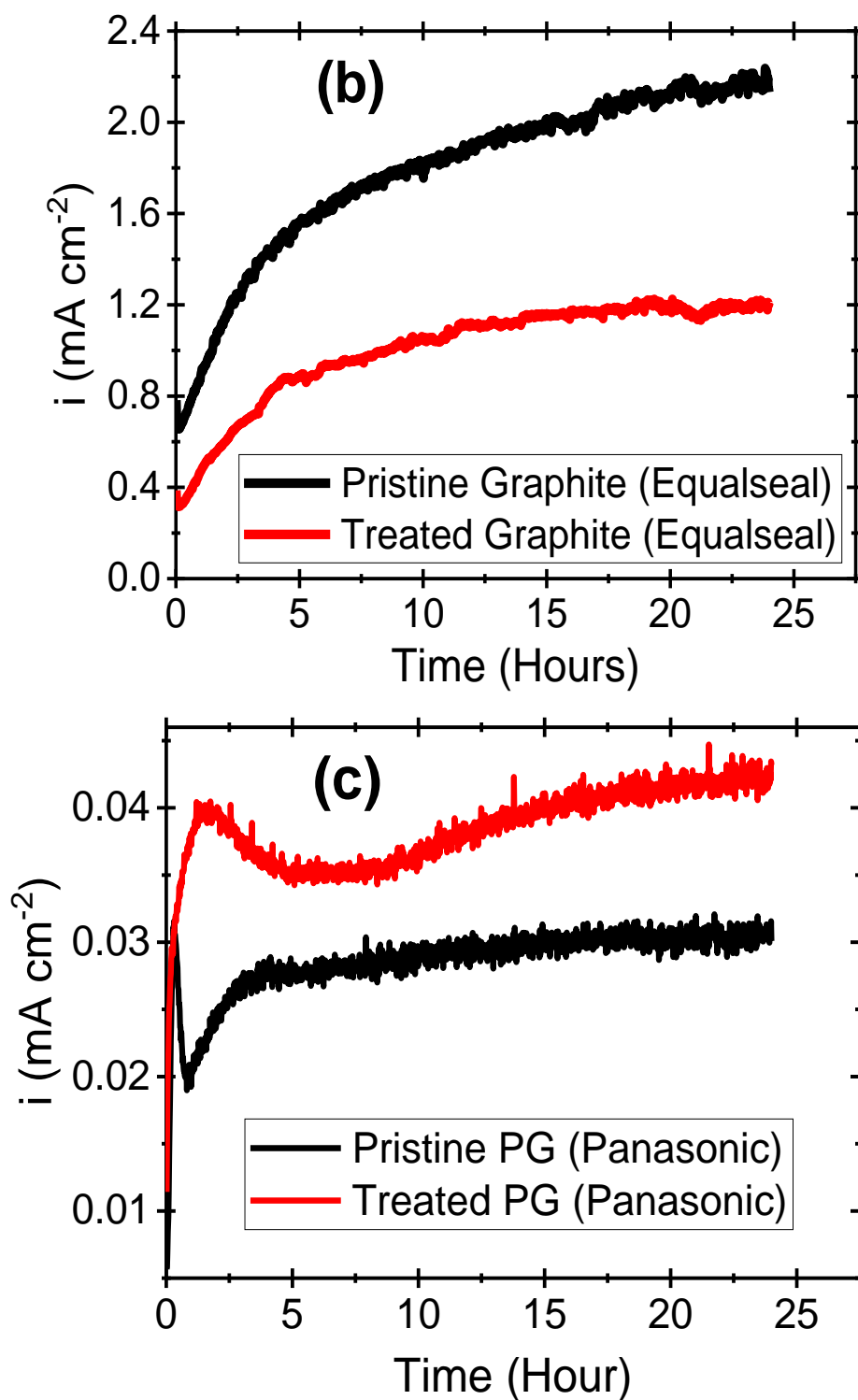
Figure 4.3: Bulk electrolysis in 0.10 M Na₂SO₄ for 24 hours at 1.6V for pristine and treated (a) PG (K&J), (b) Graphite (Equalseal) and (c) PG (Panasonic).

To quantify their corrosion parameters and mechanisms, the corrosion current densities (i_{corr}) and potentials (E_{corr}) were extrapolated from their potentiodynamic scans using Tafel methods. The PG (K&J), Graphite (Equalseal) and PG (Panasonic) results are shown in Figures 4.4a-c, while graphite rod and GFA3 are shown in Figures S4.4a and S4.4b, respectively. Irrespective of the k_0 magnitude differences between the pristine and treated samples, their i_{corr} and E_{corr} values are about the same (Table 4.1). Graphite (Equalseal) and GFA3 are exceptions: the i_{corr} values of the treated materials are about an order of magnitude lower and more relative to pristine samples. The decrease in the corrosion kinetics of the treated Equalseal graphite may be from thermal treatment induced microstructure pore size constriction.[54,90,91]
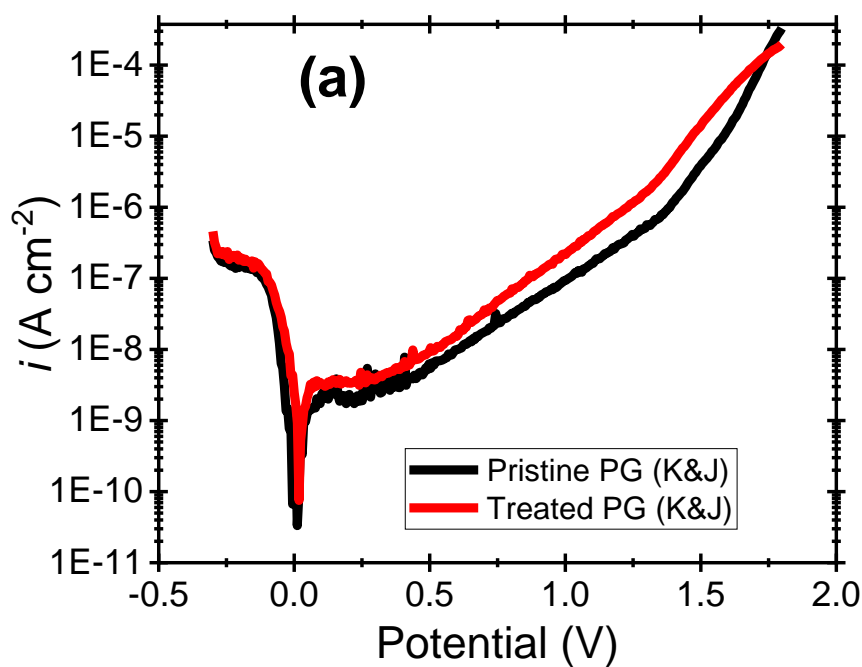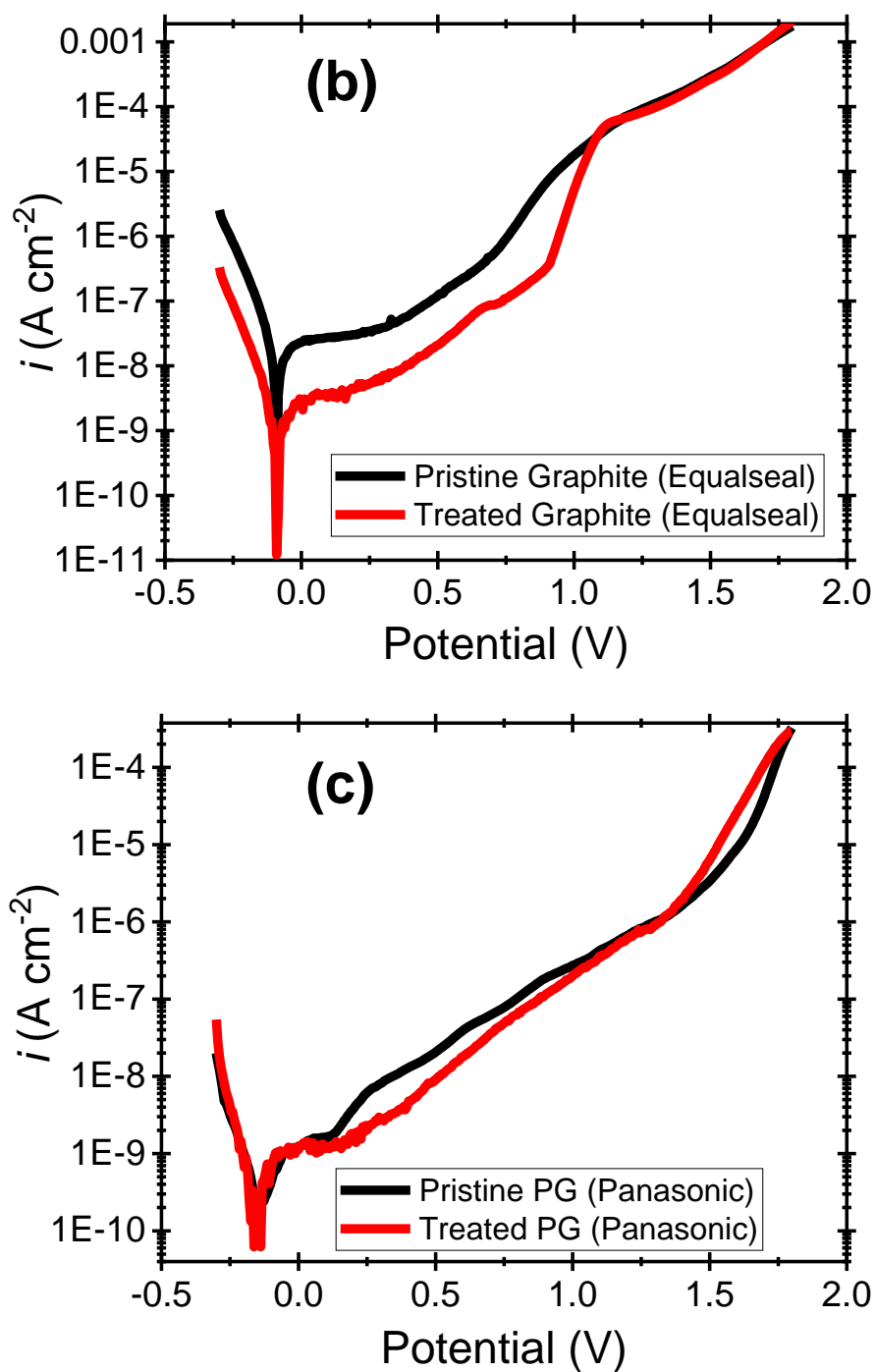
Figure 4.4: Potentiodynamic studies in 0.10 M Na_2SO_4 for 24 hours at 1.6V for pristine and treated (a) PG (K&J), (b) Graphite (Equalseal) and (c) PG (Panasonic).

The potentiodynamic scans suggest similar corrosion mechanisms of both graphite groups in 0.10M Na_2SO_4. These results can be explained by noting that thermal treatment increases graphitization by causing increased crystallinity of graphitic materials.[48,91,92] Graphitization does not change the fundamental oxidation mechanism but slows down the carbon oxidation reaction.[88] This explains the similarity in corrosion mechanisms of the pristine and treated graphite samples even though the treated samples have, in some cases, two orders of magnitude faster kinetics relative to their corresponding pristine samples. These results imply that the treatment protocol causes fast and sustained HET kinetics with unchanged corrosion kinetics compared with the pristine samples. Since potentiodynamic and bulk electrolysis are surface techniques, the actual factor(s) reflected on the surface chemistry of the treated materials may be dictated mainly by structure-induced electronic features.

To probe for structural differences between both material groups that border on the nature of the bonding-induced stability, thermogravimetric (TGA) measurements on the pristine and treated samples were performed under nitrogen. The graphite (Equalseal), PG(K&J) and PG (Panasonic) TGA results are shown in Figures 4.5a-c, while those of GFA3, artificial graphite and graphite rod are shown in Figure S4.5a-c.
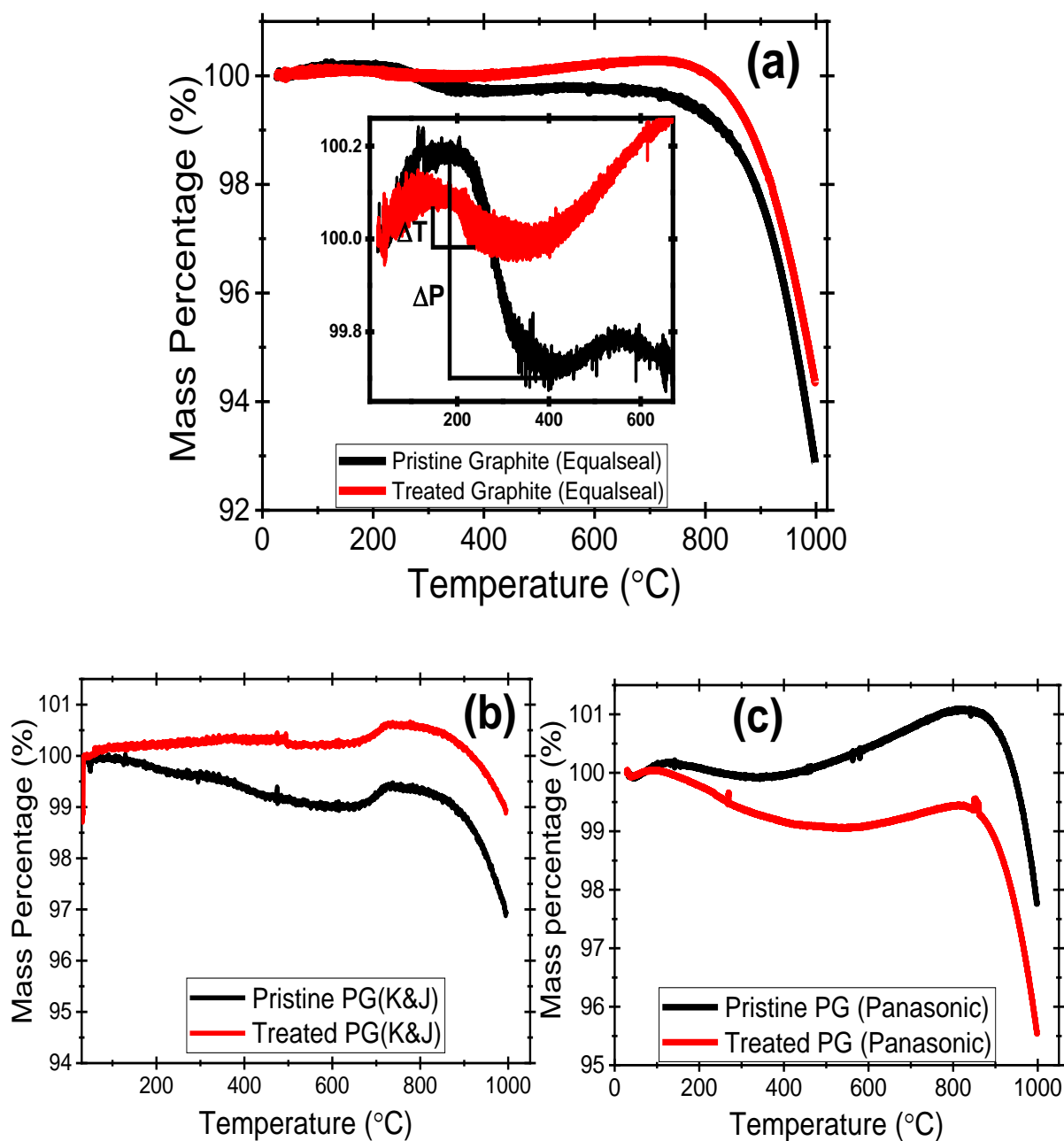
Figure 4.5: The thermogravimetric analysis (TGA) figures of pristine and treated samples of (a) Graphite (Equalseal). Insert is the magnification of the temperature range between 0 and 650 °C. (b) PG(K&J) and (c) PG (Panasonic).

The insert in Figure 4.5a shows that the pristine sample has a steeper mass change (ΔP) at about 200 – 400 °C compared to the treated sample (ΔT). These data indicate different pathways to their thermal degradation and by inference, different structures. The same is true for the other graphite samples studied. The TGA results support the observation that thermal treatment increases the thermal stability of the treated graphite relative to their pristine samples. Even though the decomposition temperatures for each sample pair are the same or nearly the same (ca 770-800 °C), the pristine samples experienced a more rapid incineration beyond their decomposition temperatures. The thermal stability of the treated relative to the pristine samples may arise from less disruption of the more crystalline nature of the treated materials.[48,91–93] The graphite rod TGA (Figure S4.5c) shows that even though both samples have the same melting temperatures, the treated sample has a steeper (faster) melting profile compared to its pristine and in contrast to the other five pairs. It is suggested that the structural rigidity of graphite rod may be responsible for this trend.

Electrochemical impedance spectroscopy (EIS) is important for understanding the interfacial properties of electrode materials, [94] and how this interfacial property can affect the ability of the material surfaces to transfer and exchange charges with a solution. [95,96] The Nyquist plots of the pristine and treated PGs (Figure 4.6) and their corresponding equivalent circuit model (Figure 4.6 insert) for the EIS in 0.10 M Na_2SO_4 suggest a constant phase element (CPE) character for both electrode materials. Their corresponding Bode plots are presented in Figure S4.6. The parameters describing the interfacial properties from the equivalent circuit model is shown in Table 4.2.
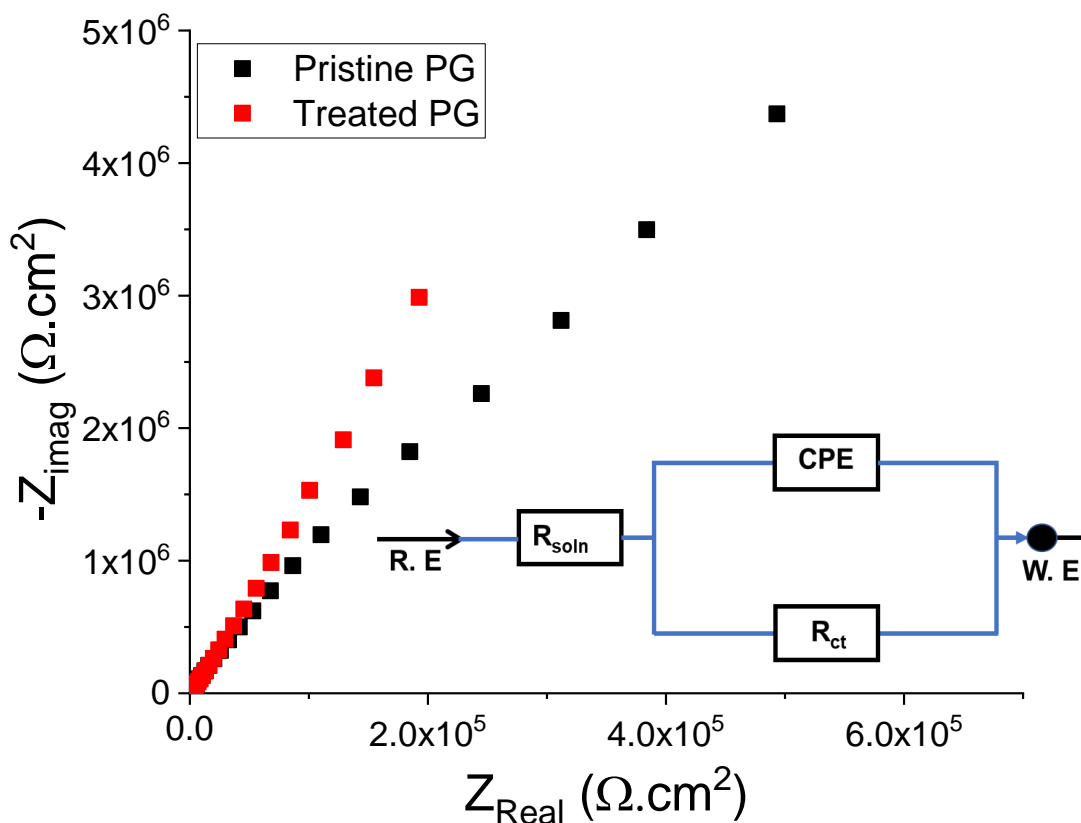
Figure 4.6: The Nyquist plots of pristine and treated PG (K&J) in 0.10 M Na_2SO_4. Insert is their equivalent circuit diagrams.

The charge transfer parameter (R_{ct}) of the treated PG is ca. six orders of magnitude greater than the pristine, while the treated PG capacitance parameter (Y_0) doubled over that of the pristine. The capacitance increase agrees with an earlier report for the treated graphite.[48] Their α values were similar though. To better understand the significant increase in the R_{ct} values of the treated graphite, the EIS data were fitted with a two time-constant equivalent electrical circuit as shown in Figure S6c. The EIS data of the treated graphite could be fitted with a much lower χ^2 value than that of pristine graphite using a two-time constant circuit. This observation indicated that thermal treatment of the PG resulted in two steps of charge transfer, which could not be clearly discerned by the Nyquist of Bode plots.

Presence of high concentration of edge defects resulted in lower R_{ct} of the pristine PG. After thermal treatment, the defects are predominantly annihilated but lattice ordering is improved, and specific surface area increased as seen from the AFM image (see discussion on AFM). Thus, the fast and sustained HET kinetics of the treated graphite is not as a simple function of interfacial charge transfers between the treated electrode surfaces and their electrolytes. Also, the differences in R_{ct} is a testament to the differences in the structure and surface chemistry of both graphite sets, [93,94] even though they appear optically indistinguishable. Here, the high R_{ct} indicates the real corrosion resistance of the material. We can say that thermally treated PG revealed higher corrosion resistance than that of pristine PG.

Table 4.2: Interfacial parameters derived from the CPE equivalent circuit model

	R_{ct} (Ω)	Y_0 ($S.s^{\alpha}$)	α	χ^2
Pristine PG	$4.64\pm4.2 \times10^{7}$	$5.90\pm4.0 \times10^{-6}$	0.951 ± 0.01	1.33×10^{-4}
Treated PG	$2.97\pm3.93 \times10^{13}$	$1.13\pm0.93 \times10^{-5}$	0.936 ± 0.02	2.70×10^{-3}

The topologies of both PG (K&J) sets were probed further by the light microscopy-coupled AFM technique.[97] The 3D topography scans of the pristine and treated PGs (Figure 4.7 a and b respectively and Figure S4.7) done at several spots on their surfaces show that the treated PG surface is more uneven compared to the pristine. The treated PG has craters of about 0.30 to 0.35 µm in depth, while that of the pristine is about 0.10 to 0.15 µm beneath the surface. Both graphite had similar grain sizes of ca. 50-100 nm.
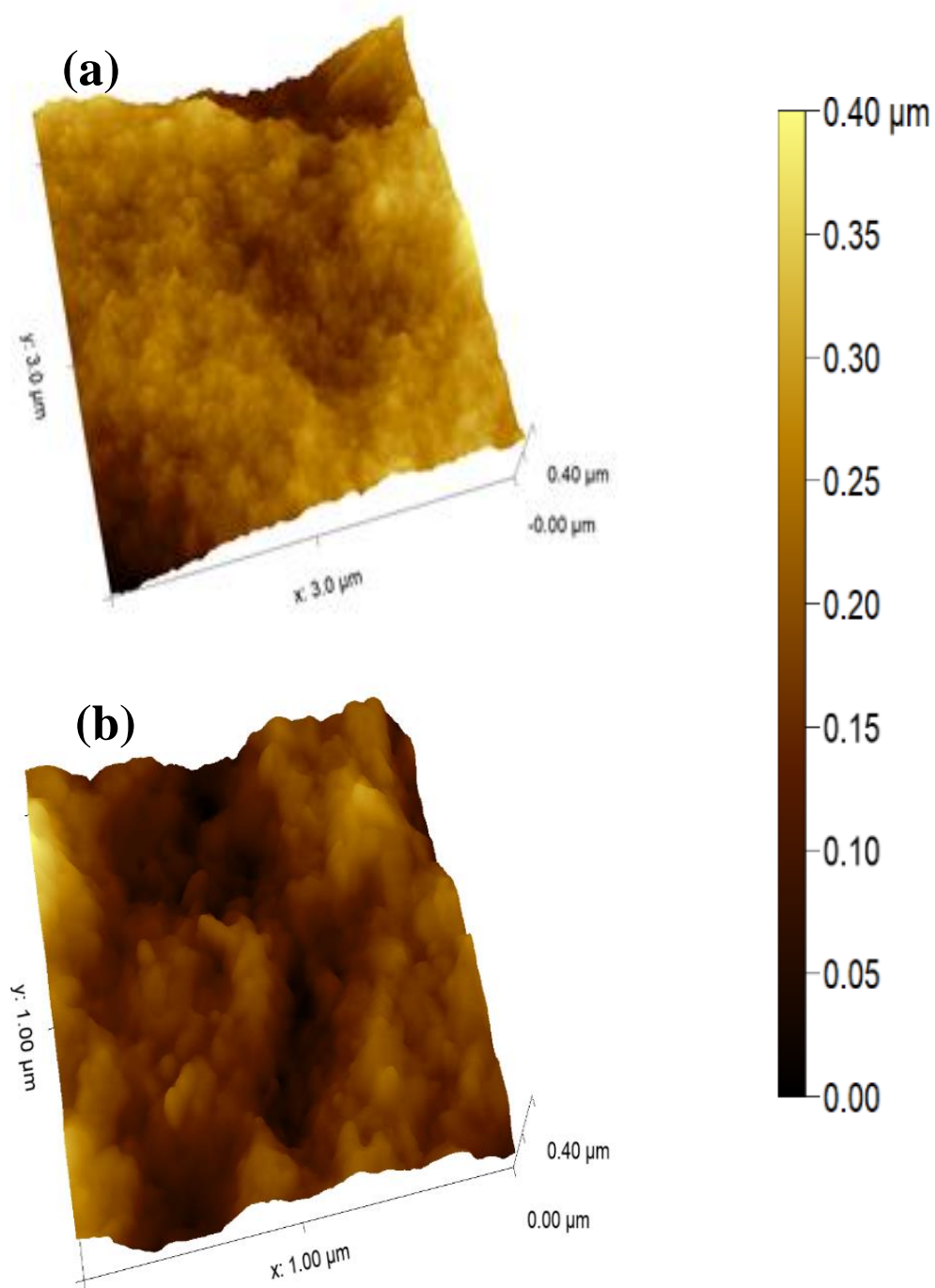
Figure 4.7: The light-microscopy-AFM images of the 3D topology scans of (a) pristine (3 µm scan) and (b) treated (1 µm scan) PG (K&J)

The roughness of the treated PG surface could account for the slow step with increased R_{ct} value,[98] and or contribute to its increased defect density and capacitance as reported earlier.[48] The AFM images agree with the CPE element as been responsible for the differences in the EIS data of the PG sets. Of note is that there are no pits on the treated PG surface. This firmly rules out edge exposure on the basal planes as a possible reason for its fast-HET kinetics.

The electronic band spectra of the PG show that there was increased π over σ trait, a weakening of the σ bonds between σ2 and σ3, and an overall increase in the density of states (both electronic and vibrational as seen from the Brillouin zone) for the treated over the pristine (Figure 4.8). Yet, the Φ values of both categories were about the same (Table 2.1). The trend in Figure 4.8 appeared for all the other graphite samples used in this study. These results suggest that even though there were structural differences and significant electronic band changes between both graphite sets, there were little to no structural influences on their Φ values as was reported for some carbon materials.[99] Thus, in terms of charge transfer across vacuum, there were no potential energy barrier differences between the pristine and treated samples. This would account for the very similar corrosion kinetics, thermodynamics and mechanisms of the pristine and treated graphites. Of importance is that since there were no apparent differences in the corrosion parameters of both graphite groups, the treated graphite step edges are not responsible for the facile HET kinetics of the graphite basal planes. [26,51,88,91]
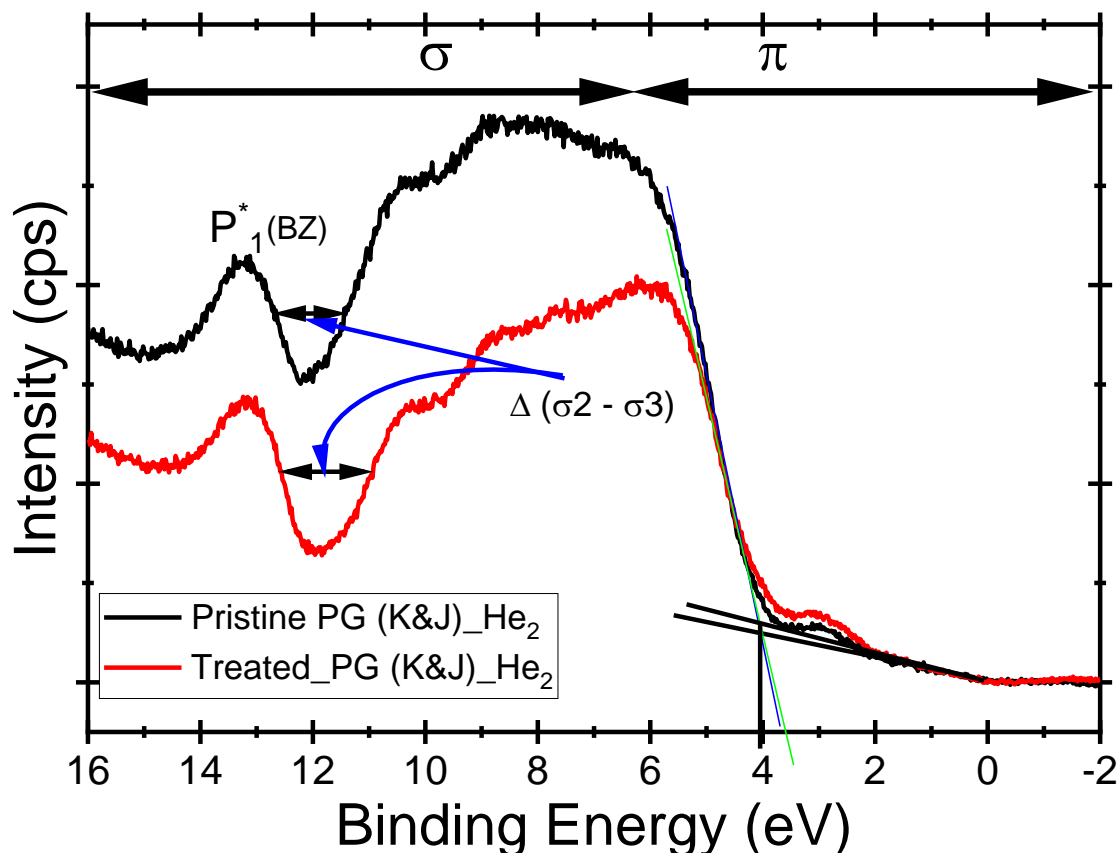
Figure 4.8: The electronic band structure of the pristine and treated PG (K&J) and the extrapolation method for Φ. P^*_1 is the vibrational density of states at the Brillouin zone (BZ).

It is suggested that thermal treatment brought about conformational excursions over an energy barrier to a native state with correlated electronic structure (**Scheme 4.1**). Strong electronic correlations with weak σ electron-electron repulsion or strong π electron-electron interaction, possess increased kinetic energy via the ability of the electrons to quantum- mechanically tunnel around in a crystal without the necessity of a lowered Φ threshold.[48, 100] This increased π- to σ attributes increase conduction,[101] and decreases corrosion.[88,89] In addition, the fact that charge delocalization along the crystalline sites (Scheme 1) are no longer susceptible to surface adsorbents, even to $Fe(CN)_6^{3-/4-}$,[26,48,102] implies that the electrons tunnel through these surface adsorbents. Thus, enhanced electron tunneling (from the bulk layer to the surface) – the fast step - results in corrosion resistance of the structure-modified, thermally treated graphite.
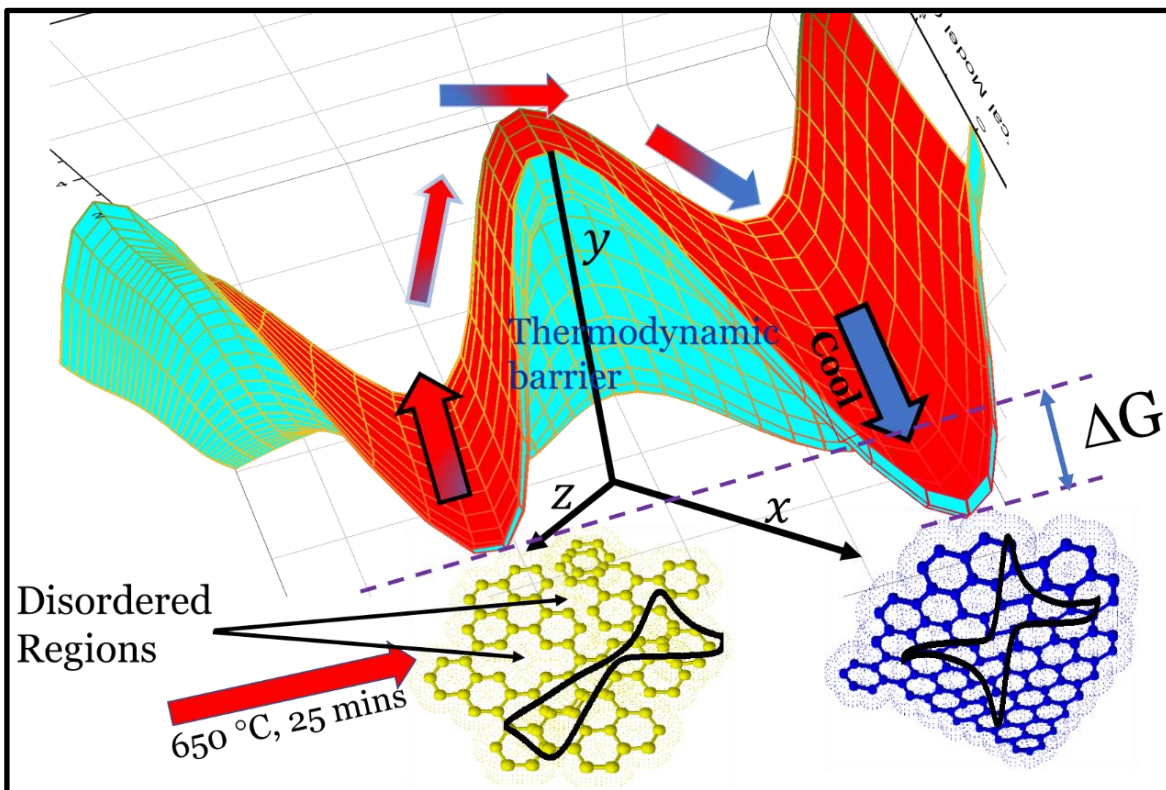
Scheme 4.1: A transverse depiction of the energy landscape of a generic pristine graphite (as used in the current work) with disordered regions and sluggish electron transfer kinetics represented by the quasi-reversible nature of the cyclic voltammogram (CV) in 1mM $Fe(CN)_6^{3-/4-}$. On heating at 650 °C in air for 25 minutes, the pristine graphite gains enough energy to transverse a huge thermodynamic barrier and cools to a polycrystalline state, with well-ordered structure that facilitates facile electron transfer kinetics as seen by the reversible nature of its CV. Even though the thermodynamic barrier is large, the actual energy difference (ΔG) between both structures is small. This considerable thermodynamic barrier is the energetic reason why polycrystalline structures formed on cooling do not revert to the pristine-like structure thus ensuring sustained fast HET kinetics over the course of weeks.

As a surface phenomenon, corrosion targets surface features that aid faster HET kinetics and that are more likely to contribute to- and accelerate corrosion leading to material degradation. [51] In the case of the thermally treated graphites, the surfaces are conduits for electron transfer but are not the originating sites for, nor the facilitators of, electron transfer. Thus, the structural and functional integrity of the treated graphites are maintained irrespective of accelerated HET.

Conclusion

Thermal treatment results in fast HET kinetics without compromising the electrochemical, thermal and corrosion stabilities of the treated graphites. The treatment abolished the level of anisotropy that is usually reported for graphite such that the graphene layers of the thermally-treated PG are properly stacked in layers. The now isotropic layers extend throughout the material from the nano- to the macroscopic scale. The isotopism and enhanced HER activity are traits previously ascribed to 2D materials only. Thermal treatment results in structural changes that tune the electronic structure to enhance π over σ traits without changes in their electronic work functions, Φ. This is because of enhanced electron tunneling, - via improved tunneling paths - which is also the reason for the increased HET kinetics and corrosion resistance of thermally-treated relative to pristine graphites. Conclusively, the thermal treatment protocol reported herein increased HET kinetics without compromises to their electrochemical, structural and corrosion stabilities. In fact, in some instances, these properties improved over the pristine graphite. Moreover, surface roughness as impediment for use of materials for various electrochemical applications would no longer be an issue.

These findings suggest that the thermal treatment protocol reported herein would be suitable for high surface area carbon materials intended for use as support systems in fuel cells. Some PGs and graphite rods could serve effectively as batteries, supercapacitors in energy storage capacities, sensors, catalysis science, and anodes for electro-oxidative reactions and in other applications where fast HET kinetics without compromise to their stability is a criterion.

Methods and Materials

Chemicals and Materials

All chemicals and reagents were used as received from the suppliers. Flexible pyrolytic graphite sheets (Panasonic Electronic Components; $115 \times 180 \times 0.025$ mm^3 thick, Gray, Part number EYG-S121803) Digi-Key electronics (Thief River Falls, MN, USA). Plain (No insert) flexible graphite (Equalseal, [Warren, OH]) sheets ($8.25'' \times 9.5'' \times 1/16''$) Acros Organics (Bridgewater, NJ, USA). Artificial graphite sheets (T68; 50 mm $\times$ 20 mm $\times$ 25 µm) (t-Global Technology Co. Ltd, Taiwan). Pyrolytic graphite blocks, PG1 (32 ± 2 mm $\times$ 16 ± 2 mm $\times$ 0.75 ± 0.5 mm thick, K & J Magnetics [Plumsteadville, PA, USA]). Graphite rods (40767-KD: Graphite rod, 6.15 mm (0.242 in) dia. $\times$ 152 mm (6 in) long, 99.9995% (metals basis, Alfa Aesar [Haverhill, MA, USA]). Graphite blocks (99.99%, $40 \times 40 \times 3$ mm^3 thick) Maibang Carbon (Henan, Mainland China). Ag/AgCl/3 M NaCl (aq) reference electrodes (0.209 V vs. SHE) and reference electrode cells (Bioanalytical Systems Inc (BASi), West Lafayette, IN, USA)). Battery felt SIGRACELL$^®$ GFA3 ($297 \times 210 \times 3$ mm^3 thick) and Soft Felt SIGRATHERM GFA5 ($297 \times 210 \times 5$ mm^3, SGL Carbon Company GmbH [Meitingen, Germany]).

Potassium hexacyanoferrate (III) (Fe(CN)$_6^{3/4-}$; ACS reagent, $\geq$99.0%) and potassium chloride crystal (SigmaUltra; >99.0%, Sigma Chemical Co., [St. Louis, MO, USA]). Sodium sulfate crystals (Na$_2$SO$_4$; ACS reagent, 99.0%), Alfa Aesar (Tewksbury, MA), Advanced abrasives (SandBlaster, 3M [St. Paul, MN, USA]); Teflon tape (Dupont, [Elk Grove Village, IL]) Low resistance copper foil tape with conductive adhesive ($0.25'' \times 1296'' \times 0.0011''$ thick, Kraftex$^®$ [Woodchester, Stroud, England]). Premium microscope slides (plain, Fisher Scientific, USA). Loctite clear silicone waterproof sealant (Westlake, OH, USA). GE Silicone 2+ (General Electric [Huntersville, NC, USA]). The tube furnace was a high temperature Lindberg/Blue M type model furnace [Thermo Scientific (Asheville, NC, USA)]. All aqueous stock solutions were prepared with MilliQ ® (18 MΩ) water.

Sample Preparation for Thermal Treatment

Flexible graphite sheets, PG sheets, Battery Felt SIGRACELL® GFA3, and graphite rods were cut into pieces of ca. 4-5 cm long. One end of each cut graphite rod piece was polished with a 100-grit sandblaster followed by a finishing polishing with a 320-grit sandblaster. The PG blocks were exfoliated using Scotch® tape to expose fresh and pristine surfaces prior to thermal treatment and/or the start of control experiments using these pristine surfaces.

Thermal Treatment

The thermal treatment protocol for graphite samples in air for 25 minutes at 650 °C is as reported.[48] After thermal treatment, the samples were cooled slowly to room temperature.

Electrode Preparation for Electrochemical Measurements

Electrodes were made by fixing one side of the graphite to a glass slide with silicon grease. Low resistance copper foil tape was attached to one end of the graphites and run through the entire length of the glass slide. A small length was extended further for attachment to the potentiostat. A designated area of the electrode material was exposed to electrolytes by covering the other areas of the graphite with sealants.

Electrochemical Measurements

Cyclic Voltammetry

Cyclic voltammetry (CV) studies of the various graphites, as working electrodes, were performed with a VersaStat 3 potentiostat/galvanostat (Princeton Applied Research). Graphite blocks (99.99%, $40 \times 40 \times 3$ mm^3 thick) served as the counter electrodes, while Ag/AgCl (3M NaCl) were the reference electrodes. A 1 mM $[Fe(CN)_6]^{3-/4-}$ (1 M KCl) solution served as the electrolyte for the determination of the heterogeneous electron transfer (HET) kinetics of the graphites investigated. Cyclic voltammetry and other electrochemical measurements were performed within hours to several days after the thermal treatment of the graphite samples.

Potential Window Determination

Cyclic voltammetry measurements to determine the cathodic and anodic potential limits for the onset of hydrogen and oxygen evolution, respectively, at defined current densities were carried out in a 1M H_2SO_4 solution. The acid solution was purged with nitrogen gas prior to and during the cathodic CVs runs.

Chronoamperometry Study

Controlled potential coulometry experiments, for each graphite pairs of pristine and thermally treated samples, were run at 1.6 V in 0.10 M Na_2SO_4 for 24 hours using a Gamry Interface 1000 Potentiostat/Galvanostat/ZRA (Gamry Instruments, [Hartsville, PA, USA]). The electrolysis experiments were performed in a 1L reaction vessel. The counter electrode was a $15 \times 9.5 \times 0.5$ cm^3 thick high surface area GFA5 felt.

Potentiodynamic Polarization Studies

Potentiodynamic studies were performed in a 1L reaction vessel using 0.10 M Na_2SO_4 as the electrolyte. The counter electrode ($15 \times 9.5 \times 0.5$ cm^3) was made from high surface area GFA5 felt. Prior to start of the potential scans, an open circuit potential (OCP) was run, while continuously being purged with nitrogen gas and stirring, for at least 90 minutes and the values stored. Scanning of the potentials was carried out over a range between -0.3 V (vs ref electrode) to 1.8 V (vs ref electrode) at a scan rate of 1 mV/s, with the graphite materials serving as the working electrodes. Continuous purging with nitrogen gas while stirring simultaneously was maintained throughout the OCP runs and potentiodynamic scans.

Electrochemical Impendance Spectroscopy (EIS) Study

Potentiostatic EIS measurments were performed at room temperature using a Gamry Reference 600 Potentiostat/Galvanostat/ZRA- (Gamry Instruments, [Hartsville, PA, USA]). The counter electrode was a $15 \times 9.5 \times 0.5$ cm^{3}high surface area GFA5 felt. The EIS measurements were performed after open circuit conditions were run for at least two hours to attain equilibrium. The voltage (AC) was10 mV root mean square and the initial frequency was 10 kHz with a final frequency of 0.01 Hz. A total of 10 points was collated per decade.

Thermal Gravimetric Analysis (TGA)

Thermogravimetric analysis (TGA) of pristine and treated samples were performed using a TGA Q50 V20.13 Build 39 (TA Instruments; New Castle, DE, USA). Incineration of the samples was accomplished by using a standard furnace type in a platinum pan sample holder. The temperature of the pan was increased from baseline temperatures to 1000 °C at a rate of 10 °C/min. Combustion was performed in a nitrogen gas atmosphere flowing at a rate of 60 mL/min. The sample weights before combustion were between 1 mg and 5 mg and were weighed again on cooling down to room temperature after each experimental run.

Optical Imagery-Atomic Force Microscopy (AFM) Spectroscopy

The combined light microscopy-AFM single platform instrumentation technique for high resolution image acquisition of the pristine and treated pyrolytic graphite (K&J) was carried out as previously reported.[97]

Raman Spectroscopy

Raman scattering spectral measurements were carried out as described.[48] The data were collected with a WITec™ alpha300 R Raman instrument (GmbH, Germany). A 100-mW, frequency doubled, Nd:YAG (λ = 532.5 nm) laser focused through a 20× Nikon objective (NA = 0.4, WD = 3.9 mm) creates a spot size of ~10 μm. Manual attenuation of the laser power, during measurements, was necessary to reduce or eliminate fluorescence and thermally induced artifacts during data collection while achieving sufficient signal-to-noise ratio to distinguish graphite bands which were qualitatively similar. This was important since the laser power was varied to probe three different depths or layer profiles: surfaces of the materials, sub-surfaces comprising of some layers beneath the surface and deep layer probing. Spectral acquisition of single spectrum "spot" scans was done using an alpha300 R via a UHT-300 spectrometer (grating = 600 grooves/mm, entrance aperture = 50 μm), with an Andor™ DU970N-BV, 1600×200-pixel, CCD array detector. Each Raman spectrum was an average of 10 spectral accumulations at 0.50 seconds integration time. Optical images were saved from each sample area probed. Sample spots for Raman measurements were done on defect-free surfaces for samples with visible defects or edge exposures, as judged from their acquired and now saved optical images.

Ultraviolet Photoelectron Spectroscopy (UPS)

Binding energy determinations were accomplished by using the data acquired from ultraviolet photoelectron spectroscopy (UPS) in an ultrahigh vacuum (UHV) with a base pressure $< 10^{-10}$ Torr. The X-ray lamp was a dual anode XR 04-548 (Physical Electronics) while the X-ray source was an Al-Kα source operated at 400 W and an X-ray incident angle of 54.7° and normal emission. The kinetic energy of the photoelectrons was measured with an Omicron EA 125 hemispherical energy analyzer having a resolution of 0.02 eV, using both He I (21.2 eV) and He II (40.8 eV) excitation lines.

Data Processing

All data were processed using both Microsoft Excel 2016® version and Origin version 2018b® software. All graphs were plotted using the Origin version 2018b graph plotting component.

Supporting Information – Appendix C

More information on the CVs, Raman Spectroscopy and optical imaging, bulk electrolysis chronoamperomograms and TGA results.

Literature Cited

(1) Štulík, K. Activation of Solid Electrodes. *Electroanalysis*. **1992**, *4*, 829– 834.

(2) Swain, G. M. Solid Electrode Materials: Pretreatment and Activation. In *Handbook of Electrochemictry*; Zoski, C. G., Ed.; Elsevier B.V.: Amsterdam, 2007; pp 111–153.

(3) McCreery, R. L. Advanced Carbon Electrode Materials for Molecular Electrochemistry. *Chem. Rev.* **2008**, *108*, 2646–2687.

(4) McCreery, R. L.; McDermott, M. T. Comment on Electrochemical Kinetics at Ordered Graphite Electrodes. *Anal. Chem.* **2012**, *84*, 2602–2605.

(5) Velický, M.; Bradley, D. F.; Cooper, A. J.; Hill, E. W.; Kinloch, I. A.; Mishchenko, A.; Novoselov, K. S.; Patten, H. V.; Toth, P. S.; Valota, A. T.; Worrall, S. D.; Dryfe, R. A. W. Electron Transfer Kinetics on Mono- and Multilayer Graphene. *ACS Nano* **2014**, *8*, 10089–10100.

(6) Güell, A. G.; Cuharuc, A. S.; Kim, Y. R.; Zhang, G.; Tan, S. Y.; Ebejer, N.; Unwin, P. R. Redox-Dependent Spatially Resolved Electrochemistry at Graphene and Graphite Step Edges. *ACS Nano* **2015**, *9*, 3558–3571.

(7) Li, Z.; Wang, Y.; Kozbial, A.; Shenoy, G.; Zhou, F.; McGinley, R.; Ireland, P.; Morganstein, B.; Kunkel, A.; Surwade, S. P.; Li, L.; Liu, H. Effect of Airborne Contaminants on the Wettability of Supported Graphene and Graphite. *Nat. Mater.* **2013**, *12*, 925–931.

(8) Li, Z.; Kozbial, A.; Nioradze, N.; Parobek, D.; Shenoy, G. J.; Salim, M.; Amemiya, S.; Li, L.; Liu, H. Water Protects Graphitic Surface from Airborne Hydrocarbon Contamination. *ACS Nano* **2016**, *10*, 349–359.

(9) Velický, M.; Bissett, M. A.; Toth, P. S.; Patten, H. V.; Worrall, S. D.; Rodgers, A. N. J.; Hill, E. W.; Kinloch, I. A.; Novoselov, K. S.; Georgiou, T.; Britnell, L.; Dryfe, R. A. W. Electron Transfer Kinetics on Natural Crystals of MoS2and Graphite. *Phys. Chem. Chem. Phys.* **2015**, *17*, 17844-17853.

(10) Laurila, T.; Sainio, S.; Caro, M. Hybrid Carbon Based Nanomaterials for Electrochemical Detection of Biomolecules. *Prog. Mater. Sci*. **2017**, *88*, 499-594.

(11)   Chandra, S.; Miller, A. D.; Bendavid, A.; Martin, P. J.; Wong, D. K. Y. Minimizing Fouling at Hydrogenated Conical-Tip Carbon Electrodes during Dopamine Detection in Vivo. *Anal. Chem.* **2014**, *86*, 2443–2450.

(12)   Hu, L.; Peng, X.; Huo, K.; Chen, R.; Fu, J.; Li, Y.; Lee, L. Y. S.; Wong, K.-Y.; Chu, P. K. Dominant Factors Governing the Electron Transfer Kinetics and Electrochemical Biosensing Properties of Carbon Nanofiber Arrays. *ACS Appl. Mater. Interfaces* **2016**, *8*, 28872– 28879.

 (13)   Sofer, Z.; Jankovský, O.; Šimek, P.; Sedmidubský, D.; Šturala, J.; Kosina, J.; Mikšová, R.; Macková, A.; Mikulics, M.; Pumera, M. Insight into the Mechanism of the Thermal Reduction of Graphite Oxide: Deuterium-Labeled Graphite Oxide Is the Key. *ACS Nano* **2015**, *9*, 5478–5485.

(14)   Mao, X.; Guo, F.; Yan, E. H.; Rutledge, G. C.; Alan Hatton, T. Remarkably High Heterogeneous Electron Transfer Activity of Carbon-Nanotube-Supported Reduced Graphene Oxide. *Chem. Mater.* **2016**, *28,* 7422–7432.

(15)   Parker, J. F.; Kamm, G. E.; McGovern, A. D.; Desario, P. A.; Rolison, D. R.; Lytle, J. C.; Long, J. W. Rewriting Electron-Transfer Kinetics at Pyrolytic Carbon Electrodes Decorated with Nanometric Ruthenium Oxide. *Langmuir* **2017**, *33*, 9416–9425.

(16)   Taylor, S. M.; Pătru, A.; Perego, D.; Fabbri, E.; Schmidt, T. J. Influence of Carbon Material Properties on Activity and Stability of the Negative Electrode in Vanadium Redox Flow Batteries: A Model Electrode Study. *ACS Appl. Energy Mater.* **2018**, *1*, 1166–1174.

 (17)   Ferrari, A. C.; Bonaccorso, F.; Fal'ko, V.; Novoselov, K. S.; Roche, S.; Bøggild, P.; Borini, S.; Koppens, F. H. L.; Palermo, V.; Pugno, N.; Garrido, J. A.; Sordan, R.; Bianco, A.; Ballerini, L.; Prato, M.; Lidorikis, E.; Kivioja, J.; Marinelli, C.; Ryhänen, T.; Morpurgo, A.; Coleman, J. N.; Nicolosi, V.; Colombo, L.; Fert, A.; Garcia-Hernandez, M.; Bachtold, A.; Schneider, G. F.; Guinea, F.; Dekker, C.; Barbone, M.; Sun, Z.; Galiotis, C.; Grigorenko, A. N.; Konstantatos, G.; Kis, A.; Katsnelson, M.; Vandersypen, L.; Loiseau, A.; Morandi, V.; Neumaier, D.; Treossi, E.; Pellegrini, V.; Polini, M.; Tredicucci, A.; Williams, G. M.; Hong, B. H.; Ahn, J.-H.; Kim, J. M.; Zirath, H.; van Wees, B. J.; van der Zant, H.; Occhipinti, L.; Di Matteo, A.; Kinloch, I. A.; Seyller, T.; Quesnel, E.; Feng, X.; Teo, K.; Rupesinghe, N.; Hakonen, P.; Neil, S. R. T.; Tannock, Q.; Löfwanderaq, T.; Kinaret, J. Science and Technology Roadmap for Graphene, Related Two-Dimensional Crystals, and Hybrid Systems. *Nanoscale* **2015**, *7*, 4598–4810.

(18)   Kong, Y.; Wang, Z.-L.; Wang, Y.; Yuan, J.; Chen, Z.-D. Degradation of Methyl Orange in Artificial Wastewater through Electrochemical Oxidation Using Exfoliated Graphite Electrode. *Xinxing Tan Cailiao/New Carbon Mater.* **2011**, *26*, 459– 464.

(19)   Maljaei, A.; Arami, M.; Mahmoodi, N. M. Decolorization and Aromatic Ring Degradation of Colored Textile Wastewater Using Indirect Electrochemical Oxidation Method. *Desalination* **2009**, *249*, 1074–1078.

(20)   Brownson, D. A. C.; Munro, L. J.; Kampouris, D. K.; Banks, C. E. Electrochemistry of Graphene: Not Such a Beneficial Electrode Material? *RSC Adv.* **2011**, *1*, 978-988.

(21)   Kozbial, A.; Zhou, F.; Li, Z.; Liu, H.; Li, L. Are Graphitic Surfaces Hydrophobic? *Acc. Chem. Res.* **2016**, *49*, 2765–2773.

(22)   Kozbial, A.; Li, Z.; Sun, J.; Gong, X.; Zhou, F.; Wang, Y.; Xu, H.; Liu, H.; Li, L. Understanding the Intrinsic Water Wettability of Graphite. *Carbon* **2014**, *74*, 218–225.

(23)   Poon, M.; McCreery, R. L.; Engstrom, R. Laser Activation of Carbon Electrodes. Relationship between Laser-Induced Surface Effects and Electron Transfer Activation. *Anal. Chem.* **1988**, *60*, 1725–1730.

(24)   Ranganathan, S.; Kuo, T.; Mccreery, R. L. Facile Preparation of Active Glassy Carbon Electrodes with Activated Carbon and Organic Solvents. *Anal. Chem.* **1999**, *71*, 3574–3580.

(25)   Chen, P.; Fryling, M. A.; McCreery, R. L. Electron Transfer Kinetics at Modified Carbon Electrode Surfaces: The Role of Specific Surface Sites. *Anal. Chem.* **1995**, *67*, 3115–3122.

(26)   Ji, X.; Banks, C. E.; Crossley, A.; Compton, R. G. Oxygenated Edge Plane Sites Slow the Electron Transfer of the Ferro-/Ferricyanide Redox Couple at Graphite Electrodes. *ChemPhysChem* **2006**, *7*, 1337–1344.

(27)   Martinez-Martin, D.; Longuinhos, R.; Izquierdo, J. G.; Marele, A.; Alexandre, S. S.; Jaafar, M.; Gómez-Rodríguez, J. M.; Bañares, L.; Soler, J. M.; Gomez-Herrero, J. Atmospheric Contaminants on Graphitic Surfaces. *Carbon* **2013**, *61*, 33–39.

(28)   Misra, R. P.; Blankschtein, D. Insights on the Role of Many-Body Polarization Effects in the Wetting of Graphitic Surfaces by Water. *J. Phys. Chem. C* **2017**, *121*, 28166–28179.

(29)   Liu, H.; Li, L. Graphitic Materials: Intrinsic Hydrophilicity and Its Implications. *Extreme Mechanics Letts*. **2017**, *14*, 44–50.

(30)   Lai, C. Y.; Tang, T. C.; Amadei, C. A.; Marsden, A. J.; Verdaguer, A.; Wilson, N.; Chiesa, M. A Nanoscopic Approach to Studying Evolution in Graphene Wettability. *Carbon* **2014**, *80*, 784–792.

(31)   Davey, N. M.; Seymour, R. J. Platinum Metals in Electronics. *Platin. Met. Rev.* **1985**, *29*, 2–11.

(32)   Rawashdeh-Omary, M. A.; Omary, M. A.; Fackler, J.; Galassi, R.; Pietroni, B. R.; Burini, A. Chemistry and Optoelectronic Properties of Stacked Supramolecular Entities of Trinuclear Gold (I) Complexes Sandwiching Small Organic Acids. *J. Am. Chem. Soc*. **2001**, *123*, 9689–9691.

(33)   Zorić, I.; Zäch, M.; Kasemo, B.; Langhammer, C. Gold, Platinum, and Aluminum Nanodisk Plasmons: Material Independence, Subradiance, and Damping Mechanisms. *ACS Nano* **2011**, *5*, 2535–2546.

(34)   Fontana, L.; Venditti, I.; Fratoddi, I.; Leahu, G.; Belardini, A.; Li Voti, R.; Sibilia, C.; Matassa, R.; Familiari, G. Gold and Silver Nanoparticles Based Networks as Advanced Materials for Optoelectronic Devices. In *18th Italian National Conference on Photonic Technologies (Fotonica 2016)*; **2016**, DOI: 10.1049/cp.2016.0896.

(35)   Coustan, L.; Shul, G.; Bélanger, D. Electrochemical Behavior of Platinum, Gold and Glassy Carbon Electrodes in Water-in-Salt Electrolyte. *Electrochem. commun.* **2017**, *77*, 89-92.

(36)   Bengio, D.; Mendes, E.; Pellet-Rostaing, S.; Moisy, P. Electrochemical Behavior of Platinum and Gold Electrodes in the Aprotic Ionic Liquid N,N-Trimethyl butyl ammonium Bis(Trifluoromethanesulfonyl) Imide. *J. Electroanal. Chem.* **2018**, *823*, 445–454.

(37)   Cataldi, T. R. I.; Rubino, A.; Laviola, M. C.; Ciriello, R. Comparison of Silver, Gold and Modified Platinum Electrodes for the Electrochemical Detection of Iodide in Urine Samples Following Ion Chromatography. *J. Chromatogr. B Anal. Technol. Biomed. Life Sci.* **2005**, *827*, 224-231.

(38)   Shkir, M.; Yahia, I. S.; Ganesh, V.; Bitla, Y.; Ashraf, I. M.; Kaushik, A.; AlFaify, S. A Facile Synthesis of Au-Nanoparticles Decorated PbI_2 single Crystalline Nanosheets for Optoelectronic Device Applications. *Sci. Rep.* **2018**, *8*, 13806.

(39)   Cherevko, S.; Keeley, G. P.; Kulyk, N.; Mayrhofer, K. J. J. Pt Sub-Monolayer on Au: System Stability and Insights into Platinum Electrochemical Dissolution. *J. Electrochem. Soc.* **2016**, *163*, H228-H233.

(40)   Mohamed, M. A.; Abdelwahab, N. S.; Banks, C. E. Electroanalytical Sensing of the Antimicrobial Drug Linezolid Utilising an Electrochemical Sensing Platform Based upon a Multiwalled Carbon Nanotubes/Bromocresol Green Modified Carbon Paste Electrode. *Anal. Methods* **2016**, *8*, 4345-4353.

(41)   Macpherson, J. V. A Practical Guide to Using Boron Doped Diamond in Electrochemical Research. *Phys. Chem. Chem. Phys.* **2015**, *17*, 2935-2949.

(42)   Cobb, S. J.; Ayres, Z. J.; Macpherson, J. V. Boron Doped Diamond: A Designer Electrode Material for the Twenty-First Century. *Annu. Rev. Anal. Chem.* **2018**, *11*, 463-484.

(43)   Kraft, A. Doped Diamond: A Compact Review on a New, Versatile Electrode Material. *Int. J. Electrochem. Sci*. **2007**, *2*, 355-385.

(44)   Ashraf, A.; Wu, Y.; Wang, M. C.; Yong, K.; Sun, T.; Jing, Y.; Haasch, R. T.; Aluru, N. R.; Nam, S. Doping-Induced Tunable Wettability and Adhesion of Graphene. *Nano Lett.* **2016**, *16*, 4708– 4712.

(45)   Tian, T.; Lin, S.; Li, S.; Zhao, L.; Santos, E. J. G.; Shih, C. J. Doping-Driven Wettability of Two-Dimensional Materials: A Multiscale Theory. *Langmuir* **2017**, *33*, 12827– 12837.

(46)   Hong, G.; Han, Y.; Schutzius, T. M.; Wang, Y.; Pan, Y.; Hu, M.; Jie, J.; Sharma, C. S.; Müller, U.; Poulikakos, D. On the Mechanism of Hydrophilicity of Graphene. *Nano Lett.* **2016**, *16*, 4447– 4453.

(47)   Kozbial, A.; Trouba, C.; Liu, H.; Li, L. Characterization of the Intrinsic Water Wettability of Graphite Using Contact Angle Measurements: Effect of Defects on Static and Dynamic Contact Angles. *Langmuir* **2017**, *33*, 959–967.

(48)   Nwamba, O. C.; Echeverria, E.; McIlroy, D. N.; Austin, A.; Shreeve, J. M.; Aston, D. E. Thermal Modification of Graphite for Fast Electron Transport and Increased Capacitance. *ACS Appl. Nano Mater.* **2019**, *2*, 228–240.

(49)   Henry, P. A.; Raut, A. S.; Ubnoske, S. M.; Parker, C. B.; Glass, J. T. Enhanced Electron Transfer Kinetics through Hybrid Graphene-Carbon Nanotube Films. *Electrochem. commun.* **2014**, *48*, 103-106.

(50)   Wang, X.; Wang, W.; Lowry, G.; Li, X.; Guo, Y.; Li, T. Preparation of Palladized Carbon Nanotubes Encapsulated Iron Composites: Highly Efficient Dechlorination for Trichloroethylene and Low Corrosion of Nanoiron. *R. Soc. Open Sci.* **2018**, *5*, 172242.

(51)   Frankel, G. S. Fundamentals of Corrosion Kinetics. In *Active Protective Coatings*; Hughes A., Mol J., Zheludkevich M., Buchheit R. (eds); Springer, Dordrecht. *Springer Ser. Mater. Sci.* **2016**, *233*, pp. 17-32.

(52)   Nicholson, R. S. Theory and Application of Cyclic Voltammetry f m Measurement of Electrode Reaction Kinetics. *Anal. Chem.* **1965**, *37*, 1351–1355.

(53)   Shen, W.-X.; Xu, J.-M.; Dai, S.-G.; Zhang, Z.-F. A Porous and Conductive Graphite Nanonetwork Forming on the Surface of KCu_7S_4 for Energy Storage. *Front. Chem.* **2018**, *6*, 555.

(54)   Pimenta, M. A.; Dresselhaus, G.; Dresselhaus, M. S.; Cançado, L. G.; Jorio, A.; Saito, R. Studying Disorder in Graphite-Based Systems by Raman Spectroscopy. *Phys. Chem. Chem. Phys.* **2007**, *9*, 1276–1291.

(55)   Ferrari, A. C.; Meyer, J. C.; Scardaci, V.; Casiraghi, C.; Lazzeri, M.; Mauri, F.; Piscanec, S.; Jiang, D.; Novoselov, K. S.; Roth, S.; Geim, A. K. Raman Spectrum of Graphene and Graphene Layers. *Phys. Rev. Lett.* **2006**, *97*, 187401.

(56)   Ferrari, A. C. Raman Spectroscopy of Graphene and Graphite: Disorder, Electron-Phonon Coupling, Doping and Nonadiabatic Effects. *Solid State Commun.* **2007**, *143*, 47-57.

(57)   Cançado, L. G.; Pimenta, M. A.; Neves, B. R. A.; Medeiros-Ribeiro, G.; Enoki, T.; Kobayashi, Y.; Takai, K.; Fukui, K. I.; Dresselhaus, M. S.; Saito, R.; orio, A. Anisotropy of the Raman Spectra of Nanographite Ribbons. *Phys. Rev. Lett.* **2004**, *93*, 047403.

(58)   Cançado, L. G.; Pimenta, M. A.; Saito, R.; Jorio, A.; Ladeira, L. O.; Grueneis, A.; Souza-Filho, A. G.; Dresselhaus, G.; Dresselhaus, M. S.; Dresselhaus, M. S. Stokes and Anti-Stokes Double Resonance Raman Scattering in Two-Dimensional Graphite. *Phys. Rev. B - Condens. Matter Mater. Phys.* **2002**, *66*, 035415.

(59)   Nemanich, R. J.; Solin, S. A. First- and Second-Order Raman Scattering from Finite-Size Crystals of Graphite. *Phys. Rev. B* **1979**, *20*, 392.

(60)   Vidano, R. P.; Fischbach, D. B.; Willis, L. J.; Loehr, T. M. Observation of Raman Band Shifting with Excitation Wavelength for Carbons and Graphites. *Solid State Commun.* **1981**, *39*, 341-344.

(61)   Lespade, P.; Marchand, A.; Couzi, M.; Cruege, F. Caracterisation de Materiaux Carbones Par Microspectrometrie Raman. *Carbon* **1984**, *22*, 375-385.

(62)   Vázquez-Santos, M. B.; Geissler, E.; László, K.; Rouzaud, J. N.; Martínez-Alonso, A.; Tascón, J. M. D. Comparative XRD, Raman, and TEM Study on Graphitization of PBO-Derived Carbon Fibers. *J. Phys. Chem. C* **2012**, *116*, 257–268.

(63)   Chia, X.; Eng, A. Y. S.; Ambrosi, A.; Tan, S. M.; Pumera, M. Electrochemistry of Nanostructured Layered Transition-Metal Dichalcogenides. *Chem. Rev*. **2015**, *115*, 11941–11966.

(64)   Lim, C. S.; Tan, S. M.; Sofer, Z.; Pumera, M. Impact Electrochemistry of Layered Transition Metal Dichalcogenides. *ACS Nano* **2015**, *9*, 8474–8483.

(65)   Chia, X.; Ambrosi, A.; Lazar, P.; Sofer, Z.; Pumera, M. Electrocatalysis of Layered Group 5 Metallic Transition Metal Dichalcogenides (MX_2, M = V, Nb, and Ta; X = S, Se, and Te). *J. Mater. Chem. A* **2016**, *4*, 14241-14253.

(66)   Chia, X.; Adriano, A.; Lazar, P.; Sofer, Z.; Luxa, J.; Pumera, M. Layered Platinum Dichalcogenides (PtS_2, $PtSe_2$, and $PtTe_2$) Electrocatalysis: Monotonic Dependence on the Chalcogen Size. *Adv. Funct. Mater.* **2016**, *26*, 4306-4318.

(67)   Chia, X.; Pumera, M. Layered Transition Metal Dichalcogenide Electrochemistry: Journey across the Periodic Table. *Chem. Soc. Rev.* **2018**, *47*, 5602-5613.

(68)   Jaramillo, T. F.; Jørgensen, K. P.; Bonde, J.; Nielsen, J. H.; Horch, S.; Chorkendorff, I. Identification of Active Edge Sites for Electrochemical H_2 evolution from MoS2nanocatalysts. *Science* **2007**, *317*, 100-102.

(69)   Back, S.; Yeom, M. S.; Jung, Y. Active Sites of Au and Ag Nanoparticle Catalysts for CO_2 Electroreduction to CO. *ACS Catal.* **2015**, *5*, 5089–5096.

(70)   Rowley-Neale, S. J.; Brownson, D. A. C.; Smith, G. C.; Sawtell, D. A. G.; Kelly, P. J.; Banks, C. E. 2D Nanosheet Molybdenum Disulphide (MoS_2) Modified Electrodes Explored towards the Hydrogen Evolution Reaction. *Nanoscale* **2015**, *7*, 18152-18168.

(71)   Yu, Y.; Huang, S. Y.; Li, Y.; Steinmann, S. N.; Yang, W.; Cao, L. Layer-Dependent Electrocatalysis of MoS_2 for Hydrogen Evolution. *Nano Lett.* **2014**, *14*, 553–558.

(72)   Kagkoura, A.; Tzanidis, I.; Dracopoulos, V.; Tagmatarchis, N.; Tasis, D. Template Synthesis of Defect-Rich MoS_2-Based Assemblies as Electrocatalytic Platforms for Hydrogen Evolution Reaction. *Chem. Commun.* **2019**, *55*, 2078-2081.

(73)   Khalil, A.; Liu, Q.; Muhammad, Z.; Habib, M.; Khan, R.; He, Q.; Fang, Q.; Masood, H. T.; Rehman, Z. U.; Xiang, T.; Wu, C. Q.; Song, L. Synthesis of Ni_9S_8/MoS_2 Heterocatalyst for Enhanced Hydrogen Evolution Reaction. *Langmuir* **2017**, *33*, 5148–5153.

(74)   Velický, M.; Toth, P. S. From Two-Dimensional Materials to Their Heterostructures: An Electrochemist's Perspective. *Appl. Mater. Today* **2017**, *8*, 68-103.

(75)   Xia, J.; Yan, J.; Shen, Z. X. Transition Metal Dichalcogenides: Structural, Optical and Electronic Property Tuning via Thickness and Stacking. *FlatChem*. **2017**, *4*, 1-19.

(76)   Li, M. Y.; Chen, C. H.; Shi, Y.; Li, L. J. Heterostructures Based on Two-Dimensional Layered Materials and Their Potential Applications. *Mater. Today* **2016**, *19*, 322-335.

(77)   Verma, A.; Kotaka, T.; Tabuchi, Y.; Mukherjee, P. P. Mechano-Electrochemical Interaction and Degradation in Graphite Electrode with Surface Film. *J. Electrochem. Soc.* **2018**, *165*, A2397-A2408.

(78)   Goriparti, S.; Miele, E.; De Angelis, F.; Di Fabrizio, E.; Proietti Zaccaria, R.; Capiglia, C. Review on Recent Progress of Nanostructured Anode Materials for Li-Ion Batteries. *J. Power Sources* **2014**, *257*, 421-443.

(79)   Wang, Z. L.; Xu, D.; Wang, H. G.; Wu, Z.; Zhang, X. B. In Situ Fabrication of Porous Graphene Electrodes for High-Performance Energy Storage. *ACS Nano* **2013**, *7*, 2422–2430.

(80)   Zhang, R.; Bao, J.; Pan, Y.; Sun, C.-F. Highly Reversible Potassium-Ion Intercalation in Tungsten Disulfide. *Chem. Sci.* **2019**, *10*, 2604-2612.

(81)   Xu, J.; Dou, Y.; Wei, Z.; Ma, J.; Deng, Y.; Li, Y.; Liu, H.; Dou, S. Recent Progress in Graphite Intercalation Compounds for Rechargeable Metal (Li, Na, K, Al)-Ion Batteries. *Adv. Sci.* **2017**, *4*, 1700146.

(82)   Xu, J.; Wang, D.; Lian, R.; Gao, X.; Liu, Y.; Gogotsi, Y.; Chen, G.; Wei, Y. Structural Prediction and Multilayer Li^+ Storage in Two-Dimensional VC_2 Carbide Studied by First-Principles Calculations. *J. Mater. Chem. A* **2019**, DOI:10.1039/C9TA01476D.

(83)   Hui, J.; Burgess, M.; Zhang, J.; Rodríguez-López, J. Layer Number Dependence of Li^+ Intercalation on Few-Layer Graphene and Electrochemical Imaging of Its Solid-Electrolyte Interphase Evolution. *ACS Nano* **2016**, *10*, 4248–4257.

(84)   Tao, L.; Qiao, M.; Jin, R.; Li, Y.; Xiao, Z.; Wang, Y.; Zhang, N.; Xie, C.; He, Q.; Jiang, D.; Yu, G.; Li, Y.; Wang, S. Bridging the Surface Charge and Catalytic Activity of a Defective Carbon Electrocatalyst. *Angew. Chemie Int. Ed.* **2019**, *58*, 1019–1024.

(85)   Maass, S.; Finsterwalder, F.; Frank, G.; Hartmann, R.; Merten, C. Carbon Support Oxidation in PEM Fuel Cell Cathodes. *J. Power Sources* **2008**, *176*, 444-451.

(86)   Avasarala, B.; Moore, R.; Haldar, P. Surface Oxidation of Carbon Supports Due to Potential Cycling under PEM Fuel Cell Conditions. *Electrochim. Acta* **2010**, *55*, 4765-4771.

(87)   Abouelamaiem, D. I.; Mostazo-López, M. J.; He, G.; Patel, D.; Neville, T. P.; Parkin, I. P.; Lozano-Castelló, D.; Morallón, E.; Cazorla-Amorós, D.; Jorge, A. B.; Wang, R.; Ji , S.; Titirici, M.-M.; Shearing, P. R.; Bretta, D. J. L. New Insights into the Electrochemical Behaviour of Porous Carbon Electrodes for Supercapacitors. *J. Energy Storage* **2018**, *19*, 337–347.

(88)   Gao, Y.; Wang, Z.; Lu, G. Atomistic Understanding of Structural Evolution, Ion Transport and Oxygen Stability in Layered $NaFeO_2$. *J. Mater. Chem. A* **2019**, *3*, 2619–2625.

(89)   Forouzandeh, F.; Li, X.; Banham, D. W.; Feng, F.; Ye, S.; Birss, V. Understanding the Corrosion Resistance of Meso- and Micro-Porous Carbons for Application in PEM Fuel Cells. *J. Electrochem. Soc.* **2018**, *165*, F3230-F3240.

(90)   Gupta, G.; Slanac, D. A.; Kumar, P.; Wiggins-Camacho, J. D.; Kim, J.; Ryoo, R.; Stevenson, K. J.; Johnston, K. P. Highly Stable Pt/Ordered Graphitic Mesoporous Carbon Electrocatalysts for Oxygen Reduction. *J. Phys. Chem. C* **2010**, *114*, 10796–10805.

(91)   Kuila, T.; Mishra, A. K.; Khanra, P.; Kim, N. H.; Lee, J. H. Recent Advances in the Efficient Reduction of Graphene Oxide and Its Application as Energy Storage Electrode Materials. *Nanoscale* **2013**, *5*, 52-71.

(92)   Randviir, E. P.; Banks, C. E. Electrochemical Impedance Spectroscopy: An Overview of Bioanalytical Applications. *Anal. Methods*. **2013**, *5*, 1098-1115.

(93)   Song, Y.; Hu, H.; Feng, M.; Zhan, H. Carbon Nanotubes with Tailored Density of Electronic States for Electrochemical Applications. *ACS Appl. Mater. Interfaces* **2015**, *7*, 25793–25803.

(94)   Ambrosi, A.; Bonanni, A.; Sofer, Z.; Cross, J. S.; Pumera, M. Electrochemistry at Chemically Modified Graphenes. *Chem. - A Eur. J.* **2011**, *17*, 10763 – 10770.

(95)   Erickson, A.; Ballinger, T. Ultra-Thin AFM Enables Integration with Light Microscope. *Micros. Today* **2018**, *26*, 28-32.

(96)   Fakharan, Z.; Naji, L.; Madanipour, K. Surface Roughness Regulation of Reduced-Graphene Oxide/Iodine – Based Electrodes and Their Application in Polymer Solar Cells. *J. Colloid Interface Sci.* **2019**, *540*, 272-284.

(97)   Suzuki, S.; Watanabe, Y.; Homma, Y.; Fukuba, S. Y.; Heun, S.; Locatelli, A. Work Functions of Individual Single-Walled Carbon Nanotubes. *Appl. Phys. Lett.* **2004**, *85*, 127.

(98)   Morosan, E.; Natelson, D.; Nevidomskyy, A. H.; Si, Q. Strongly Correlated Materials. *Adv. Maters.* **2012**, *24*, 4896-4923.

(99)   Joachim, C.; Gimzewski, J. K.; Aviram, A. Electronics Using Hybrid-Molecular and Mono-Molecular Devices. *Nature* **2000**, *408*, 541–548.

(100)   Boopathi, S.; Narayanan, T. N.; Senthil Kumar, S. Improved Heterogeneous Electron Transfer Kinetics of Fluorinated Graphene Derivatives. *Nanoscale* **2014**, *6*, 10140-10146.

Chapter 5: Conclusion

A new thermal treatment protocol for graphites resulted in steady and consistent ΔE_P values from aqueous cyclic voltammetry over 64 days with no appreciable aging from air oxidation on storage. The initially enhanced and sustained heterogeneous rate constants of graphite samples when probed with the $Fe(CN)_6^{3-/4-}$ redox couple remains essentially unchanged over the test periods. All graphite types exhibit the same resistance to aging and very similar behaviors relative to their controls through results from FTIR, Raman, XPS, UPS and water contact angle measurements. The facile and sustained HET kinetics in 1 mM ferri-ferrocyanide solution is attributable to structural and electronic changes and not from surface functional group changes or edge-density contributions.

These findings suggest that the same or very similar underlying mechanism(s) via thermal treatment promote a more stable structure as a well-ordered or higher-order state (e.g., mainly aromatic, crystalline microstates) than the original graphites, being described by the folding funnel model. This new graphite state, or ensemble, possesses a degree of crystallinity along the lattice sites that enables carrier hopping irrespective of adventitious oxygen-containing and hydrocarbon moieties synonymous with aging-induced sluggish electron transfer kinetics. This then suggests that the electronic structure is less perturbed and signifies a reduction of Coulombic (repulsive) contributions. The one-dimensional Hubbard model explains the surface-to-electronic chemistry of heat-treated graphite materials having enhanced and sustained electronic/electrochemical properties compared to their controls regardless of any adventitious functional surface groups indicated or even those changes that would remain potentially undetected as below the limits of investigation.

Water contact angles reveal sensitivity to the electronic nature of the treated graphites as distinct from the expected surface chemistry effects. Additionally, capacitance of graphite felts arise from sub-surface and not surface-bound oxygen-containing species as previously suggested. The overall increase in DOS with enhanced and delocalized π over σ traits cause electronic property enhancements in the treated graphites. Chemical structural disorder in graphite provides preferential initiation sites for the thermally-induced structural and electronic re-organization in the treated samples. Irrespective of the enhanced and sustained HET kinetics and capacitance of the treated graphite, there were no compromises on their structural and functional integrity. Enhanced electron tunneling across the interfaces, rather than simple interfacial transfer of charges was suggested as the main reason for the increased HET kinetics of the treated over the pristine graphites.

Based on the fast and sustained HET kinetics of the thermally-treated graphite electrode materials, this new treatment protocol can be used in applications hinging on fast electron transfer and/or increased capacitance, such as sensing, electro-oxidative reactions in water purification, batteries and supercapacitors, catalysis, oxygen reduction for fuel cell, HPLC detectors, and in the semiconductor industry.

Appendix A - Thermal Modification of Graphite for Fast Electron Transport and Increased Capacitance

(d1) **(d2)** **(e1)** **(e2)** **(f1)** **(f2)**
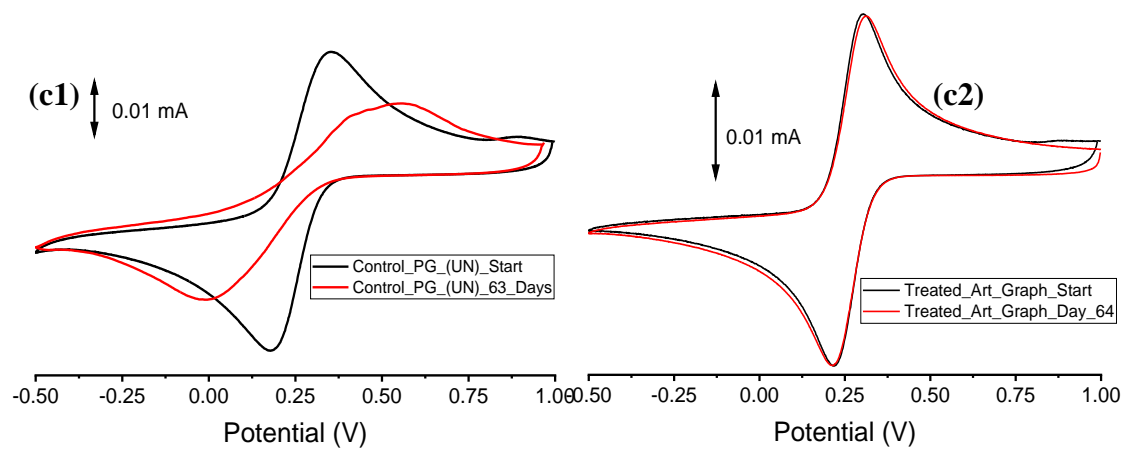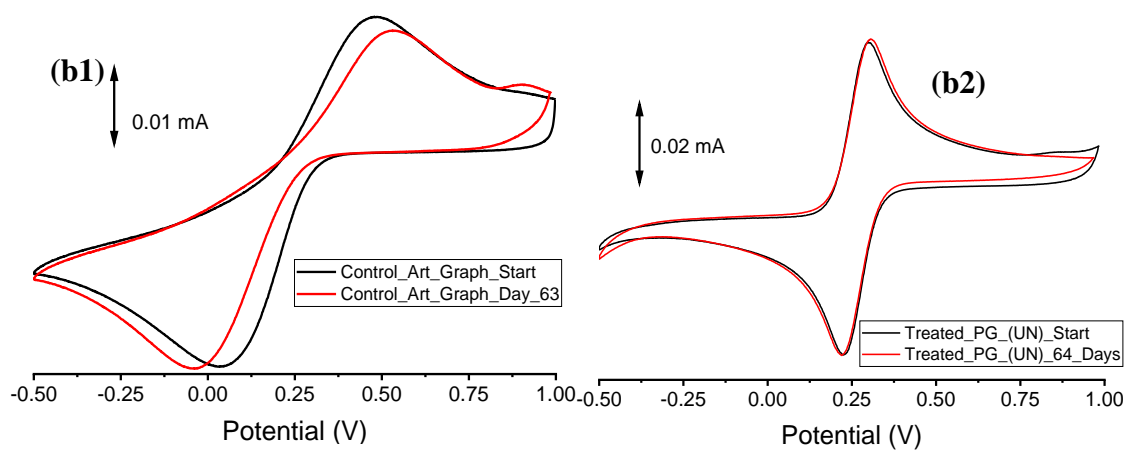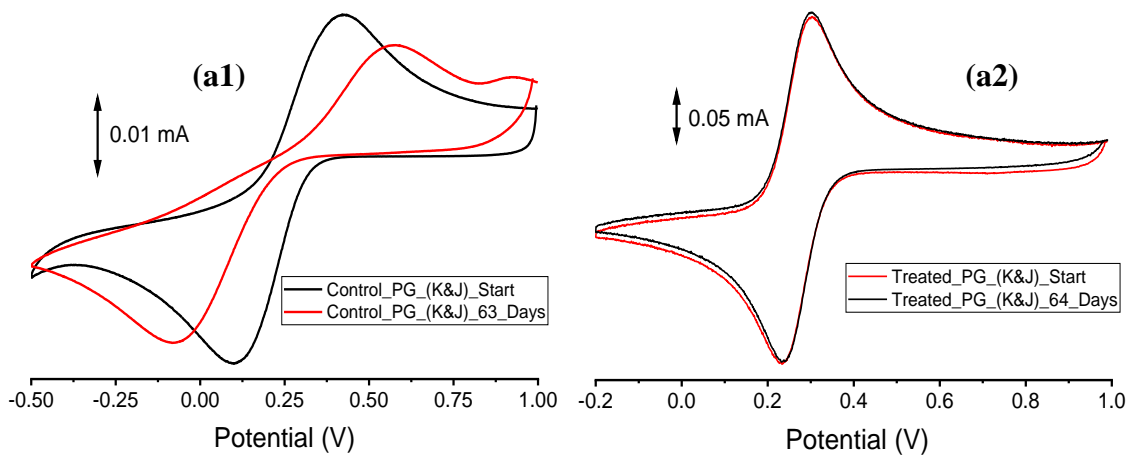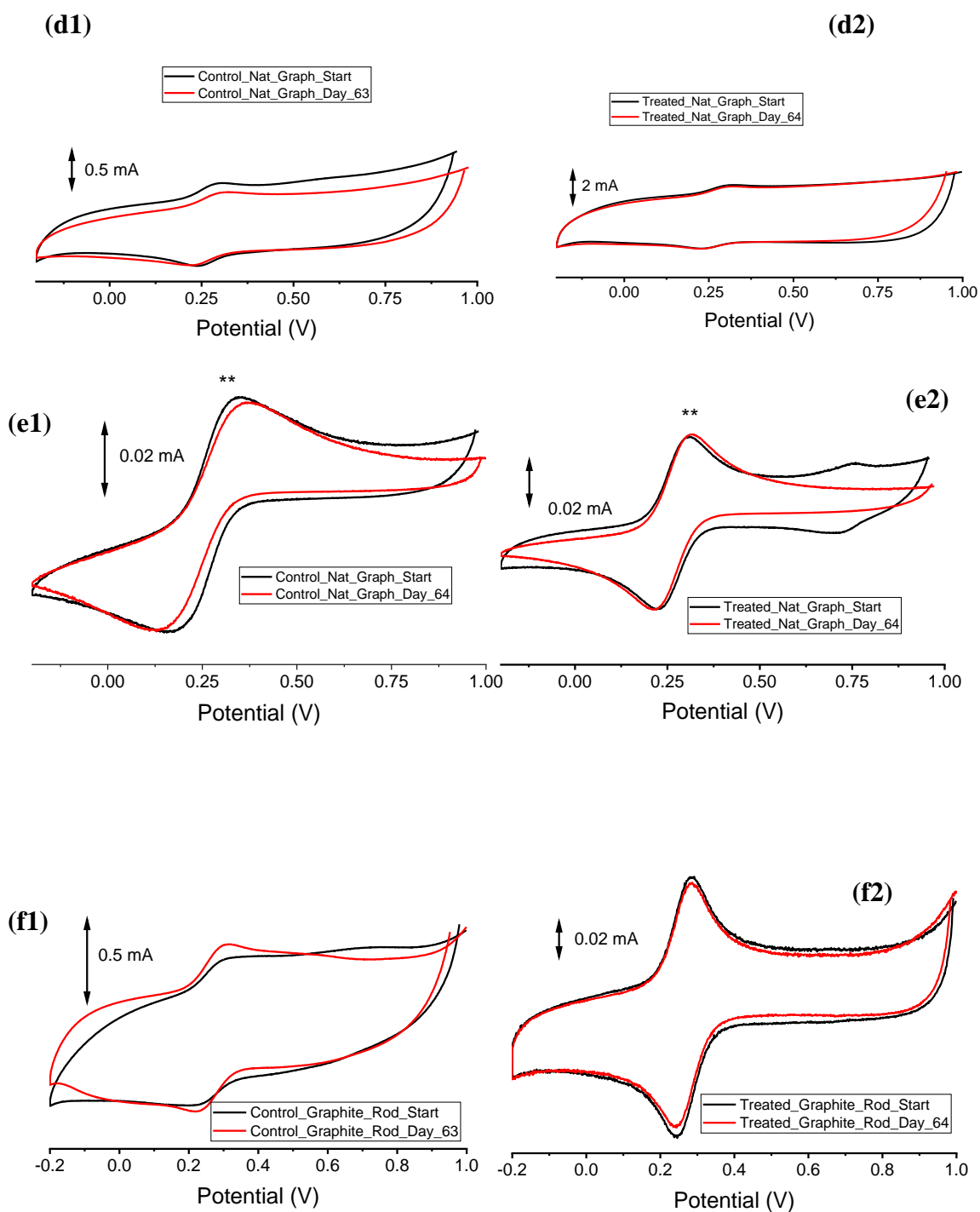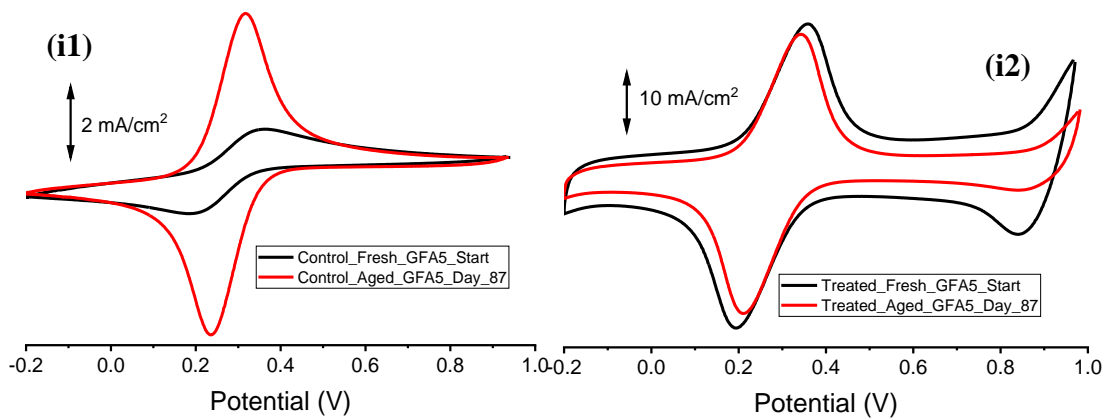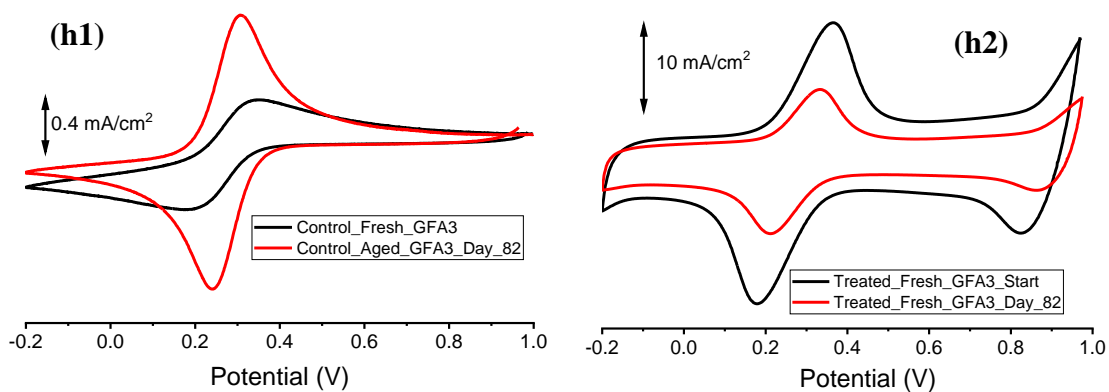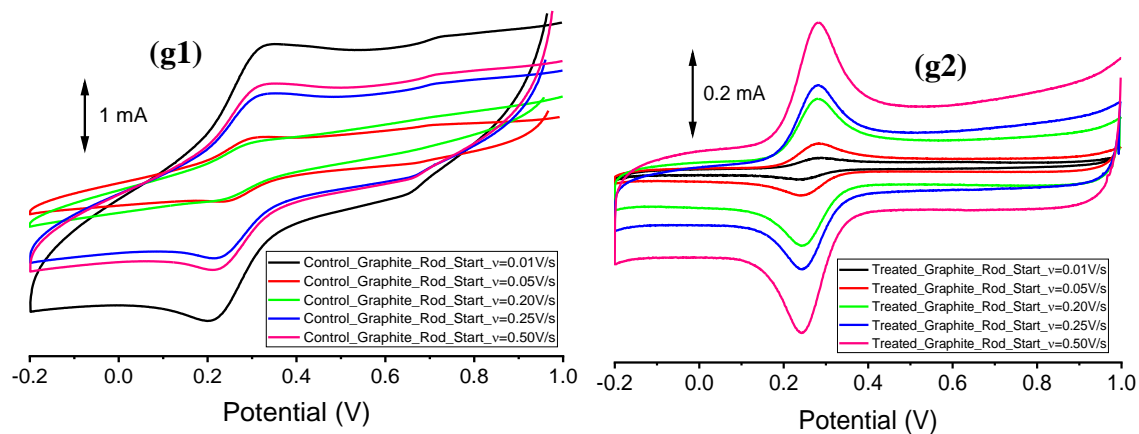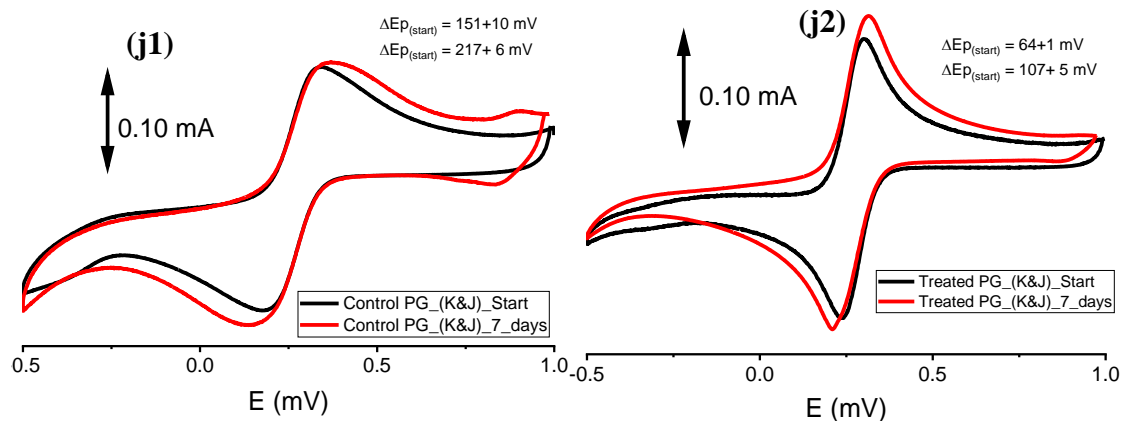
Figure S2.1: a1 to i2 are the cyclic voltamograms for the aged graphites in air for at least 63 days (pristine) and 64 days (treated). j1 and j2 are representative cyclic voltamograms of aged pristine and treated PG(K&J) Magnetics in 1mM ferri-ferrocyanide for 7 days.

** Mechanical stress or agitation by exfoliating the borders (edges) of the Natural Graphite

In other to accentuate the possible thermal modification effect on Natural Graphite, the borders or edges of both the control and treated Natural Graphite were peeled off to mechanically stress and thus "agitate" the graphite molecule, resulting in surface roughening, deformation and ultimately changing its surface chemistry.[1] This is supposed to stress the material and test the efficacy of the treatment. Indeed, the mechanical stress reduced the capacitance of both the control and the treated but while the control had increased ΔEp and more pronounced aging effects, the treated exhibited very little aging tendency as is deduced from the ΔEP at start and end of experiment. Besides, the control now starts off with a wide ΔEp (**see Table 2.1**).

The ΔEp of 40mV for the treated graphite is an indication of enhanced porosity and the exhibition of thin layer tendency. Besides, the fact that the treated graphite rod shows huge capacitance increases with increasing scan rate (ν) without any change in ΔEp is a testament to the porosity of the thermally treated material in comparison to its control. This is further supported by its WCA measurements in where the treated material was now totally porous, with water percolating through the fabric of the material. Increasing capacitance at higher scan rate could be explained by the porosity of the material in which higher scan rates only serves to drive ions further into the matrix of the material previously

inaccessible by mere percolation as is obtained with low scan rates. Another point to note is that the increase in scan rate resulted in capacitance increase without asymmetric behavior (compare with control) suggestive of a decrease in charge transfer resistance and faster ion diffusion (rather than the opposite) at higher scan rate (due to the now enhanced porosity of the material). The implication of this finding is that we now have a material with promising candidature for supercapacitors; combining both high-energy storage densities with fast and or high levels of power delivery.[2] [3] The area of the electrodes are 0.331 cm^2.

The control and aged graphite felts have decreased ΔE_p with increased oxidative and cathodic peak current densities without accompanying capacitance increase. This behavior is suggestive of more exposed surface area of the fiber bundles without an accession of the capacitive advantage of these exposed bundles.

(a)

(b)

(b)

(bi)

(c)

100 μm   Mag = 100 X   EHT = 10.00 kV   Signal A = SE2
Signal B = SE2

(ci)

100 μm   Mag = 100 X   EHT = 10.00 kV   Signal A = SE2
Signal B = SE2

(d)

10 μm   Mag = 500 X   EHT = 10.00 kV   Signal A = SE2
Signal B = SE2

(di)

10 μm   Mag = 500 X   EHT = 10.00 kV   Signal A = SE2
Signal B = SE2

(e)

(ei)

(f)

(fi)
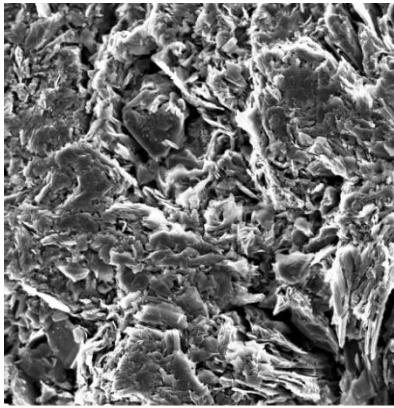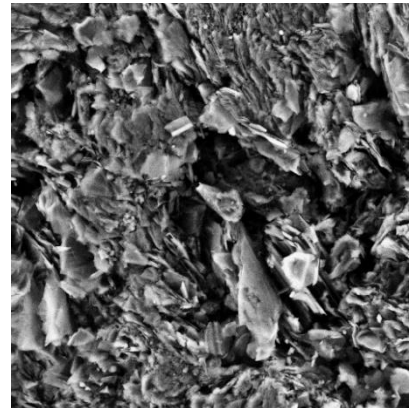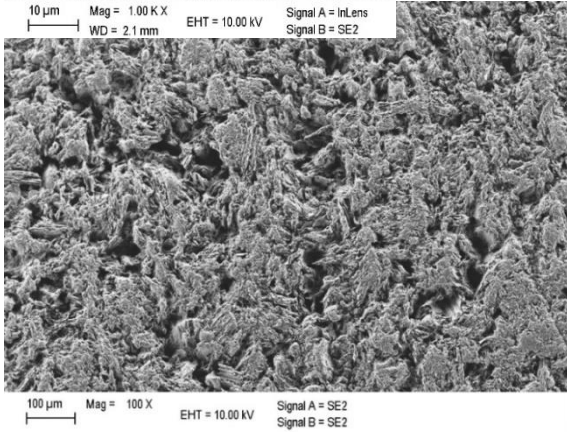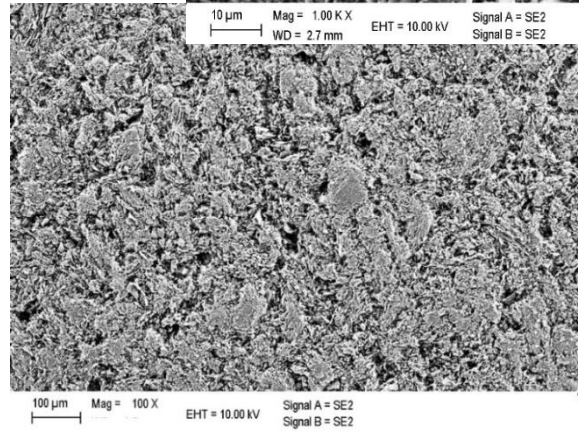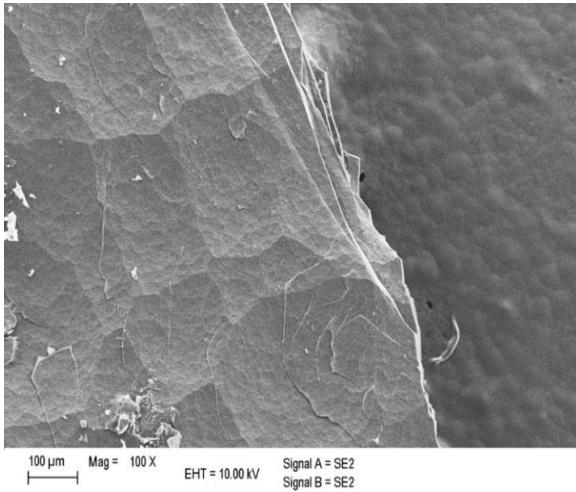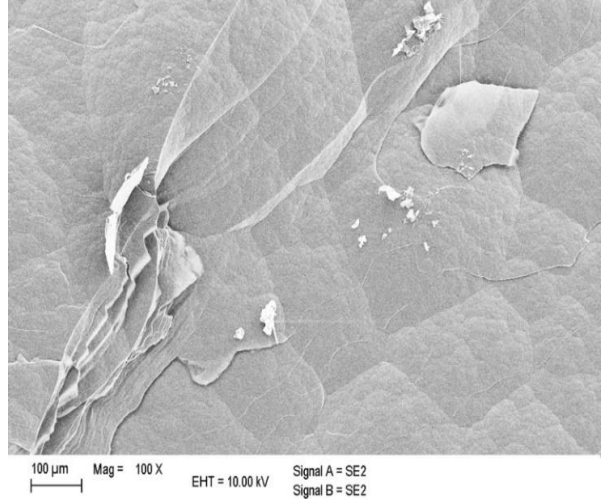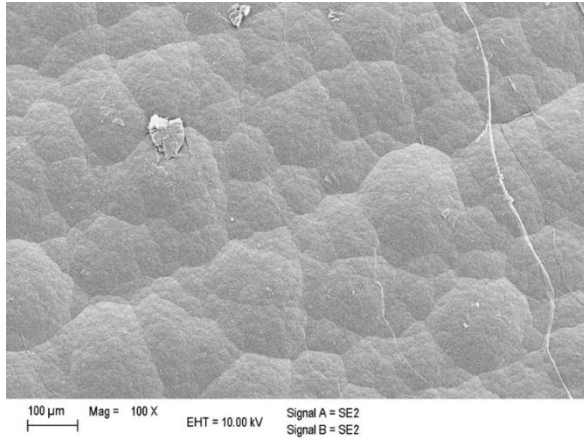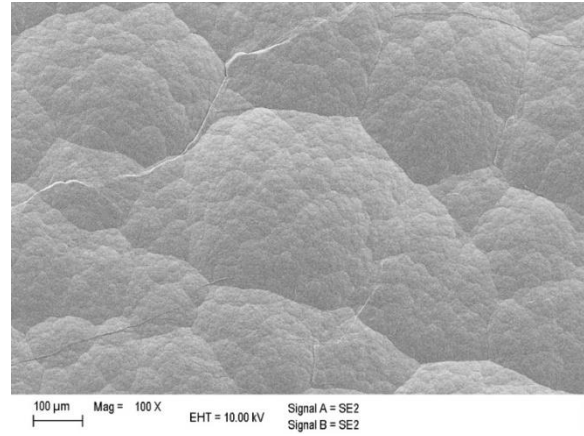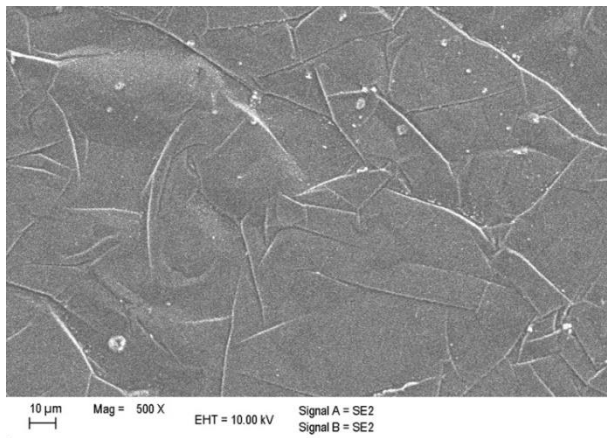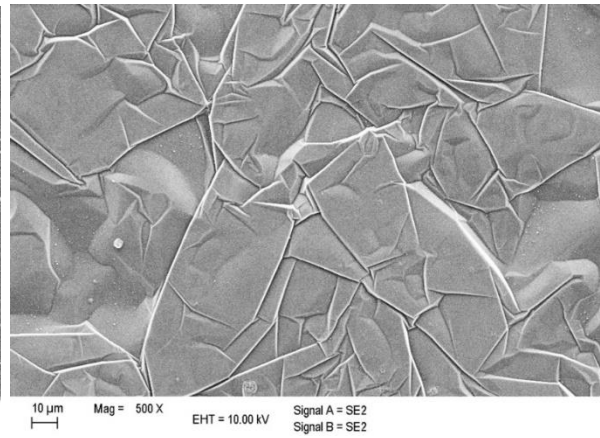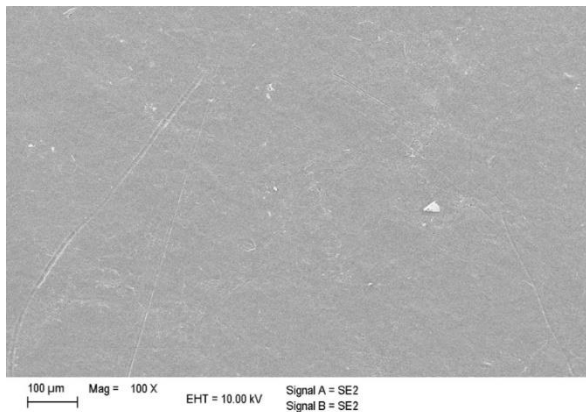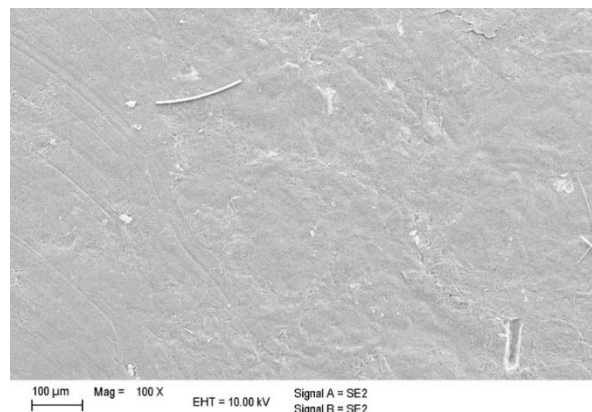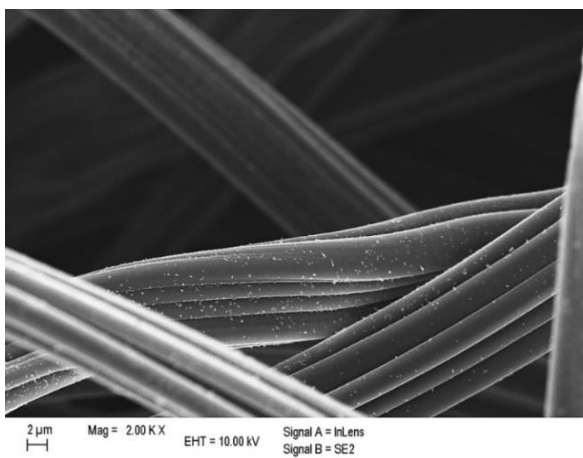
(g)　　　　　　　　　　　　　　　**(gi)**
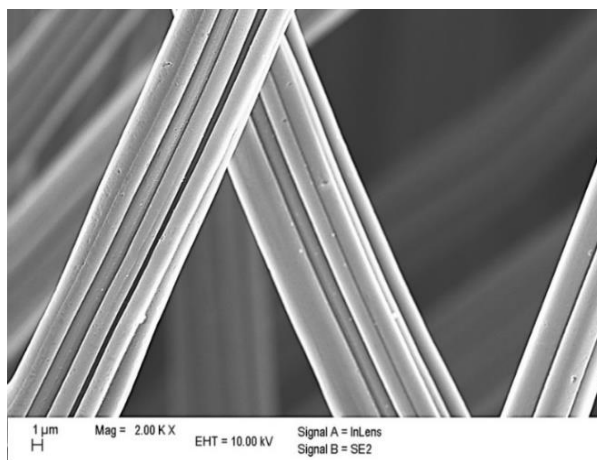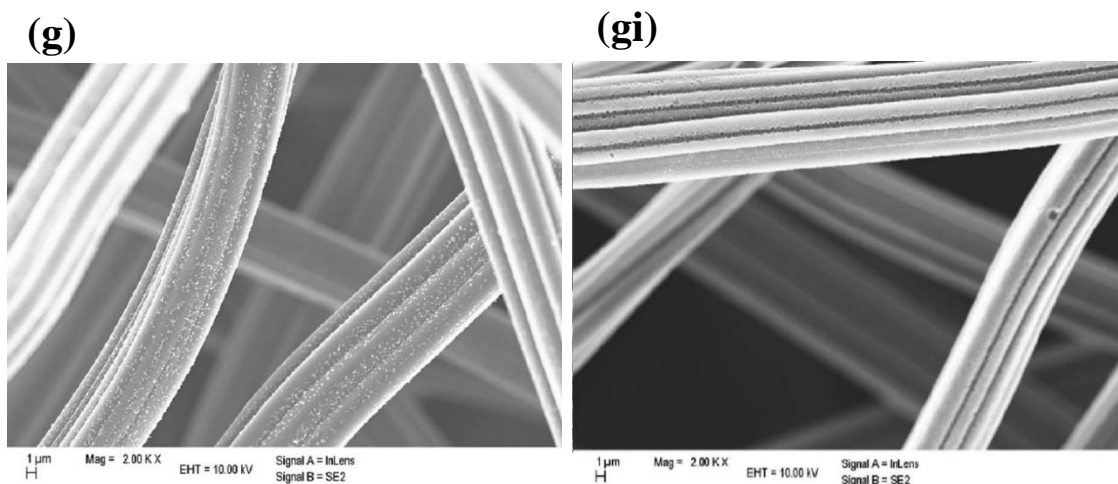
Figure S2.2: a (left) and ai (right) are the SEM images of the control and treated graphite rod. Inset are their magnifications (1.0k X). The images show no apparent difference(s) in surface morphology before and after thermal treatment. b (left) and bi (right) are the SEM images of the control and treated PG (K&J). The absence of pits or edges suggest that edge density induced from pitting is not a contributor to the enhanced facile heterogeneous electron transfer kinetics either early on or later during aging. c (left) and ci (right) are the SEM images of the control and treated PG (United Nuclear). The absence of pits or edges suggest that edge density induced from pitting is not a contributor to the enhanced facile heterogeneous electron transfer kinetics either early on or later during aging. d (left) and di (right) are the SEM images of the control and treated Artificial graphite. There is no apparent difference in surface morphology to account for the differences in electron transport capability. e (left) and ei (right) are the SEM images of the control and treated Natural graphite. Besides the treated sample looking more crusted, there is no apparent difference in surface morphology to account for the differences in their electronic properties. f (left) and fi (right) are the SEM images of the control and treated GFA3. g (left) and gi (right) are the SEM images of the control and treated GFA3.

(a)
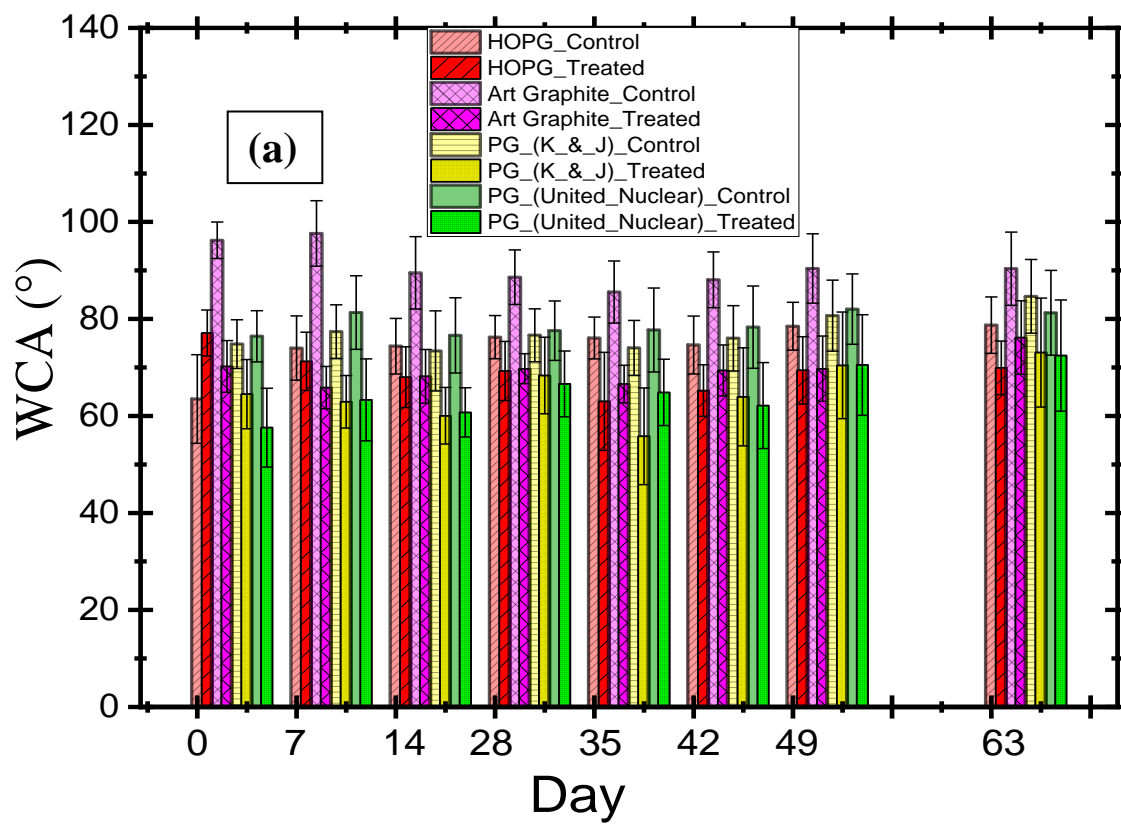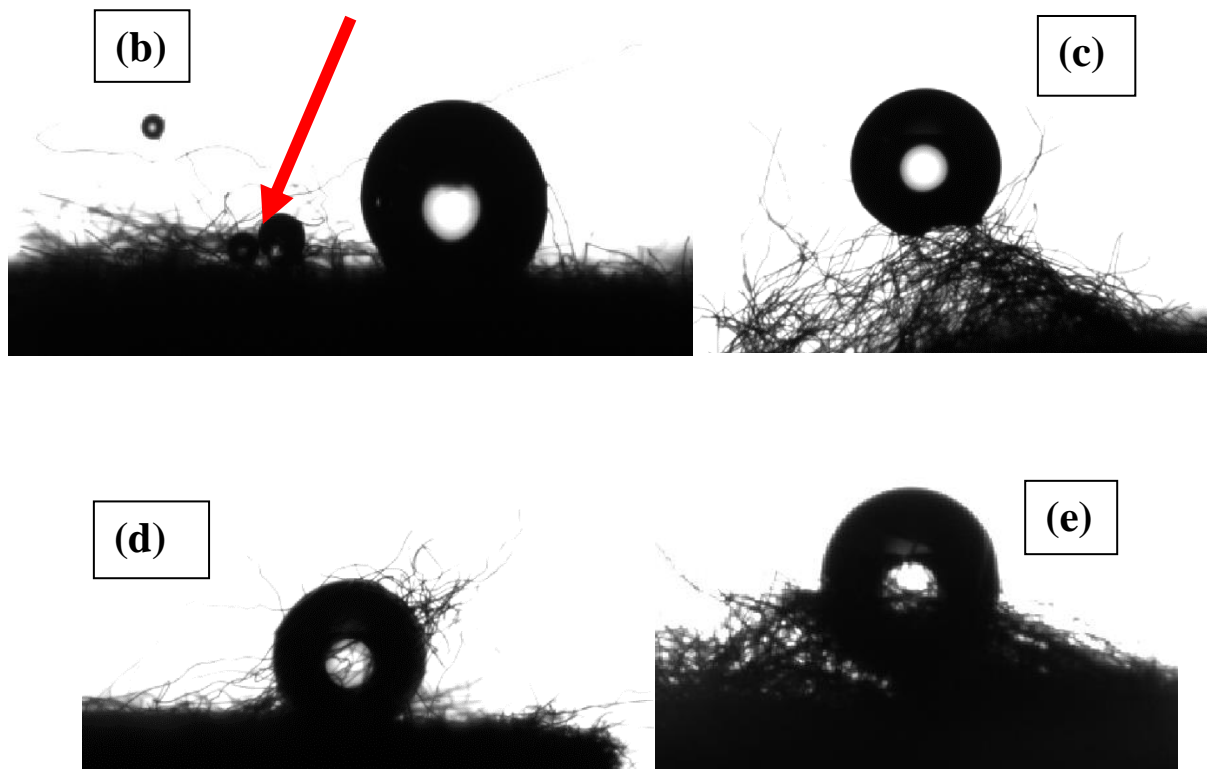
Figure S2.3: Water contact angles (WCA) with (a) HOPG at the numbered day of test (0, 7, 14, 21, 28, 35, 42, 63) clustered from left-to-right with artificial graphite, PG(K&J), and PG(UN) treated sample data overlaying the control data of mostly higher values; **(b-e):** In these pictures taken on the 35th day of the experiment, water had just been pushed through the fiber matrix at the spot indicated by the arrow (**b**). There is apparent wetting at the spot indicated by the red arrow, yet water droplets, beading at angles of 180° can be seen at the site of the forced entry through the felt (**c-e**). In contrast, there are two water drops on the right side of this picture (**b**), indicating regions of non-wetting or hydrophobicity.
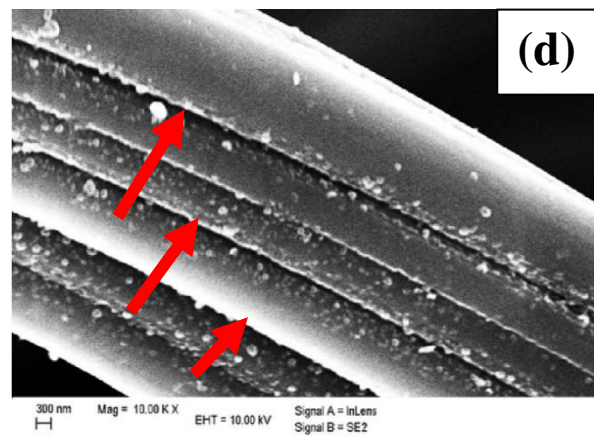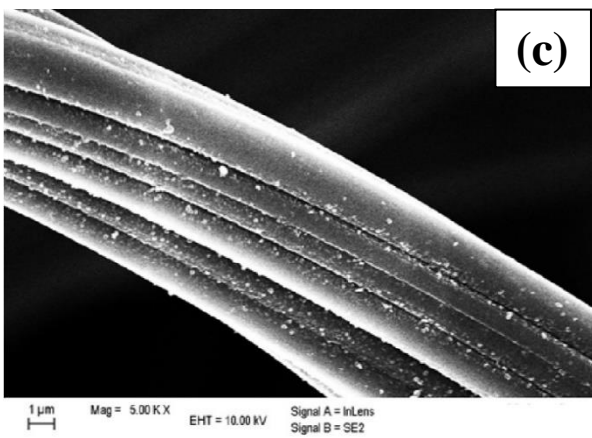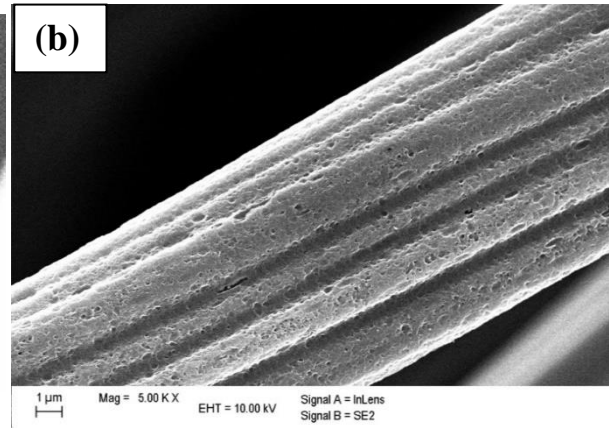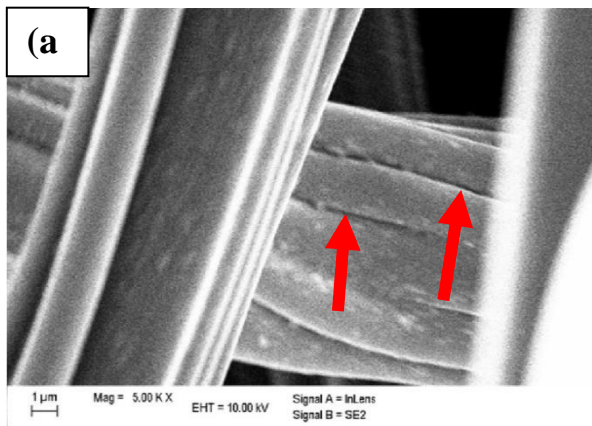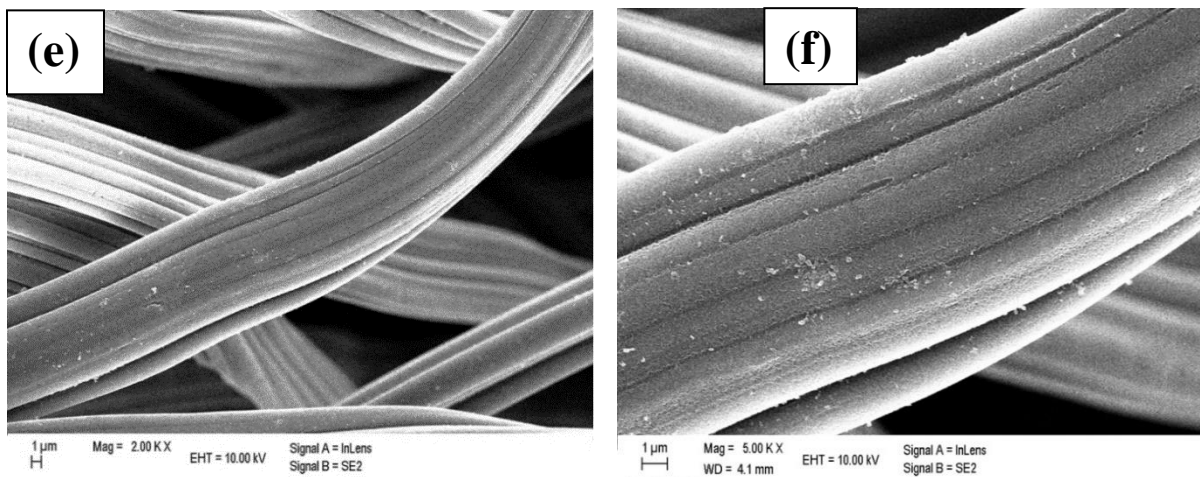
Figure S2.4 (a and b): The SEM of, (a) control and aged GFA3 and (b) treated and Aged GFA3. The red arrows point at possible places where the fiber bundles are splitting open to allow electrolyte and water entry. These fiber degradations are the main contributors to the porosity of the materials as revealed by CV. **Figure S2.4 (c-f):** The SEM of (c, d) control and aged GFA5 and (e, f) treated and Aged GFA3. The red arrows point at possible places where the fiber bundles are split open to allow electrolyte and water entry. These fiber degradations are the main path to the porosity of the materials as revealed by CV.
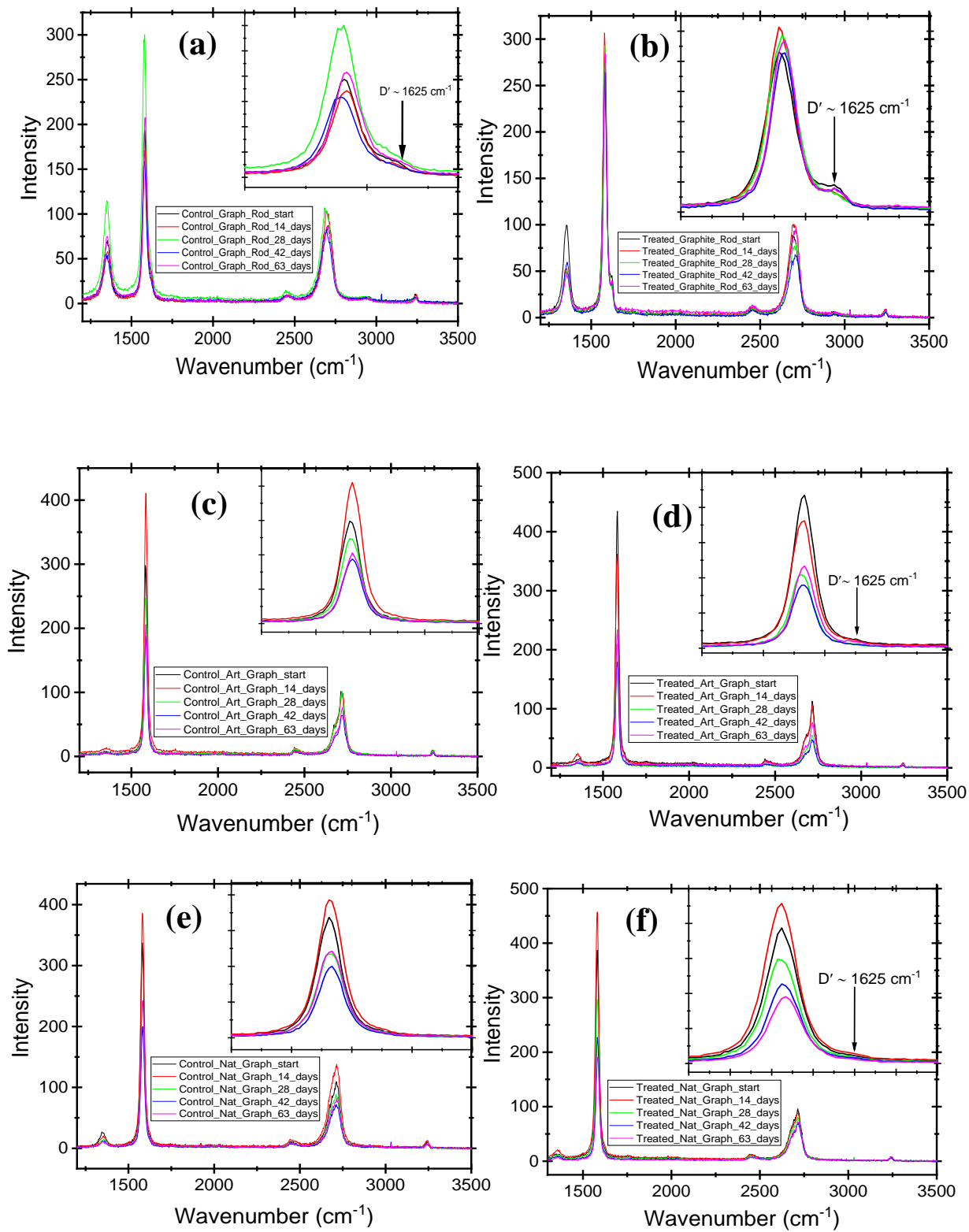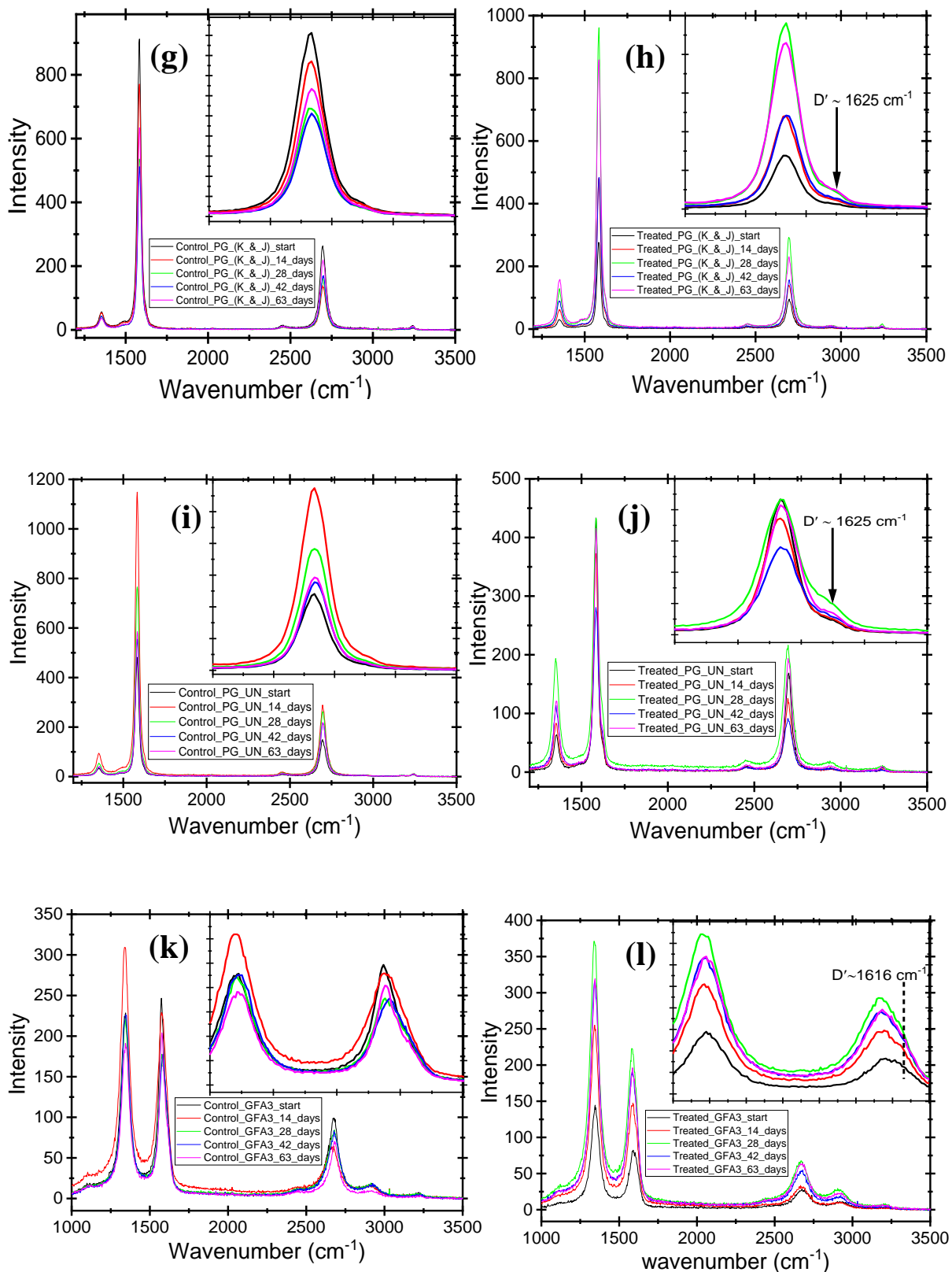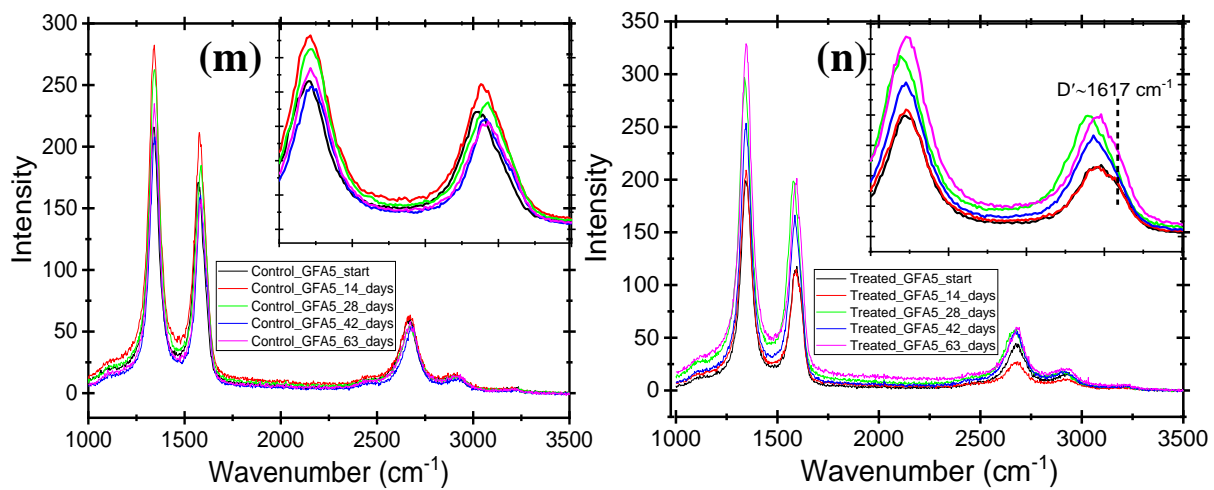
Figure S2.5 (a-n): The Raman spectra of the control and treated graphites from start to the end of the experiment.

Table S2.1: Lamellar spacing, La (nm) calculated from the Raman data

Electrode	Type	0 day (start)	14 days	28 days	42 days	63 days
HOPG-ZYH	C*	-	-	-	-	-
	T	999.91 ± 222.41	1271.6 ± 245.62	800.62 ± 93.48	710.19 ± 82.92	841.23 ± 35.44
PG_(K&J)	C	304.27 ± 6.87	201.32 ± 64.67	258.84 ± 23.22	227.26 ± 7.56	310.70 ± 19.23
	T	162.83 ± 11.57	154.54 ± 5.34	159.84 ± 13.71	104.03 ± 3.70	133.62 ± 65.83
PG_(UN)	C	274.36 ± 20.33	217.15 ± 38.12	254.94 ± 14.93	251.97 ± 19.52	248.61 ± 33.23
	T	119.33 ± 13.20	58.56 ± 25.25	44.21 ± 1.49	44.88 ± 2.71	67.27 ± 4.21
Art graphite	C	795.35 ± 101.28	749.39 ± 171.64	682.86 ± 106.10	703.65 ± 74.58	653.00 ± 100.14
	T	821.60 ± 300.19	442.42 ± 224.72	539.65 ± 94.63	515.54 ± 114.05	443.71 ± 80.11
Nat graphite	C	498.03 ± 284.43	523.82 ± 234.19	315.64 ± 38.11	548.50 ± 285.66	330.05 ± 119.48
	T	491.17 ± 72.90	426.48 ± 74.43	506.56 ± 53.30	502.06 ± 41.90	412.25 ± 86.53
Graphite rod	C	69.10 ± 23.11	46.27 ± 11.95	49.14 ± 2.91	65.13 ± 8.05	107.34 ± 56.39
	T	87.88 ± 49.65	136.77 ± 28.78	88.76 ± 27.06	102.14 ± 15.19	92.75 ± 17.13
GFA3	C	18.32 ± 3.92	15.32 ± 1.00	14.47 ± 1.25	14.61 ± 0.51	17.20 ± 3.25
	T	10.27 ± 1.62	11.40 ± 0.27	10.90 ± 0.66	11.67 ± 0.07	11.94 ± 0.09
GFA5	C	13.94 ± 1.03	15.21 ± 2.66	15.79 ± 2.75	15.44 ± 0.74	15.19 ± 2.13
	T	11.43 ± 0.28	10.47 ± 0.14	12.68 ± 0.31	12.48 ± 0.35	15.43 ± 0.72

* The HOPG-ZYH control had no D band required for the calculation of the lamellar spacing, La

Peak	Position (eV)	Area	FWHM (eV)	% L	% G
Aliphatic O	532.029	47.025	2.231	12	88

Peak	Position (eV)	Area	FWHM (eV)	% L	% G
Oxides in carbon flakes	535.474	79.174	3.175	0	100

(c)

Peak	Position (eV)	Area	FWHM (eV)	% L	% G
O bridging Si & aliph C	533.059	891.05	3.06	13	87
O in ethers, OH, COOH, lactone	532.854	347.9	1.788	0	100

(d)

Peak	Position (eV)	Area	FWHM (eV)	% L	% G
O bridging Si & aliph C	532.509	284.655	3.779	0	100
O in ethers, OH, COOH, lactone	532.917	536.734	2.414	3	97

Peak	Position (eV)	Area	FWHM (eV)	% L	% G
SiO$_4$	102.21	85.637	1.874	31	69
Si-O-Si	103.173	40.974	2.073	100	0

Peak	Position (eV)	Area	FWHM (eV)	% L	% G
Si-OH	102.713	76.29	2.822	11	89

Figure S2.6: The XPS plots of HOPG-ZYH for (a) control & fresh HOPG-ZYH (O1s), (b) treated & fresh HOPG-ZYH (O1s), (c) control & aged HOPG-ZYH (O 1s), (d) treated & aged HOPG-ZYH (O 1s), (e) control & aged HOPG-ZYH (Si 2p), and (f) treated & aged HOPG-ZYH (Si 2p).

Supporting Information (Index A)

Thus, employing the Hubbard model, in its simplistic form as presented by Tasaki[4] to treat the new crystalline nature of the thermally annealed graphites, let's treat its lattice Λ as a collection of sites $x, y, \cdots$ By introducing the term $c^{\dagger}_{x,\sigma}$, we represent an operator which creates an electron with spin $\sigma = \uparrow, \downarrow$ at site $x \in \Lambda$. Thus, the corresponding annihilation operator is $c_{x,\sigma}$, and $n_{x,\sigma} = c^{\dagger}_{x,\sigma} c_{x,\sigma}$ is the number operator. Been electrons, these fermion operators obey the canonical anticommutation relations

$$\left\{ c^{\dagger}_{x,\sigma} c_{x,\tau} \right\} = \delta_{x,y} \delta_{\sigma,\tau}$$

and

$$\left\{ c^{\dagger}_{x,\sigma}, c^{\dagger}_{y,\tau} \right\} = \left\{ c_{x,\sigma}, c_{y,\tau} \right\} = 0$$

With these terms established and outlined, we will define the Hamiltonian of the Hubbard model as the sum of two energy components such that

$$H = H_{hop} + H_{int}$$

Substituting the terms already defined above into the hopping Hamiltonian H_{hop}, we have

$$H_{hop} = \sum_{x,y \in \Lambda} \sum_{\sigma = \uparrow, \downarrow} t_{x,y} c^{\dagger}_{x,\sigma} c_{y,\sigma}$$

Whereby $t_{x,y} = t_{y,x}$, which is assumed to be real, represents the quantum mechanical probability that an electron hops from site x to y (or from y to x)

The interaction Hamiltonian H_{int} is represented as

$$H_{int} = \sum_{x \in \Lambda} \sum_{\sigma=\uparrow,\downarrow} U_x n_x, _\sigma n_x, \chi_{\theta,x,\sigma},$$

$$H_{int} = \sum_{x \in \Lambda} U_x n_x, _\uparrow n_{x,\downarrow}, _\uparrow \chi_{\theta,x,\downarrow}$$

Where $U_x > 0$ is a constant. The Hamiltonian represents a non-linear interaction which raises the energy by U_x when two electrons occupy a single-orbital at x. We have introduced a shielding or screening factor, χ in the Hubbard interaction Hamiltonian term, H_{int} in which the repulsion energy (as represented by the Coulombic energy) is greater than 0 but diminished by the additional term, χ, − which has a negative value − and can be interpreted as the screening of the Coulomb interaction by the electrons in different orbital states. We have introduced an angle parameter, θ to the screening factor such that the electron wavefunctions are angled in such a way as to enhance shielding from, say adventitious functional groups on the surface of the graphite. It is this shielding factor that hinders aging while the other components of the Hubbard Hamiltonian keep the entire system correlated.

References

(1)   Varley, T. S.; Rosillo-Lopez, M.; Sehmi, S.; Hollingsworth, N.; Holt, K. B. Surface Redox Chemistry and Mechanochemistry of Insulating Polystyrene Nanospheres. *Phys. Chem. Chem. Phys.* **2015**, *17*, 1837-1846.

(2)   Lang, X.; Hirata, A.; Fujita, T.; Chen, M. Nanoporous Metal/Oxide Hybrid Electrodes for Electrochemical Supercapacitors. *Nat. Nanotechnol.* **2011**, *6*, 232–236.

(3)   Jiang, J.; Li, Y.; Liu, J.; Huang, X.; Yuan, C.; Lou, X. W. Recent Advances in Metal Oxide-Based Electrode Architecture Design for Electrochemical Energy Storage. *Adv. Mater*. **2012**, *24*, 5166-5180.

(4)   Tasaki, H. The Hubbard Model - An Introduction and Selected Rigorous Results. *J. Phys.: Condens. Matter*. **1998**, *10*, 4353.

(5)   Ferrari, A. C.; Bonaccorso, F.; Fal'ko, V.; Novoselov, K. S.; Roche, S.; Bøggild, P.; Borini, S.; Koppens, F. H. L.; Palermo, V.; Pugno, N.; Garrido, J. A.; Sordan, R.; Bianco, A.; Ballerini, L.; Prato, M.; Lidorikis, E.; Kivioja, J.; Marinelli, C.; Ryhänen, T.; Morpurgo, A.; Coleman, J. N.; Nicolosi, V.; Colombo, L.; Fert, A.; Garcia-Hernandez, M.; Bachtold, A.; Schneider, G. F.; Guinea, F.; Dekker, C.; Barbone, M.; Sun, Z.; Galiotis, C.; Grigorenko, A. N.; Konstantatos, G.; Kis, A.; Katsnelson, M.; Vandersypen, L.; Loiseau, A.; Morandi, V.; Neumaier, D.; Treossi, E.; Pellegrini, V.; Polini, M.; Tredicucci, A.; Williams, G. M.; Hong, B. H.; Ahn, J.-H.; Kim, J. M.; Zirath, H.; van Wees, B. J.; van der Zant, H.; Occhipinti, L.; Di Matteo, A.; Kinloch, I. A.; Seyller, T.; Quesnel, E.; Feng, X.; Teo, K.; Rupesinghe, N.; Hakonen, P.; Neil, S. R. T.; Tannock, Q.; Löfwanderaq, T.; Kinaret, J. Science and Technology Roadmap for Graphene, Related Two-Dimensional Crystals, and Hybrid Systems. *Nanoscale* **2015**, *7*, 4598–4810.

Appendix B - In-Situ Prussian Blue Synthesis on Thermally-Activated Graphite

a

| 1 µm | Mag = 10.00 K X | EHT = 15.00 kV | Signal A = InLens |
| | WD = 12.8 mm | | Signal B = SE2 |

b

| 1 µm | Mag = 10.00 K X | EHT = 15.00 kV | Signal A = InLens |
| | WD = 11.2 mm | | Signal B = SE2 |

c

| 1 µm | Mag = 10.00 K X | EHT = 15.00 kV | Signal A = InLens |
| | WD = 11.2 mm | | Signal B = SE2 |

d

| 100 nm | Mag = 50.00 K X | EHT = 15.00 kV | Signal A = InLens |
| | WD = 11.2 mm | | Signal B = SE2 |
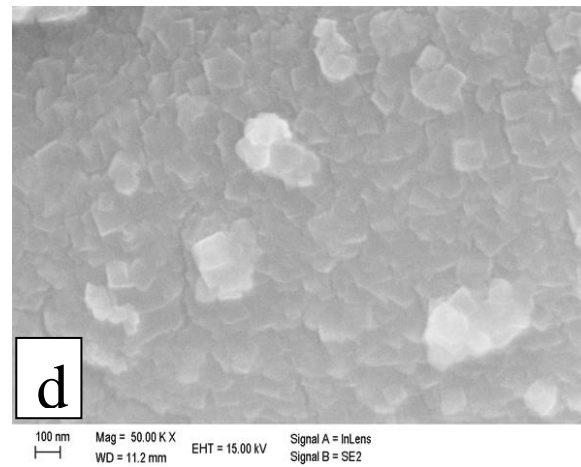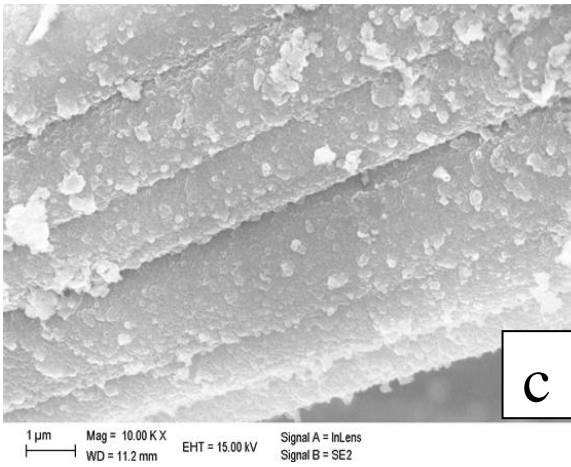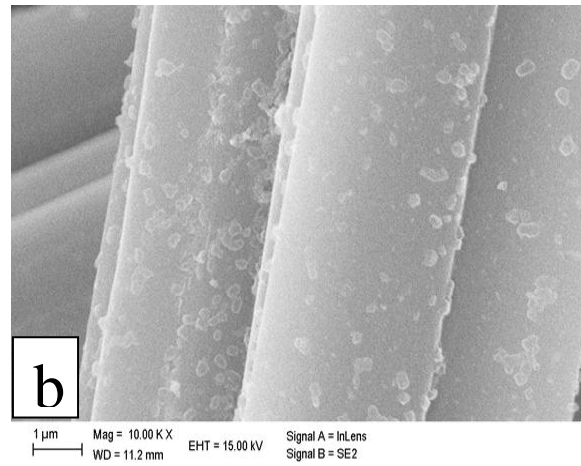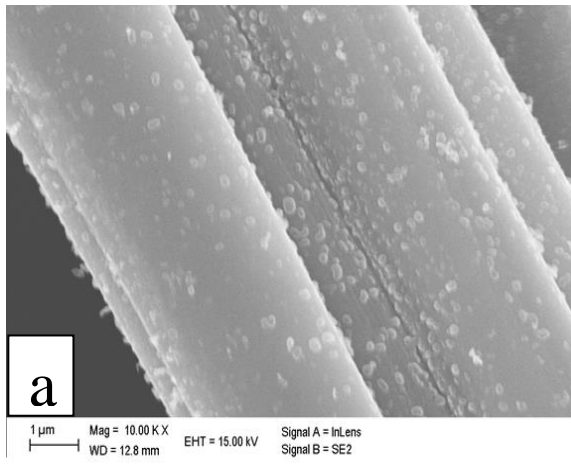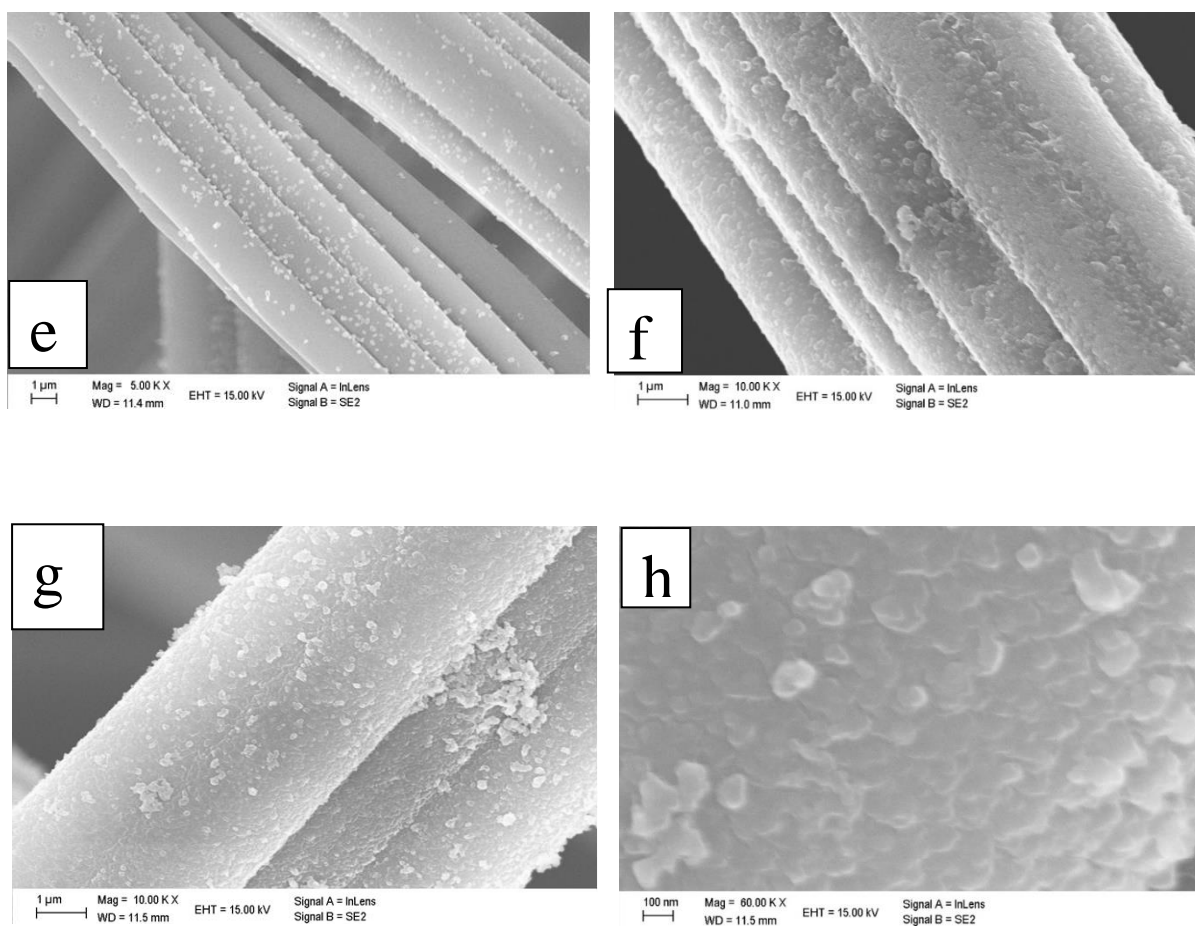
Figure S3.1: Surface morphology images acquired via SEM of a: Pristine GFA3 (no PBNP); b: Pristine GFA3-PBNP (2x dipped); c: Pristine GFA3-PBNP (3x dipped) and d: Pristine GFA3-PBNP (3x dipped) at higher magnification; e: Treated GFA3 (no PBNP); f: Treated GFA3-PBNP (2x dipped); g: Treated GFA3-PBNP (3x dipped) and h: Treated GFA3-PBNP (3x dipped) at higher magnification.
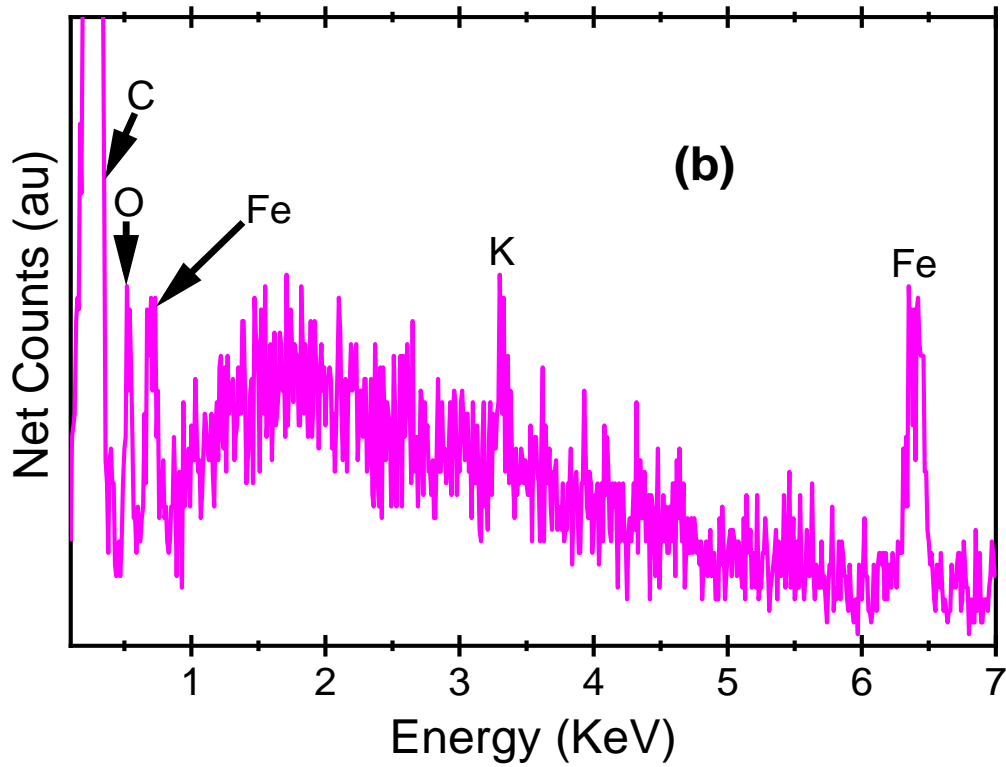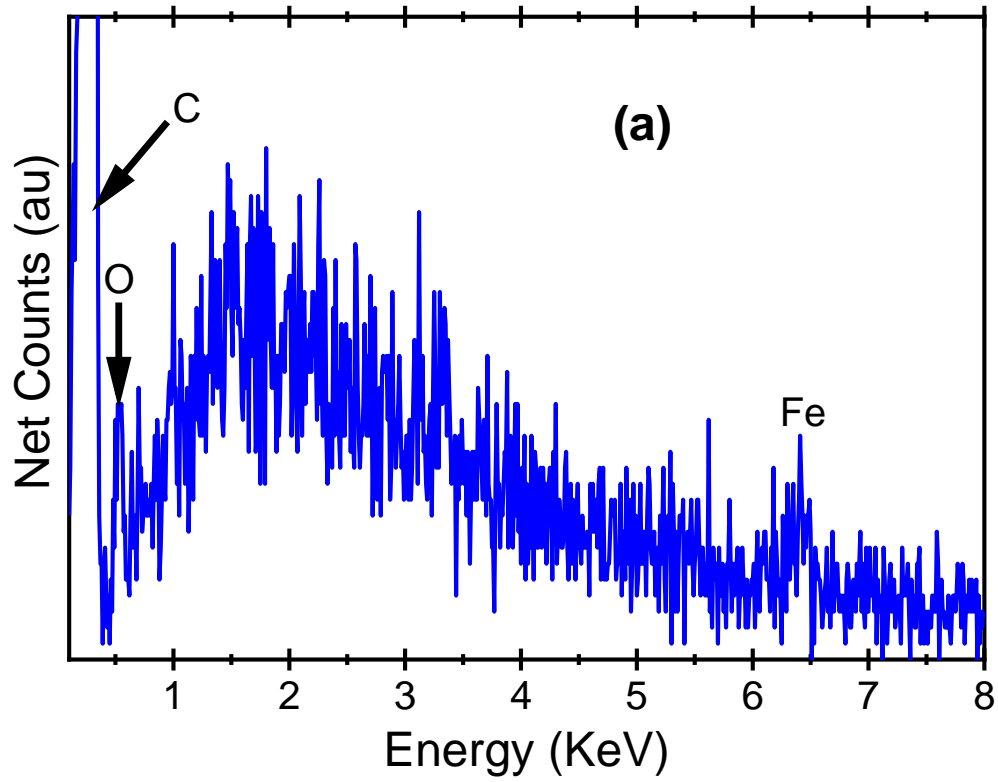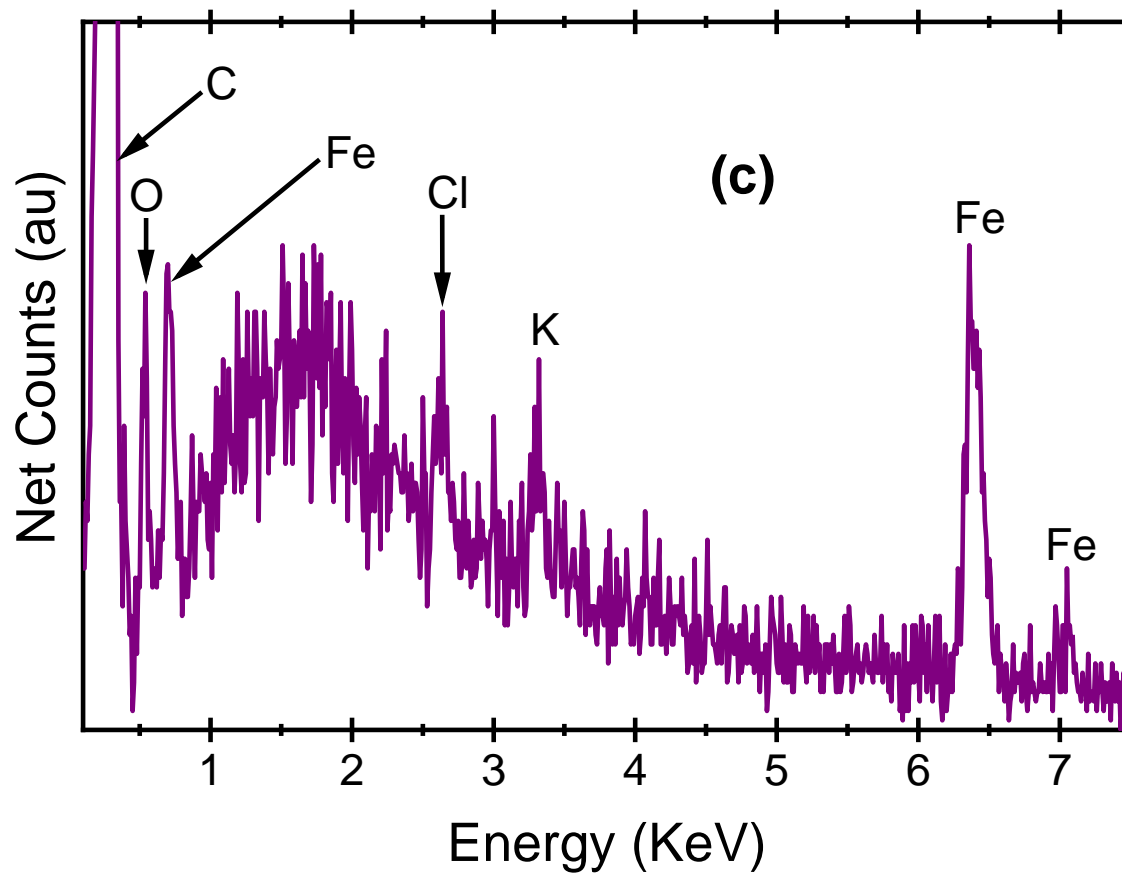
Figure S3.2: The EDS plots of (a) Pristine GFA3-PBNP_(2x dipped); (b) Pristine GFA3-PBNP_(3x dipped) and (c) Treated GFA3-PBNP_(3x dipped).
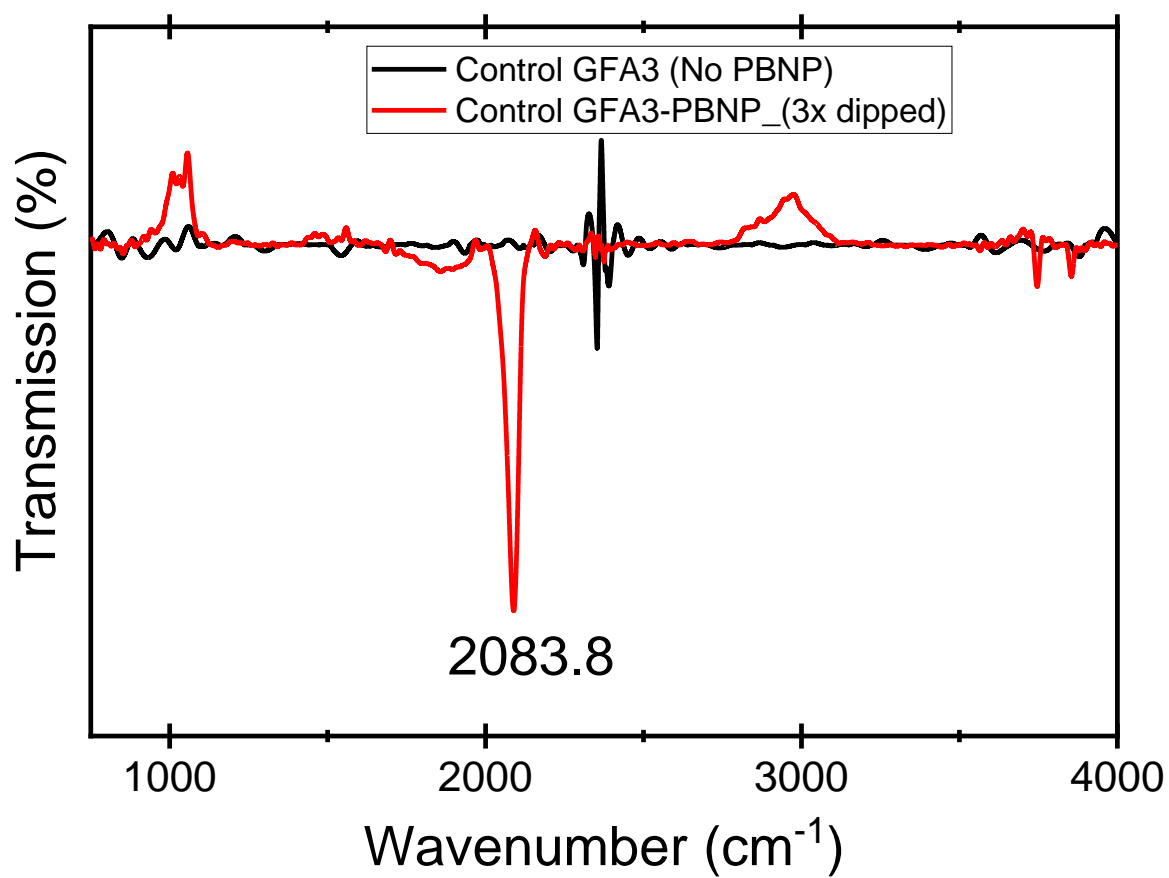
Figure S3.3: ATR-FTIR spectrum of control (pristine)-GFA3-PBNP
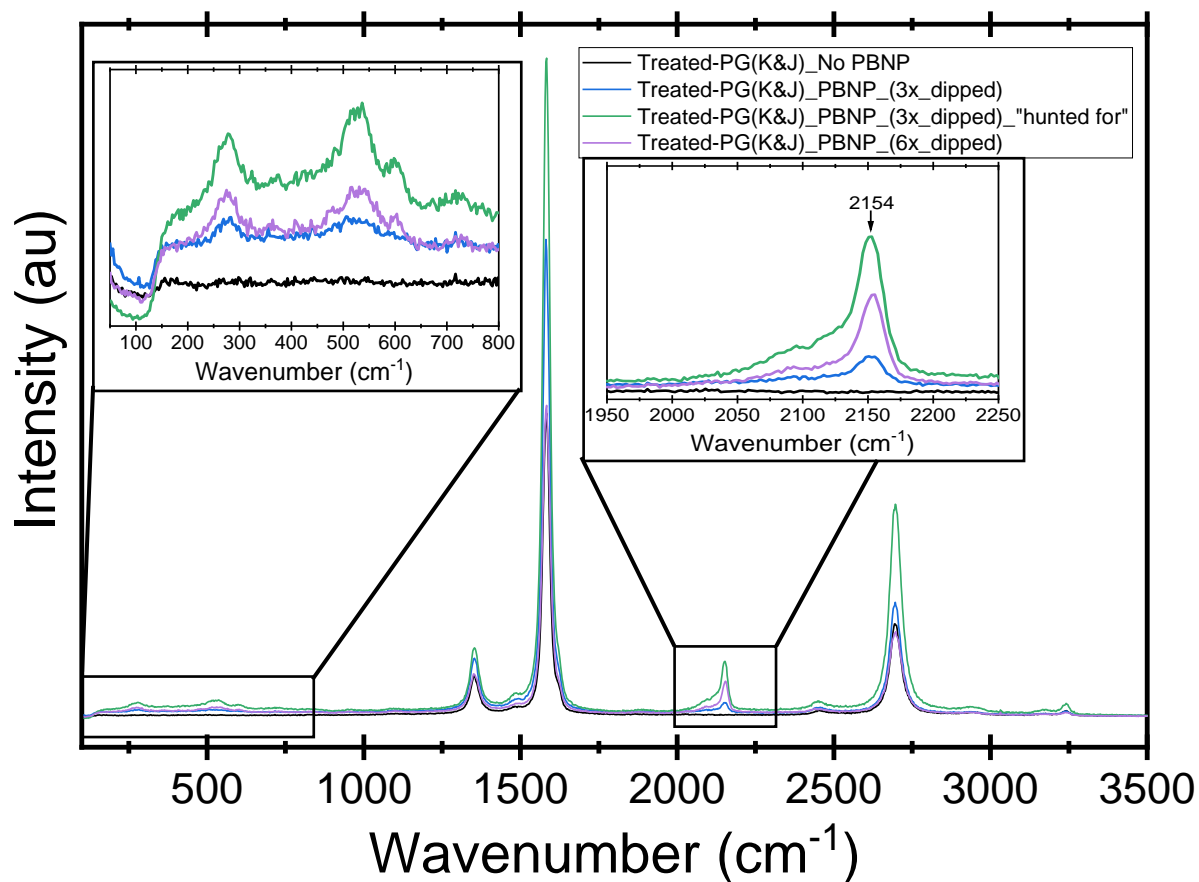
Figure S3.4: Raman spectra of the Treated-PG(K&J) in the absence and presence of PBNP (3x dipped and 6x dipped). The plot labelled (3x dipped)_"hunted_for" was obtained by scanning the surface of the PG to find out if there is a local concentration of PBNP enough to excite Raman intensities stronger than the intensities of the "3x dipped", which were repeatedly obtained several times. The left insert is the region at 750 cm^{-1} and less showing the various stretching and deformation modes of the M-CN. The right insert is the Raman of a single fiber that showed a mode at 2153 cm^{-1}.
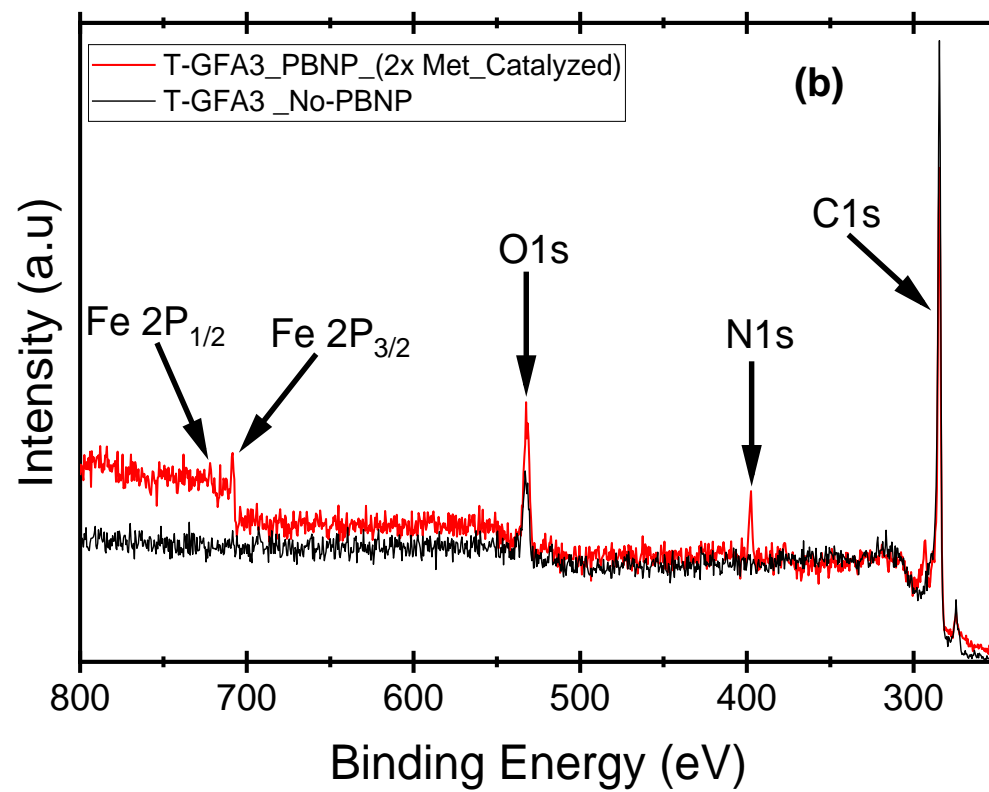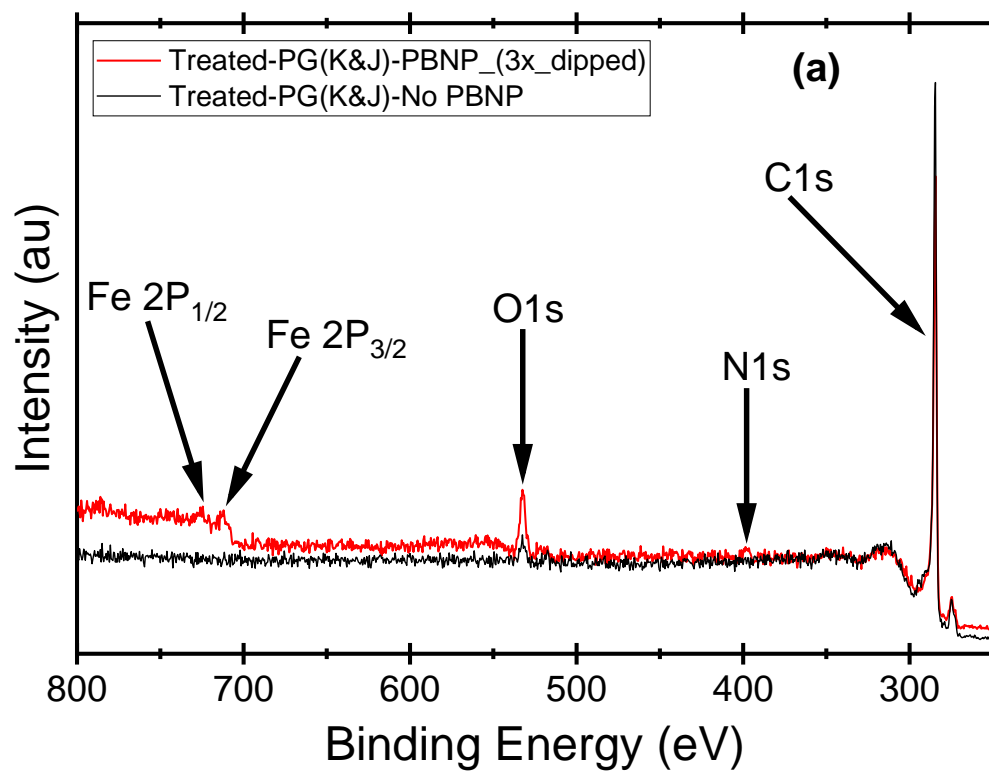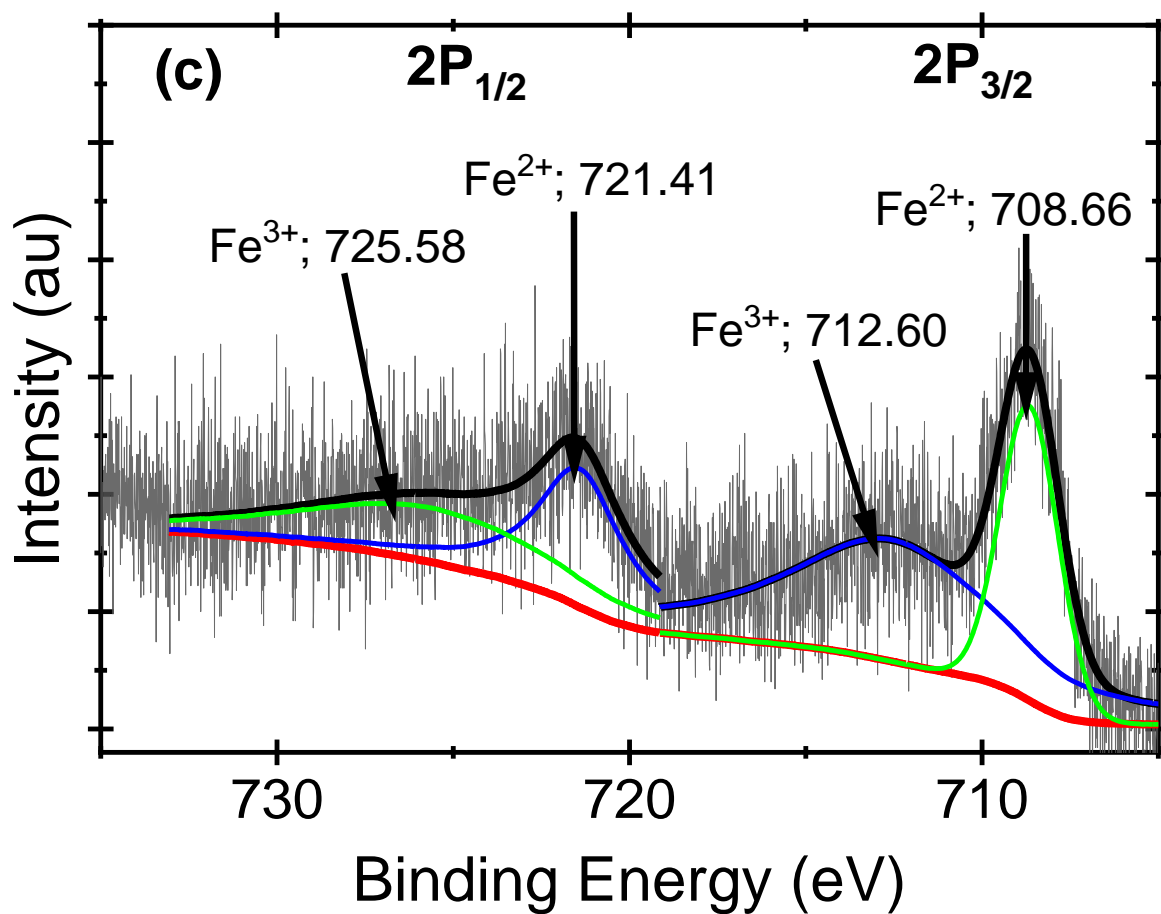
Figure S3.5: Wide angle ("survey") XPS spectra of (a) treated PG(K&J)-PBNP (3x dipped) and treated PG(K&J) (No PBNP). (b) Treated GFA3-PBNP_(2x Met-Cat) and Treated GFA3-No PBNP. (c) High resolution Fe2P XPS spectra of Treated GFA3-PBNP_(2x Met-Cat).
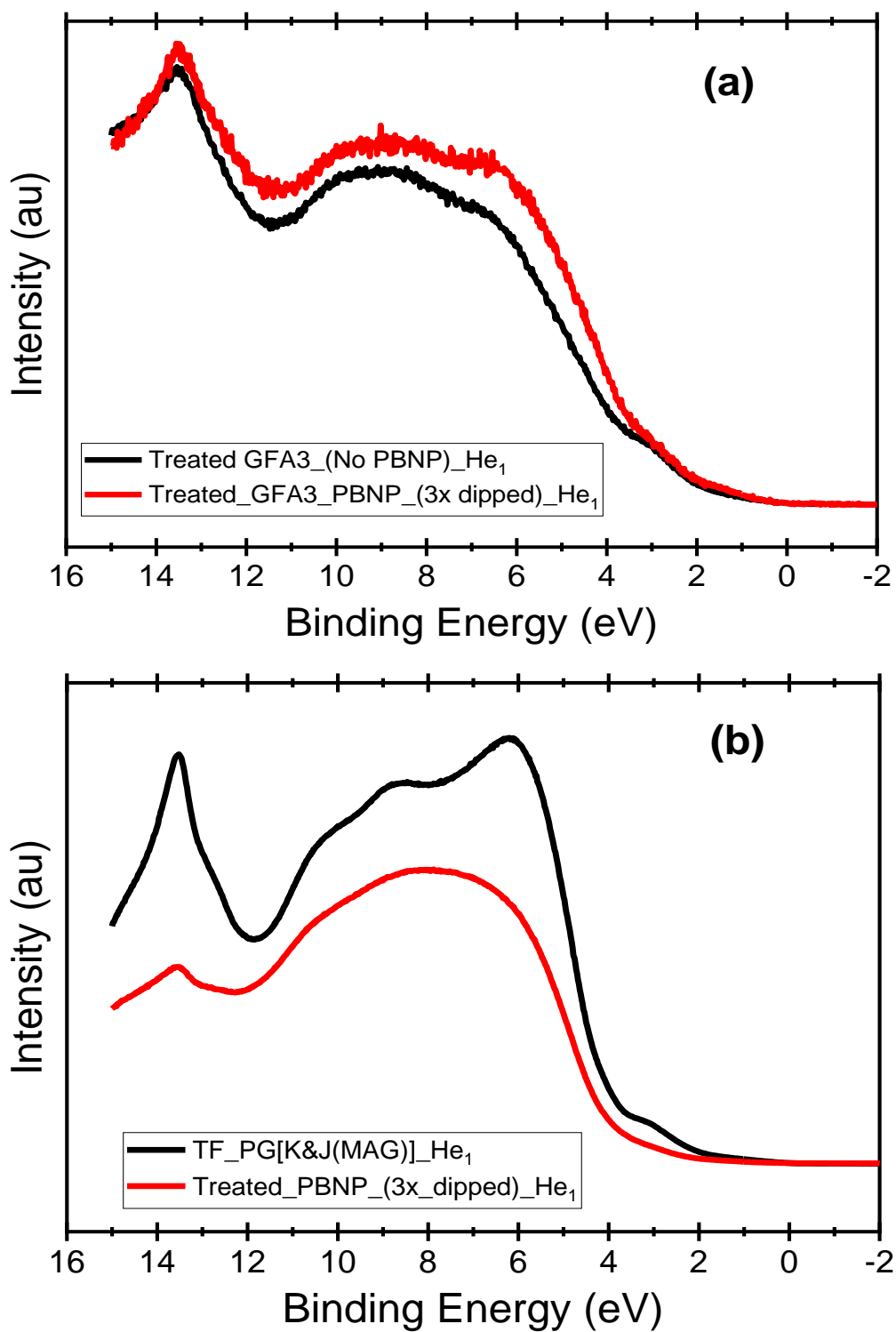
Figure S3.6: (a) the valence band spectra at the HOMO obtained from the He$_2$ and (b) He$_1$ lines of the treated PG(K&J)-PBNP_ (3x dipped) and its control, treated PG(K&J)_(No PBNB).
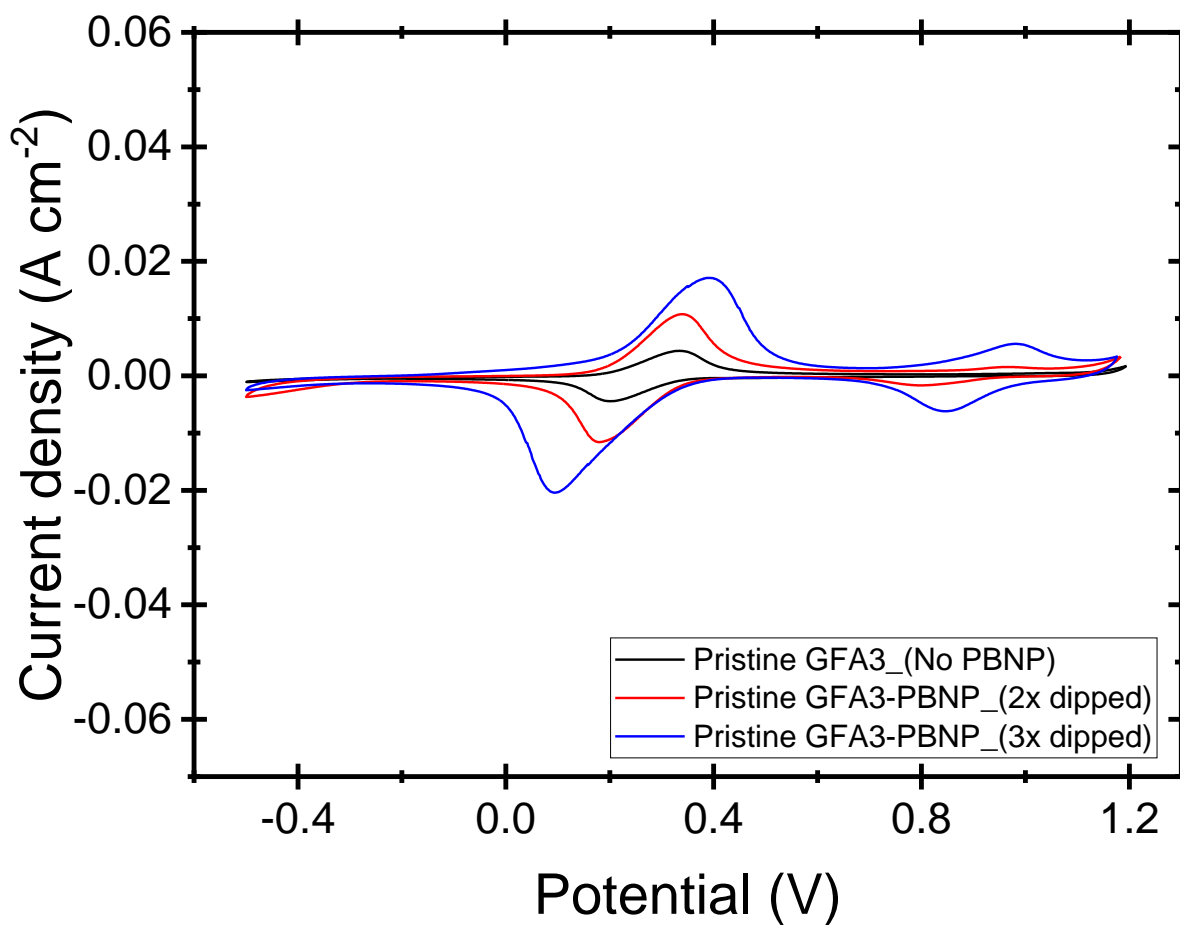
Figure S3.7: The CV in 1 mM Fe(CN) 1M KCl of Pristine GFA3 (No PBNP), pristine GFA3-PBNP_(2x dipped) and pristine GFA3-PBNP_(3x dipped). $\nu = 0.05$ V.s^{-1}.
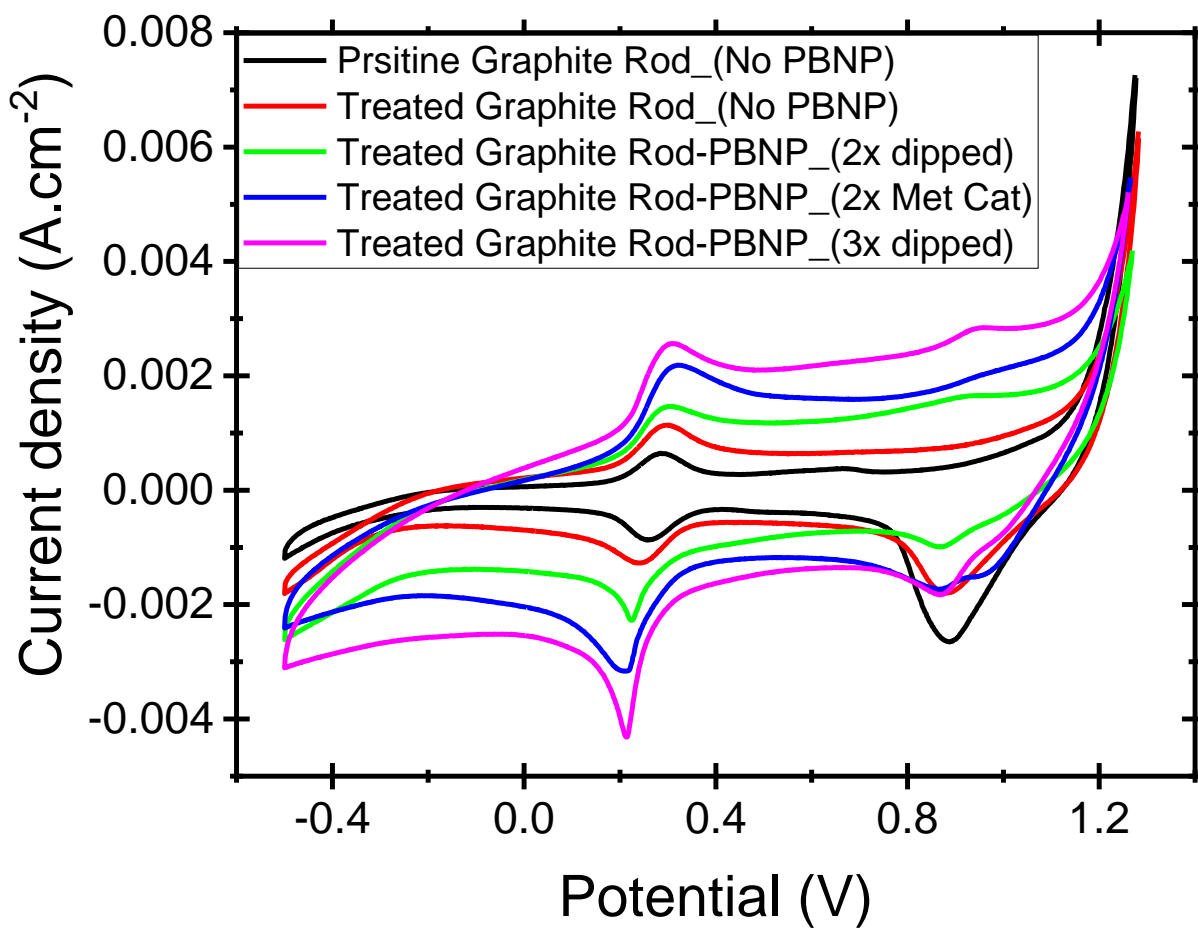
Figure S3.8: The CV in 1M KCl of pristine graphite rod (GR), treated GR and treated GR-PBNP at various dipping cycles of the synthesis reagents.

Appendix C- Increased Electron Transfer Kinetics and Thermally Treated Graphite Stability through Improved Tunneling Paths
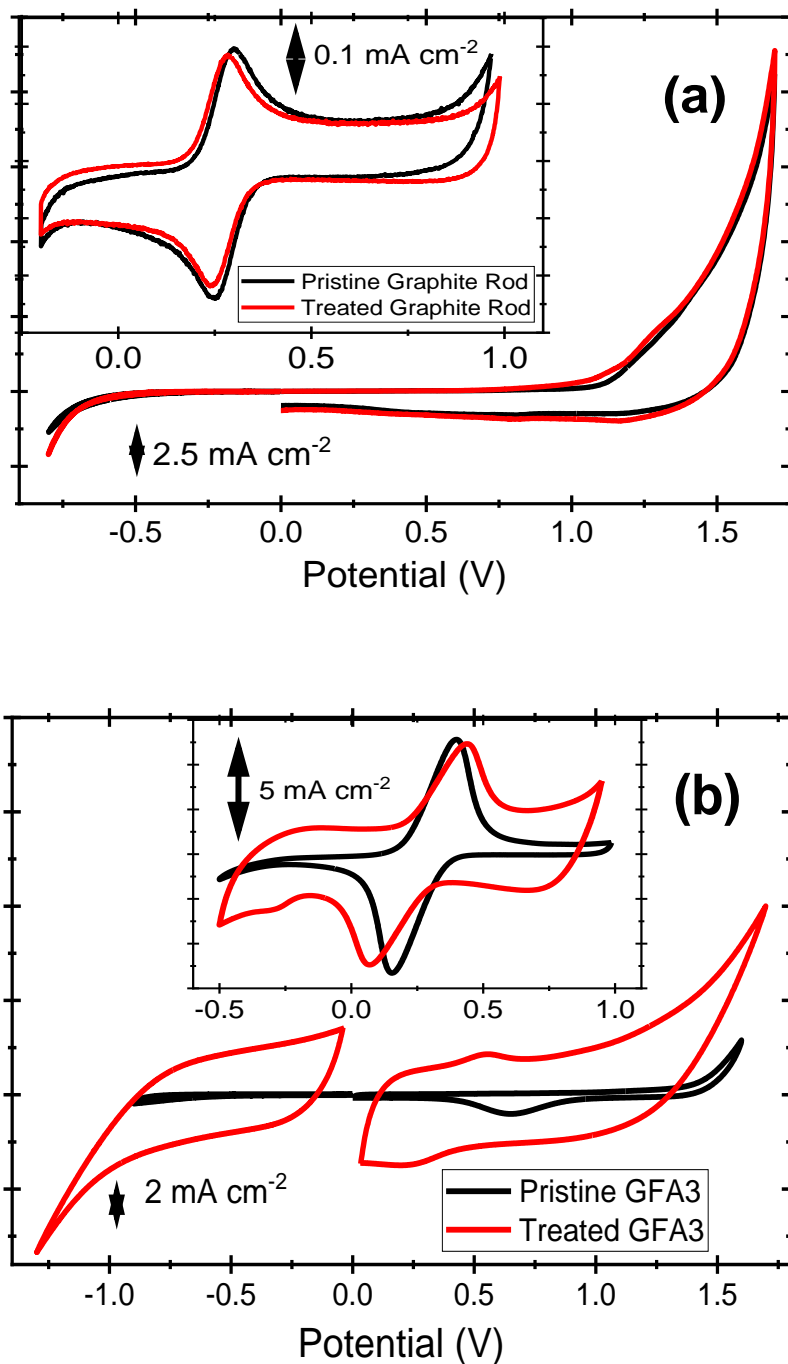
Figure S4.1: The potential windows in 1 M H_2SO_4 of (a) pristine and treated graphite rod, (b) pristine and treated GFA3. Inserts of (a) and (b) are their cyclic voltammograms (CVs). Cyclic voltammograms (CVs) were run in 1mM $Fe(CN)_6^{3-/4-}$ (1M KCl) and at $\nu = 0.05$ V/s.
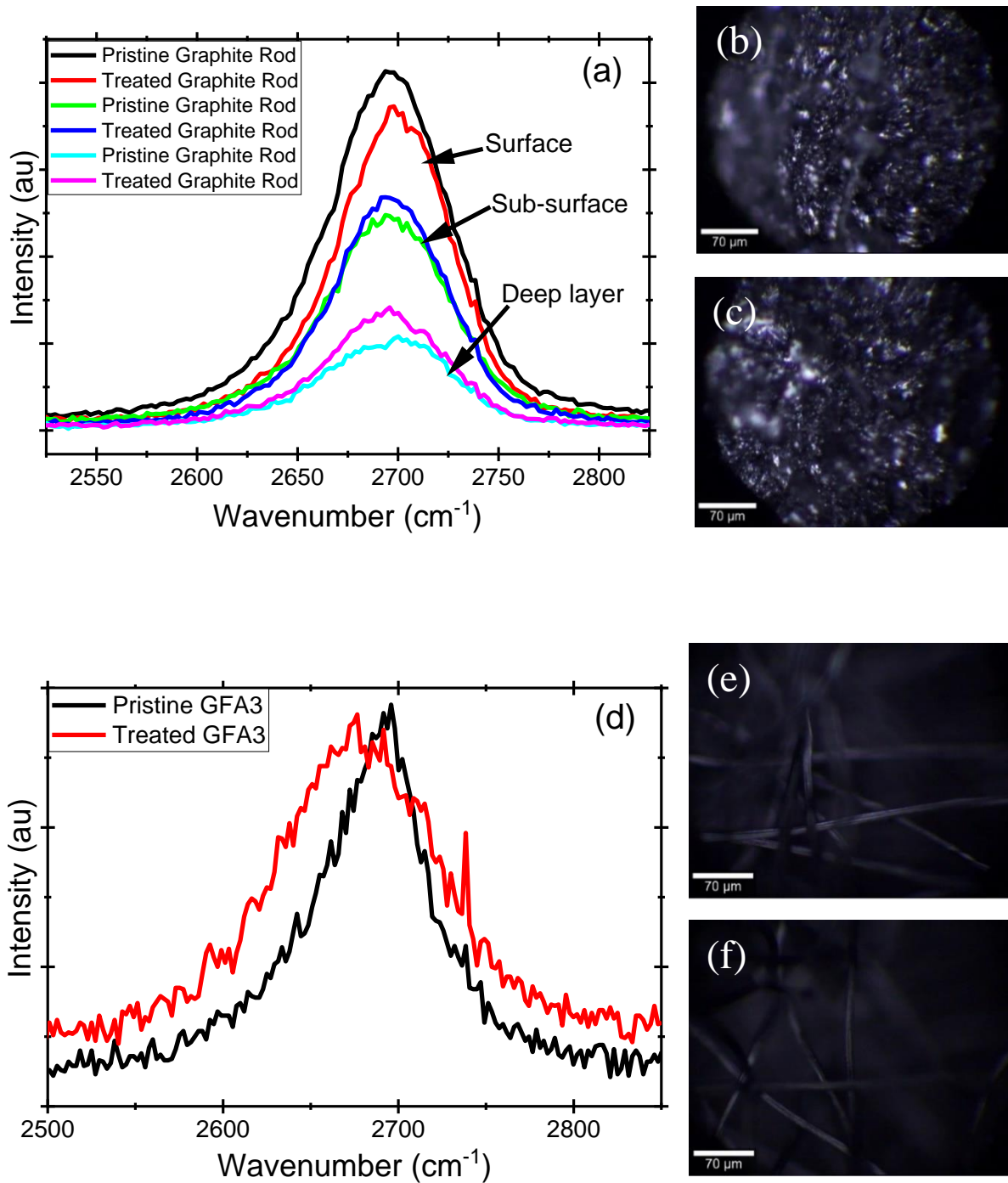
Figure S4.2: Raman spectra of the 2D band of pristine and treated (a) graphite rod, (d) GFA3. Optical images, respectively, of pristine and treated (c, d) graphite rod, and (e, f) GFA3.
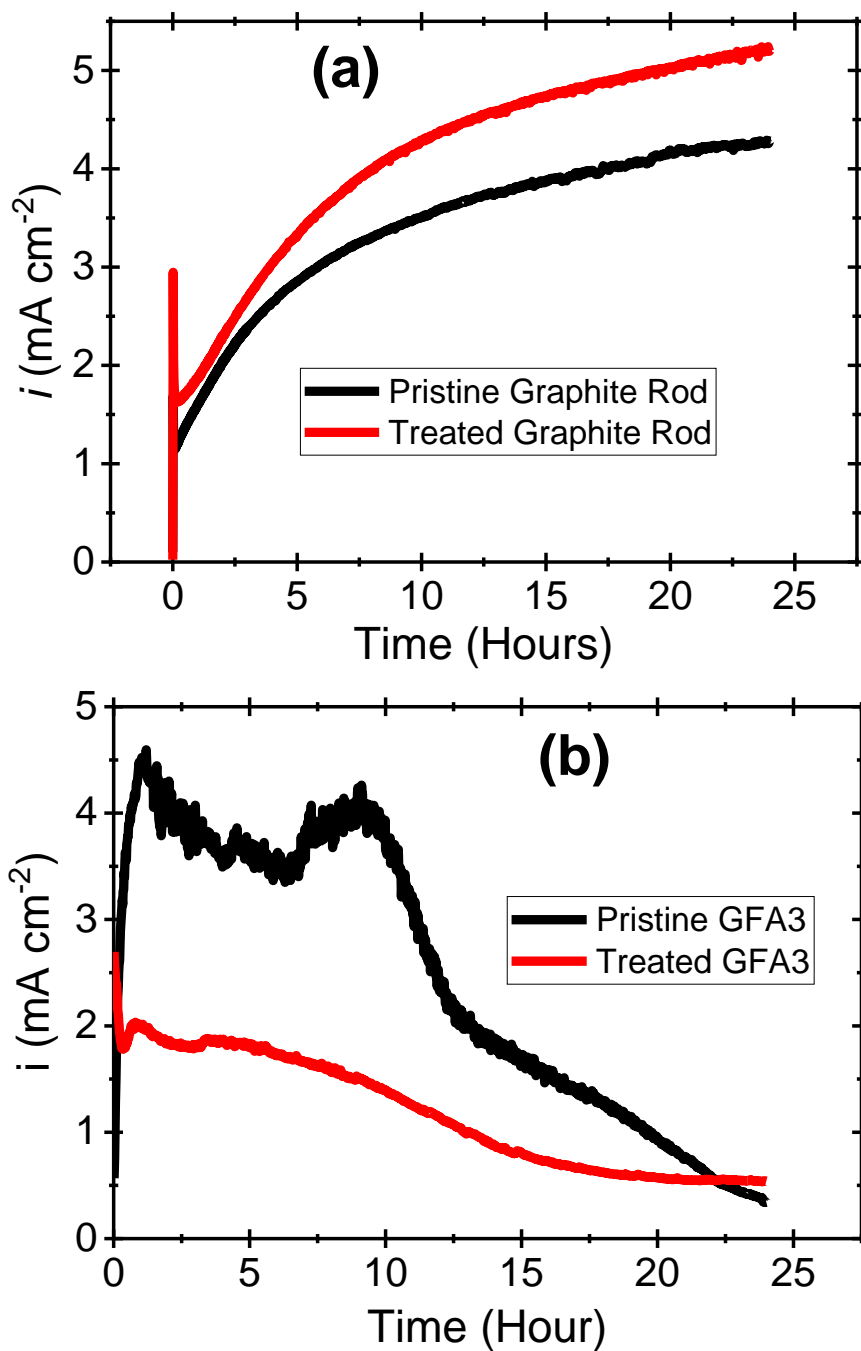
Figure S4.3: Bulk electrolysis in 0.10 M Na$_2$SO$_4$ for 24 hours at 1.6V for pristine and treated (a) graphite rod and (b) GFA3.
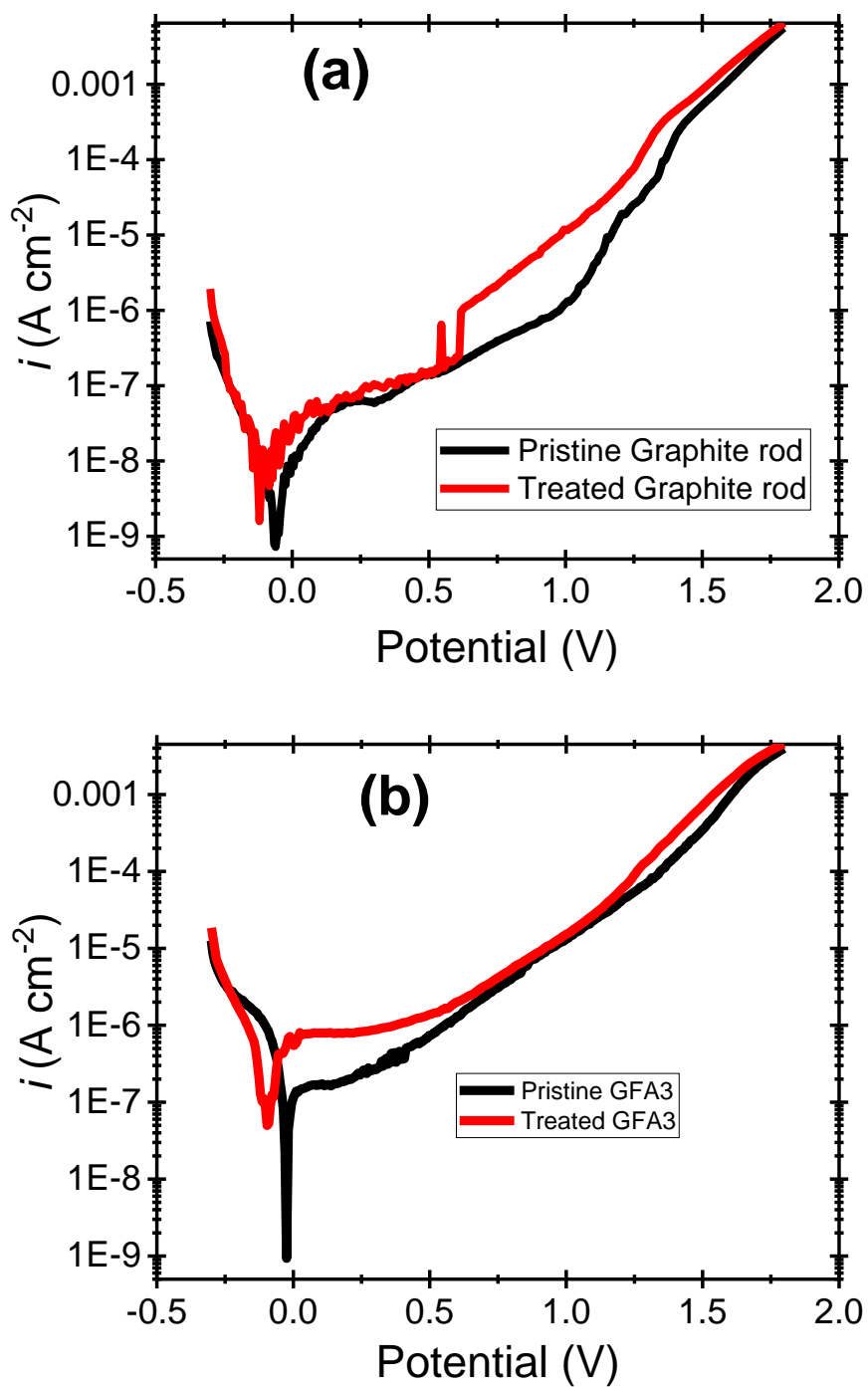
Figure S4.4: Potentiodynamic studies in 0.10 M Na_2SO_4 for 24 hours at 1.6V for pristine and treated (a) graphite rod and (b) GFA3.
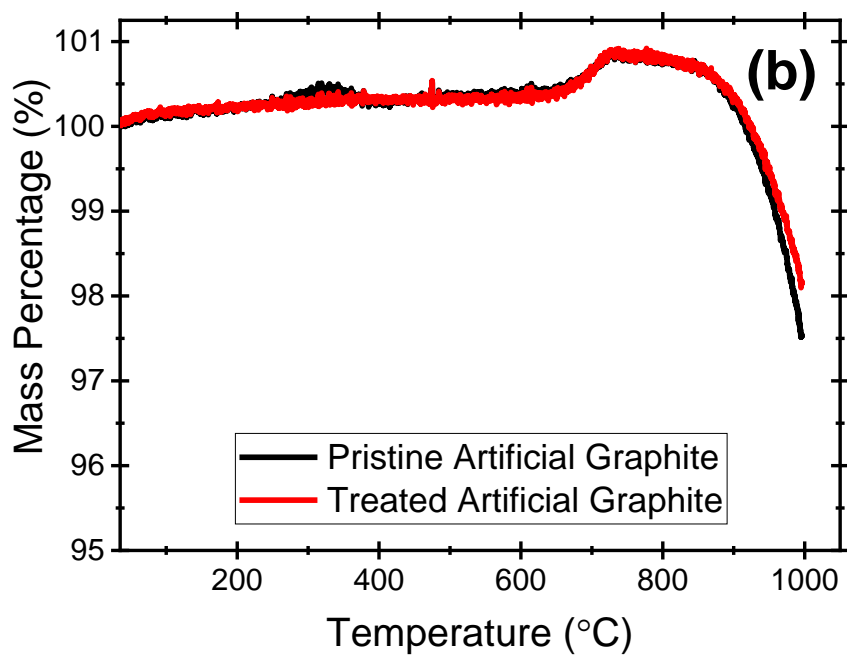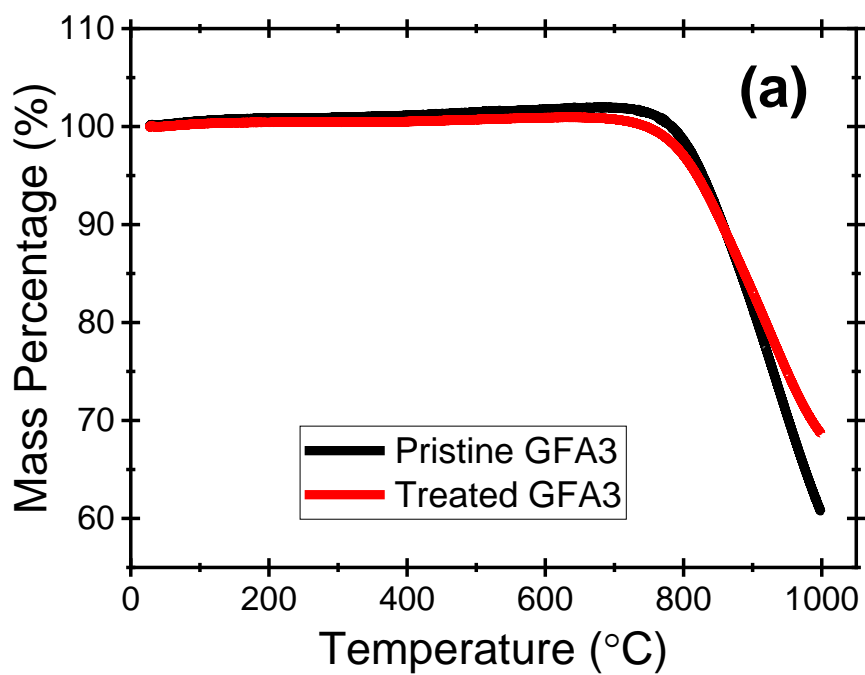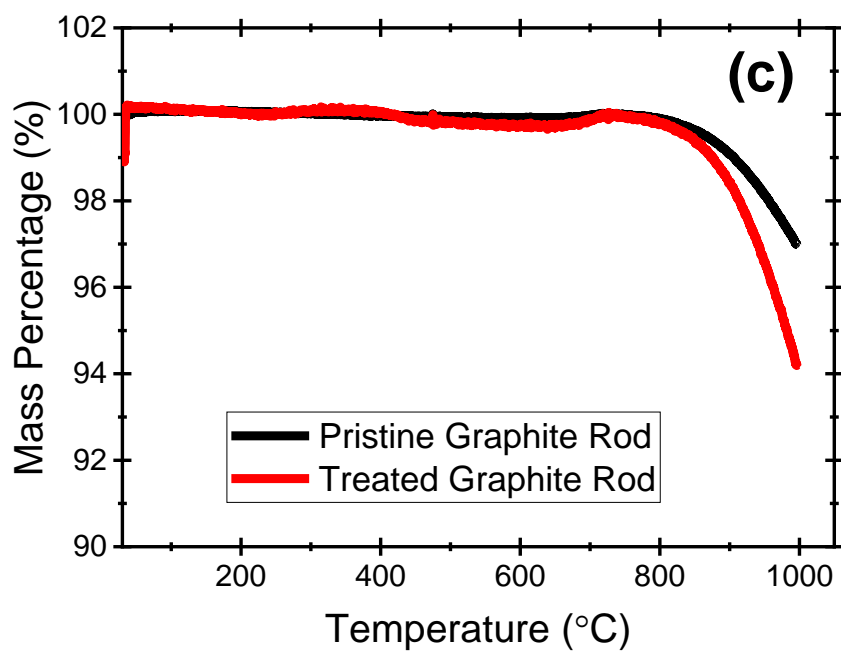
Figure S4.5: The thermogravimetry analysis (TGA) figures of pristine and treated samples of (a) GFA3 (b) artificial graphite and (c) graphite rod.
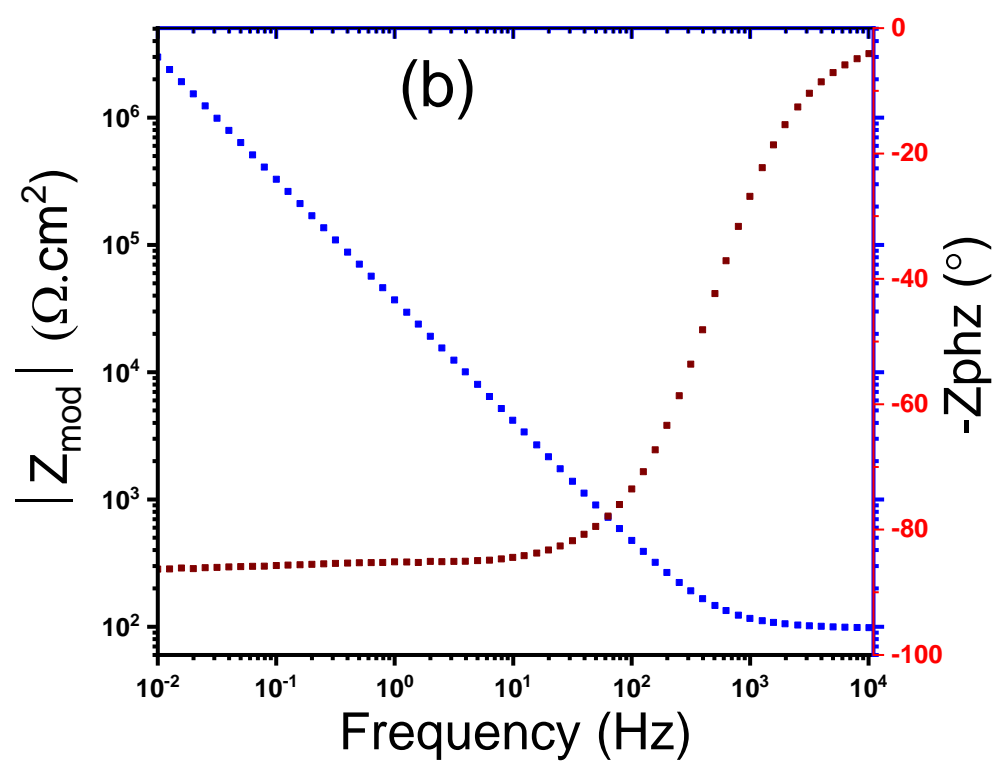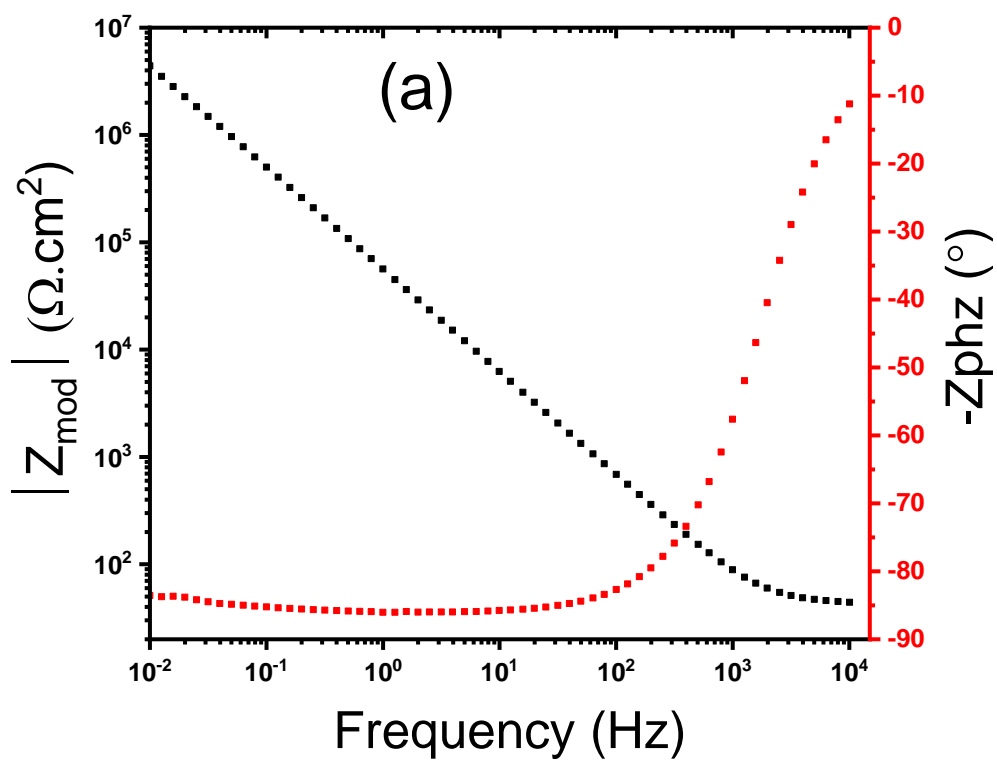
Figure S6: The Bode plots of (a) pristine and (b) treated PG (K&J) in 0.10 M Na$_2$SO$_4$.

(a)

(b)

0.40 µm

0.35

0.30

0.25

0.20

0.15

0.10

0.05

0.00

(c)

(d)

0.40 μm

0.35

0.30

0.25

0.20

0.15

0.10

0.05

0.00
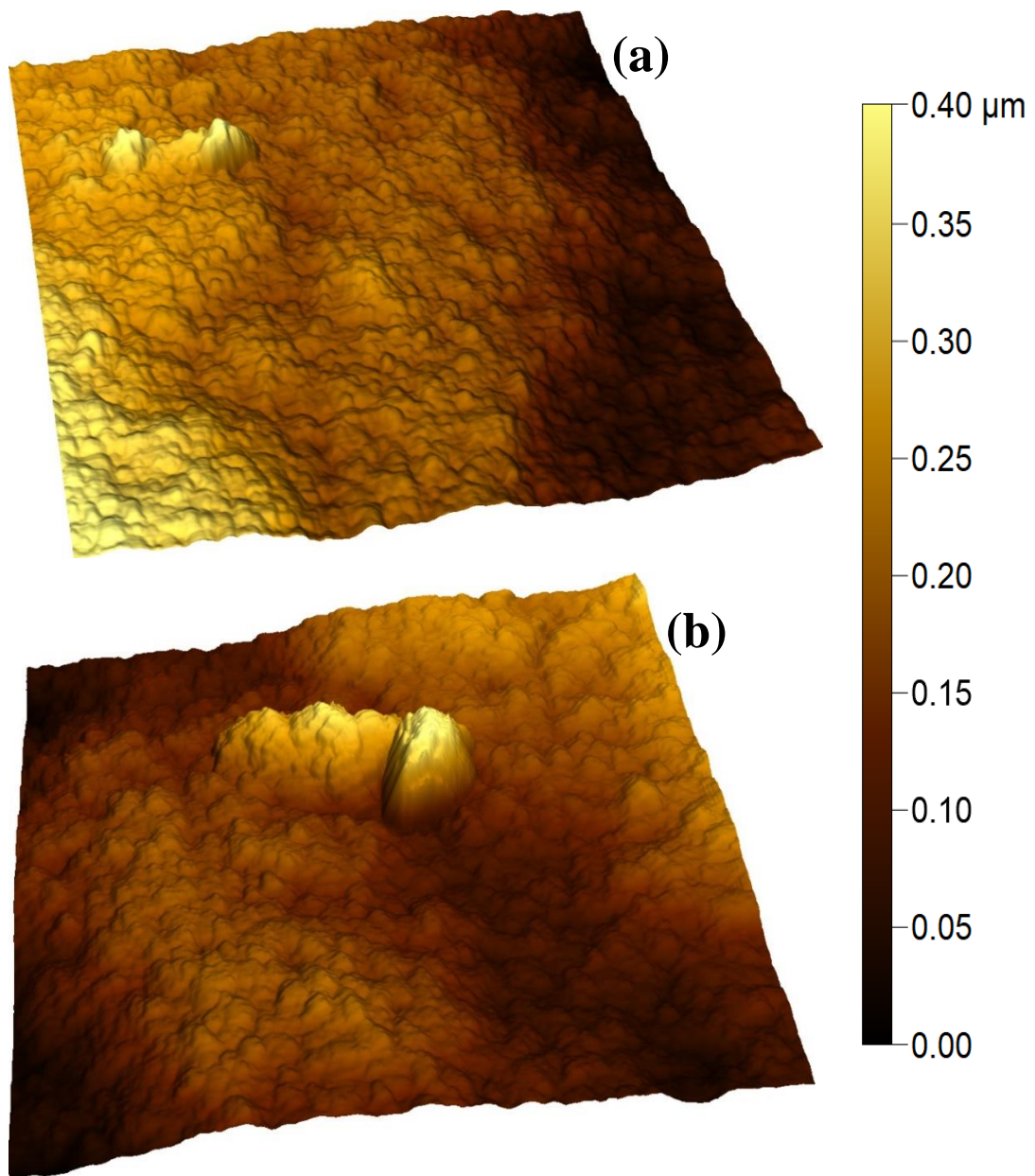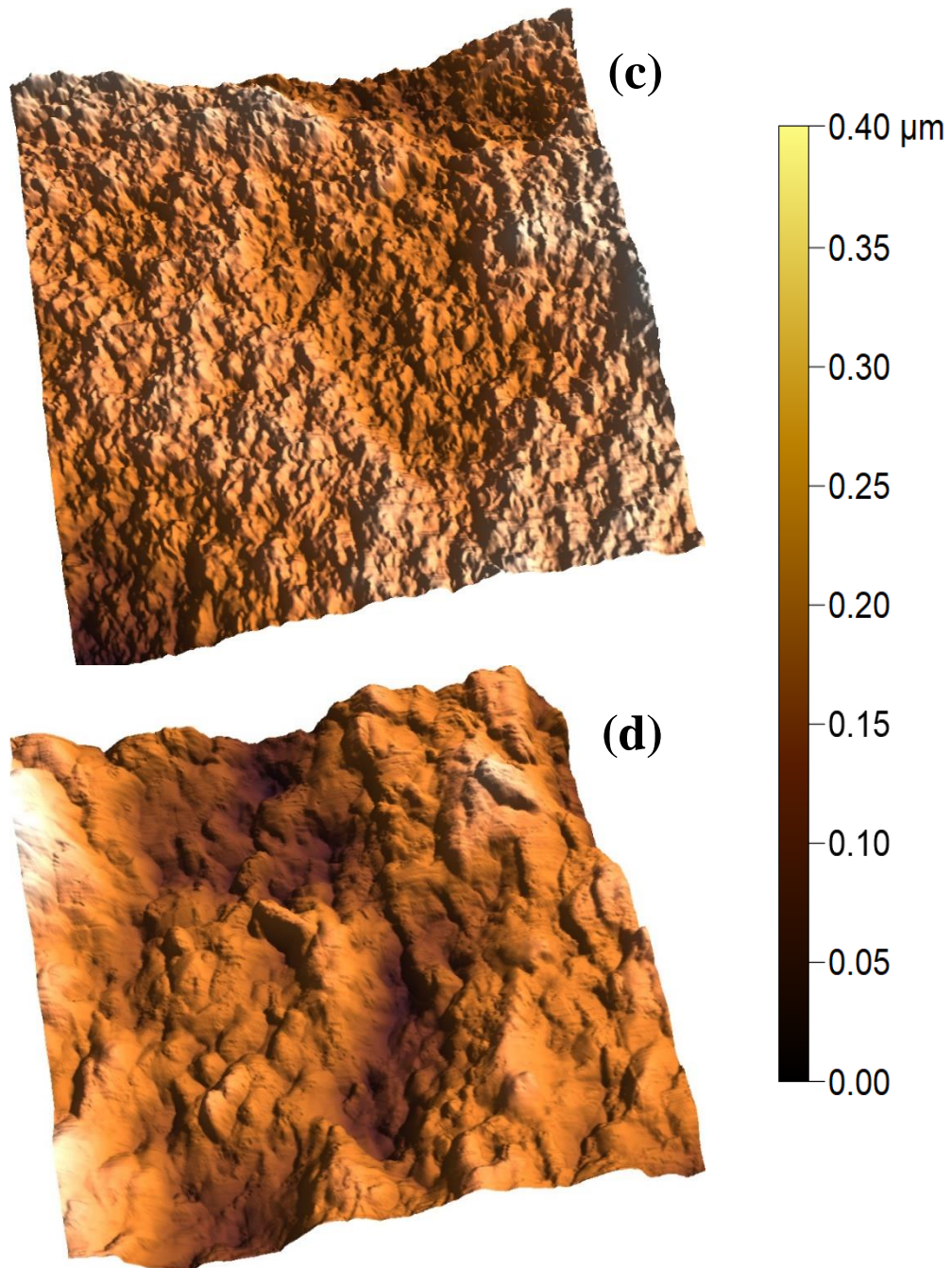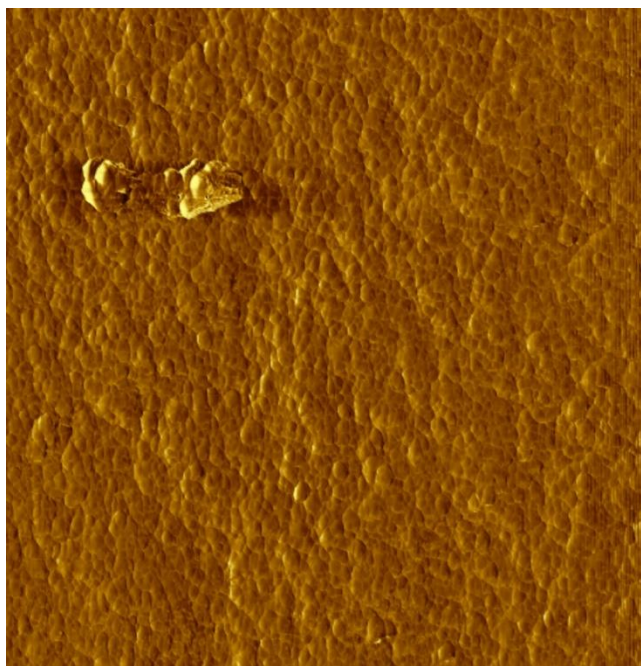
(e)
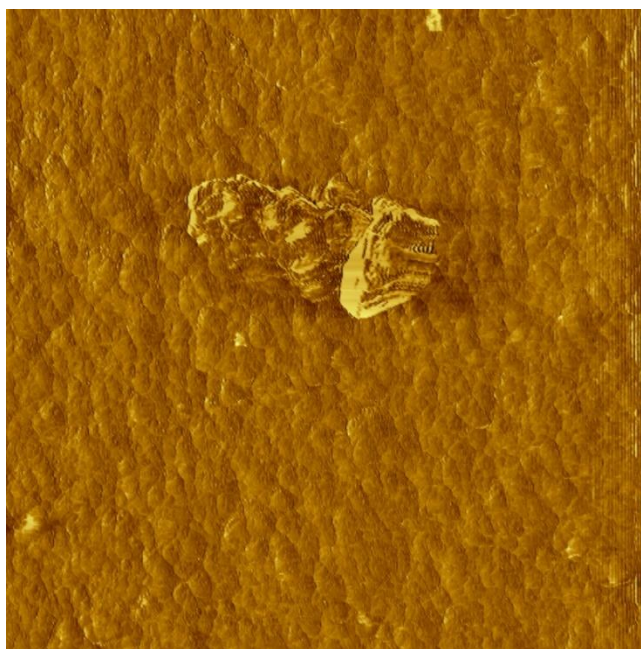
(f)

Figure S7: The light-microscopy-AFM images of the 3D topology (6 μm scans) of (a) pristine, (b) treated PG (K&J); (c) 3 μm scan of pristine and (d) 1 μm scan of treated PG (K&J); 6 μm phase scans of (e) pristine, (f) treated PG (K&J).